From Material Design to Building-Envelope Performance: Multiscale Evaluation of Phase-Change-Material-Enhanced Hemp–Lime Composites

Ziqi Zhang

Under the supervision of
Dr. Miroslava Kavgic
Dr. Martin Noël

Thesis submitted to the University of Ottawa
in partial Fulfillment of the requirements for the
Doctorate in Philosophy degree in Civil Engineering



uOttawa

Department of Civil Engineering
Faculty of Engineering
University of Ottawa

© Ziqi Zhang, Ottawa, Canada, 2026

Abstract

Hemp-lime composites (HLCs) are increasingly used in sustainable building envelopes because they combine bio-based insulation, moisture buffering, and carbon storage. Their wider use is nevertheless limited by modest thermal energy storage capacity. This thesis addresses that limitation by integrating shape-stabilised, bio-derived phase change materials (PCMs) into HLC to increase latent heat storage while retaining the hygrothermal functions required for building-envelope applications.

The scientific contribution of this work is to link PCM-impregnated hemp-shiv characterisation, binder design, composite performance, and envelope-scale modelling within one PCM-HLC framework. Unlike previous studies that mainly examined isolated PCM additions, this thesis generates new knowledge on how hemp-shiv size, high PCM substitution, SCM-modified binders, casting direction, specimen scale, and multilayer wall configuration jointly governs PCM-HLC performance. Material characterisation showed that smaller hemp shiv increased capillary entrapment and enabled PCM substitution levels of up to 70% under the tested preparation route. To support this high loading, the study developed a binder design incorporating supplementary cementitious materials (SCMs). Silica fume and metakaolin improved the hemp-binder interface and reduced mass loss to below 0.5%, indicating that the cohesive mix design can maintain composite stability during testing and operation.

Comprehensive characterisation of the 70% PCM-HLC revealed a clear multi-criteria performance trade-off. Specific heat capacity increased by up to 80% during phase transition, and baseline sensible heat capacity increased by 60%. These gains were accompanied by matrix densification to 796 kg/m^3, a reduction in compressive strength to 0.18 MPa, and a 66% decrease in moisture buffering value. Even with these reductions, the composite retained sufficient strength for non-load-bearing insulation and remained within the Nordtest Good to Excellent moisture-buffering classifications.

To translate the material findings into building-envelope design, the thesis proposed and numerically optimised a multilayer PCM-HLC sandwich panel for cold climates using finite-volume simulations. The analysis showed that PCM effectiveness is strongly seasonal under the simulated Ottawa climate and the adopted HVAC control assumptions. A double-PCM-layer design reduced the modelled summer cooling load to zero for the representative summer week, but could act as a winter thermal bridge unless the envelope thickness reached at least 14 cm. For space-constrained applications, an optimised 10 cm configuration using a single interior PCM layer, an internal air-cavity thermal break, and exterior HLC insulation provided the most favourable balance of storage and resistance among the configurations tested. Under the same modelling conditions, this design reduced the simulated summer cooling demand to zero and lowered winter heating energy by 27% relative to a monolithic HLC baseline. Overall, the thesis advances understanding of how PCM loading, binder design, porosity, moisture buffering, and thermal resistance interact across material and envelope scales. It also establishes quantitative thresholds and design guidance for using PCM-HLC as a climate-responsive, bio-based building-envelope material.

Keywords: Hemp-lime composites; phase change materials; shape-stabilised fatty acids; passive thermal energy storage; bio-based concrete; hygrothermal performance; sustainable building envelopes.

Acknowledgement

I want to first extend my profound appreciation to my supervisors, Dr. Miroslava Kavgic and Dr. Martin Noël, who have always been so patient, thoughtful, and caring. Thank you for always appreciating my ideas, investing your time and effort into discussing and developing methodologies and experiments from scratch with me, guiding me with your expertise and knowledge, and providing steady support every step of the way. Your rigor and passion for engineering have fundamentally shaped who I am today.

I am also deeply grateful to my examination committee, Dr. Cynthia Cruickshank, Dr. Di Wang, Dr. Phalguni Mukhopadhyaya, and Dr. Reza Foruzanmehr. They offered precious insights and ideas, complemented my research from unique perspectives, and genuinely cared about the progress and future improvement of my work.

I would also like to thank our faculty and staff, including but not limited to Luc Cloutier, Philippe Jolette, Dr. Mus Majeed, and Dr. Gamal Elnabelsya. Navigating a Ph.D. involves countless administrative and logistical hurdles outside of research, and they always went above and beyond to help me through them.

To my labmates and friends who shared long hours troubleshooting experimental setups, discussing numerical models, and refining data analyses. Your technical insights, encouragement, and suggestions that made all the experiments manageable.

My family have always listened patiently to my concerns and supported me both emotionally and financially. Especially to my mom, Fame Yang, who devoted her full love taking care of me and following up with my research so that I can keep everything going: your unconditional love and unwavering support provided a safe harbor through every high and low of this doctoral pursuit. You carried me across the finish line.

This work is dedicated to everyone who offered a helping hand, a listening ear, or a word of encouragement along the way.

Table of Contents

Abstract ii

Acknowledgement iv

List of Figures xiii

List of Tables xix

Nomenclature and symbols xxii

1. Chapter 1: Introduction 1

1.1. Background and rationale 1

1.2. Research objectives 2

1.3. Contribution to the field 3

1.4. Outline of the thesis 4

2. Chapter 2: Literature Review 5

2.1. Hemp Shiv 5

2.1.1. General discussion 5

2.1.2. Hemp shiv size effect on HLC density and compressive strength 6

2.1.3. Hemp shiv size effect on HLC hygrothermal properties 8

2.1.4. Hemp shiv size characterisation method 9

2.2. PCM, HL, and SCM 9

2.2.1. PCM 9

2.2.2. Fatty acids for PCM-HLC 11

2.2.3. Eutectic mixtures and phase-change prediction 13

2.2.4. Impregnation into hemp shiv carriers 17

2.2.5. Hemp to PCM ratio 19

2.2.6. HL 20

2.2.7. SCMs 20

2.3. Binder and HLC mix design 24

2.4. HLC specimen preparation 27

2.4.1. Fatty acids' impact on HLC 27

2.4.2. Mixing and casting procedures of HLC 27

2.4.3. Compaction direction and methods 28

2.5. Experimental methodology assessing HLC 30

2.5.1. Compressive strength test 30

2.5.2. Moisture buffering test 34

2.5.3. Thermal conductivity 35

2.5.4. Thermal resistance 39

2.5.5. Specific heat capacity 39

2.5.6. Thermal diffusivity 40

2.6. Research gap 40

2.6.1. Research gaps overview 40

2.6.2. Motivations by chapter 42

3. Chapter 3: Research Methodology 44

3.1. Research Method Overview 44

3.2. Phase I Experimental Analysis (Chapter 4): Characterisation of Raw Materials and Preliminary Casting 45

3.2.1. Characterization of raw materials 45

3.2.2. Preliminary casting of PCM-HLC 50

3.3. Phase I Experimental Analysis (Chapter 5): Casting Direction and Size Effects of PCM-HLC 54

3.3.1. Sample preparation 55

3.3.2. Compressive strength 57

3.3.3. Thermal properties 58

3.3.4. Moisture buffering value 59

3.4. Phase I Experimental Analysis (Chapter 6): PCM Mix Proportioning 60

3.4.1. Mixing, moulding, and curing 61

3.4.2. Experimental testing 62

3.5. Phase I Experimental Analysis (Chapter 7): Sandwich Block Casting 63

3.5.1. Sample Preparation 64

3.5.2. SEM 65

3.5.3. HFMA thermal test 65

3.6. Phase II Numerical Analysis (Chapter 7): Preliminary Modelling and Validation of Sandwich PCM-HLC 65

3.7. Phase II Numerical Analysis (Chapter 7): Simulation and Sensitivity Analysis of Sandwich PCM-HLC Using Cold-Region Weather Data 65

4. Chapter 4: Material Characterisation and Preliminary Casting 67

4.1. Materials and methods 67

4.1.1. Hemp shiv 67

4.1.2. Binder 69

4.1.3. PCMs 70

4.2. Raw Materials Characterisation Results and Discussion 71

4.2.1. Hemp shiv particle size distribution 71

4.2.2. Initial moisture content 73

4.2.3. Water absorption 74

4.2.4. Moisture retention 75

4.2.5. Density of fatty acids 77

4.2.6. Density of binders 77

4.2.7. Impurities and fibre content 77
4.2.8. SEM 79
4.2.9. Thermal behaviour 80
4.2.10. XRF 85
4.3. Preliminary casting of PCM-HLC 87
4.3.1. Stage I: Maximum PCM Substitution Determination 87
4.3.2. Stage II: Development of SCM-Modified Hybrid Binders 91
4.4. Summary 96
5. Chapter 5: Casting direction and specimen-size effects of PCM-HLC 97
5.1. Novelty and contributions 97
5.2. Sample development 98
5.2.1. Raw materials 98
5.2.2. Compositions of PCM-HLC samples 99
5.3. Results and discussion 99
5.3.1. Compressive strength 99
5.3.2. Sample densities for hygrothermal properties 104
5.3.3. Thermal properties 105
5.3.4. Moisture buffering capacity 111

5.4. Summary 116

6. Chapter 6: Influence of PCM substitution on the hygrothermal and mechanical behaviour of PCM-HLC 118

6.1. Sample development 118

6.1.1. Raw materials 118

6.1.2. Compositions of PCM-HLC samples 119

6.2. Results and discussion 120

6.2.1. Mechanical properties 120

6.2.2. Thermal properties 128

6.2.3. Moisture buffering value 134

6.2.4. Performance trade-off with increased PCM substitution 138

6.3. Summary 141

7. Chapter 7: Experimental and numerical analysis of a multilayer PCM-HLC sandwich panel 143

7.1. Sample development 144

7.1.1. Raw materials 144

7.1.2. Compositions of PCM-HLC samples 145

7.2. Preliminary model validation of PCM-HLC sandwich block 146

7.2.1. Model geometry 146

7.2.2. Governing equations 147

7.2.3. Model validation setup 148

7.2.4. Mesh independence 149

7.2.5. Results and discussion 149

7.3. Numerical model baseline performance 153

7.3.1. Database 153

7.3.2. HVAC control strategy 155

7.3.3. Results and discussion 157

7.4. Sensitivity study: outer insulation thickness (10-16 cm) 160

7.4.1. Geometric sensitivity strategy 160

7.4.2. Model geometry 160

7.4.3. Results and discussion 161

7.5. Sensitivity study: middle-layer thermal resistance 165

7.5.1. Air-cavity strategy 165

7.5.2. Results and discussion 165

7.6. Sensitivity study: PCM phase-change temperature 171

7.6.1. Phase-change-temperature strategy 171

7.6.2. Results and discussion 173

7.7. Sensitivity study: single-PCM-layer configuration 175

7.7.1. Results and discussion 177

7.8. Summary 179

8. Chapter 8: Conclusions, limitations, and future recommendations 181

8.1. General conclusions 181

8.2. Research contributions 182

8.3. Limitations and future work 183

References 186

Appendix A 214

List of Figures

Fig. 2.1. The shape of hemp shivs [39]. 6

Fig. 2.2. Influence of 13 different types of hemp shives with bulk densities ranging from 70.8 kg/m^3 to 158 kg/m^3, tested at 30 days and 180 days [7]. 8

Fig. 2.3. Geometric parameters used to characterize the shape of hemp shivs [39]. 9

Fig. 2.4. DSC diagram of a binary fatty acid mixture of 87.8% CA - 12.2% MA. 13

Fig. 2.5. Phase diagrams of a binary eutectic fatty acid [110]. 16

Fig. 2.6. Vacuum impregnation of CA-PA/WF composites [133]. 18

Fig. 2.7. Mass loss of CA-PA/WF composites with different mass ratios [133].. 19

Fig. 2.8. HL in the literature [22]. 20

Fig. 2.9. Comparative performance of HLC [11]. LCB represents HL: crushed brick, LMK represents HL: MK, LNHL represents HL: natural hydraulic lime. The number indicates the % of SCM being used. Water demend B > A > regular mix design. 25

Fig. 2.10. Relationship between density and thermal conductivity of hemp concrete walls and the relationship established by Cerezo [170]. BM – builder's mix, CM – commercial mix, G – HL:slag binder, G + WR – HL:slag binder with water retainer, M – HL:metakaolin binder, M + WR – HL:metakaolin binder with water retainer. 25

Fig. 2.11. Thermal conductivity of hemp concretes versus density and water content [171]. 26

Fig. 2.12. A graphical representation of the relationship between hemp shiv particle orientations and compaction directions. 29

Fig. 2.13. Compaction setup of HLC samples cut from cylindrical specimen [44]. 29

Fig. 2.14. Compressive strength vs dry density at 28 days of the formulations tested and from several studies from the literature [185]. 31

Fig. 2.15. Thermal conductivity setup using FOX 304 Heat Flow Meter [43]..... 36

Fig. 3.1. Overview of the methodology. 44

Fig. 3.2. Sample ImageJ analysis (left) before processing and (right) after processing. 45

Fig. 4.1. Optical photos of (a) hemp shivs as received; (b) ground medium – sized hemp shivs; and (c) ground small – sized hemp shivs. 68

Fig. 4.2. (a) A portion of the hemp shiv sampler awaiting measurements, (b) hemp shiv sample used for SEM, and (c, d) particle size distribution analysis before and after ImageJ processing. 69

Fig. 5.1. Stress-strain analysis of compressive strength across varying sample orientations and dimensions. 99

Fig. 5.2. Visual observation of the PCM-HLC compressive strength test (left) initial contact and compaction stage; (right) progression of surface cracking and localized spalling at the ultimate failure stage. 101

Fig. 5.3. Thermal conductivity vs. temperature relationship. 106

Fig. 5.4. The correlation of dry density and thermal conductivity. 108

Fig. 5.5. Comparison of specific heat capacity results in this study and in the literature. 110

Fig. 5.6. Box chart of MBV of HLC over 8 cycles, with density and its upper and lower error bounds shown in red, and quasi – steady state MBV shown in green. 112

Fig. 5.7. Density changes of the HLC (including the weight of the tape) measured following the NORDTEST procedures. 113

Fig. 5.8. Moisture buffering capacity with cycles 114

Fig. 6.1. Relationship between dry density and compressive stress for PCM-HLC across varying PCM concentrations. Numerical labels with different colours indicate the specific PCM substitution percentage (0–70%). 120

Fig. 6.2. Experimental compressive strength and density of PCM-HLC as a function of PCM content (0–70%). Error bars represent the maximum and minimum experimental values for each interval. 121

Fig. 6.3. Influence of PCM content on the specific strength of PCM-HLC composites. 124

Fig. 6.4. SEM micrographs at x500 magnifications: (a, b) PCM-HLC at 70% PCM, (c, d) PCM-HLC at 30% PCM, and (e, f) HLC with 0% PCM. 126

Fig. 6.5. Thermal conductivity of PCM-HLC as a function of PCM substitution rate (0% to 70%). 128

Fig. 6.6. Evolution of thermal conductivity of studied composites as a function of density [248]. HC represents hemp concrete that was modified by adding different amounts of MPCM (0, 5, 10, and 15 wt%) 129

Fig. 6.7. Influence of PCM substitution level on the specific heat capacity of the PCM-HLC. 130

Fig. 6.8. Correlation between %PCM substituted and PCM-HLC thermal diffusivity. 131

Fig. 6.9. Correlation between PCM substitution rate and the thermal resistance of the PCM-HLC. 133

Fig. 6.10. The percentage mass change of PCM-HLC samples over five consecutive moisture adsorption and desorption cycles. 134

Fig. 6.11. Stability of MBV for each cycle across various PCM-HLC. 135

Fig. 6.12. Impact of PCM substitution level on the MBV of the PCM-HLC. 137

Fig. 6.13. Normalized performance radar chart illustrating the multi-dimensional trade-offs in PCM-HLC across substitution levels from 0% to 70%..... 139

Fig. 7.1. The sandwich panel design with PCM-HLC core. 145

Fig. 7.2. Geometry of the sandwich block being modelled. 146

Fig. 7.3. Experimental setup for numerical model validation: (a) 10 cm cube sandwich specimen, (b) schematic illustration of specimen with peripheral insulation to ensure unidirectional heat flux, and (c) model setup in ANSYS. 148

Fig. 7.4. Experimental validation of numerical model against experimental HFM result. 150

Fig. 7.5. SEM micrographs of the multi-layer building envelope system components: (a) the 70% PCM-HLC layer; (b) the porous morphology of the middle and

outer insulation layers; and (c) the dense, continuous surface topography of the lime plaster indoor facing. 152

Fig. 7.6. Outdoor temperature profile over a typical summer and winter week. 154

Fig. 7.7. HVAC control strategy showing heating and cooling setpoints..... 156

Fig. 7.8. Dynamic thermal response of the 10 cm PCM-HLC sandwich panel versus a monolithic HLC control under representative Ottawa summer and winter conditions. 157

Fig. 7.9. Comparative energy performance of a 10 cm thickness monolithic HLC and sandwich PCM-HLC in typical summer and winter conditions. 159

Fig. 7.10. Sandwich PCM-HLC geometry for insulation layer scaling parametric study. 161

Fig. 7.11. Comparison of interior surface temperatures for monolithic HLC and sandwich PCM-HLC across varying wall thicknesses (10–16 cm) in typical summer and winter weeks. 162

Fig. 7.12. Comparative energy performance of 10–16 cm thickness monolithic HLC and sandwich PCM-HLC in the typical winter week. 163

Fig. 7.13. Comparative analysis of a 10 cm thickness air-core sandwich PCM-HLC design against the original sandwich PCM-HLC and a monolithic control under typical summer and winter weeks. 166

Fig. 7.14. Comparative energy performance of 10 cm thickness monolithic HLC, sandwich PCM-HLC, and air-core sandwich PCM-HLC in the typical summer and winter week. 167

Fig. 7.15. Comparative analysis of a 12 cm thickness air-core sandwich PCM-HLC design against original sandwich PCM-HLC and a monolithic control under representative summer conditions..... 169

Fig. 7.16. Comparative energy performance of 12 cm thickness monolithic HLC, sandwich PCM-HLC, and air-core sandwich PCM-HLC under typical summer and winter weeks..... 170

Fig. 7.17. Comparative dynamic thermal response of a 12 cm monolithic HLC baseline and 12 cm air – core sandwich PCM-HLC configurations utilizing spatial phase – change temperature gradients under representative summer and winter conditions. .. 173

Fig. 7.18. Comparative energy performance of 12 cm thickness monolithic HLC and air-core sandwich PCM-HLC across different phase change temperatures..... 175

Fig. 7.19. Schematic illustration of singular PCM sandwich design. 176

Fig. 7.20. Dynamic thermal response of the 10 cm building envelope configurations showing interior surface temperature profiles under typical summer and winter weeks. 177

Fig. 7.21. Comparative seasonal heating and cooling energy consumption across monolithic, original double PCM layer sandwich, and optimised singular PCM sandwich design building envelope configurations. 178

List of Tables

Table 2.1. The effect of hemp shiv size on the density and compressive strength of HLC..... 7

Table 2.2. Summary of MPCM incorporation rate across studies. 10

Table 2.3. Thermal properties of pure fatty acids [13, 107, 110, 111, 114–123]. 12

Table 2.4. Fatty acids binary mixtures and their carriers from the literature..... 15

Table 2.5. The theoretical fatty acids eutectic mass ratios and their predicted thermal properties. 17

Table 2.6. Comparison of C – S - H and C – A - S – H..... 21

Table 2.7. Comparison of SCMs..... 23

Table 2.8. Principal standards employing 50 mm and 100 mm cubes. 31

Table 2.9. HLC studies that used different sample sizes for compressive strength test. 33

Table 2.10. The FOX 304 HFM specifications..... 37

Table 2.11. Insulation values for some of the commercial insulation materials [211]. 39

Table 4.1. Statistical value for the initial moisture content. 73

Table 4.2. Density of fatty acids. 77

Table 4.3. Binder density. 77

Table 4.4. The single-component fatty acids' thermal properties. 81

Table 4.5. Comparison of capric acid properties across different supplies and studies. 82

Table 4.6. Thermal properties of binary fatty acids. 84

Table 4.7. Chemical compositions of binders [22]. 86

Table 4.8. Evaluation of casting viability of PCM-HLC across varying hemp shiv sizes, PCM, and binder ratios. 90

Table 4.9. Chemical and molar composition of binder mixes adjusted for constant CaO/SiO_2 stoichiometry..... 92

Table 5.1. Mechanical properties of PCM-HLC specimens (Mean ± SD). 102

Table 5.2. The average dry density for various compaction directions and thicknesses. 104

Table 5.3. Experimental HFM temperature settings for thermal testing. 105

Table 6.1. Varying PCM substitution ratio – PCM-HLC compositions..... 119

Table 6.2. Statistical analysis of MBV 136

Table 7.1. Monolithic HLC and PCM-HLC Sandwich panel compositions. 146

Table 7.2. Material properties of the sandwich PCM-HLC and the monolithic HLC..... 149

Table 7.3. Mesh independence of the model. 149

Table 7.4. Sources of the input values in the simulation. 155

Table 7.5. Energy savings and calculated efficiency per unit thickness for various thicknesses of sandwich PCM-HLC wall. 164

Table 7.6. PCM phase transition temperature ranges used for gradient sandwich panel simulations. 172

Table A.1. Physical and chemical properties of HL [270]. 214

Table A.2. Physical and chemical specifications of slag from the distributor's mill certificate..... 214

Table A.3. Physical and chemical properties of metakaolin provided by the manufacturer [227]..... 215

Table A.4. Physical and chemical properties of silica fume [271]. 216

Table A.5. Physical and chemical properties of CA [272]. 216

Table A.6. Physical and chemical properties of LA [272]. 217

Table A.7. Physical and chemical properties of MA [272]. 218

Table A.8. Physical and chemical properties of PA [272]..... 218

Table A.9. Physical and chemical properties of SA [272]..... 219

Nomenclature and symbols

K_1	slope of the absorption curve
W_t	water absorption (%)
f_c	fibre content (%)
m_0	initial mass (gm)
m_d	dry mass (gm)
m_f	dry mass of the fibres
T_w	interior surface temperatures
T_{amb}	ambient temperature
B/H	binder to hemp ratio
Cp	specific heat capacity (J/kg·K)
COV	coefficient of variation
DTGA	differential thermogravimetric analysis
EDX	energy dispersive X – ray spectroscopy
FA	fatty acid
FE – SEM	field emission scanning electron microscopy
GHG	greenhouse gas
HLC	hemp – lime composite
IRA	initial rate of absorption
K	thermal conductivity (W/m·K)
MBV	moisture buffer value (g/m²·RH)
HFM(A)	heat flow meter (apparatus)
R	thermal resistance (m²·K/W)
RH	relative humidity
TGA	thermogravimetric analysis
XRF	X – ray fluorescence
ρ	density (kg/m^3)
M	mass (kg)

V	Volume (m^3)
W	initial water content (%)
t	time (seconds)
α	thermal diffusivity (m^2/s) $x10^{-6}$
CA	capric acid
LA	lauric acid
MA	myristic acid
PA	palmitic acid
SA	steric acid

1. Chapter 1: Introduction

1.1. Background and rationale

Thermal and hygrothermal regulation are central to building energy use, indoor environmental quality, and material durability. Heating, cooling, and dehumidification account for approximately 50% of global building energy consumption and more than 40% of associated greenhouse gas emissions [1]. Poor regulation can also increase moisture-related deterioration and support microbial growth, with implications for occupant health [2]. These pressures have directed attention toward passive thermal energy storage (TES) within building envelopes [3–6]. Two material strategies are especially relevant: phase change materials (PCMs), which store latent heat, and hemp-lime composites (HLCs), which provide bio-based insulation and moisture buffering.

HLC, often referred to as hempcrete, is a promising bio-based insulation material because it combines carbon storage, high porosity, and moisture-buffering capacity [7–9]. It can attenuate indoor temperature fluctuations, but its thermal storage capacity remains limited compared with materials designed specifically for latent heat storage. Reported specific heat capacities for HLC range from 1,000 to 1,590 J/kg·K [10], with performance governed by dry density, hemp-to-binder ratio, and pore structure [11].

Integrating PCMs into HLC offers a route to envelope materials that combine latent heat storage, insulation, and moisture regulation. A central challenge is that PCMs require a stable carrier to prevent leakage in the liquid phase. Porous bio-aggregates, including hemp shiv, corn cob, flax, delignified wood, and biochar, have therefore been investigated as carriers for shape-stabilised PCMs [12–15]. Hemp shiv is particularly relevant because its porous structure can host PCM while retaining the low-conductivity and hygroscopic functions needed in HLC [7–9, 16].

Several binder-related challenges must be resolved before PCM-HLC can be used reliably. Hydrated lime (HL), when used as the sole binder, has slow setting behaviour, low early-age strength, and energy-intensive production [17]. Supplementary

cementitious materials (SCMs), including silica fume and metakaolin, can improve HLC properties and reduce reliance on HL [18–21]. However, the compatibility of SCM-based binders with high PCM incorporation remains insufficiently defined.

Methodological variability also limits comparison across PCM-HLC studies. HLC properties are sensitive to compaction direction, specimen scale, and testing protocol [22], yet these variables are not consistently controlled. Hemp shiv properties also vary with growing conditions, harvest season, and processing method [23]. As a result, PCM incorporation, shiv morphology, binder composition, and manufacturing method interact within a coupled material system [24].

Despite its potential, PCM-HLC remains unresolved across four linked levels. Material properties must be characterised before composite mixing. Composite-level trade-offs among PCM loading, binder design, leakage resistance, strength, thermal storage, and moisture buffering require clearer quantification. Testing variables such as casting direction and specimen size must be controlled to support reproducibility. At the envelope level, the balance between thermal resistance and latent heat storage under cold-climate conditions remains insufficiently understood.

These gaps define the structure of the thesis. Objective 1 addresses raw-material and binder-design questions. Objective 2 examines testing variables that affect interpretation. Objective 3 quantifies the main composite trade-offs. Objective 4 translates the material findings into a multilayer building-envelope design. Together, the objectives connect material design with envelope behaviour without treating either scale in isolation.

1.2. Research objectives

This research develops an integrated framework for designing and evaluating PCM-HLC for cold-climate building envelopes. Four objectives guide the thesis:

Objective 1. Material characterisation and mix-design development (Chapter 4): characterise hemp shiv and PCM-impregnated shiv, then establish how shiv size and binder composition influence stable PCM-HLC formation.

Objective 2. Experimental behaviour and testing framework (Chapter 5): evaluate how casting direction and specimen size affect the mechanical, thermal, and moisture-buffering response of PCM-HLC.

Objective 3. Composite performance and trade-off analysis (Chapter 6): quantify how PCM substitution changes thermal storage, strength, density, and moisture-buffering capacity.

Objective 4. Building-envelope performance evaluation and parametric design (Chapter 7): assess how PCM-HLC can be configured in a multilayer envelope to balance latent heat storage and thermal resistance under cold-climate conditions.

Together, these objectives provide a coherent path from material characterisation to composite behaviour and envelope application.

1.3. Contribution to the field

This thesis contributes to sustainable building science by clarifying how PCM-HLC can be designed, tested, and applied as a multifunctional envelope material.

1. Material and mix-design contribution: The thesis links hemp-shiv size, PCM impregnation, and binder demand, providing a basis for stable high-PCM HLC formulations.

2. Testing contribution: The work evaluates casting direction and specimen size as variables that affect interpretation of PCM-HLC mechanical and hygrothermal data.

3. Composite-performance contribution: The thesis maps the trade-offs between thermal storage, strength, density, and moisture buffering across a broad PCM substitution range.

4. Envelope-design contribution: The work translates composite-level findings into a multilayer PCM-HLC envelope concept for cold-climate conditions.

The central contribution is an evidence-based framework that connects hemp-shiv morphology, PCM loading, binder design, composite performance, and simulated envelope behaviour. For researchers, this framework clarifies which mechanisms remain observed, inferred, or hypothetical. For practitioners, it supports more targeted selection of PCM-HLC formulations and multilayer wall configurations.

1.4. Outline of the thesis

The thesis is organised into eight chapters:

Chapter 1 introduces the research context, defines the objectives, and summarises the original contributions.

Chapter 2 reviews the literature on raw-material characterisation, binder design, HLC casting and testing protocols, and PCM-enhanced bio-based composites. It identifies the research gaps that motivate the thesis.

Chapter 3 describes the experimental and numerical methodology used throughout the research.

Chapter 4 presents material characterisation and preliminary casting. It examines hemp-shiv morphology and evaluates feasible PCM-HLC mix designs.

Chapter 5 examines casting direction and specimen-size effects on PCM-HLC mechanical and hygrothermal behaviour.

Chapter 6 investigates how PCM substitution affects PCM-HLC mechanical, thermal, and moisture-buffering properties.

Chapter 7 develops and evaluates a multilayer PCM-HLC sandwich panel for cold-climate building envelopes.

Chapter 8 summarises the main findings, discusses limitations, and proposes directions for future research.

2. Chapter 2: Literature Review

2.1. Hemp Shiv

2.1.1. General discussion

Hemp (Cannabis sativa L.) is cultivated for fibres and seeds, but the inner woody core, or hemp shiv, is often treated as a low-value by-product after fibre extraction [25–28]. Redirecting this bio-aggregate into construction can reduce waste while supporting lower-carbon envelope materials [16, 29–34].

The value of hemp shiv in HLC arises from its low bulk density, high porosity, thermal insulation, and moisture-buffering capacity [35]. These same features also make the material variable and difficult to standardise. Reported properties depend on growing conditions, retting, grinding, sieving, and storage, which can alter particle size, pore structure, and chemical composition [26, 36, 37].

The main unresolved issue is therefore not whether hemp shiv can function as a bio-aggregate, but how its variable morphology should be characterised and controlled when it is modified with PCM and incorporated into HLC.

2.1.2. Hemp shiv size effect on HLC density and compressive strength

Hemp shiv particle size strongly influences HLC because it affects packing density, pore connectivity, and the binder-aggregate interface [38]. Grinding generally increases matrix uniformity and interfacial contact, but it also changes the natural tubular structure that contributes to moisture transport and thermal insulation. The range of hemp-shiv shapes considered in the literature is shown in Fig. 2.1.



Fig. 2.1. The shape of hemp shivs [39].

The literature agrees that particle size influences density, but its effect on compressive strength remains inconsistent. Some studies report higher strength after reducing shiv size, whereas others show lower early-age strength or delayed strength development [16, 38, 40–44]. These contradictions suggest that particle size cannot be interpreted independently of binder chemistry, curing age, density, and compaction method.

The most defensible conclusion is that no universal optimum shiv size exists for conventional HLC. Instead, particle-size effects depend on the balance between packing, carbonation, binder continuity, and pore preservation. For PCM-HLC, the additional

uncertainty is whether PCM filling and surface coating preserve, weaken, or reverse these particle-size relationships. Reported effects of hemp-shiv size on HLC density and compressive strength are summarised in Table 2.1.

Table 2.1. The effect of hemp shiv size on the density and compressive strength of HLC.

Study	Particle-size comparison	Density trend	Compressive-strength trend	Key remark
Bourdot et al. [38]	0–5 mm fines vs. 0–20 mm mix (fine fraction raised 15 → 30%)	↗ (not quantified)	↗ 10.5%	More fines → denser & stronger HLC
Brzyski et al. [40]	8.4 mm → 2.74 mm	↗ 377 → 382 kg m^{-3}	↘ 0.51 → 0.40 MPa (- 22%)	Finer particles raise density but lower early-age strength
Mahmood et al. [43]	0.74 mm → 0.30 mm	Keep constant	↘ ≈ 32–36%	Better binder coverage with fines
Stevulova et al. [42]	4.29 mm → 0.94 mm (with a fraction of fine shiv)	↗ 790 → 1 110 kg m^{-3}	↗ 0.3 → 1.86 (long-term; qualitative)	Fines improve long-term strength across binders
Stevulova et al. [41]	33.7 mm → 7.3 mm	↗ 1040 → 1 150 kg m^{-3} (+10.6%)	↗ 2.73 → 5.20 MPa (+90%)	Strong density and strength gains with fines
Nguyen et al. [44]	coarse vs. fine (sizes not given)	n/a	Coarse ↗ at 28 d; no difference at 90 d	Size effect time-dependent; early microcracking postulated
Arnaud et al. [16]	8.9 mm → 3.1 mm	↗ 390 → 430 kg m^{-3} (+10.3%)	Coarse ↗ +52% at 28 d; fine ↗ +30–50% at 120 d	Fines gain strength over longer curing

2.1.3. Hemp shiv size effect on HLC hygrothermal properties

The hygrothermal literature is similarly mixed. Finer particles often reduce thermal conductivity by improving packing uniformity, but some studies report negligible or opposite trends [38, 40, 41, 43]. Moisture buffering is also contested because larger particles can retain more capillary water, while finer particles can expose more exchange surface area [11, 40, 43, 45].

These contradictions indicate that shiv size affects thermal and moisture behaviour through several competing pathways: pore volume, pore connectivity, exposed internal surface area, and density. The literature has not yet established how these pathways change when fatty-acid PCM occupies part of the hemp-shiv pore network.

Longer-term studies further show that curing age can change the apparent effect of shiv size, with reported thermal conductivity differences of up to 34% at 30 days and 27% at 180 days [7]. This time dependence reinforces the need to treat shiv size as a material variable, not only a batching descriptor. The influence of hemp-shiv type and density on HLC performance is illustrated in Fig. 2.2.

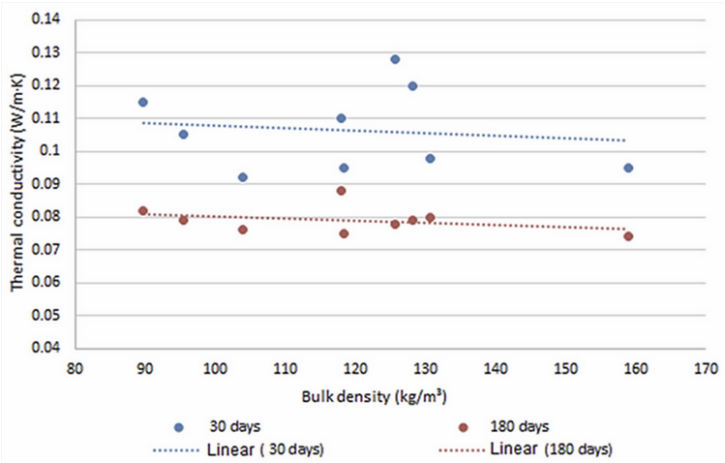


Fig. 2.2. Influence of 13 different types of hemp shives with bulk densities ranging from 70.8 kg/m^3 to 158 kg/m^3, tested at 30 days and 180 days [7].

2.1.4. Hemp shiv size characterisation method

Because hemp shiv is irregular, particle-size characterisation varies across the literature. Manual measurement and sieving provide useful information but are labour-intensive and can be difficult to compare across studies [40, 46–48]. Digital image analysis, particularly ImageJ-based Feret-diameter measurement following RILEM TC 236-BBM, offers a more reproducible basis for describing irregular shiv geometry [7, 13, 39, 43, 49].

The remaining gap is the translation of characterisation data into PCM-HLC mix design. Existing methods can describe shiv size, but they do not by themselves explain how PCM impregnation changes binder demand, leakage resistance, or composite performance. The geometric parameters used to characterise hemp shivs are defined in Fig. 2.3.

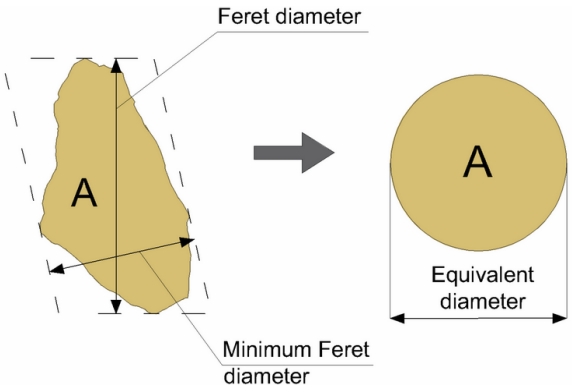


Fig. 2.3. Geometric parameters used to characterize the shape of hemp shivs [39].

2.2. PCM, HL, and SCM

2.2.1. PCM

Hemp shiv provides low thermal conductivity and moisture buffering, but its sensible heat storage is limited. PCMs address this limitation by storing and releasing latent heat during solid-liquid phase transition [50–52]. For HLC, the central question is

how to add latent heat capacity without sacrificing leakage resistance, workability, moisture transport, or mechanical integrity.

The literature distinguishes two main PCM incorporation routes: micro-encapsulated PCMs and shape-stabilised PCMs. Micro-encapsulation improves dispersion but is limited by capsule rupture, cost, and reduced allowable PCM fraction [53–58]. Shape-stabilised PCMs immobilise liquid PCM in a porous carrier and can reach higher mass fractions, but they depend strongly on carrier pore structure and interfacial compatibility [13, 59–64].

For hemp-based composites, this distinction is important because the carrier is also part of the load bearing and moisture-buffering matrix. Table 2.2 shows the incorporation rates, and the different carriers that has been used in the field.

Table 2.2. Summary of MPCM incorporation rate across studies.

Study	PCM type	Matrix	Incorporation rate (wt%)
Abdellatef and Kavgic [53]	Micronal and Nextek MPCM	HLC	9–18
Ada et al. [55]	Micronal DS 5001X	HLC	40
Vevere et al. [65]	MPCM	Polyurethane cryogenic insulation foams	25
Aksoy and Yilmaz [66]	MPCM with gelatin – gum arabic shell and n – octadecane core	Viscose yarn (Textile)	15–20
Zou et al. [67]	MPCM	Copper foam	35–40

Across building-envelope studies, PCMs generally improve thermal inertia and shift peak loads [68–84]. The unresolved challenge is integration: higher PCM content

can improve heat storage, but it can also increase leakage risk, reduce strength, alter pore accessibility, and complicate binder-aggregate bonding [85–96].

This challenge has shifted attention toward organic shape-stabilised PCMs using bio-based or waste-derived carriers [60, 97–106].

Hemp shiv is a logical carrier because of its connected pore structure and capillary retention, yet dedicated studies on fatty-acid PCM in hemp shiv remain limited [13, 64, 107, 108].

The key knowledge gap is therefore not the thermal value of PCMs in general, but the coupled effect of PCM impregnation on hemp-shiv morphology, binder compatibility, moisture transport, and mechanical behaviour in PCM-HLC.

2.2.2. Fatty acids for PCM-HLC

Fatty acids are relevant to PCM-HLC because they are bio-based, relatively stable, low-corrosivity organic PCMs with tunable phase-change temperatures [109]. Capric acid (CA), lauric acid (LA), myristic acid (MA), palmitic acid (PA), and stearic acid (SA) are commonly considered because their binary mixtures can be adjusted toward building-comfort temperature ranges.

For indoor thermal comfort, useful PCM melting ranges commonly fall near 20-30 °C [110–113]. Pure fatty acids do not all fall within this range, so eutectic mixtures are used to tune melting temperature and latent heat. Table 2.3 provides the relevant thermal-property of some of the commonly used pure fatty acids.

Table 2.3. Thermal properties of pure fatty acids [13, 107, 110, 111, 114–123].

Commercial name	CAS number	Formula	Fusion temperature (°C)	Latent heat of Fusion (J/g)	Specific heat (J/g/K) in liquid (L) and solid (S) phase	Thermal conductivity (W/m/K)
Capric acid	334–48–5	$C_{10}H_{20}O_2$	29.6–33.2	139.77–168.77	L: 2.088–2.1 S: 1.9–2.097	L: 0.149–0.17 S: 0.21
Lauric acid	143–07–7	$C_{12}H_{24}O_2$	41–45.3	172.65–217.29	L: 2.1–2.3 S: 1.7–1.8	L: 0.147–0.19 S: 0.15–0.37
Myristic acid	544–63–8	$C_{14}H_{28}O_2$	49–56.1	178.14–210.70	L: 2.159–2.4 S: 1.7–2.180	L: 0.15–0.21 S: 0.17–0.39
Palmitic acid	57–10–3	$C_{16}H_{32}O_2$	58.9–64	185.4–233.24	L: 2.267–2.8 S: 1.9–2.059	L: 0.159–0.22 S: 0.3
Stearic acid	57–11–4	$C_{18}H_{36}O_2$	53.8–70.8	174.6–258.98	L: 2.2–2.5 S: 1.6–1.8	L: 0.17–0.21 S: 0.159–0.35

Differential scanning calorimetry (DSC) is used in the literature to distinguish onset, peak, and endset temperatures during melting and crystallisation. The onset temperature is normally the most appropriate value for comparing equilibrium melting behaviour, whereas peak and endset values are more sensitive to heating rate, sample mass, and thermal lag [124–126]. The DSC response of the binary fatty-acid mixture is shown in Fig. 2.4.

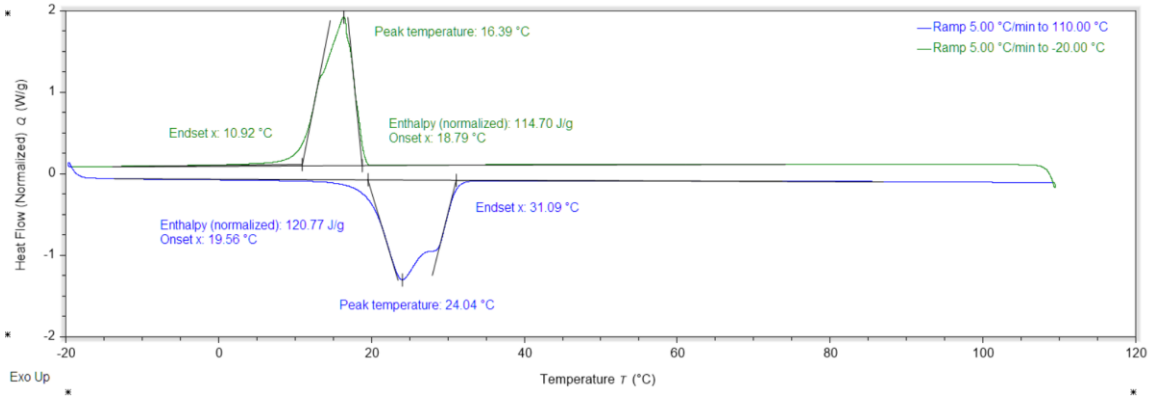


Fig. 2.4. DSC diagram of a binary fatty acid mixture of 87.8% CA - 12.2% MA.

For fatty-acid PCMs, both melting and crystallisation should be reported because supercooling can shift the usable discharge temperature below the melting onset. This distinction matters for building applications, where charge and discharge must occur within the operating temperature range.

Thus, DSC data are most useful when they support material selection and comparison, rather than when they are treated as a complete predictor of composite performance.

2.2.3. Eutectic mixtures and phase-change prediction

Eutectic fatty-acid mixtures are used to tune phase-change temperature while retaining chemical stability. The literature commonly uses the Schroder-van Laar equation and phase diagrams to estimate eutectic ratios before experimental validation [63, 127–130].

The eutectic behaviour of binary mixtures can be predicted using the Schröder – van Laar equation [63, 127–130]:

$$T_m = \left[\frac{1}{T_A} - \frac{R\ ln(X_A)}{\Delta H_A}\right]^{-1} \quad (1)$$

Where T_m is the phase change temperature of the eutectic mixture, T_A is the phase change temperature, ΔH_A is the latent heat of component A, X_A is the mole fraction of component A in the mixture, and R is the gas constant, which is 8.315 $\frac{J}{mol} \cdot K$.

Reported binary fatty-acid systems show that theoretical predictions can guide mixture selection, but DSC validation remains necessary because impurities and non-ideal mixing can shift the measured eutectic temperature and enthalpy. Binary fatty-acid mixtures and their reported carriers are summarised in Table 2.4.

Table 2.4. Fatty acids binary mixtures and their carriers from the literature.

Eutectic mixture	Acronym	Mass ratios (wt%)	Fusion temperature (°C)	Carriers
Capric acid – lauric acid [13]	CA – LA	73–27	21.7	Hemp shivs
Capric acid – lauric acid [110]	CA – LA	66.75–33.25	19.26	-
Capric acid – lauric acid [63]	CA – LA	67–33	22.81	50 wt% with polymethyl methacrylate (PMMA)
Capric acid – lauric acid [131]	CA – LA	65.12–34.88	19.67	Phase change wallboards
Capric acid – myristic acid [13]	CA – MA	83–17	24.1	Hemp shivs
Capric acid – myristic acid [58]	CA – MA	78–22	24.3	A porous clay RP
Capric acid – myristic acid [122]	CA – MA	83–17	24.14	-
Capric acid – myristic acid [63]	CA – MA	72–28	25.36	50 wt% with PMMA
Capric acid – myristic acid [110]	CA – MA	78.39–21.61	20.08	-
Capric acid – stearic acid [13]	CA – SA	91–9	26.0	Hemp shivs
Capric acid – stearic acid [26]	CA – SA	77–23	27.78	50 wt% with PMMA
Capric acid – stearic acid [132]	CA – SA	83–17	24.73	52 wt% with wood fibres
Capric acid – palmitic acid [31]	CA – PA	88–12	26.1	Hemp shivs
Capric acid – palmitic acid [133]	CA – PA	85–15	24.54	15–60 wt% with wood flour
Lauric acid – myristic acid [13]	LA – MA	73–27	33.6	Hemp shivs
Lauric acid – myristic acid [58]	LA – MA	64–36	33.43	A porous clay
Lauric acid – myristic acid [63]	LA – MA	58–42	35.18	70 wt% with PMMA
Lauric acid – palmitic acid [13]	LA – PA	79–21	34.6	Hemp shivs
Lauric acid – stearic acid [13]	LA – SA	87–13	40.2	Hemp shivs
Lauric acid – stearic acid [12]	LA – SA	86–14	37.5	Carbonized corn cob
Capric – palmitic – stearic acid [62]	CA – PA – SA	79.3:14.7:6.0	25.71	70 wt% with expanded vermiculite
Capric acid – myristic acid – stearic acid [127]	CA – MA – SA	-	22.92	-

Phase diagrams provide the same practical message: mixing two fatty acids lowers the onset melting temperatures until the eutectic composition is reached [110, 119, 134]. This allows binary systems to be selected for target comfort ranges rather than relying on the melting point of a single acid. Phase diagrams for a binary eutectic fatty-acid system are presented in Fig. 2.5.

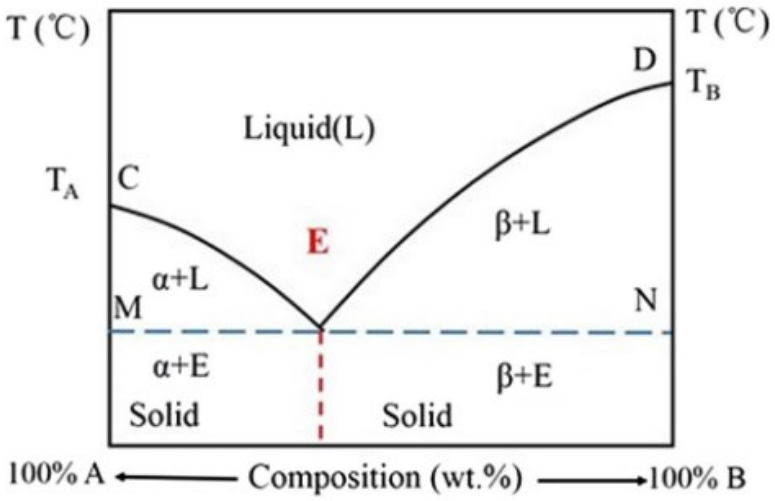


Fig. 2.5. Phase diagrams of a binary eutectic fatty acid [110].

Among the reported binary systems, CA-MA is particularly relevant because its eutectic temperature can be positioned near the lower comfort range, while some alternatives show excessive undercooling or poor carrier impregnation [13, 119, 135].

The remaining literature gap is that predicted fatty-acid mixtures are often evaluated as PCMs alone, whereas their behaviour after impregnation into hemp shiv and incorporation into HLC is less well established. The theoretical eutectic ratios and predicted thermal properties are listed in Table 2.5.

Table 2.5. The theoretical fatty acids eutectic mass ratios and their predicted thermal properties.

Eutectic mixture	Acronym	Theoretically calculated eutectic mass ratios	Temperature of Fusion T_E (°C)	Heat of Fusion (J/g)
Capric acid – myristic acid	CA – MA	0.85–0.15	22.64	165

Overall, eutectic prediction narrows the candidate PCM range, but it does not replace composite-level testing of leakage, thermal response, and binder compatibility.

2.2.4. Impregnation into hemp shiv carriers

After fatty-acid selection, the key integration step is impregnation into a porous carrier. Impregnation capacity depends on both process conditions and carrier properties, including pore size distribution, microstructure, hydrophilicity, and surface tension [46, 136].

Direct impregnation and vacuum impregnation are the two most common routes. Direct impregnation is simpler, but vacuum impregnation generally improves PCM penetration by removing trapped air and driving liquid PCM into the pore network [13, 137].

Heating above the eutectic melting point is required to maintain the PCM in liquid form during impregnation [12, 127, 129]. However, the literature shows that successful absorption alone is not sufficient; excess PCM on the shiv surface can still create leakage and binder-compatibility problems.

Comparative studies generally favour vacuum impregnation because it improves retention and reduces thermal-cycling leakage relative to direct absorption [13, 133, 138]. The vacuum-impregnation process is illustrated in Fig. 2.6.

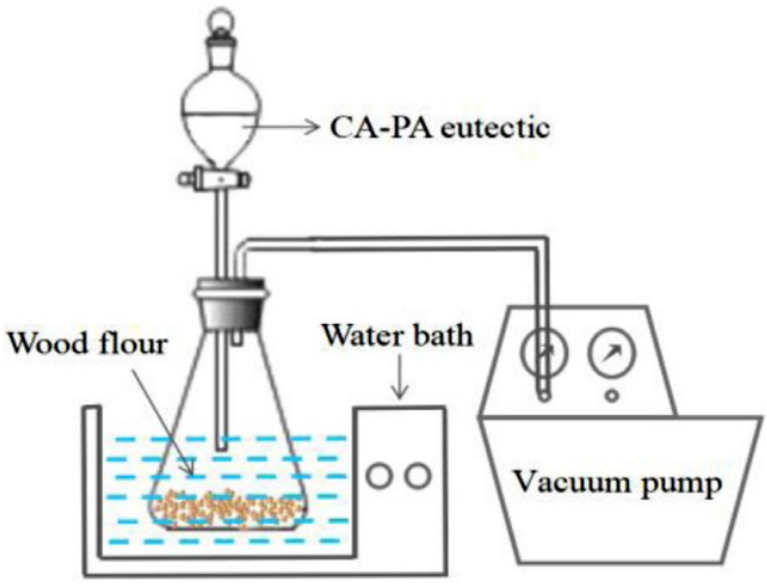


Fig. 2.6. Vacuum impregnation of CA-PA/WF composites [133].

The remaining uncertainty is how high impregnation levels affect the downstream HLC matrix. High PCM retention can improve thermal storage, but the same PCM may alter shiv wettability, binder contact, and the pore network available for moisture exchange. Mass loss for CA-PA/WF composites at different mass ratios is shown in Fig. 2.7.

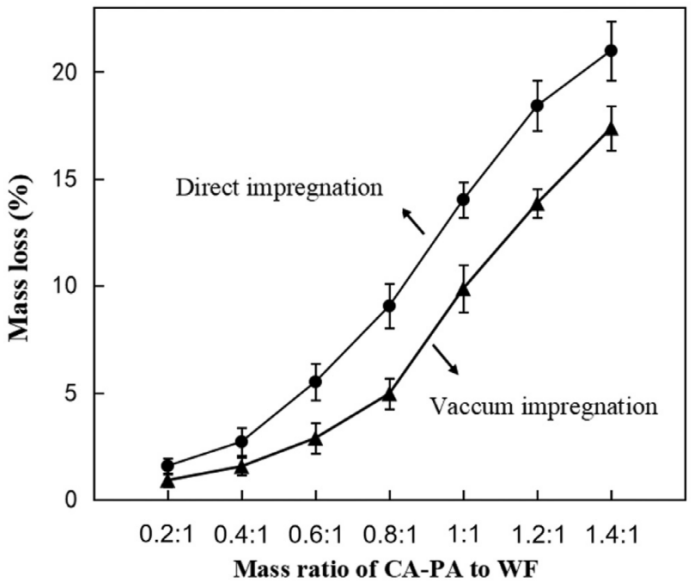


Fig. 2.7. Mass loss of CA-PA/WF composites with different mass ratios [133].

2.2.5. Hemp to PCM ratio

Reported PCM-to-carrier ratios vary widely because the optimum fraction depends on PCM chemistry, carrier porosity, binder system, application, climate, and cost [12, 13, 58, 62, 63, 132, 133, 139]. Higher PCM loading can increase latent heat storage and thermal lag, but it often reduces strength, alters workability, and increases the risk of segregation or leakage.

The literature therefore frames PCM loading as a trade-off rather than a maximisation problem. What remains insufficiently resolved is how these trade-offs evolve across a broad PCM substitution range within a single HLC binder and testing framework.

A stronger evidence base is needed to connect PCM dosage with thermal storage, moisture buffering, workability, and mechanical performance under comparable conditions.

2.2.6. HL

HL ($Ca(OH)_2$) is widely used in HLC because it provides vapour permeability, alkalinity, and mineral bonding with bio-aggregates such as hemp shiv. An example of HL used in the HLC literature is provided in Fig. 2.8.



Fig. 2.8. HL in the literature [22].

Its sustainability varied depending on applications. Lime production releases CO_2 during calcination, but some of this carbon can be reabsorbed through carbonation during service life [140, 141]. In HLC, this carbonation potential is combined with biogenic carbon storage in hemp shiv, making HL relevant to low-carbon construction even though its production remains energy-intensive.

Pure HL also has technical limitations, including slow setting, low early-age strength, and regional supply constraints [142]. These limitations explain why the literature increasingly combines HL with SCMs to improve strength development, durability, and binder efficiency.

2.2.7. SCMs

SCMs are used to reduce reliance on HL and improve binder performance. Their contribution is both environmental and technical: industrial by-products such as slag and

silica fume can lower embodied impacts, while reactive silica and alumina can form additional cementitious phases that improve matrix cohesion [18, 143–150].

The main binding products discussed in the literature are calcium-silicate-hydrate (C-S-H) and calcium-alumino-silicate-hydrate (C-A-S-H). These phases densify the binder matrix and improve mechanical performance, but their formation depends on SCM chemistry, water demand, and lime availability [144–146].

Table 2.6 summarizes the distinctions between these two critical binding phases.

Table 2.6. Comparison of C – S - H and C – A - S – H.

Feature	C – S - H	C – A - S – H
Role in strength	Primary binder, provides ~90% of structural strength.	Secondary binder in blended systems.
Formation	Hydration of tricalcium/dicalcium silicates.	Al^{3+} incorporation from aluminous SCMs.
Typical abundance	High (major gel phase) [146].	Lower (dependent on SCM replacement level).
Effect on early strength	Governs both early and long-term strength.	Often occurs after the formation of carbonate-containing phases [147], boosting durability.

For PCM-HLC, slag, metakaolin, and silica fume are especially relevant because they represent different balances of reactivity, water demand, availability, and environmental impact.

Slag is calcium-, silica-, and alumina-rich, relatively available, and commonly associated with durability and lower permeability [143, 151, 152]. Its lower reactivity can be advantageous where cost and large-scale availability matter, but it may be less effective for rapid strength gain.

Metakaolin has high pozzolanic reactivity and can improve packing, strength, and matrix cohesion, but it is manufactured by calcination and therefore has a higher processing burden than some industrial by-products [153–156].

Silica fume has very high amorphous silica content and can refine microvoids, but its high surface area increases water demand and can reduce workability [148, 157–159]. These differences mean that SCM selection cannot be based on strength alone.

The unresolved question is how these SCMs perform in the presence of fatty-acid PCM, where binder hydration, water demand, surface wettability, and hemp-shiv bonding may differ from conventional HLC. The principal SCMs discussed in the literature are compared in Table 2.7.

Table 2.7. Comparison of SCMs.

Property	Silica Fume	Metakaolin	Slag
Primary composition	Silica (SiO_2): 85–95%	Silica (SiO_2): 45–55% Alumina (Al_2O_3): 40–50%	Silica (SiO_2): 30–40% Alumina (Al_2O_3): 10–20% Calcium Oxide (CaO): 30–40%
Particle size	Ultra – fine (0.1 to 1 μm)	Fine (1 to 2 μm)	Granular (10–45 μm) [160]
Reactivity	Highly reactive	High early reactivity	Slower, long – term reactivity
Strength	Increases compressive strength	High early and long-term strength	Steady long-term strength gain
Workability	Lower flowability and increases water demand	Improves flowability and water retention	Improves workability and reduces water demand
Availability	Regional dependent	Globally available (Medium)	Globally available (High)
Environmental impact	Low (Recycled industrial byproduct)	Moderate (requires high temperatures to produce)	Low (Recycled industrial byproduct)
Cost	The most expensive	More expensive	More cost – effective

2.3. Binder and HLC mix design

HLC mix design controls the balance among density, strength, insulation, and moisture buffering. The most influential variables are the hemp-to-binder ratio, binder composition, and water content. These variables are interdependent because hemp shiv is porous and deformable, while the binder controls cohesion and stiffness [161].

The literature consistently shows that increasing binder content tends to raise density and compressive strength, but it can also increase thermal conductivity and reduce the pore volume available for moisture exchange [11, 16, 43, 162]. Partial HL replacement with SCMs can reduce binder-related impacts and improve mechanical behaviour, but the effect depends on SCM chemistry and water demand [18, 143, 148].

Reported H:B and HL:SCM ratios vary widely across HLC studies [11, 16, 18, 40, 43, 53, 114, 143, 163–169]. This variation makes the literature difficult to compare directly, but it also shows that HLC design is application-specific rather than governed by a single universal ratio.

Across the reviewed studies, lower H:B ratios, meaning higher binder contents, generally produce denser and stronger composites. The trade-off is that density is often positively associated with thermal conductivity, as illustrated in Fig. 2.9 and Fig. 2.10.

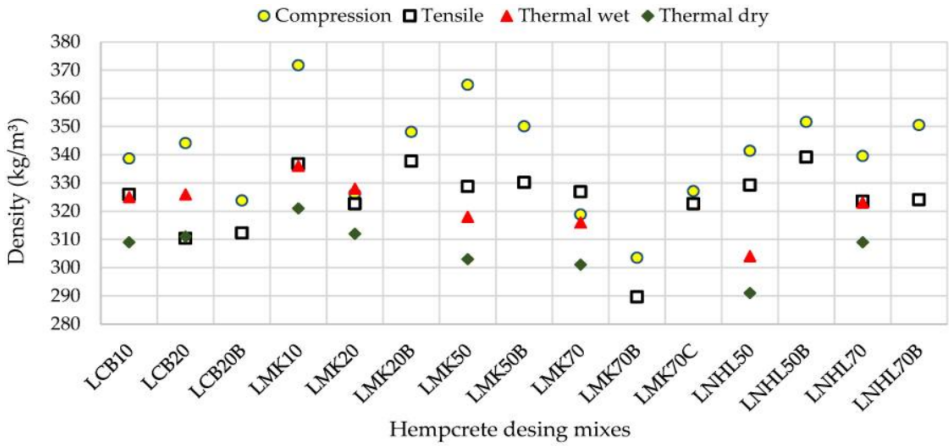


Fig. 2.9. Comparative performance of HLC [11]. LCB represents HL: crushed brick, LMK represents HL: MK, LNHL represents HL: natural hydraulic lime. The number indicates the % of SCM being used. Water demend B > A > regular mix design.

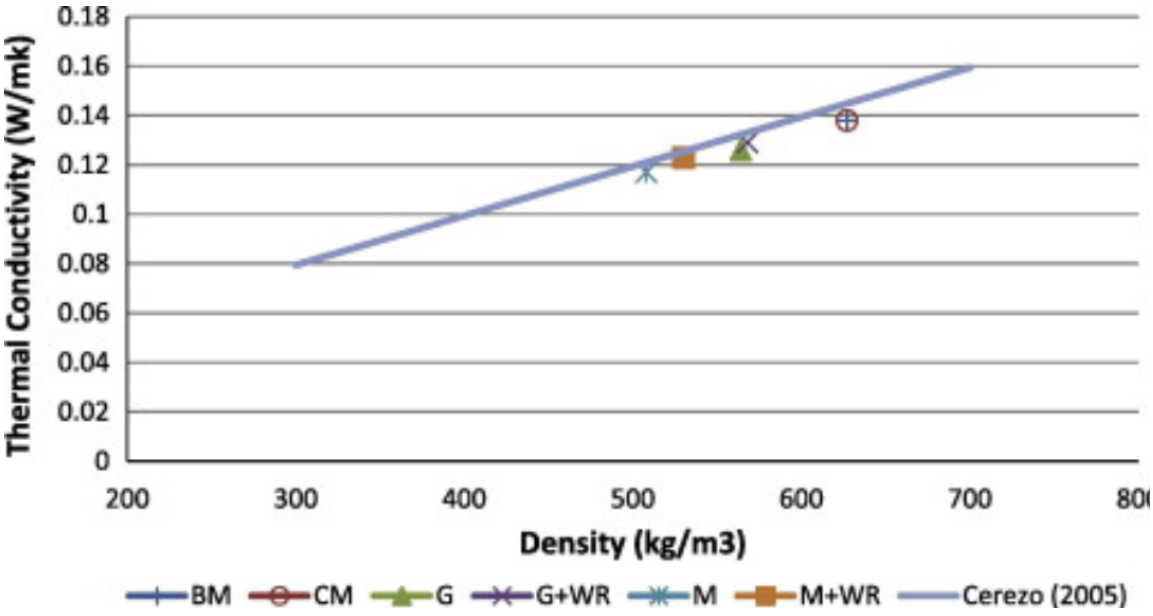


Fig. 2.10. Relationship between density and thermal conductivity of hemp concrete walls and the relationship established by Cerezo [170]. BM – builder's mix, CM – commercial mix, G – HL:slag binder, G + WR – HL:slag binder with water retainer, M – HL:metakaolin binder, M + WR – HL:metakaolin binder with water retainer.

Conversely, higher H:B ratios reduce binder content and density, which can improve insulation by preserving void volume. However, low binder content can compromise cohesion, handling strength, and dimensional stability. The relationship among hemp-concrete thermal conductivity, density, and water content is shown in Fig. 2.11.

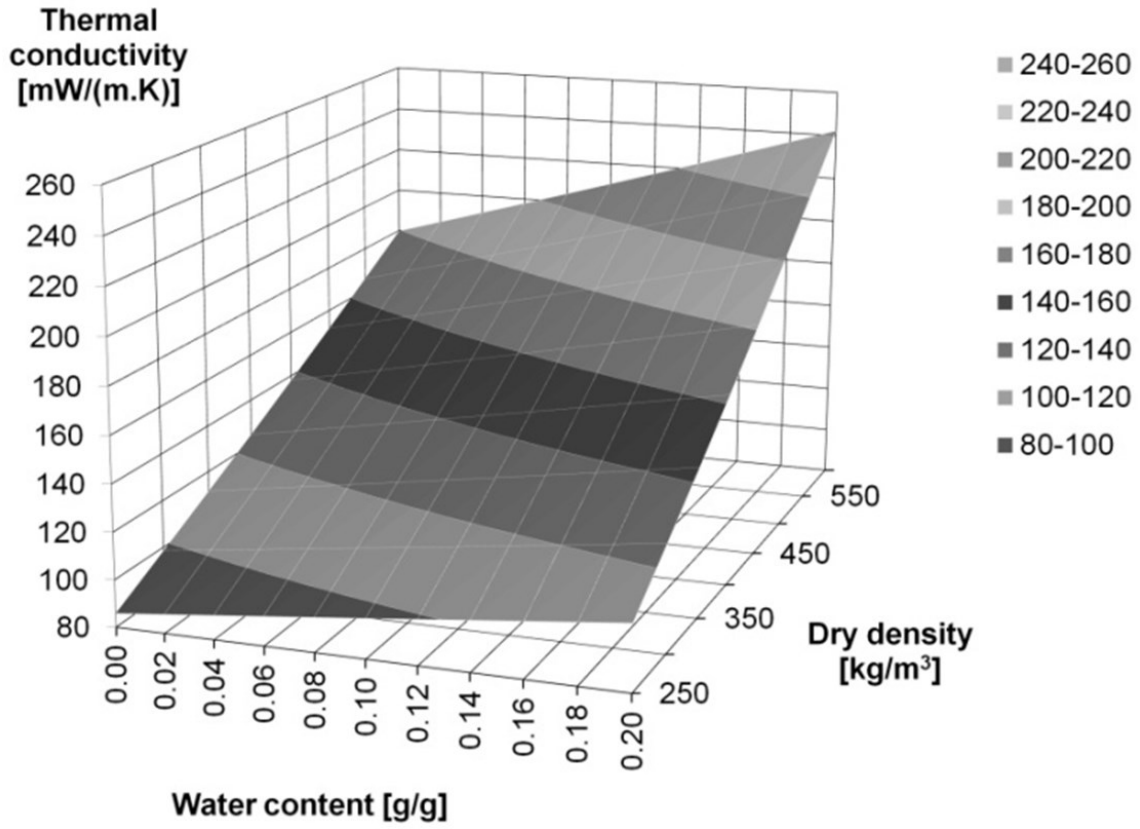


Fig. 2.11. Thermal conductivity of hemp concretes versus density and water content [171].

Water content adds another source of uncertainty. Excess water can delay setting, weaken the binder-shiv interface, and promote mould during drying, while insufficient water limits hydration and carbonation [26, 172, 173]. Because hemp shiv and SCMs have different sorption and surface-area characteristics, a fixed water ratio is rarely transferable across binder systems.

The mix-design gap is therefore a coupled one: PCM-HLC requires enough binder and water for cohesion, but excessive binder, water, or PCM can reduce the hygrothermal advantages that make HLC useful.

2.4. HLC specimen preparation

2.4.1. Fatty acids' impact on HLC

Fatty acids complicate HLC mix design because they can alter wettability, water demand, binder hydration, and particle bonding. The literature reports both beneficial and detrimental effects, which suggests that the outcome depends on dosage, binder chemistry, and carrier configuration [174–178].

One interpretation is that fatty acids can reduce water uptake by occupying hemp-shiv pores. A competing interpretation is that their hydrophobic surfaces can reduce binder wetting and increase water or binder demand. Evidence from cementitious systems and PCM-HLC therefore points to a material-specific balance rather than a universal fatty-acid effect [64, 175, 178].

The functional benefits remain important: fatty acids can add latent heat storage and may improve water repellency in some binder systems [64, 179, 180]. The unresolved issue is whether these benefits can be achieved without undermining cohesion, moisture buffering, or long-term stability.

This gap is especially relevant for high-PCM HLC, where fatty-acid dosage is large enough to modify both the hemp-shiv surface and the binder environment.

2.4.2. Mixing and casting procedures of HLC

Mixing procedures for HLC generally follow a common logic: pre-wet the aggregate, add binder, then adjust the remaining water to obtain a workable and cohesive

mixture [167, 181]. The details vary among studies, which makes density, water demand, and strength difficult to compare.

Density-controlled casting methods have been proposed to reduce this variability [169]. Their value is not the specific equation used, but the principle that fresh mass, target volume, and compaction must be controlled if differences in binder composition or PCM content are to be interpreted.

$$\frac{R_{dry}}{R_{total}} = \frac{\rho_{target}}{m_{total}} \quad (2)$$

Here, R_{dry} includes the ratio of hemp shiv, fatty acids, and binder (HL and SCMs), while R_{total} is the sum of ratios of all components, including mixing water.

The literature therefore supports density control as a comparability requirement, while also showing that cured density can still shift because of water absorption, hydration, and drying.

2.4.3. Compaction direction and methods

Casting and compaction influence HLC properties alongside mix composition [44, 47, 182, 183]. The main issue is anisotropy: elongated hemp particles, density gradients, and binder settlement can make mechanical, thermal, and hygric properties depend on casting and testing direction.

Long hemp particles tend to align with compaction direction, and their capillary structure can make heat and moisture transport direction-dependent [161]. This mechanism explains why orientation is often considered when interpreting HLC thermal conductivity and strength. Hemp-shiv orientation relative to compaction direction is illustrated in Fig. 2.12.

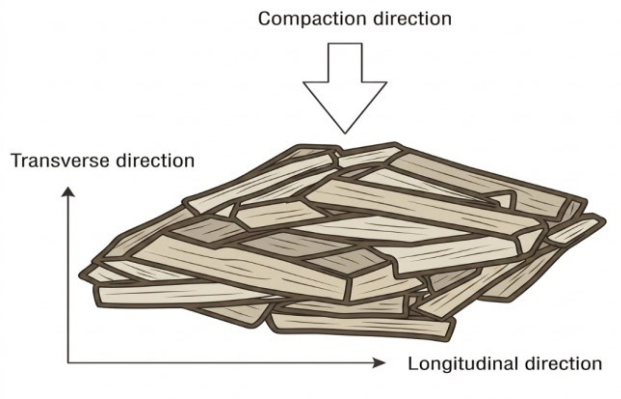


Fig. 2.12. A graphical representation of the relationship between hemp shiv particle orientations and compaction directions.

Nguyen et al. [44] illustrated this issue by comparing samples measured parallel and perpendicular to compaction direction, as shown in Fig. 2.13.

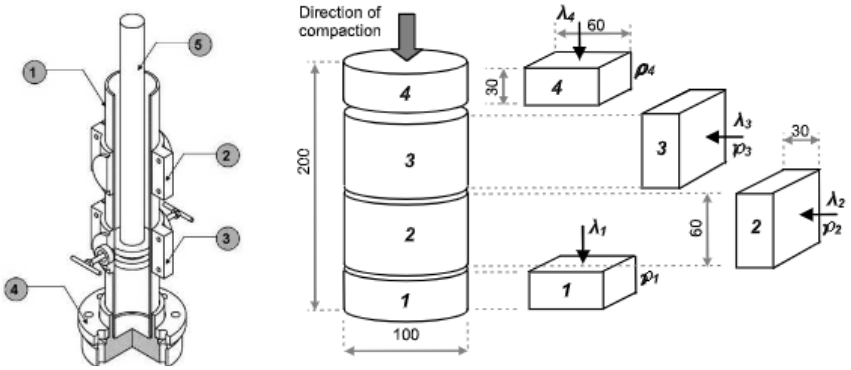


Fig. 2.13. Compaction setup of HLC samples cut from cylindrical specimen [44].

The literature also reports density gradients caused by binder settlement, with lower-density upper regions and denser lower regions [161]. Such gradients can affect compressive strength, thermal conductivity, and moisture transport, but the magnitude depends on compaction intensity, shiv size, binder content, and specimen geometry.

Overall, compaction presents a design trade-off. Greater densification can improve strength but may reduce moisture buffering and increase thermal conductivity

[47, 171, 183, 184]. Most evidence, however, comes from conventional HLC rather than PCM-HLC.

For PCM-HLC, the unresolved question is whether PCM impregnation dampens anisotropy by filling pores or amplifies it by changing binder distribution, pore morphology, and surface wettability.

Consequently, literature on HLC preparation motivates careful reporting of shiv size, density, compaction direction, specimen geometry, and binder composition whenever PCM-HLC properties are compared.

2.5. Experimental methodology assessing HLC

2.5.1. Compressive strength test

Although HLC is generally used in non-load-bearing applications, compressive strength remains a useful indicator of handling, installation, and material consistency. The difficulty is that HLC deforms more like a low-strength insulation material than structural concrete, so test geometry and loading protocol strongly influence reported values.

The literature lacks a single compressive-strength standard for HLC. Researchers use different cube sizes, cross-head speeds, and standards borrowed from mortar, concrete, insulation, or lightweight materials [16, 43, 170, 185–194]. This makes direct strength comparison uncertain. Compressive strength and dry density across formulations and studies are compared in Fig. 2.14.

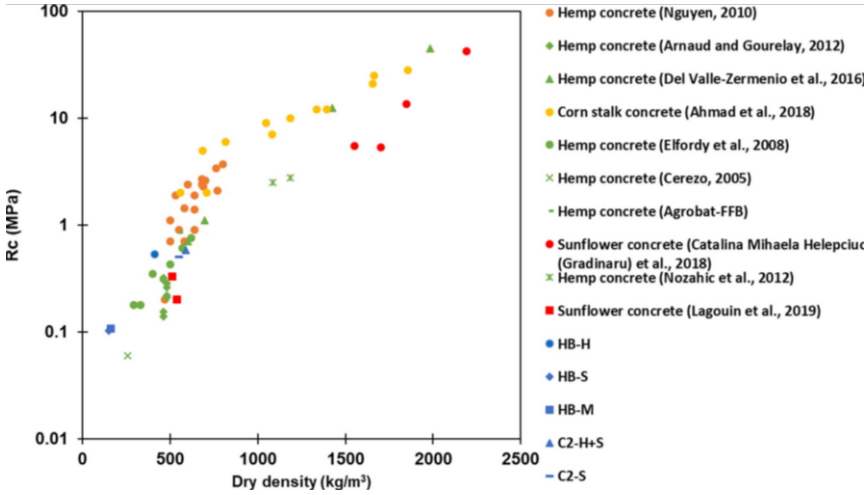


Fig. 2.14. Compressive strength vs dry density at 28 days of the formulations tested and from several studies from the literature [185].

Table 2.8 and Table 2.9 show that 50 mm and 100 mm cubes are both common, but they reflect different testing traditions.

Table 2.8. Principal standards employing 50 mm and 100 mm cubes.

50 mm x 50 mm x 50 mm Cubes	100 mm x 100 mm x 100 mm Cubes
ASTM C513 for hardened lightweight insulating concrete for compressive strength	BS EN 12390–1 for hardened concrete
ASTM C109 for hydraulic cement and other mortars	EN 826:2013 Thermal insulating products for building applications – Determination of compression behaviour
ASTM C165 Compressive Properties of Thermal Insulations (258×258×12.7 mm), ASTM D1621–16(2023), and ASTM D6817 M - 13a Specification for Rigid Cellular Polystyrene Geofoam	(No equivalent ASTM insulation standards typically use this cube size)

Standards for insulation and hydraulic mortars better reflect HLC's low-strength, deformable response than standards developed for dense structural concrete [187–191]. Even so, the literature has not resolved how specimen size affects HLC strength, particularly when PCM changes density and internal structure.

In contrast, BS EN 12390–1 [190] and EN 826:2013 [191] are aimed at dense concrete and building insulation boards, respectively, and use 100 mm cubes primarily for convenience in concrete labs. Although larger samples will reduce variability when the material is heterogeneous, these standards accommodate concrete, which is not designed to reflect the lower density or deformable behaviour typical of HLC.

A list of specimen sizes used by recent studies is shown in Table 2.9.

Table 2.9. HLC studies that used different sample sizes for compressive strength test.

Author & Year	Sample size (mm)	Loading rate / Testing speed	Material tested
Elfordy et al., 2008 [186]	50 mm cubes	5 mm min^{-1} (crosshead speed)	Lime – hemp concrete (“hempcrete”)
Page et al., 2017 [192]	50 mm cubes	3 mm min^{-1} (crosshead speed)	Hybrid hemp – flax composite (hemp + flax fibres)
Şahin, 2022 [193]	50 mm cubes	30 N s^{-1} (force – controlled)	Lightweight hemp composite (hemp shiv + Portland cement binder)
Walker et al., 2014 [194]	100 mm cubes (EN 459–2 [195] and EN 196–1 [196])	50 N s^{-1} (force – controlled)	Hemp – lime concrete with calcium – lime, natural hydraulic lime, supplementary cementitious material binders, and commercial binders
Mahmood et al., 2024 [43]	100 mm cubes (EN 12390–1 [190] and EN 826:2013 [191])	2 mm min^{-1} (displacement – controlled)	Hemp – lime biocomposite, hemp shiv + HL binder + supplementary cementitious materials
Stevulova et al., 2012 [41]	100 mm cubes	Not specified (tested on an ELE ADR 2000 press)	Lightweight composites with 40 vol% hemp shives, 29 vol% of MgO – cement, and 31 vol% of water

Recent HLC studies therefore provide useful testing precedents but not a unified protocol. The remaining methodological gap is to quantify whether specimen size changes the measured strength and whether that effect differs with casting direction.

From a regional perspective, ASTM standards are more commonly adopted in North America and are generally preferred over European standards. Considering technical accuracy and compliance with standards, 50 mm cubes are recommended for compressive strength testing of HLC. Given its lightweight, porous, and lime – based nature, HLC is best tested under protocols developed for lime – based and thermal insulation materials.

Because HLC strength data are often used for comparison rather than structural design, consistency of sample size, curing age, and loading protocol is essential for interpreting trends across studies.

2.5.2. Moisture buffering test

Moisture buffering arises from hemp shiv chemistry and pore structure. Cellulose, hemicellulose, and lignin provide polar sites for moisture interaction, while the fibrous pore network supports vapour sorption, capillary condensation, storage, and release [181, 197, 198].

MBV provides a standardised way to quantify this behaviour [53, 181, 199]. Many MBV studies have focused on conventional HLC, although reported values depend on specimen conditioning, exposure cycles, and test duration [181, 199]. The open question is how fatty-acid PCM affects moisture exchange when it occupies pores and changes surface wettability.

2.5.3. Thermal conductivity

Thermal conductivity is commonly measured using steady-state heat-flow methods, but reported values depend on temperature, specimen size, density, moisture state, and edge insulation [43, 64, 199–203]. In hemp concrete, Collet et al. measured conductivity across formulations and water contents and combined heat-flow measurements with self-consistent modelling, showing that density and water content should be interpreted together rather than treated as independent corrections [171]. Studies of moist hygroscopic insulation using heat-flow-meter methods further show that wet samples require extended equilibration because moisture migrates from the hot side to the cold side; shortening the test can overestimate conductivity, while vapour transport and latent heat contribute to the apparent heat flux [204, 205]. Measurements at high moisture levels should therefore report conditioning relative humidity, mean moisture content, specimen thickness, mean temperature, temperature gradient, and the criterion used to define hygrothermal steady state. For PCM-HLC, these controls are particularly important because moisture redistribution may coincide with PCM phase change, making a single apparent conductivity difficult to interpret [64, 200–203].

For heterogeneous bio-based materials, specimen thickness matters because thicker samples better average local variations, while thinner samples can be more affected by contact resistance and edge effects. The thermal-conductivity test setup used in the literature is shown in Fig. 2.15.

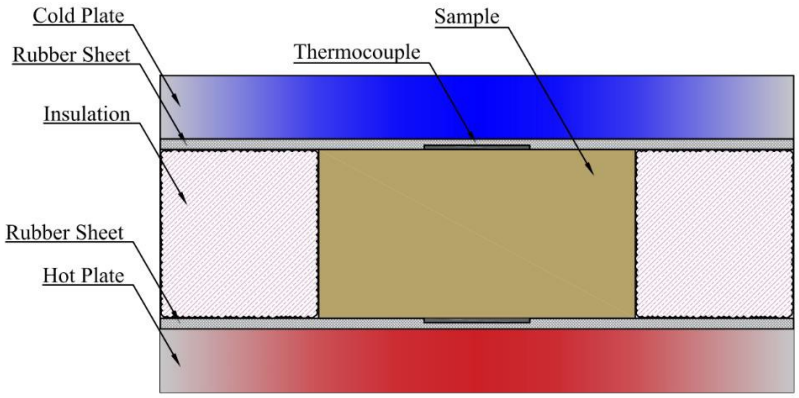


Fig. 2.15. Thermal conductivity setup using FOX 304 Heat Flow Meter [43].

Instrument limitations and target accuracy therefore shape specimen geometry, as summarised in Table 2.10.

Table 2.10. The FOX 304 HFM specifications.

Maximum sample Thickness	102 mm (4″)
Sample size	305 x 305 mm (12 sq. in.)
Temperature range	- 20 °C to 75 °C
Extended temperature Range options	- 30 °C to 95 °C
Temperature control accuracy	± 0.01 °C
Accuracy	± 1%
Reproducibility	± 0.5%
Thermal conductivity range	0.005 to 0.35 W/m K (0.035 to 2.4 BTU in/hr ft^2 °F) External thermocouple kit: up to 2.5 W/m K
Heat flux transducers area	100 x 100 mm (4 sq. in.)

Common HFM specimen sizes range from approximately 150 mm by 150 mm to 260 mm by 260 mm, with thicknesses commonly between 50 mm and 80 mm [43, 114, 169, 199].

For PCM-HLC, thickness has an additional implication: if the thermal gradient crosses the PCM melting range, different regions of the specimen may contain solid and liquid PCM. This creates a gap in how thermal-conductivity tests should be interpreted for phase-changing bio-composites.

When measuring the steady-state thermal properties of heterogeneous insulation materials, the relationship between the material's structural heterogeneity and the sensor/transducer size is critical [206, 207]. In standard HFM instruments, heat flux transducers embed a matrix of thermopiles to capture the energy passing through a material. When analyzing a heterogeneous structure, if the heat flux sensor is too small relative to the material's structural features (e.g., large air pockets, structural binders, voids, or varying densities), it measures a localized hotspot or cold spot. The sensor must

span an area large enough to integrate across local variations and defects to compute an accurate bulk thermal conductivity. While ASTM C518 [208] provides the baseline standard for steady-state heat flow meters and recommends large sample sizes of 300 mm x 300 mm to ensure that a large central heat flux transducer evaluates an isotropic, homogeneous, or uniformly heterogeneous area, ASTM C1919-22 [207] supplements the practice by testing on smaller samples down to 100 mm x 100 mm while utilizing a centralized smaller heat flux sensor area of 10 mm to 50 mm.

When evaluating complex, heterogeneous materials under standard HFM protocols, several hard physical and structural measurement limitations emerge:

• Thermal Inhomogeneity & Anisotropy: If fibers align preferentially in one direction (common in bio-based HLC), the 1D heat flow assumption fundamental to ASTM C518 might be diverted laterally, violating the calibration constants of the central sensor.

• Macro-Porosity and Edge-Convection Effects: When samples are downscaled using masks under ASTM C1919, highly porous or granular heterogeneous structures risk convective looping along the boundary between the material and the surrounding protective edge mask [207, 209].

• Contact Resistance Inaccuracies: Heterogeneous surfaces are rarely perfectly flat. Variations in rigid aggregates create localized air gaps against the rigid plates of the HFM apparatus, adding contact thermal resistance that artificially deflates the measured conductivity value.

• Micro-Sensor Edge-Loss Vulnerability: Shifting to micro-scale heat flux transducers introduces intense lateral heat distortion. Without a perfectly guarded perimeter, the sensor captures multi-directional flux instead of pure perpendicular thickness transmission, which might yield reproducibility error margin on highly localized heterogeneities.

2.5.4. Thermal resistance

Thermal resistance expresses resistance to heat flow for a given material thickness and is therefore central to envelope design [210, 211]. Unlike thermal conductivity, it scales with thickness and is sensitive to contact resistance in thin samples [212, 213]. Insulation values for selected commercial materials are compared in Table 2.11.

Table 2.11. Insulation values for some of the commercial insulation materials [211].

Material	Ranges RSI/25.4 mm (R/in.)	Average RSI/25.4 mm (R/in.)
Cellulose fibre, wet sprayed or blown	0.53 to 0.67 (R - 3 to 3.8)	0.63 (R - 3.6)
Straw bale	0.23 to 0.28 (R - 1.3 to 1.6)	0.26 (R - 1.45)
Wood fibre	0.58 (R - 3.3)	0.58 (R - 3.3)
Fibreboard (beaverboard)	0.41 (R - 2.3)	0.41 (R - 2.3)
Compressed straw board	0.35 (R - 2.0)	0.35 (R - 2.0)
Cork	0.65 to 0.67 (R - 3.7 to 3.8)	0.65 (R - 3.7)

For PCM-HLC, the literature suggests a tension between high thermal storage and sufficient thermal resistance. Higher PCM content can increase heat capacity, but it may also increase density and conductivity. This balance is especially important for cold-climate envelopes.

2.5.5. Specific heat capacity

Specific heat capacity (C_p) describes a material's ability to store sensible heat and is directly relevant to indoor temperature moderation [10, 11, 214]. For PCM-HLC, C_p must be interpreted together with latent heat storage because the effective heat-storage capacity changes near the phase-transition temperature.

2.5.6. Thermal diffusivity

Thermal diffusivity combines conductivity, density, and specific heat capacity to describe how quickly a material responds to changing temperature [203, 215]. The unresolved issue for PCM-HLC is how diffusivity should be interpreted when phase change, moisture state, and density vary together.

2.6. Research gap

2.6.1. Research gaps overview

The reviewed literature identifies four connected gaps that motivate the experimental programme. The first concerns material characterisation and mix design. Existing methods describe hemp shiv and binder systems, but they do not fully explain how PCM impregnation changes shiv-binder interaction, binder demand, leakage resistance, and stable PCM-HLC formation.

1. Material characterisation and mix-design gaps

Conventional HLC studies provide useful knowledge on shiv size, density, moisture behaviour, and morphology. Their transferability to PCM-HLC remains uncertain because PCM changes pore occupancy, surface wettability, and binder contact.

The resulting gap is the lack of a clear relationship between PCM-impregnated shiv properties and the binder requirements needed to form cohesive, leakage-resistant PCM-HLC.

2. Experimental behaviour and testing-framework gaps

The second gap is methodological. HLC properties are sensitive to casting direction, specimen size, density, and testing protocol, yet these variables are not consistently reported or controlled.

Although anisotropy and size effects are recognised in conventional HLC, their relevance to high-PCM PCM-HLC remains unclear because PCM can alter pore structure, density, and interfacial bonding.

3. Composite performance and trade-off analysis gaps

The third gap concerns coupled composite performance. PCM improves latent heat storage, but it may also change strength, moisture buffering, density, and binder hydration. Existing studies often use limited PCM ranges, which makes it difficult to identify usable performance thresholds.

A broader trade-off analysis is therefore needed to connect PCM substitution level with thermal, mechanical, and hygric outcomes under comparable testing conditions.

4. Building-envelope performance evaluation and optimisation gaps

The fourth gap is the translation from material performance to envelope behaviour. PCM-HLC may offer thermal storage and moisture regulation, but cold climates require sufficient static thermal resistance when the PCM is solid. Few studies resolve this storage-resistance balance in a bio-based multilayer envelope.

5. Overview of research gaps

Taken together, the literature lacks an integrated framework linking PCM-modified shiv properties, binder demand, testing consistency, composite trade-offs, and envelope-level performance.

These unresolved challenges motivate the experimental programme developed in the following chapters: material characterisation and preliminary casting, casting-direction and specimen-size assessment, PCM-substitution trade-off analysis, and multilayer envelope evaluation.

2.6.2. Motivations by chapter

Chapter 4 addresses material characterisation and preliminary casting.

The literature provides methods for describing hemp shiv and binder systems, but it does not fully show how PCM-impregnated shiv size affects binder demand or how SCM-modified binders perform under high fatty-acid PCM loading.

The corresponding work therefore focuses on linking shiv morphology, PCM retention, binder composition, cohesion, and leakage resistance.

Chapter 5 addresses casting direction and specimen-size effects of PCM-HLC.

Because conventional HLC is anisotropic and specimen-size dependent, but PCM-HLC may have altered pore and binder structures, the literature does not yet show whether the same testing assumptions remain valid at high PCM loading.

The corresponding work evaluates casting direction and specimen geometry as sources of variation in mechanical, thermal, and moisture-buffering measurements.

Chapter 6 addresses PCM mix proportioning.

Previous studies usually examine limited PCM contents, leaving the trade-off among latent heat storage, density, strength, and moisture buffering insufficiently mapped.

The corresponding work therefore examines a broad PCM substitution range to identify performance thresholds for application-specific PCM-HLC design.

Chapter 7 addresses multilayer PCM-HLC envelope design.

The literature shows that PCM can improve thermal storage, but cold-climate envelopes must also maintain thermal resistance when PCM is solid. This motivates a multilayer design approach that balances storage, insulation, and moisture regulation under dynamic boundary conditions.

3. Chapter 3: Research Methodology

3.1. Research Method Overview

This chapter describes the experimental and numerical methods used to characterise raw materials, prepare PCM-HLC specimens, measure mechanical and hygrothermal properties, and evaluate sandwich-panel performance. The methods are grouped as standardised tests, adapted literature procedures, and newly developed comparative tests.

Fig. 3.1 summarises the two-phase workflow. Phase I covers raw-material characterisation, preliminary PCM-HLC casting, specimen preparation, and experimental testing. Phase II develops and validates a numerical model for sandwich PCM-HLC panels, then uses the model to assess cold-climate envelope performance.

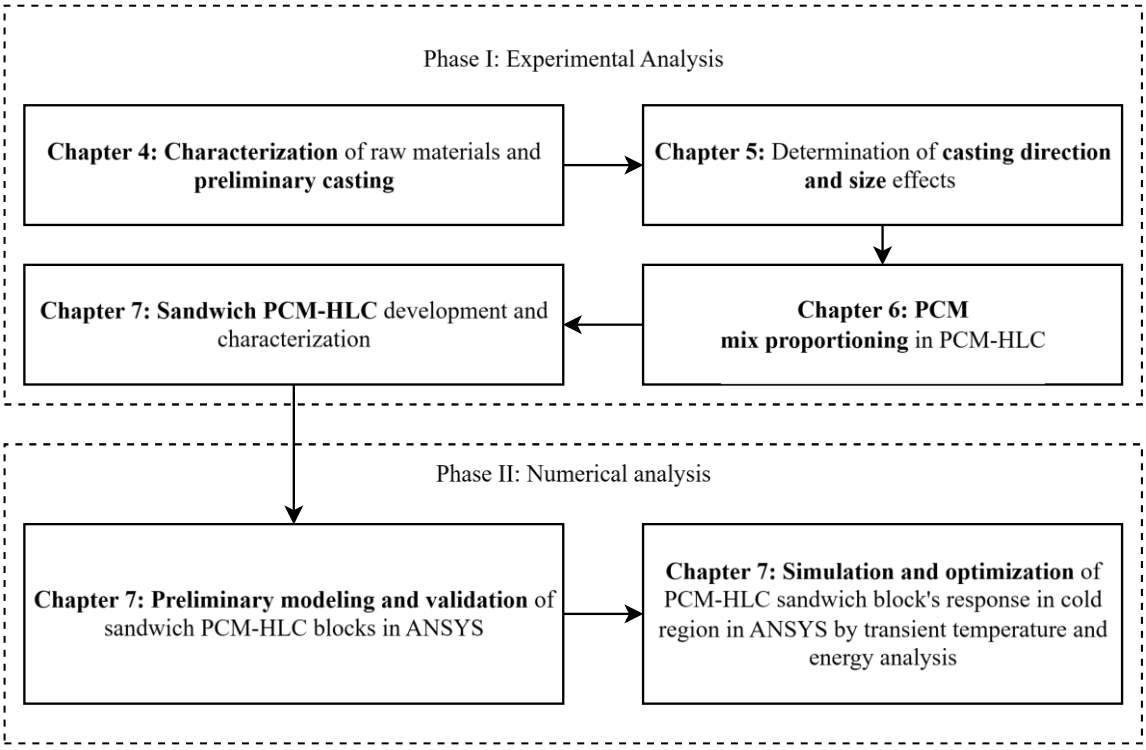


Fig. 3.1. Overview of the methodology.

3.2. Phase I Experimental Analysis (Chapter 4): Characterisation of Raw Materials and Preliminary Casting

3.2.1. Characterization of raw materials

The PCM-HLC specimens comprised hemp shiv, binder, and fatty-acid PCMs. Raw-material characterisation focused on the properties most likely to affect batching, PCM retention, hydration, and hygrothermal performance.

3.2.1.1. Size, morphology, and particle-size distribution of hemp shivs

For each shiv fraction, more than 2000 particles were separated on A4 sheets, scanned at 600 dpi, converted to 8-bit grayscale, and analysed in ImageJ following the RILEM TC 236-BBM approach. Touching or overlapping particles were excluded to improve particle-boundary detection, as illustrated in Fig. 3.2.

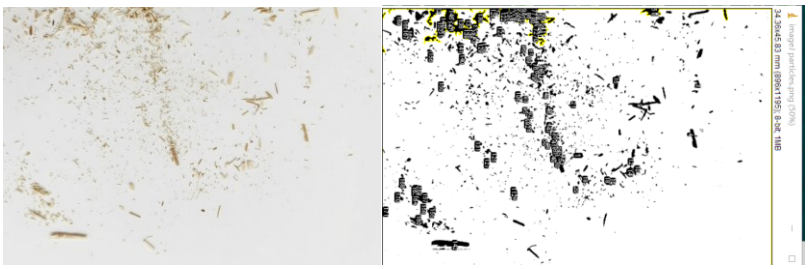


Fig. 3.2. Sample ImageJ analysis (left) before processing and (right) after processing.

3.2.1.2. Density of hemp shivs

3.2.1.2.1. Bulk density

Bulk density and skeletal density were measured because they describe different levels of pore inclusion. Bulk density includes inter-particle voids and is relevant to batching, whereas skeletal density estimates the density of the solid shiv material.

Bulk density was measured on oven-dried shiv samples using a calibrated cylindrical container. The shiv was dried at 60 °C to constant mass, cooled in the closed

container, levelled by repeated inversion, weighed, and related to the occupied volume determined by water filling.

The measurement was repeated three times for each shiv fraction, and bulk density was calculated using (3) [216]:

$$\rho = \frac{M}{V} \tag{3}$$

Where ρ represents the bulk density (g/cm³), M is the mass of the shiv (g), and V is the volume of the sample (cm³).

3.2.1.2.2. Skeletal density by gas pycnometer

Skeletal density was measured by helium pycnometry (Micromeritics AccuPyc II 1345) at 21 ± 1 °C. Tests used a purge-fill pressure of 19.5 psig, an equilibration rate of 0.0050 psig/min, and at least 2 g of material occupying approximately two-thirds of the 112 cm³ cell. Each reported value is the average of 10 purge cycles.

3.2.1.2.3. Vacuum impregnation

To reduce moisture-related error, all shiv samples were dried at 60 °C for 24 h before testing. Vacuum impregnation was then applied at 90 kPa for 10 min to remove trapped air from the porous shiv structure [64, 217], as shown in Fig. 3.5.



Fig. 3.5. Vacuum chamber over a heat plate setup.

3.2.1.3. Initial moisture content

Initial moisture content was measured on ten replicate shiv samples of approximately 10 g. Samples were weighed at room conditions (55% RH), oven-dried at 60 °C to constant mass and reweighed after cooling.

Initial moisture content was calculated from the wet and dry masses using (7) [216]:

$$W\,(\%) = 100 \times \frac{(m_w - m_d)}{m_d} \tag{7}$$

Where W represents the initial water content (%), m_w is the initial mass/wet mass of the sample under room humidity (g), and m_d is the dry mass of the sample (g).

3.2.1.4. Water absorption

Water absorption was measured using the standardised procedure shown in Fig. 3.6 [18, 49].

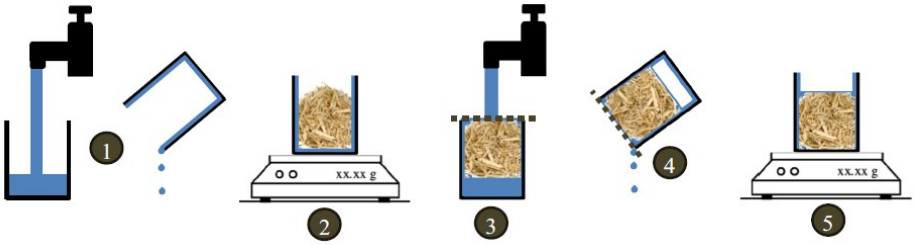


Fig. 3.6. Experimental procedure to measure the water absorption [49].

For each test, 5-10 g of shiv was weighed, dried at 60 °C to constant mass, and immersed in water. Excess water was drained after immersion, with a permeable synthetic mesh bag used for fine particles to prevent material loss.

Immersion durations were 1, 15, 240, and 2880 min. Each duration was tested in triplicate on separate shiv samples, and the bag mass was deducted where applicable.

Water absorption was calculated using (8). The initial absorption rate was determined from the slope of the absorption curve at 1 min when plotted against logarithmic time.

$$W_t = IRA + K_1 Log(t) \quad (8)$$

Where W_t is the water absorption at any given time, IRA is the initial rate of absorption, and K_1 is the slope of the absorption curve.

3.2.1.5. Moisture retention

Moisture retention was assessed on 5-10 g shiv samples dried at 60 ± 5 °C to constant mass, immersed in water for 24 h, and drained gravitationally for 10 min before the saturated mass was recorded.

The saturated samples were dried in a ventilated oven at 60 ± 5 °C and reweighed after 1, 2, 4, 6, 8, 12, 24, 28, 32, 36, 40, 44, and 48 h to quantify moisture loss.

Three independent shiv samples were tested for each fraction. Moisture retention was calculated from the mass change at each interval and used to compare drying behaviour among particle sizes.

3.2.1.6. Impurities and fibre content

Impurity and fibre content were measured using the water-separation method adapted from Mahmood et al. [43]. A 10 g oven-dried shiv sample was submerged in 3 L of water, stirred for 5 min at 750 RPM, and left to settle for 10 min. Floating shiv-rich particles were collected, and the remaining suspension was passed through a No. 200 (75 μm) sieve to recover fine fibres and impurities.

The impurity level f_i was then calculated using the following equation:

$$f_i(\%) = 100 \times \frac{m_d}{m_i} \quad (9)$$

Where m_i is the dry mass of the impurities (g), m_d is the initial dry mass of the hemp shiv sample (g).

Impurities included residual fibres, leaves, outer stem fragments, and root particles. Fibre content was then estimated by handpicking and weighing the fibre fraction, providing a low-cost check on raw-material purity before HLC casting.

3.2.1.7. SEM

SEM specimens were coated with 10 nm of gold-palladium and examined in environmental mode at 2 mbar (200 Pa) and 15 kV. These settings were selected for non-conductive, moisture-sensitive organic materials [13].

3.2.1.8. Thermal behaviour by DSC

DSC was used to determine the phase-change behaviour of CA, LA, MA, PA, SA, and selected eutectic mixtures. Samples of less than 10 mg were sealed in Tzero aluminium pans, with an empty pan used as the reference. Thermal data were collected and analysed using TA Instruments TRIOS software.

The DSC protocol used a heat-cool-heat cycle to standardise thermal history: equilibration at 10 °C, heating to 80 °C at 5 °C/min, a 15 min hold, cooling to 10 °C at 5 °C/min, a second 15 min hold, and a second heating step to 80 °C. The 5 °C/min rate was selected from the literature to balance peak resolution and signal sensitivity [218]. Instrument calibration was checked with indium as required by instrument use.

3.2.1.9. XRF chemical composition

Binder chemical composition was measured by X-ray fluorescence using a Rigaku Supermini200 benchtop wavelength-dispersive spectrometer with a 200 W Pd-anode X-ray tube.

3.2.2. Preliminary casting of PCM-HLC

Preliminary casting was used to identify PCM-HLC mixtures that could retain high PCM contents while remaining cohesive, dimensionally stable, and resistant to PCM leakage.

3.2.2.1. PCM impregnation

PCM was incorporated by submerging hemp shiv in liquid fatty acids at 80 °C under vacuum. This temperature kept the PCM molten while vacuum exposure promoted infiltration into the shiv pore network [12, 64, 137] (Fig. 3.7).



Fig. 3.7. A diagrammatic representation of PCM impregnation into hemp shivs.

After impregnation, samples rested for 5 days to reduce early leakage [13]. The PCM substitution rate was calculated using:

$$\text{Replacement rate (\%)} = \frac{m_{PCM}}{m_{PCM} + m_{hemp}} \times 100 \quad (10)$$

Where m_{PCM} is the mass of PCM, m_{hemp} is the mass of the hemp shiv.

The impregnated shiv was then used to cast PCM-HLC specimens. After curing, the specimens were screened using the cohesion and leakage tests described below.

The screening matrix varied PCM substitution rate, hemp-to-binder ratio, and SCM substitution level. This allowed unstable mixtures to be excluded before larger specimens were prepared for later chapters.

3.2.2.2. Sample preparation

The mixing procedure was adapted from the literature [148]. PCM-impregnated shiv and binder were each pre-wetted with one-tenth of the total water, then combined while the remaining water was added gradually. Mixing continued for at least 5 min, or until a uniform and workable consistency was obtained.

Preliminary PCM-HLC specimens were cast in 50 mm × 50 mm × 50 mm wooden moulds to screen mix feasibility using a small, repeatable specimen geometry.

Fresh PCM-HLC was compacted on a vibration table for 30 s at 60 Hz. Material was added or removed during compaction until the filled mould was level with the top edge.

Specimens were demoulded immediately to limit internal setting stresses [43] and cured for 28 days at 22 ± 1 °C and 55 ± 4% RH.

3.2.2.3. Cohesion test

Two cohesion checks were used because PCM-HLC mixtures can appear workable during mixing but lose integrity after curing. The first was the fresh-state test-ball method, which identifies the minimum water and binder needed to form a cohesive mixture [24, 43]. Water was adjusted in 10 g increments until a hand-formed ball retained its shape, showed no excessive water release, and split cleanly when pressed [172, 219] (Fig. 3.8).



Fig. 3.8. Optical photo of (a) a failed test ball that cannot retain its shape, and (b) a test ball that retained its shape.

A post-curing abrasion test was developed for this study to compare the internal bonding of low-strength PCM-HLC specimens after 28 days of curing. Conventional cohesion or shear tests require larger specimens and more complex analysis [220], whereas the proposed test provides a simple screening method for many mix designs using the same specimen geometry.

Each specimen was weighed to the nearest 0.01 g, placed on a sieve mounted over a collection plate, and abraded for 180 s at 60 Hz while held in position. The final mass was then recorded, and cohesion was classified from the percentage of gravimetric particle loss:

- < 1% mass loss: negligible fine-particle loss and no visible change in specimen geometry, indicating excellent cohesion.
- 1-5% mass loss: limited detachment or local surface peeling while the specimen retained its geometry, indicating acceptable cohesion.
- > 5% mass loss: significant particle loss, visible degradation, or partial collapse, indicating insufficient cohesion.

The thresholds were established from repeated preliminary observations of particle loss and visible damage. They are intended for comparative screening rather than as a standardised mechanical property. Repeatability was supported by fixed specimen dimensions, vibration frequency, test duration, mass-loss measurement, and replicate specimens. The method is therefore useful for ranking PCM-HLC mixes before full mechanical testing, while its limitation is that it does not replace compressive, tensile, or shear-strength measurements (Fig. 3.9).

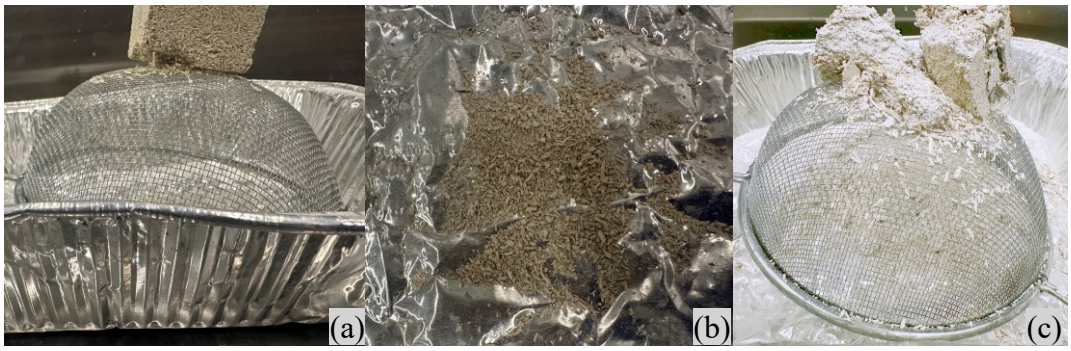


Fig. 3.9. (a) Cohesion test setup on a vibration table, (b) lost 1% - 5% particles during the test, and (c) a failed specimen (> 5% mass loss) during the test.

3.2.2.4. Leakage test

The leakage test was developed because shape retention after curing does not necessarily confirm PCM retention during thermal cycling. Specimens cured for 28 days were subjected to 50 heat-cool cycles on absorbent paper to reveal visible PCM migration (Fig. 3.10).

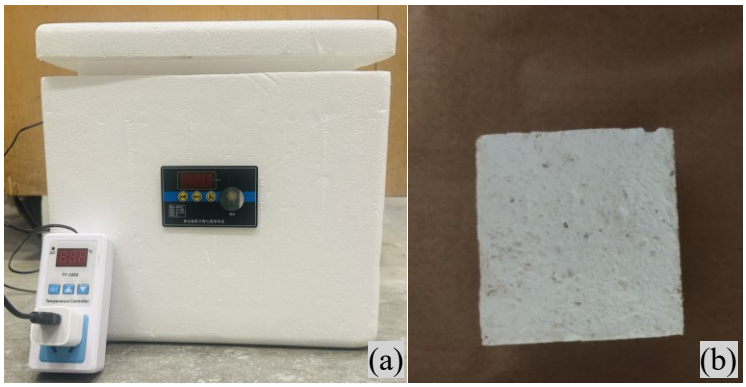


Fig. 3.10. Optical photo illustrates (a) a temperature and timer-controlled heating box for thermal cycling, (b) the specimen placed on top of a piece of paper towel and the heating mat, to observe the sign of leakage.

During each cycle, the heating mat was raised to 60 °C and held for 30 min, then switched off until the specimen cooled naturally to 21 ± 1 °C. The specimen was held at room temperature for another 30 min before the next heating step. Leakage was assessed by inspecting the absorbent paper after 50 cycles. The test is qualitative, but it provides a practical and repeatable comparison of leakage risk under conditions above the PCM melting range.

3.3. Phase I Experimental Analysis (Chapter 5): Casting Direction and Size Effects of PCM-HLC

This stage evaluated whether casting direction and specimen thickness affect PCM-HLC mechanical, thermal, and moisture-buffering properties. These variables are recognised in conventional HLC, but their influence after PCM impregnation required direct testing (Fig. 3.11).

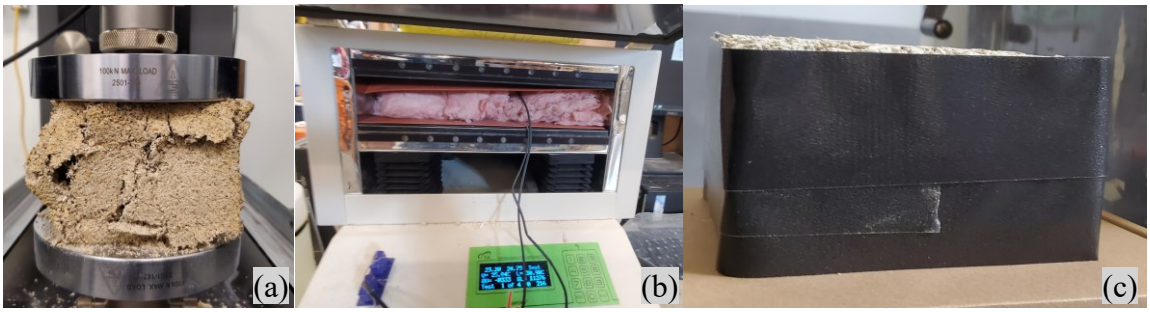


Fig. 3.11. PCM-HLC specimens for mechanical, thermal, and moisture buffering test.

3.3.1. Sample preparation

3.3.1.1. Mixing

The base mixing procedure followed Section 3.2.2.2.

3.3.1.2. Moulding

Rectangular moulds of 150 mm × 150 mm × 50 mm and 150 mm × 150 mm × 80 mm were used for thermal and moisture-buffering tests. Specimens were cast in horizontal and vertical compaction directions to examine anisotropic behaviour [44, 53] (Fig. 3.12).

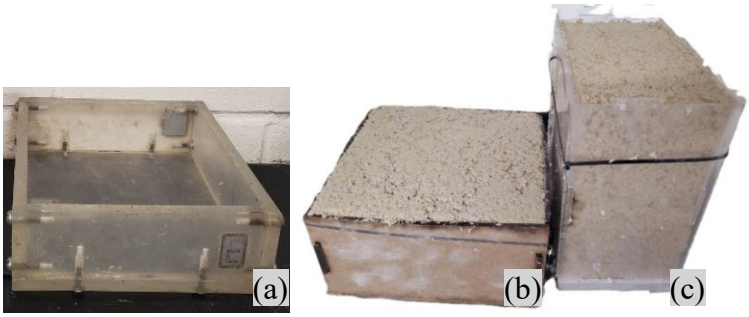


Fig. 3.12. Optical photo of (a) A horizontal 150 mm x 150 mm x 50 mm mould; (b) Sample casted in horizontal direction; (c) Samples casted in a vertical direction.

Compressive-strength specimens were cast in 50 mm and 100 mm cubic moulds to evaluate specimen-size and directional effects (Fig. 3.13).

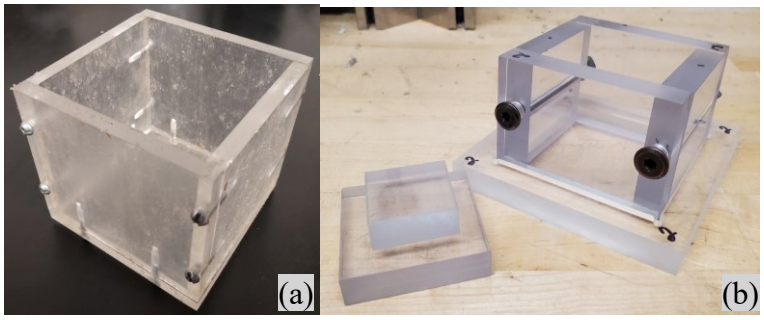


Fig. 3.13. (a) A 100 mm cubic mould, and (b) a 50 mm cubic mould.

3.3.1.3. Vibration compaction

Vibration compaction followed the preliminary casting protocol: fresh PCM-HLC was compacted for 30 s at 60 Hz, and material quantity was adjusted until the surface was level with the mould top. This method was adopted from Mahmood's standardisation work [43].

3.3.1.4. Curing

Rectangular specimens remained in moulds for 48 h to prevent deformation at low early-age strength. The 50 mm and 100 mm cubes were demoulded immediately to limit internal setting stresses [43]. All specimens were then cured for 28 days at 22 ± 1 °C and 55 ± 4% RH.

Following the curing period, samples were prepared based on their testing requirements:

- Hygrothermal samples: dried at 60 °C to constant mass (variation < 0.1%) before testing.
- Compressive-strength samples: tested after 28 days of curing without oven drying to represent room-condition mechanical performance.

3.3.2. Compressive strength

Compressive strength was measured after 28 days of curing. Each result represents the mean of three specimens. Tests used 50 mm cubes following ASTM C109 and ASTM C513, or 100 mm cubes following BS EN 12390-1 [190] and BS EN 826:2013 [191]. Loading was applied with an INSTRON 68FM-100 UTM equipped with a 100 kN load cell, using a displacement rate of 3 mm/min for 50 mm cubes. Results were reported to the nearest 0.1 MPa.

Failure was defined as the peak of the load-displacement curve [53]. When no clear peak occurred, the compressive strength was taken as the stress at 10% strain. The test was stopped after major mechanical failure because post-peak readings can reflect compression of collapsed material rather than intact specimen strength.

Stress was calculated from load divided by cross-sectional area. Strain was estimated from machine displacement divided by initial specimen height because external strain gauges were not used. The modulus of elasticity was therefore used only for comparative analysis and was calculated from the 10-40% portion of the maximum-stress range using:

$$E = \frac{\sigma}{\varepsilon} = \frac{\frac{F}{A}}{\frac{\Delta L}{L}} \tag{11}$$

Where E is the Modulus of elasticity (MPa), σ indicates the stress (MPa), ε shows the strain (-), F is the applied load (N), A denotes the cross – sectional area (mm^2), and ΔL refers to the device displacement (mm). L shows the initial length of the specimen (mm).

Using the 10-40% stress range reduced the influence of initial microcrack closure and provided a more consistent comparative stiffness value for these composites.

3.3.3. Thermal properties

(a) Thermal conductivity

Thermal conductivity was measured using a FOX 304 heat-flow-meter apparatus in accordance with ASTM C518-17 [208]. The apparatus was calibrated with NIST 1450b SRM [221]. Specimens were dried at 60 ± 1 °C to constant mass and tested at mean temperatures of 12.5, 22.5, 32.5, and 40 °C. Edge insulation was added to reduce lateral heat loss (Fig. 3.14).



Fig. 3.14. The HFM setup with insulation materials wrapping around the specimen.

(b) Specific heat capacity

Specific heat capacity was measured using the same FOX 304 apparatus and dried specimens. Tests were conducted at average temperatures of 20 °C and 30 °C to capture temperature dependence near the PCM transition range.

(c) Thermal diffusivity

Thermal diffusivity (α) was calculated from thermal conductivity, density, and specific heat capacity using:

$$\alpha = \frac{k}{\rho \cdot C_p} \quad (12)$$

Where α represents thermal diffusivity, k denotes thermal conductivity, ρ is density, and C_p is the specific heat capacity of the material. Unit is in $m^2/s \times 10–^6$.

(d) Thermal resistance

Thermal resistance (R – value, or RSI in metric) is the inverse of thermal conductivity for a given material thickness [222]. Thermal conductivity can be used to calculate thermal resistance using the following formula, provided the sample's thickness (L) is known:

$$R = L / k \quad (13)$$

The unit is either in SI units ($m^2 \cdot K/W$) or converted to imperial units ($ft2 \cdot °F \cdot h/BTU$) using the standard conversion factor of 5.678263.

3.3.4. Moisture buffering value

Moisture-buffering value (MBV) was measured using the Nordtest protocol [223]. Specimens provided at least 0.01 m^2 of exposed area, with all sides sealed except the top surface. The 150 mm × 150 mm × 80 mm and 150 mm × 150 mm × 50 mm specimens met the exposed-area requirement while limiting material use (Fig. 3.15).

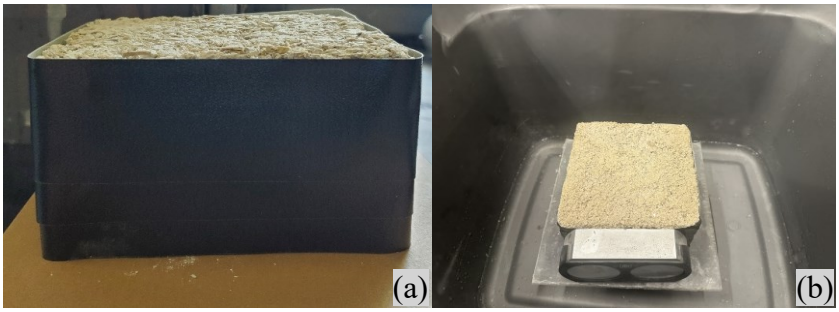


Fig. 3.15. (a) Sample preparation, (b) the MBV test setup.

Relative humidity was controlled with saturated salt solutions following ASTM E104-20a [224]: NaCl solution for 75 ± 2% RH and $MgCl_2$ solution for 33 ± 2% RH. At 23 ± 1 °C, specimens were cycled between 75% RH for 8 h and 33% RH for 16 h until consecutive-cycle mass change was less than 5%.

Specimen mass was recorded with a 0.01 g precision balance, and MBV was calculated using (14).

$$MBV = \frac{\Delta m}{A \cdot \Delta RH} \tag{14}$$

Where MBV represents the moisture buffering value, Δm is the moisture uptake or release during the humidity cycle, A is the exposed surface area of the sample, and ΔRH is the difference between the highest and lowest relative humidity values during the cycle.

3.4. Phase I Experimental Analysis (Chapter 6): PCM Mix Proportioning

This stage examined how PCM substitution level affects PCM-HLC performance and material economy. Specimens used the molar-ratio binder design developed in Chapter 4 and the testing framework established in Chapter 5.

3.4.1. Mixing, moulding, and curing

3.4.1.1. Mixing

The mixing procedure followed Section 3.3.1.1.

3.4.1.2. Moulding

Specimens were cast in 150 mm × 150 mm × 50 mm rectangular moulds and 50 mm cubic moulds, as shown in Fig. 3.12 and Fig. 3.13.

3.4.1.3. Hydraulic press compaction

Hydraulic press compaction was adopted to increase specimen density and evaluate the upper performance range of PCM-HLC. A target wet density of 1000 kg/m³ was selected from trial casting as the highest density achievable with the available moulds and mix design.

Fresh PCM-HLC was compacted using a 10-ton hydraulic press. A 50 mm wooden block was placed between the piston and the mixture to distribute pressure more uniformly across the specimen surface.

To reduce segregation and improve interlayer contact, specimens were compacted in two stages. Half of the mixture was first compacted to half thickness, and the surface was keyed to approximately 2 mm depth before the remaining mixture was added and compacted to the final thickness. Fig. 3.16 shows the created surface roughness pattern intended to enhance mechanical interlocking and interfacial bonding between the composite layers.

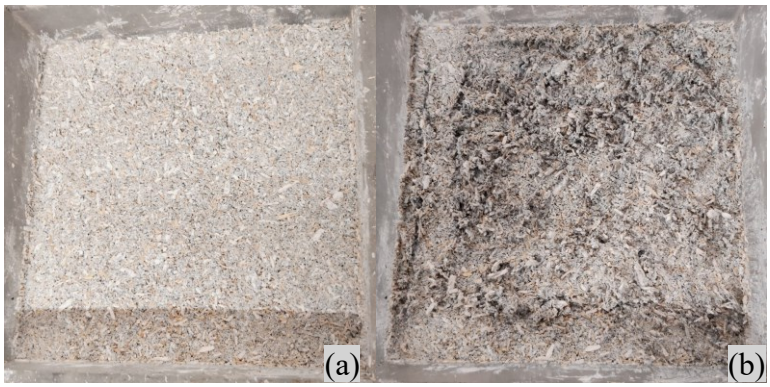


Fig. 3.16. The specimen showing (a) the initial 25 mm layer after primary compaction, and (b) the same layer after the keying process.

3.4.1.4. Curing

After compaction, specimens were demoulded immediately and cured for 28 days at 22 ± 1 °C and 55 ± 4% RH. Before MBV testing, specimens were conditioned for 7 days at 22 ± 1 °C and 30 ± 4% RH to stabilise internal moisture content (Fig. 3.17).



Fig. 3.17. Part of the cured PCM-HLC specimens with different PCM substitution rates.

3.4.2. Experimental testing

Mechanical and hygrothermal testing followed the procedures described in Section 3.3.

3.5. Phase I Experimental Analysis (Chapter 7): Sandwich Block Casting

This stage developed a multilayer PCM-HLC sandwich panel. The design used two PCM-HLC layers with different phase-change ranges and 70% shape-stabilised PCM substitution to respond to inward and outward thermal gradients (Fig. 3.18).

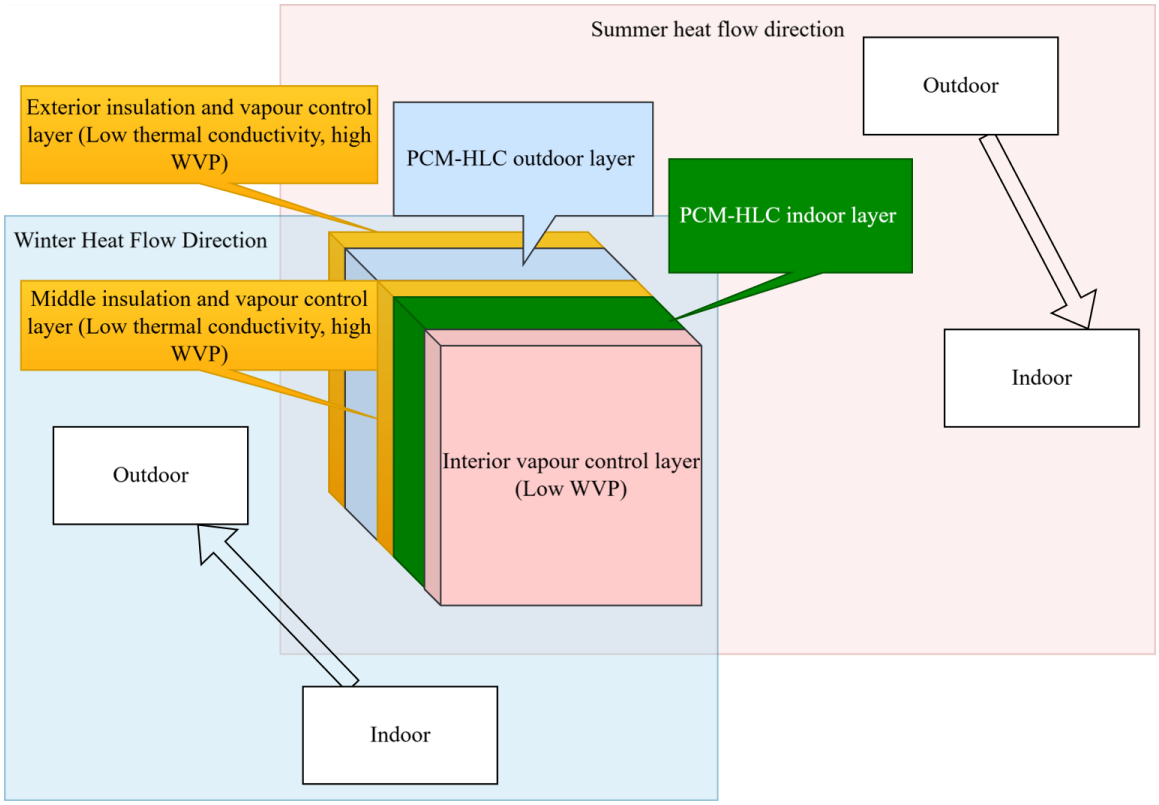


Fig. 3.18. Schematic illustration of the sandwich panel design.

The exterior facings and middle insulation layer encapsulated the PCM-HLC layers, added leakage protection, and contributed vapour control, thermal resistance, and moisture buffering. The layer arrangement was also used to study how storage and insulation functions can be combined in one bio-based assembly.

3.5.1. Sample Preparation

3.5.1.1. Mixing, moulding, and curing

3.5.1.1.1. Mixing

Materials for each layer were weighed and mixed separately according to the specified layer ratios. The base mixing procedure followed Section 3.3.1.1.

3.5.1.1.2. Moulding

A 10 cm × 10 cm × 15 cm acrylic mould was used to cast 10 cm × 10 cm × 10 cm sandwich specimens (Fig. 3.19).

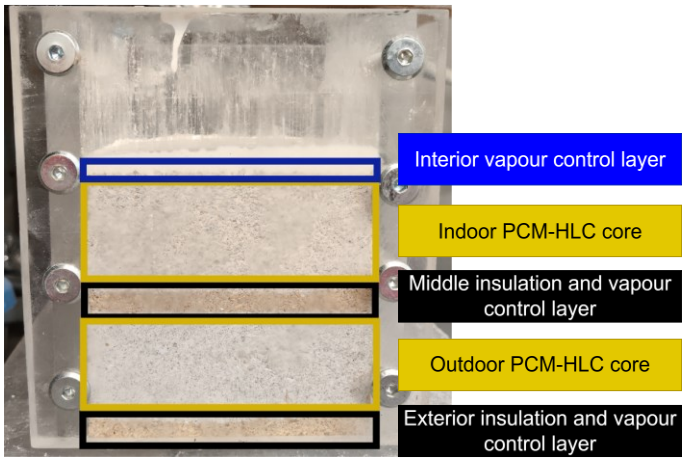


Fig. 3.19. 10 cm x 10 cm x 10 cm sandwich PCM-HLC specimen.

The sandwich specimens were compacted layer by layer so that each functional layer reached its target thickness and density. Layer thicknesses followed the proportions shown in Fig. 7.1.

Each fresh layer was initially compacted thicker than its final target thickness to account for cumulative densification during later compaction steps. The process continued until the full sandwich specimen reached its final dimensions and the intended layer proportions.

3.5.1.1.3. Curing

After compaction, specimens were kept in closed containers at 21 ± 1 °C and 55 ± 4% RH. Because the fresh lime-plaster layer required early strength before handling, specimens were demoulded after 48 h and then cured for another 26 days under the same conditions [225].

3.5.2. SEM

The microstructure of each layer was examined by SEM using the procedure described in Section 3.2.1.7.

3.5.3. HFMA thermal test

Thermal properties were measured using the HFMA procedure described in Section 3.3.3, and the results are discussed in Section 7.2.3.

3.6. Phase II Numerical Analysis (Chapter 7): Preliminary Modelling and Validation of Sandwich PCM-HLC

An ANSYS Fluent model was developed to complement the experimental sandwich-panel tests. The model was validated against HFMA measurements, followed by a mesh-independence study using three mesh sizes. The validated model was then used for cold-climate simulations.

3.7. Phase II Numerical Analysis (Chapter 7): Simulation and Sensitivity Analysis of Sandwich PCM-HLC Using Cold-Region Weather Data

The numerical study evaluated transient thermal response and energy consumption for PCM-HLC sandwich wall assemblies under active HVAC control. Boundary conditions represented a cold-weather profile for Ottawa, Canada, and thermophysical properties were kept consistent with the experimentally validated model.

Four parametric design strategies were evaluated using transient temperature response and energy consumption:

- Increasing wall thickness: increasing the insulation layer in 2 cm increments to produce 12, 14, and 16 cm total wall thicknesses.
- Integrating a stagnant air gap: replacing the solid HLC insulation layer with an air gap to assess potential energy-savings improvement.
- Optimising PCM: adjusting the PCM phase-change temperature to identify a useful annual operating range.
- Reducing the PCM layer: comparing the original two-PCM-layer assembly with a 10 cm design containing one PCM layer and a thicker insulation or air-gap layer.

These simulations were used to develop climate-specific design guidance for low-carbon PCM-HLC envelope systems [226].

4. Chapter 4: Material Characterisation and Preliminary Casting

This chapter establishes the material and mix-design basis for the PCM-HLC investigated in later chapters. It characterises hemp shiv morphology, moisture behaviour, binder chemistry, fatty-acid PCM thermal properties, and preliminary PCM-HLC casting performance.

The chapter's original contribution is the combined use of ImageJ-based shiv morphology analysis, moisture retention testing, PCM thermal screening, and two-stage preliminary casting to define practical PCM-HLC material limits.

- Stage I determines the maximum practical PCM substitution level for different hemp-shiv sizes using HL as the baseline binder.
- Stage II then uses this limit to assess whether SCM-modified binders can reduce HL content while maintaining cohesion and leakage resistance.

Together, these stages provide the material selection and mix-design rationale used in the mechanical, hygrothermal, and envelope-scale studies that follow.

The chapter concludes by linking the raw-material results to the PCM-HLC formulations selected for Chapters 5-7.

4.1. Materials and methods

4.1.1. Hemp shiv

Hemp shiv used in Chapters 4-7 was supplied by BioComposites Group through Terrafibre Products Company (Edmonton, AB, Canada) and stored at 20 ± 2 °C and 55 ± 5% RH before use.

The shiv was mechanically ground to obtain large, medium, and small fractions with representative particle lengths of 10.4, 4.8, and 1.5 mm, respectively (Fig. 4.1). These fractions enabled particle size to be evaluated as a controlled material variable.



Fig. 4.1. Optical photos of (a) hemp shivs as received; (b) ground medium – sized hemp shivs; and (c) ground small – sized hemp shivs.

Grinding was used not only to reduce size variability but also to expose internal pore networks that could affect PCM impregnation and binder contact. The resulting fractions were characterised by particle-size distribution, density, moisture-related properties, and SEM imaging (Fig. 4.2).

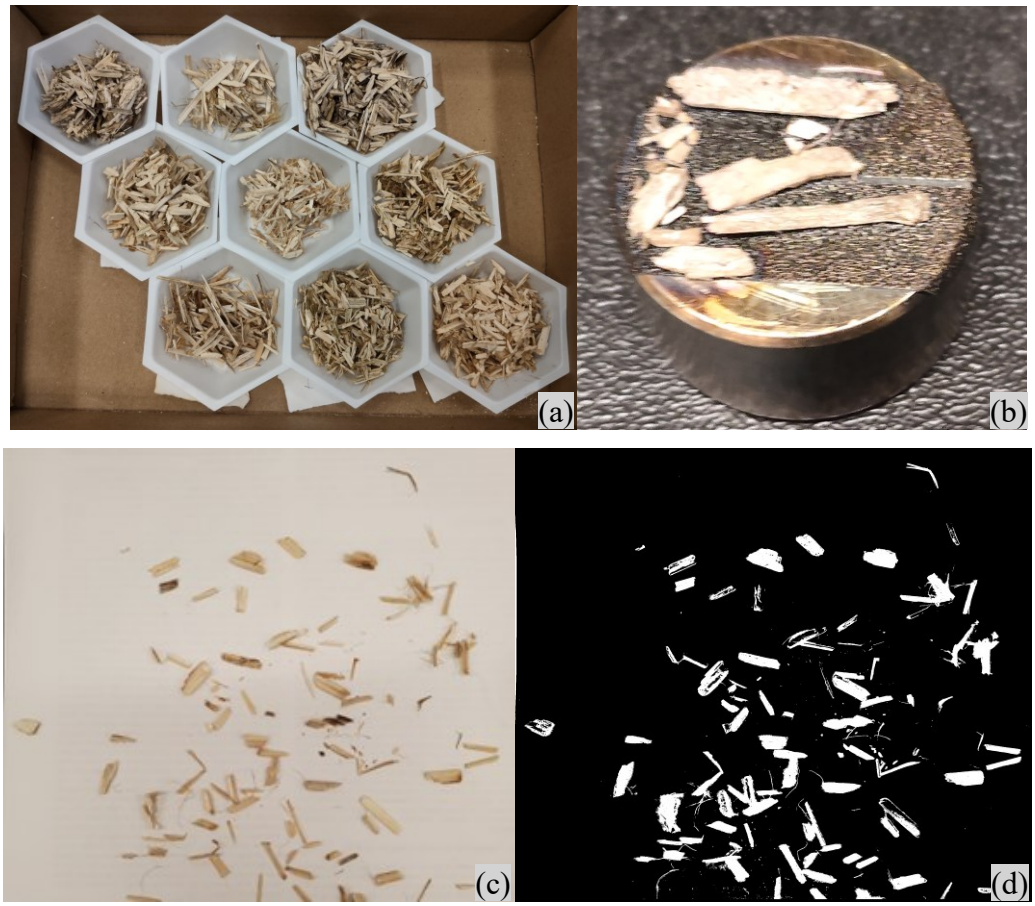


Fig. 4.2. (a) A portion of the hemp shiv sampler awaiting measurements, (b) hemp shiv sample used for SEM, and (c, d) particle size distribution analysis before and after ImageJ processing.

4.1.2. Binder

4.1.2.1. HL

The primary binder was high-calcium HL ($Ca(OH)_2$) supplied by Graymont Inc. It contained 90-100% calcium hydroxide with minor quartz, as reported in Appendix A(a).

4.1.2.2. Supplementary cementitious material (SCM)

4.1.2.2.1. Slag

Ground granulated blast-furnace slag (GGBS) Type S was supplied by Lafarge's Stoney Creek Plant and met ASTM C989/C989M-24 [160]. Key chemical and physical properties are listed in Appendix A(b).

4.1.2.2.2. Metakaolin

EnviroPozz metakaolin was supplied by Whitemud Resources Inc. and complied with CSA A3000 and ASTM C618 requirements for natural SCMs [227–229]. Its properties are listed in Appendix A(c).

4.1.2.2.3. Silica fume

MasterLife SF 100 silica fume was obtained from Lafarge's Ottawa facility. Its chemical and safety data are provided in Appendix A(d).

4.1.3. PCMs

The PCMs were bio-based fatty acids: 98% purity CA, 98% LA, 95% MA, 98% PA, and 95% SA, supplied by Sigma-Aldrich/Millipore Sigma Canada Ltd. Their physical and chemical properties are provided in Appendix A(e).

Binary fatty-acid mixtures were prepared from calculated mass ratios by heating the components to 80 °C, mixing until homogeneous, cooling to room temperature, and storing them in sealed containers.

The PCM screening focused on identifying phase-change ranges suitable for indoor and outdoor building conditions rather than cataloguing every possible fatty-acid combination.

4.2. Raw Materials Characterisation Results and Discussion

4.2.1. Hemp shiv particle size distribution

(i) Noise reduction

ImageJ analysis required a noise-reduction step because small shiv fragments created overlapping particles, shadows, and clustered fibres in scanned images. These artefacts were manually excluded to avoid counting merged particles as individual shiv fragments (Fig. 4.3).

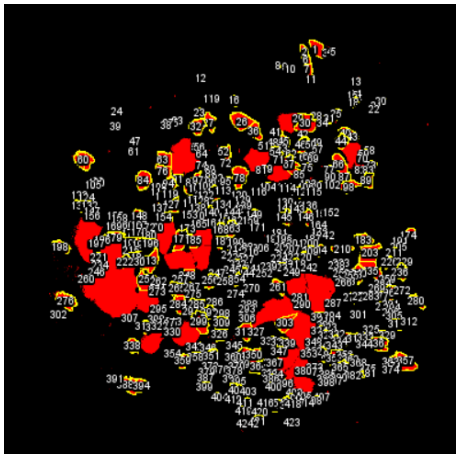


Fig. 4.3. ImageJ pre – processed hemp shiv image before noise elimination.

The pixel resolution also set a lower measurement limit. To reduce this error, shiv fractions were first sieved and then analysed separately, allowing particle-size statistics to be calculated within a more appropriate image scale.

(ii) Statistical analysis

After outlier removal, particle-size distributions were analysed in OriginPro. Particle length was defined as the longest measured dimension, and Fig. 4.4 compares the distributions of the three mechanically ground shiv fractions.

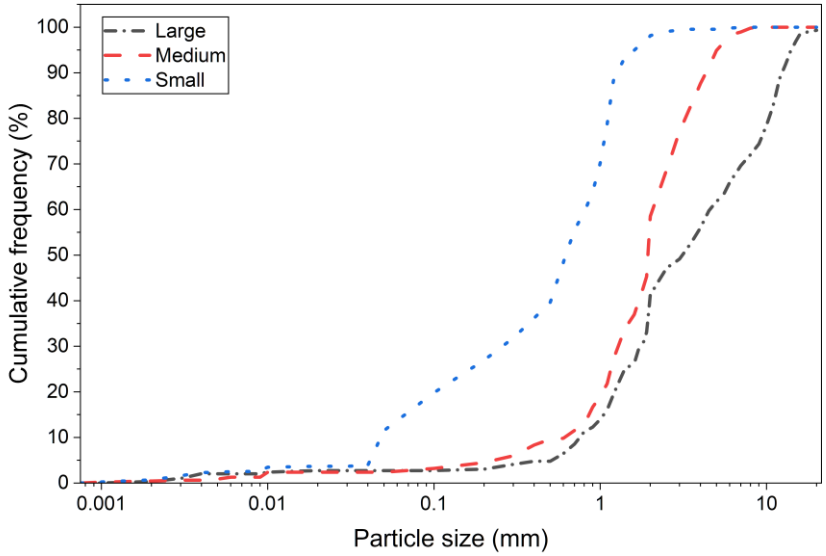


Fig. 4.4. Particle size distribution of three distinct sizes (large, medium, and small) of hemp shivs.

The D90 particle lengths for large, medium, and small shiv were 10.4, 4.8, and 1.5 mm, respectively. The corresponding D50 values were 3.6, 2.2, and 0.72 mm.

The small fraction also had the narrowest length distribution, with a standard deviation of ±0.7 mm compared with ±1.6 mm for medium shiv and ±3.9 mm for large shiv. This result shows that mechanical grinding improved size uniformity, which is important for reproducible PCM uptake and binder demand.

4.2.1.1. Implications for HLC design

These morphology results indicate that small shiv provides the most consistent packing basis for PCM-HLC. Large shiv may preserve more intact longitudinal pores, but its wider size distribution can increase binder demand and produce less uniform composite structure.

4.2.2. Initial moisture content

Table 4.1 presents the statistical comparison of the initial moisture content (IMC) for three hemp-shiv sizes: small, medium, and large.

Table 4.1. Statistical value for the initial moisture content.

Fraction	Mean IMC (%)	Median (%)	IQR (%)	σ (%)	CV
Small	12.6	12.5	11.8–13.2	0.4	0.03
Medium	9.3	9.1	9.0–9.8	0.5	0.05
Large	8.4	8.3	7.3–8.7	1.1	0.13

Fig. 4.5 uses a box-whisker plot to show the statistical difference between different hemp shiv sizes, using the inter-quartile range (IQR, 25–75%), median line, mean, whiskers to 1.5 × IQR, and statistical outliers for IMC.

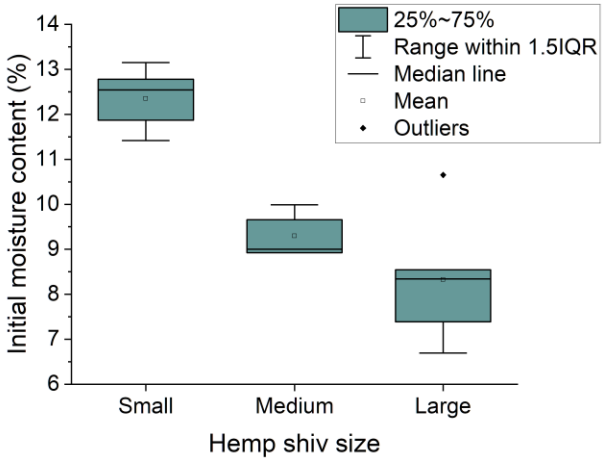


Fig. 4.5. A box plot showing the initial moisture content for different sizes of hemp shiv.

IMC decreased with increasing shiv size. Small shiv had the highest IMC, approximately 12.6%, whereas medium and large shiv measured 9.3% and 8.4%, respectively. The larger coefficient of variation for large shiv indicates greater moisture heterogeneity in the coarser fraction.

For PCM-HLC batching, this size-dependent moisture content affects water-demand correction. Unaccounted moisture in fine shiv can increase the effective water-to-binder ratio, whereas the greater variability of large shiv requires larger or more representative sampling.

Thus, IMC measurement provides a practical control point for mix design. The result is integrated with the other moisture findings in the chapter conclusion rather than repeated separately in each subsection.

4.2.3. Water absorption

Fig. 4.6 illustrates the log-time absorption profiles of the hemp-shiv specimens tested.

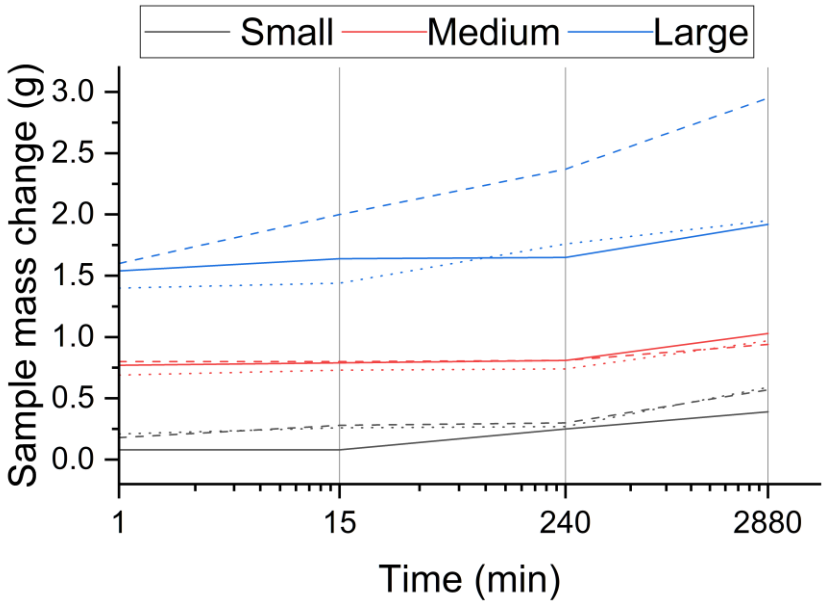


Fig. 4.6. The water absorption profile plotted against the log of time.

The mean initial rate of absorption (IRA) ± standard deviation for small, medium, and large hemp shiv is 0.07 ± 0.28 g.min^{-1}, 0.49 ± 0.03 g.min^{-1}, and 0.96 ± 0.05 g.min^{-1}, respectively. The K_1 for small, medium, and large hemp shiv is 0.10 ± 0.004 g.min^{-1}, 0.06 ± 0.02 g.min^{-1}, and 0.22 ± 0.15 g.min^{-1}, respectively. Each curve is described by the water absorption (W_t): $W_t = 0.07 + 0.10\ \mathrm{Log(t)}$, for a small hemp shiv $W_t = 0.49 + 0.06\ \mathrm{Log(t)}$, for medium hemp shiv, and $W_t = 0.96 + 0.22\ \mathrm{Log(t)}$, for a large hemp shiv at any given time t between 0 and 2880 minutes.

The absorption results show that shiv size changes both the rate and variability of water uptake. Large shiv absorbed water fastest and showed the greatest long-term variability, probably because more intact vascular bundles remain open. Small shiv showed lower initial uptake but higher surface-controlled variability, consistent with grinding-induced disruption of macro-capillary pathways.

4.2.4. Moisture retention

Moisture retention was evaluated by tracking mass loss from saturated shiv during oven drying. Fig. 4.7 compares moisture loss over time for the small, medium, and large fractions.

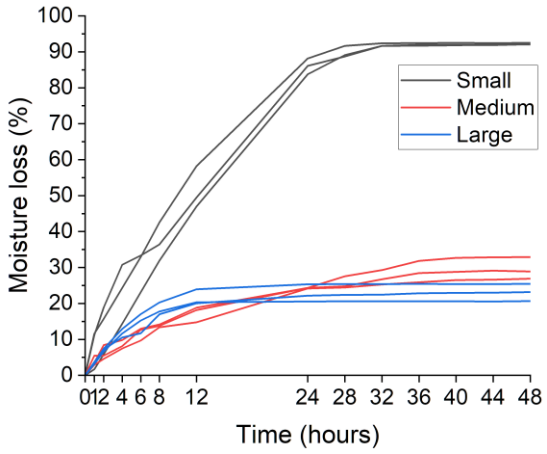


Fig. 4.7. Comparative moisture loss percentage over time for different hemp shiv sizes.

At saturation, small particles retained the most water, with an average water absorption of 1057%, followed by medium and large particles at 540% and 411%. The higher retention of small shiv is consistent with its larger specific surface area and stronger inter-particle capillary water storage.

ANOVA with Tukey's HSD test confirmed that small shiv behaved differently from the other two fractions. The differences between small and large shiv and between small and medium shiv were significant ($p = 0.0001$ and 0.0002), whereas the medium-large difference was not significant ($p = 0.124$).

The higher water absorption measured here compared with Mahmood et al. [43] is mainly methodological. This study used gravitational drainage rather than salad-spinner removal, so surface-held water between particles was intentionally retained to represent moisture exposure conditions closer to building applications.

Drying occurred in two stages. Rapid surface-water loss dominated the first 12 h, followed by slower bound water loss and internal diffusion from 12 to 48 h. Small shiv retained more moisture throughout, suggesting that finer particles may enhance humidity buffering but also require careful drying and water-demand control.

The small standard deviations across triplicate tests indicate that the moisture-retention procedure was repeatable enough to distinguish particle-size effects.

Overall, the moisture results show that particle-size reduction changes the balance between capillary uptake, surface-held water, and drying rate. This balance directly affects PCM-HLC mixing water, curing, and later moisture-buffering behaviour.

4.2.5. Density of fatty acids

The supplier-reported fatty-acid densities are summarised in Table 4.2. The solid-state density is higher than the liquid-state density because molecules are more closely packed in the crystalline phase [230, 231].

Table 4.2. Density of fatty acids.

Fatty acids	Liquid density (kg/m^3)	Solid density (kg/m^3)
CA	877	893
LA	883	1007
MA	862	990
PA	852	852
SA	845	941

4.2.6. Density of binders

Binder densities measured by pycnometer are listed in Table 4.3 and were used for mix proportioning calculations.

Table 4.3. Binder density.

	HL	Metakaolin	Silica fume	Slag
Average (kg/m^3)	2390.4	2622.1	2326.7	2856.3
Standard deviation (kg/m^3)	3.9	5.3	0.8	9.4

4.2.7. Impurities and fibre content

Impurity and fibre contents were measured because non-shiv material can alter density, water demand, mechanical response, and hygrothermal behaviour [232]. The water-separation method of Mahmood et al. [43] was used because it provides a repeatable estimate of fibre content in the 2-44% range.

All shiv fractions came from a single supplier batch. Fig. 4.8 shows typical fibres and impurities recovered from the large-shiv fraction.



Fig. 4.8. An optical photo of sample impurities and fibres.

Measured impurity contents were 10.02%, 9.99%, and 8.15% for large, medium, and small shiv, respectively. Fibre contents were similar across sizes, ranging from 7.29% to 7.34%. The slight decrease in measured impurity content after grinding may reflect reduced visual separation of leaf and root fragments rather than true impurity removal.

The nearly constant fibre content indicates that grinding changed shiv particle size more strongly than it changed fibre content. This is expected because fibres tend to remain long and entangled under mechanical stress, while shiv fragments are more easily shortened.

For PCM-HLC design, the measured fibre and impurity levels provide a material-quality baseline. Their variation was small enough that later performance differences can be interpreted mainly through shiv size, PCM loading, and binder design rather than raw-material purity.

4.2.8. SEM

SEM images in Fig. 4.9 show how 70% PCM substitution changed the hemp shiv surface and pore structure. Raw shiv contained open vascular bundles and longitudinal voids, whereas PCM-treated shiv showed a continuous fatty-acid coating on internal and external surfaces.

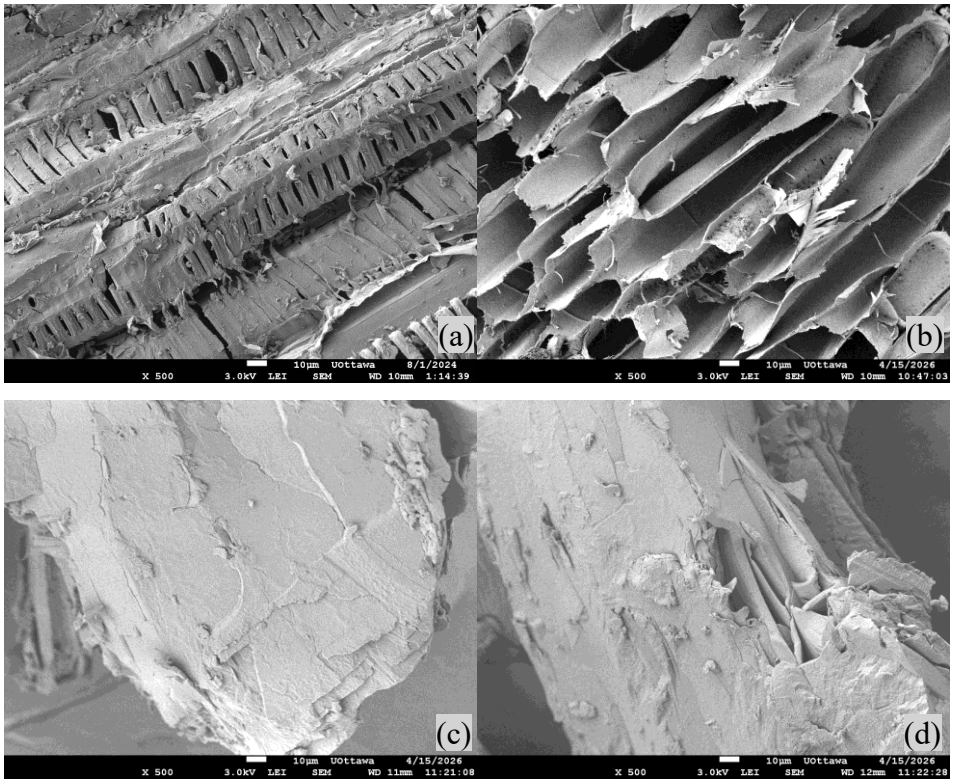


Fig. 4.9. SEM micrographs (x500 magnification) illustrating (a, b) the untreated, porous cellular structure of raw hemp shiv, and (c, d) the morphology following 70 wt% PCM impregnations, showing the infilling of vascular bundles by solidified fatty acids as a smooth coating on hemp shiv.

The open cellular structure of untreated shiv explains its high liquid uptake and supports its use as a shape-stabilising carrier. These same pores also form potential pathways for moisture transport and binder penetration in HLC.

After PCM impregnation, many visible pores were coated or filled by solidified fatty acids. This morphology supports successful PCM retention at high loading, but it also indicates why binder contact and moisture exchange may change after impregnation.

4.2.9. Thermal behaviour

Table 4.4 summarises the DSC-derived phase-change properties of the single-component fatty acids, including onset, peak, endset, melting/solidification enthalpy, and purity.

Table 4.4. The single-component fatty acids' thermal properties.

PCM	Acronym	Melting					Solidification			
		Purity (%)	T_o (°C)	T_m (°C)	T_e (°C)	$\Delta H_m\ (J.g^{-1})$	T_o (°C)	T_s (°C)	T_e (°C)	$\Delta H_s\ (J.g^{-1})$
Capric acid	CA	98	29.67	30.8	31.51	144.64	24.36	26.09	23.87	141.49
Lauric acid	LA	98	42.87	45.86	49.28	163.6	39.23	38.74	33.62	152.91
Myristic acid	MA	95	52.69	54.73	58.1	221.53	50.55	50.76	46.77	231.33
Palmitic acid	PA	98	61.91	64.8	68.48	204.5	59.5	57.9	53.93	204.47
Stearic acid	SA	98	67.82	72.44	77.45	223.01	67.58	65.89	60.91	228.23

The single-component fatty acids showed the expected increase in melting temperature and latent heat with carbon-chain length. CA had the lowest peak melting temperature, approximately 31 °C, while SA had the highest, approximately 72 °C. This range confirms that pure fatty acids alone cannot cover all target building-temperature windows.

Across repeated DSC tests, fusion-temperature standard deviations were 0.19-2.95%, and latent-heat standard deviations were 2.36-6.49%. These variations were smaller than reported differences among batches and literature sources, supporting the reliability of the measurements for material screening.

Capric acid was compared across laboratory-scale and bulk supplies because CA was a key component in later PCM-HLC formulations. All batches showed onset temperatures near 30-31 °C, but the bulk CA had slightly lower phase-change enthalpy, probably because of impurity or batch-composition differences. The thermal properties of capric acid from different supplies and studies are compared in Table 4.5.

Table 4.5. Comparison of capric acid properties across different supplies and studies.

Samples	Melting			
	T_o (°C)	T_m (°C)	T_e (°C)	$\Delta H_m\ (J.g^{-1})$
CA_1	30.02	33.03	36.53	152.23
CA_2	30.37	32.89	36.71	151.88
CA_10 kg_1	29.67	30.8	31.51	144.64
CA_10 kg_2	28.08	30.13	31.88	150.94
CA (Ke, 2017)	31.12	32.71	35.8	166.7
CA (Sawadogo, 2022)	29.8	30.4	-	140.7

Literature comparisons in Table 4.5 and Fig. 4.10 show that the measured CA values remain within the range expected for commercial fatty acids. Differences from Ke [110] and Sawadogo et al. [114] may reflect purity, heating/cooling rate, pan contact, and calibration conditions.

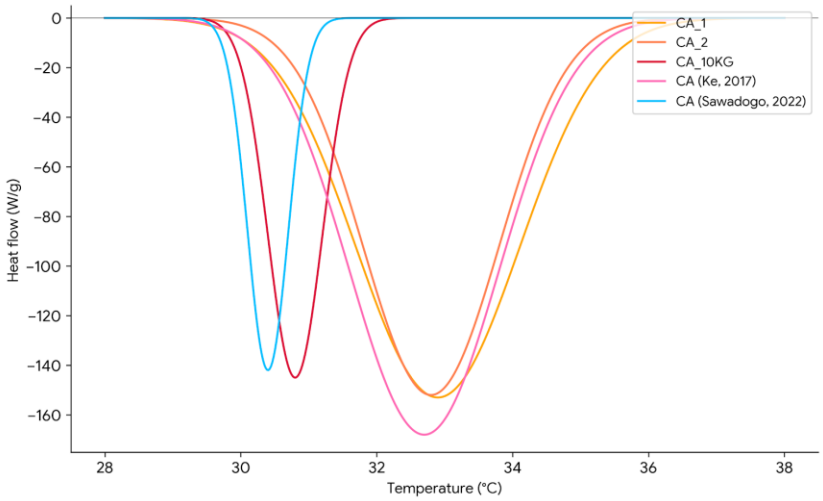


Fig. 4.10. Simulated endothermic process based on DSC results and literature for comparison across studies.

These comparisons show why each supplied batch should be characterised before use. DSC results are sensitive to purity, sample contact, and scanning rate, so literature values alone are not sufficient for quantitative PCM-HLC design.

Although batch-to-batch variation was present, all CA supplies remained within a 6% thermal-property range. This degree of variation is acceptable for screening but should be considered when scaling from laboratory specimens to larger PCM-HLC components.

Binary mixtures lowered phase-change temperatures relative to the single-component fatty acids and therefore allowed the PCM range to be tuned toward building-relevant temperatures. CA-LA reached a peak melting temperature of 25.83 °C with a latent heat of 185.43 J/g, while LA-MA showed very similar melting and solidification enthalpies, indicating good thermal reversibility.

The detailed phase-change properties of the binary mixtures are listed in Table 4.6.

Table 4.6. Thermal properties of binary fatty acids.

Mass Proportions	Acronym	Melting					Solidification			
		Purity (%)	T_o (°C)	T_m (°C)	T_e (°C)	$\Delta H_m\ (J.g^{-1})$	T_o (°C)	T_s (°C)	T_e (°C)	$\Delta H_s\ (J.g^{-1})$
68.3% - 31.7%	CA – LA	98	19.36	25.83	36.22	185.43	14.19	11.34	4.6	58.323
77.6% - 22.4%	CA – MA	96.82	23.39	32.98	45.11	109.51	9.29	5.3	- 3.05	87.86
80.5% - 19.5%	CA – MA	96.82	22.82	24.83	32.04	116.31	21.05	7.96	-7.67	111.12
87.8% - 12.2%	CA – MA	96.82	19.56	24.04	31.09	120.77	18.79	16.39	10.92	114.7
20.8% - 79.2%	LA – MA	95.93	36.45	53.14	67.21	154.98	40.85	29.87	17	166.33
29.8% - 70.2%	LA – MA	95.93	33.35	43.21	52.74	125.772	29.61	25.27	13.4	120.984

4.2.10. XRF

XRF results in Table 4.7 confirm the chemical basis for binder proportioning. HL supplied the calcium-rich phase, slag provided both CaO and SiO2, metakaolin supplied reactive silica and alumina, and silica fume provided highly concentrated SiO2. These differences informed the SCM replacement strategy used in Stage II.

Table 4.7. Chemical compositions of binders [22].

Materials (Mass %)	Na_2O	MgO	Al_2O_3	SiO_2	P_2O_5	K_2O	CaO	TiO_2	MnO	Fe_2O_3
HL	0.024	0.714	0.249	1.456	0.008	0.09	72.8	0.037	0.007	0.155
Slag	0.373	11.822	10.204	36.803	0	0.494	37.825	1.438	0.159	0.434
Metakaolin	0.11	0.435	27.874	65.142	0.017	1.773	0.312	0.669	0.006	1.225
Silica Fume	0.102	0.212	0.059	93.072	0.065	0.398	0.699	0.012	0.029	0.845

4.3. Preliminary casting of PCM-HLC

4.3.1. Stage I: Maximum PCM Substitution Determination

The objective of Stage I was to identify the highest PCM substitution level that could still produce a cohesive, handleable, and leakage-resistant PCM-HLC. HL was used as the baseline binder because it is widely available in Canada and is a conventional binder for HLC [233–235].

Large, medium, and small shiv fractions were impregnated with increasing PCM substitution levels using the vacuum impregnation method (Fig. 4.11).

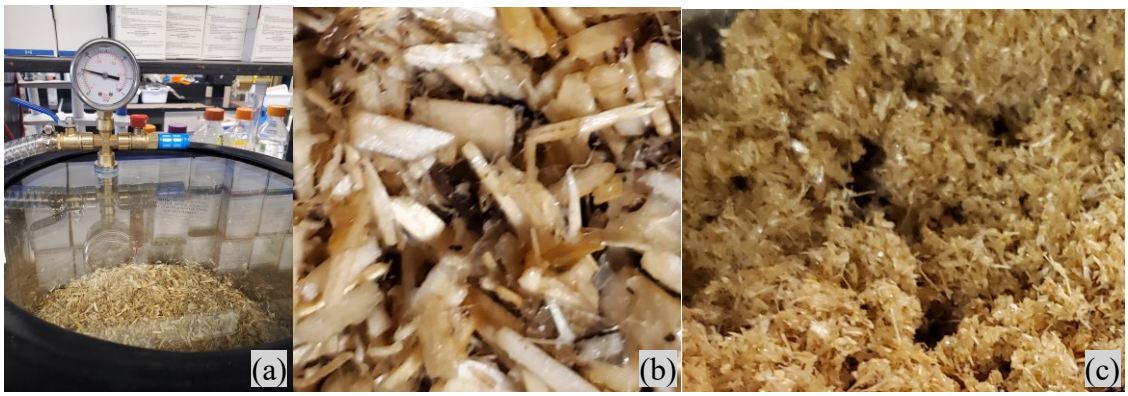


Fig. 4.11. (a) Vacuum impregnation of PCM into hemp shivs, (b) SS-PCM-large hemp shiv at 70% substitution level, and (c) SS-PCM-small hemp shiv at 70% substitution level.

The casting began at 30% PCM substitution because this value was close to the highest PCM content reported in the literature after conversion to the substitution basis used here [114]. Substitution levels above 70% repeatedly caused practical failures, including leakage during thermal cycling, incomplete curing, or loss of specimen integrity after demoulding. Representative cohesion and leakage outcomes for PCM-HLC are illustrated in Fig. 4.12.

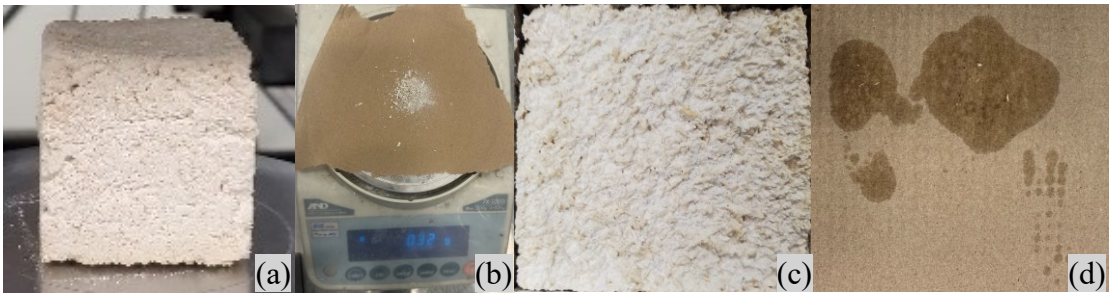


Fig. 4.12. A PCM-HLC specimen that (a) maintained its shape after the cohesion test, (b) lost < 1% particles, (c) had an intact surface, but (d) leaked after the leakage test.

These failures indicate an engineering limit rather than only a material-storage limit. Beyond 70% substitution, the composite became dominated by PCM, and the binder network was insufficient to maintain stable particle contact and leakage resistance.

Therefore, 30-70% PCM substitution was selected as the practical investigation range. The 70% level was carried forward because it was the highest loading that combined high latent-storage potential with stable casting performance under the tested conditions.

4.3.1.1. Results and discussion

SEM imaging confirmed that PCM was distributed across the shiv surface after impregnation (Fig. 4.13), supporting the use of hemp shiv as a shape-stabilised PCM carrier.

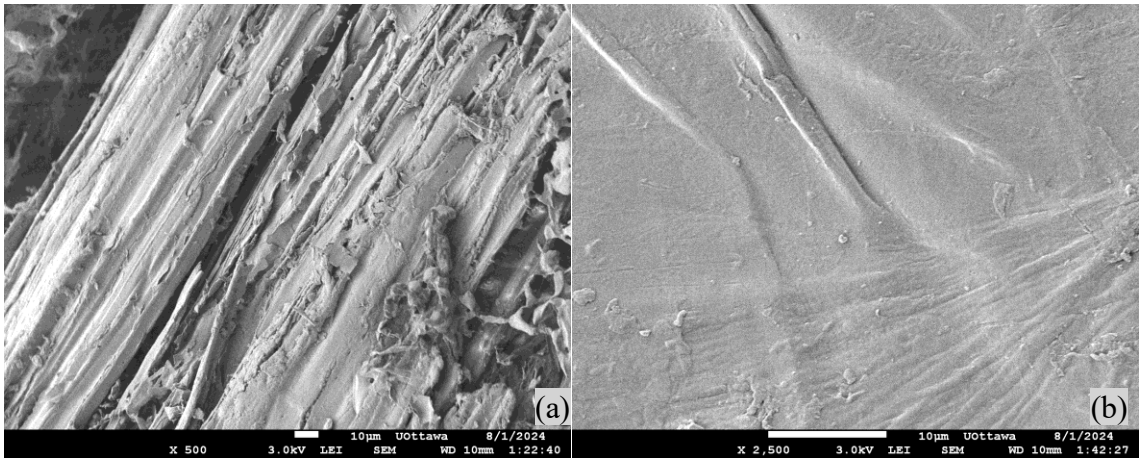


Fig. 4.13. SEM micrographs of the hemp shiv post-impregnation: (a) surface morphology of hemp shiv at x500 magnification and (b) PCM coating on hemp shiv at x2500 magnification.

Table 4.8 summarises casting viability across shiv size, PCM substitution level, and hemp-to-binder ratio. The PCM substitution levels correspond to 0.4, 0.6, 1.0, 1.5, 2.33, 4.0, and 9.0 parts PCM per part hemp shiv.

Table 4.8. Evaluation of casting viability of PCM-HLC across varying hemp shiv sizes, PCM, and binder ratios.

Hemp Shiv Size	Hemp:HL Ratio	30% PCM	40% PCM	50% PCM	60% PCM	70% PCM
Small	1:1	✓	✓	✓	X	X
	1:2	✓	✓	✓	✓	X
	1:3	✓	✓	✓	✓	✓
Medium	1:1	✓	X	X	X	X
	1:2	✓	✓	✓	X	X
	1:3	✓	✓	✓	✓	X
Large	1:1	✓	X	X	X	X
	1:2	✓	✓	X	X	X
	1:3	✓	✓	✓	✓	X

Note: ✓ indicates successful curing, shape retention, and no visible leakage during handling. X indicates curing failure, shape loss, or leakage.

The H:B ratio strongly controlled cohesion. At H:B = 1:1, most mixtures failed when PCM substitution exceeded 30%, whereas H:B = 1:3 allowed all shiv sizes to incorporate at least 60% PCM. The higher binder content provided a more continuous matrix around PCM-loaded shiv particles.

Shiv size set the upper PCM limit. At H:B = 1:3, small shiv remained stable at 70% PCM substitution, while medium and large shiv failed at lower loadings. The finer fraction likely improved binder distribution and PCM retention by increasing surface area and reducing large inter-particle voids. On this basis, small shiv and 70% PCM

substitution were selected for subsequent chapters as the highest practical loading condition.

4.3.2. Stage II: Development of SCM-Modified Hybrid Binders

Stage I showed that high PCM loading required substantial HL to maintain cohesion. However, high HL content can delay curing, increase embodied carbon, reduce moisture-buffering potential, and may interact with fatty acid PCMs [236].

Stage II therefore tested whether SCM-modified binders could maintain cohesion at the Stage I limit of 70% PCM substitution using small shiv and H:B = 1:3.

Slag, silica fume, and metakaolin were selected because they can partially replace HL while providing reactive silica and/or alumina. Testing at 70% PCM was intentionally conservative: a binder that remained stable at this upper limit was expected to remain feasible at lower PCM contents.

Binder proportions were designed using the molar-ratio method [237, 238]. The method uses oxide ratios to compare lime-SCM chemistry and to target mixtures capable of forming calcium silicate hydrate and calcium aluminate hydrate phases. The adjusted chemical and molar compositions of the binder mixes are given in Table 4.9.

Table 4.9. Chemical and molar composition of binder mixes adjusted for constant CaO/SiO_2 stoichiometry.

Binder mix design	HL : SCM (wt%)	CaO/SiO_2	SiO_2/Al_2O_3	CaO/Al_2O_3	Clay content ($SiO_2 + Al_2O_3$) (mol)
HL:slag	50 : 50	3.00	6.22	18.66	0.36
HL:metakaolin	74 : 26	3.00	4.08	12.23	0.37
HL:silica fume	80 : 20	3.00	762	2287	0.32

†The dominant oxides include $Na_2O + K_2O + MgO + CaO$, the total oxides are the sum of basic + amphoteric oxides.

A target CaO/SiO2 molar ratio of 3.0 was selected to balance reactivity, alkalinity, and comparability with the literature. This ratio preserves sufficient HL to support mould resistance during humid curing, while allowing meaningful SCM replacement. It also gives a metakaolin replacement level within the 20-30% range commonly studied in lime-SCM binders.

4.3.2.1. Results and discussion

All binder designs formed cohesive fresh-state test balls, as illustrated in Fig. 4.14.



Fig. 4.14. Optical illustration of a test ball that retained its shape.

After curing, internal cohesion differed among binders, as shown by the particle-loss examples in Fig. 4.15.

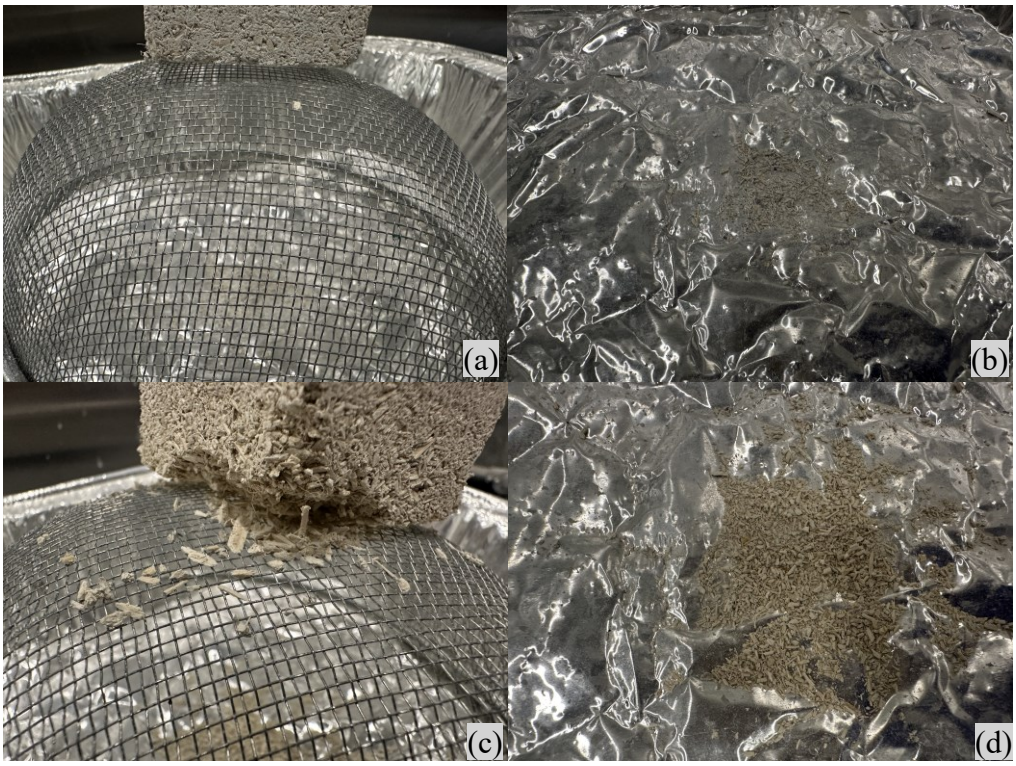


Fig. 4.15. Example of (a, b) excellent cohesion (particle loss < 1%), and (c, d) good cohesion (1% < particle loss < 5%).

The cured-specimen cohesion test showed the clearest distinction among SCMs. Silica fume and metakaolin produced excellent cohesion, with mass losses of 0.08% and 0.41%, respectively, compared with 3.93% for slag. Although all mixes met baseline stability and leakage requirements, silica fume and metakaolin were selected for later stages to reduce handling-related material loss.

SEM was used to interpret these cohesion differences. Because high PCM contents mask binder morphology with fatty-acid coatings, control specimens without PCM were examined to compare the binder matrices directly (Fig. 4.16).

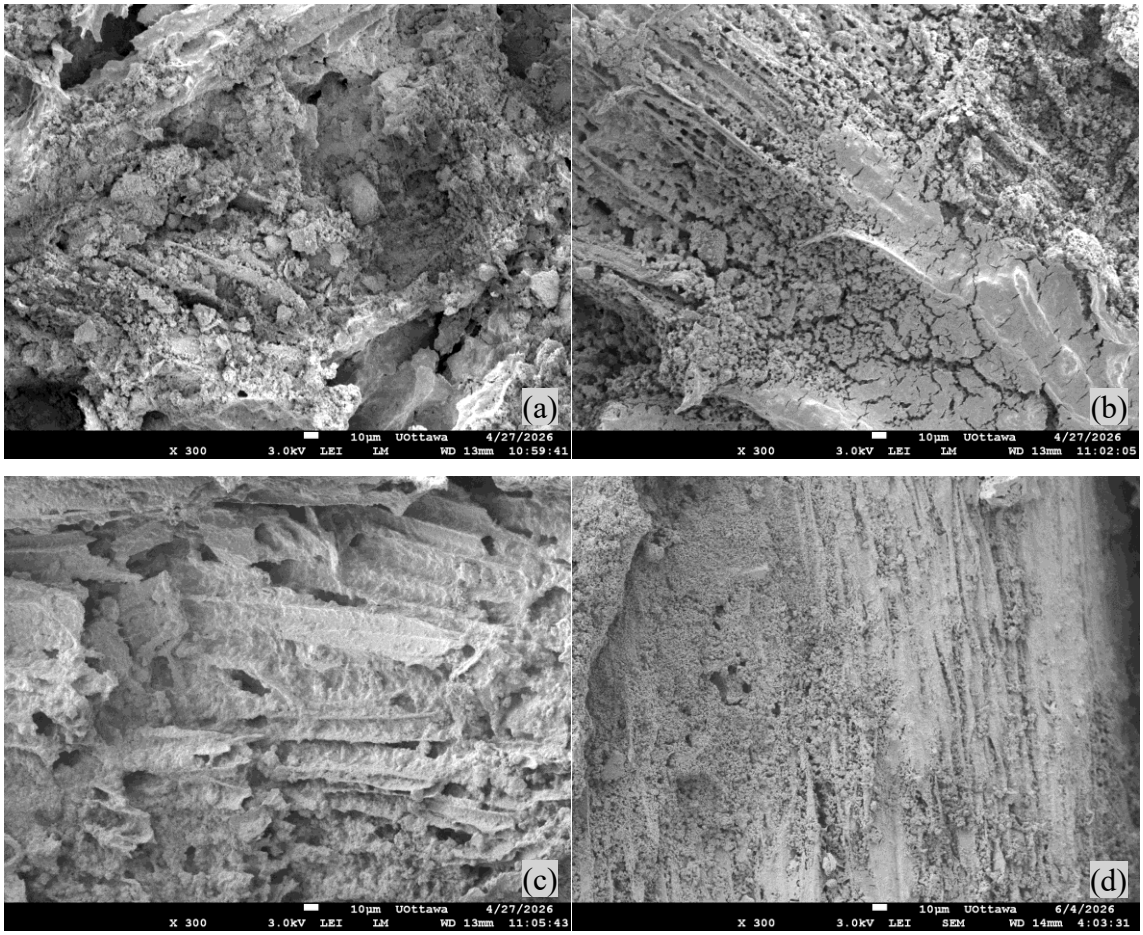


Fig. 4.16. SEM micrographs x300 magnification illustrating the morphology of HLC binder matrices without PCM: (a) Slag-based HLC, (b) metakaolin-based HLC, (c) silica fume-based HLC, and (d) HL-only HLC.

Compared with the HL-only matrix, SCM-modified binders produced denser surface topographies with fewer visible microcracks [239]. The slag-based matrix remained relatively granular and heterogeneous, which is consistent with its higher mass loss in the cohesion test.

The metakaolin matrix appeared denser and more continuous than the slag matrix. This morphology may reflect its reactive aluminosilicate content and helps explain the low mass loss observed in the cohesion test.

The silica-fume matrix showed the finest and most continuous coating around hemp shiv. Its very fine particles probably acted as micro-fillers, reducing microvoids and improving local binder continuity.

Together, the cohesion and SEM results indicate that SCM selection affects the continuity of the hemp-binder matrix at high PCM loading. The most important practical outcome is that silica fume and metakaolin both provided sufficiently cohesive matrices for later PCM-HLC testing.

The two selected binders were therefore treated as practical alternatives rather than ranked solely by the small difference in mass loss. This interpretation is consistent with literature suggesting that SCM choice may have limited influence on bulk HLC properties once adequate binder cohesion is achieved [240].

4.4. Summary

This chapter established the raw-material and preliminary casting basis for the thesis. ImageJ analysis showed that small ground shiv had the most uniform particle-size distribution, while moisture tests showed that fine shiv retained more water and required careful batching control. SEM confirmed that hemp shiv can act as a shape-stabilised carrier for fatty-acid PCM, but the PCM coating also changes the surfaces available for binder contact and moisture exchange.

Preliminary casting identified 70% PCM substitution in small shiv at H:B = 1:3 as the maximum practical loading under the tested conditions. Above this level, leakage, curing failure, or loss of specimen integrity made the composites unsuitable for further study. Stage II then showed that silica fume and metakaolin could replace part of the HL while maintaining excellent cohesion at this upper PCM limit. These findings define the material system used in Chapters 5-7 and provide a practical framework for balancing PCM storage, binder demand, cohesion, and sustainability in PCM-HLC design.

5. Chapter 5: Casting direction and specimen-size effects of PCM-HLC

5.1. Novelty and contributions

Accurate interpretation and inter-study comparison of bio-composite data require a clear understanding of how casting direction and specimen scale affect measured properties. These factors have been examined for conventional HLC, but their effects in PCM-HLC, particularly formulations using finely ground hemp shiv, remain less established. This chapter therefore evaluates casting direction and specimen size as experimental variables, with emphasis on thermal anisotropy, mechanical size effects, and hygrothermal performance.

Thermal anisotropy is a persistent issue in HLC. Previous studies report up to a 50% difference in thermal conductivity between casting directions when large hemp shivs (>10 mm) are used. PCM impregnation may further modify this response because the PCM occupies part of the hemp-shiv pore structure and changes phase during heating and cooling. In this chapter, the use of reduced-size hemp shiv was associated with a much smaller directional difference in thermal conductivity, even at 70% CA substitution. This result suggests that reducing shiv aspect ratio may help limit thermal anisotropy in PCM-HLC, although the internal distribution of PCM and pores was not directly measured in this chapter.

Beyond material properties, this chapter contributes to standardizing bio-composite testing protocols, an important step for industrial adoption. By isolating specimen thickness and size (50 mm versus 100 mm cubes) as primary variables, the results show that stiffness remained relatively stable, whereas ultimate failure strength was more sensitive to specimen scale. The 50 mm cubes showed a 27.24% higher strength than the larger standard size under the tested conditions. Although a universal correction factor would require wider multi-laboratory validation, these results provide an empirical basis for comparing compressive-strength data obtained from different specimen geometries.

Previous studies on standard bio-composites have reported that binder segregation can affect moisture transport. In the present PCM-HLC specimens, high PCM loading did not eliminate the observed influence of casting direction on MBV. The faster stabilization of vertically cast samples is consistent with the exposure of more porous side faces during testing, as suggested by the casting geometry and by explanations reported in the literature. These findings indicate that casting orientation should be considered when designing wall assemblies intended to support passive humidity regulation.

This work also highlights a possible distinction between PCM loading density and compaction density. The specimens reached dry densities near 400 kg/m³ while retaining an "excellent" Nordtest MBV classification. This observation suggests that mass added through PCM filling of hemp-shiv pores may not reduce moisture buffering in the same way as mechanical densification that closes transport macropores. This interpretation remains a working hypothesis because pore connectivity and PCM distribution were not directly quantified.

The following sections describe the sample development process and the experimental methods used to characterize compressive strength, elastic modulus, thermal conductivity, SHC, and MBV. The results are then interpreted with attention to the distinction between measured trends, literature-supported mechanisms, and proposed explanations. The work presented in this chapter is intended for later peer-review submission.

5.2. Sample development

5.2.1. Raw materials

HL, metakaolin, and small – sized hemp shivs with 70% PCM substitution rate, as described in Section 4.1, were used.

5.2.2. Compositions of PCM-HLC samples

A binder composed of 74% HL and 26% metakaolin was used in this study, as discussed in Section 4.3.2.

5.3. Results and discussion

5.3.1. Compressive strength

When evaluating low-strength construction materials such as HLC, compressive strength testing provides useful evidence of relative performance and quality, even when the material is not intended for load-bearing use. For non-structural applications, compressive strength indicates the material's ability to withstand handling, installation, and integration within a building assembly.

Fig. 5.1 shows the stress– strain curve of PCM – hemp – lime specimens under continuous uniaxial compression.

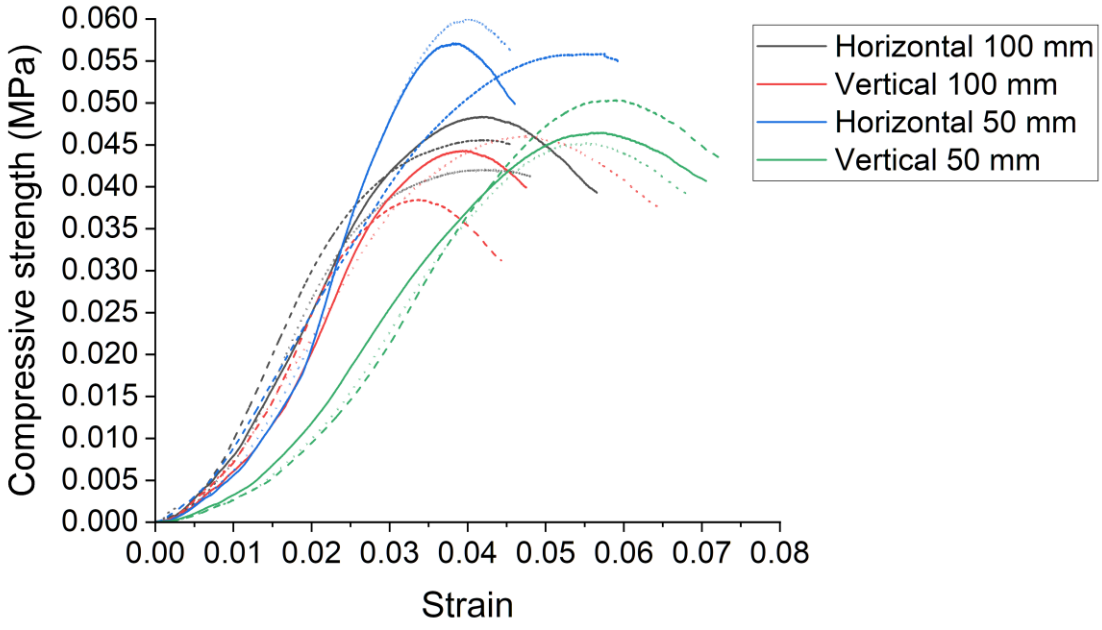


Fig. 5.1. Stress-strain analysis of compressive strength across varying sample orientations and dimensions.

The stress – strain curves indicated significant deformability prior to failure, with strains ranging from approximately 0.038 to 0.059 mm/mm. Post – failure, the internal structure was destroyed, while the external shape remained largely intact, only showing cracks and some particles falling from the samples. The stress – strain curve shows three distinct stages:

(i) Compaction stage: This initial phase is characterized by a nonlinear, changing slope as the compression platen engages surface irregularities and microcracks within the specimen, which are closed. The deformation during this stage is primarily governed by the sample's surface planarity and the porous matrix's inherent compressibility.

(ii) Linear elastic stage: Once the initial compressible voids are eliminated, the material exhibits a consistent, upward-sloping stress – strain response. In this region, the slope remains relatively constant, reflecting the composite's elastic modulus.

(iii) Shear failure stage: Initiated upon reaching the elastic limit, this stage involves the irreversible propagation of cracks until the ultimate compressive strength is attained. This is followed by a loss of stress as the internal structure undergoes failure.

Fig. 5.2 illustrates the typical mechanical response of a PCM-HLC specimen during a uniaxial compressive strength test. The left figure captures the initial compaction stage, where the compression platen contacts the specimen's surface, beginning to close internal microcracks and compress surface irregularities, creating initial cracks in the samples. The figure on the right depicts the specimen at the failure stage, characterized by the irreversible propagation of macrocracks and localized spalling of hemp shiv particles.



Fig. 5.2. Visual observation of the PCM-HLC compressive strength test (left) initial contact and compaction stage; (right) progression of surface cracking and localized spalling at the ultimate failure stage.

Table 5.1 presents the densities, compressive strength, and modulus of elasticity (E) for three specimens per mix design, along with their coefficients of variation. Compressive strengths ranged from 0.04 to 0.06 MPa, and Young's modulus ranged between 1.01 and 1.84 MPa. In this study, the coefficient of variation (COV) was used to describe the statistical relationships between the sample's mechanical properties and other factors.

Table 5.1. Mechanical properties of PCM-HLC specimens (Mean ± SD).

Sample Group	Density (kg/m^3)	COV (%)	Compressive strength (MPa)	COV (%)	E (MPa)	COV (%)
Horizontal 100 mm	404 ± 4.50	1.11%	0.045 ± 0.003	7.01%	1.64 ± 0.17	10.59%
Vertical 100 mm	409 ± 5.92	1.45%	0.043 ± 0.004	9.24%	1.31 ± 0.07	5.55%
Horizontal 50 mm	412 ± 4.25	1.03%	0.058 ± 0.002	3.66%	1.58 ± 0.02	1.32%
Vertical 50 mm	405 ± 4.61	1.14%	0.047 ± 0.003	5.71%	1.04 ± 0.04	4.37%

The highest strength and elastic modulus were observed for the highest-density specimens in the horizontally cast 50 mm group, whereas the lowest values occurred in the lowest-density specimens in the vertically cast 100 mm group. The relatively low compressive strength values are consistent with the incorporation of soft fatty acids and with the limits of vibration compaction for this formulation.

Vibration compaction densifies the mixture primarily through gravitational settlement and vibration-induced rearrangement. In reference HLC without PCM, the lower density of untreated hemp shiv limited the attainable vibration-compacted density to approximately 200 kg/m^3, consistent with Mahmood et al. [43]. This value is about half of the dry density measured for the PCM-HLC specimens in this study (approximately 400 kg/m^3). Therefore, reference HLC and PCM-HLC should not be compared solely at equal nominal compaction conditions. In this chapter, the compressive tests are used mainly to compare specimen size and testing direction within the PCM-HLC system.

For PCM-HLC, size effects were evident. The 50 mm cubic specimens exhibited 10-27% higher compressive strength, depending on loading direction, and a more pronounced linear elastic region than the larger specimens. When loading was perpendicular to the compaction direction, reducing the cube size from 100 mm to 50 mm increased strength by 10% (0.043 to 0.047 MPa) but reduced elastic modulus by 20% (1.30 to 1.04 MPa), with a density decrease of less than 1% (409 to 405 kg/m^3). When loading was parallel to the compaction direction, reducing the cube size increased compressive strength by 27% (0.05 to 0.06 MPa), while elastic modulus changed by about 4% (1.58 to 1.64 MPa) and density increased by 2% (404 to 412 kg/m^3).

Casting direction affected the 50 mm cubes more than the 100 mm cubes, indicating that directional mechanical response was size-dependent. The strength difference between loading directions was 23% for the 50 mm cubes and 5% for the 100 mm cubes. Because the formulation used fine hemp shiv particles, which are less likely to create strong particle-orientation effects than long shivs, the observed directionality may be associated more with compaction-induced structure than with hemp-shiv alignment. This interpretation is indirect because the orientation of particles, pores, and PCM was not measured.

For the 50 mm cubes, the higher strength and density suggest that the smaller mould volume may have allowed more effective vibration compaction under the selected vibration time and frequency. One potential explanation is that compaction created more continuous horizontal interfaces or void patterns along the compaction direction. If these interfaces were present, they could help explain the higher strength when loading was parallel to compaction and the earlier shear failure when loading was perpendicular. However, this proposed mechanism should be treated as a hypothesis, because void morphology and PCM distribution were not directly observed.

In the 100 mm cubes, the lower strength and smaller directional difference suggest a weaker size effect under the same compaction procedure. The larger mould

volume may have reduced the efficiency of vibration energy transfer or increased the likelihood of more heterogeneous internal defects. These factors could produce a lower-strength response that appears more isotropic at the specimen scale. Further imaging or density profiling would be needed to confirm whether this behaviour is controlled by void distribution, PCM arrangement, or binder continuity.

5.3.2. Sample densities for hygrothermal properties

Table 5.2 presents the average dry density and corresponding coefficient of variation (COV) for each mix design of the samples used for hygrothermal properties.

Table 5.2. The average dry density for various compaction directions and thicknesses.

Specimen ID	Average dry density ($kg \cdot m^{-3}$)	Upper error bound	Lower error bound	Coefficient of variation (%)
Horizontal compaction, 150x150x50 mm mould	401.4	2.96	- 2.46	0.56
Horizontal compaction, 150x150x80 mm mould	397.04	3.52	- 3.26	0.7
Vertical compaction, 150x80x150 mm mould	401.78	0.72	- 0.94	0.17

These values were calculated from specimen's oven – dried to a constant mass (less than 0.1% change). To ensure accuracy, each specimen was weighed three times, and the average of the three readings was recorded. As significant variations in sample density can affect the investigation of other contributing factors, the low-density variations among the samples in this study allow for an accurate assessment of the effects of casting direction and thickness. The average dry density of the HLCs used for thermal conductivity tests was 400.07 kg/m^3 with a COV of 0.75% across different moulds. The value was calculated from specimens with an average dry density ranging from 397.04 to

401.78 kg/m³, each exhibiting a COV of less than 1%. This consistency affirms the reliability of the trends observed in the MBV tests across cycles.

The densities obtained in this study were higher than the 140-200 kg/m³ values previously reported for vibration-compacted HLC without PCM [43]. They are, however, comparable to densities reported for HLC without PCM produced using other compaction methods, typically 300-800 kg/m³ [161, 186, 226, 241]. This difference is consistent with the high PCM substitution rate (70% by mass of hemp shiv), which adds mass within the hemp-shiv pore structure and increases composite density.

The higher binder-to-hemp ratio required for PCM-HLC may also have contributed to the increased density because additional binder can occupy part of the void volume. The low COV is consistent with the use of standardized small hemp shiv particles and a repeatable vibration procedure, which together improved specimen consistency. Because density is a primary factor influencing HLC properties [24, 41, 42, 53, 186, 194], the low density variation in this chapter supports a more focused assessment of casting direction and thickness.

5.3.3. Thermal properties

5.3.3.1. Thermal conductivity and PCM phase transition

The thermal conductivity of the PCM-HLC specimens was measured at mean temperatures of 12.5 °C, 22.5 °C, 32.5 °C, and 40 °C between the hot and cold plates of the heat flow meter (HFM), as shown in Table 5.3.

Table 5.3. Experimental HFM temperature settings for thermal testing.

Mean temperature (°C)	Hot plate temperature (°C)	Cold plate temperature (°C)
12.5	20	5
22.5	40	5
32.5	45	20
40.0	55	25

The resulting thermal conductivity values ranged from 0.0727 W/(m·K) to 0.0918 W/(m·K), as shown in Fig. 5.3.

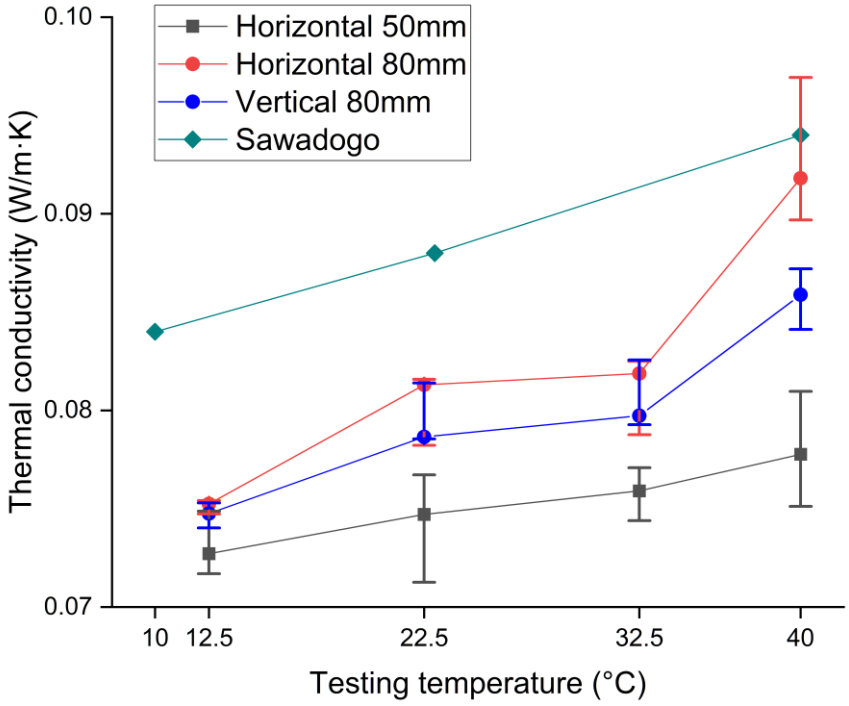


Fig. 5.3. Thermal conductivity vs. temperature relationship.

The HFM test results showed low COVs of 2.82%, 8.31%, and 5.79% for Horizontal 50 mm, Horizontal 80 mm, and Vertical 80 mm, respectively. This low variability is attributed primarily to the reduced influence of hemp particle heterogeneity and to the consistent dry density observed across specimens.

The consistency of the HFM results supports comparison with previous studies. Conventional HLC without PCM commonly shows an approximately linear increase in thermal conductivity with mean testing temperature [43], partly because the conductivity of entrapped air increases from 0.0253 W/(m·K) at 12.5 °C to 0.0268 W/(m·K) at 32.5 °C [242]. In contrast, the PCM-HLC results in Fig. 5.3 showed a nonlinear response, particularly for the 80 mm specimens. The lower-than-expected conductivity at a mean temperature of 32.5 °C may be related to PCM phase transition during HFM testing. At

this mean temperature, the hot plate is at 45 °C and the cold plate is at 20 °C, so the specimen likely contains a thermal gradient in which material near the hot plate is at least partly liquid while material near the cold plate remains solid.

This interpretation is supported by the lower thermal conductivity of liquid capric acid (K approximately 0.141 W/(m·K)) compared with its solid state (K approximately 0.372 W/(m·K)) [243]. As the melting region develops through the sample thickness, an increasing fraction of the lower-conductivity liquid phase could offset the expected conductivity increase from air and the solid matrix.

The nonlinear plateau was less pronounced in the horizontal 50 mm specimen. A possible explanation is that the thinner specimen had a shorter heat-transfer path and a smaller total PCM volume relative to its exposed area. These conditions may have changed the proportion of solid and liquid PCM during testing, producing an offsetting effect of different magnitude from that in the 80 mm specimens.

The phase transition may therefore influence the measured composite conductivity through two linked effects. First, latent heat absorption can slow the temperature rise within the specimen. Second, liquid-state CA is less conductive than solid-state CA. Together, these effects may explain the reduced conductivity at 32.5 °C and the plateau between 22.5 °C and 32.5 °C. At 40 °C, beyond the phase-transition range, continued warming of air and liquid PCM is consistent with the renewed upward trend. This pattern agrees with [64], although the larger percentage increases observed here may reflect the higher CA substitution rate in the present PCM-HLC.

The average thermal conductivity of the PCM-HLC was calculated from four testing temperatures: 12.5 °C, 22.5 °C, 32.5 °C, and 40 °C. Values ranged from 0.07272 W/(m·K) to 0.09181 W/(m·K). Fig. 5.4 compares the dry densities and average thermal conductivities from this study with selected literature values.

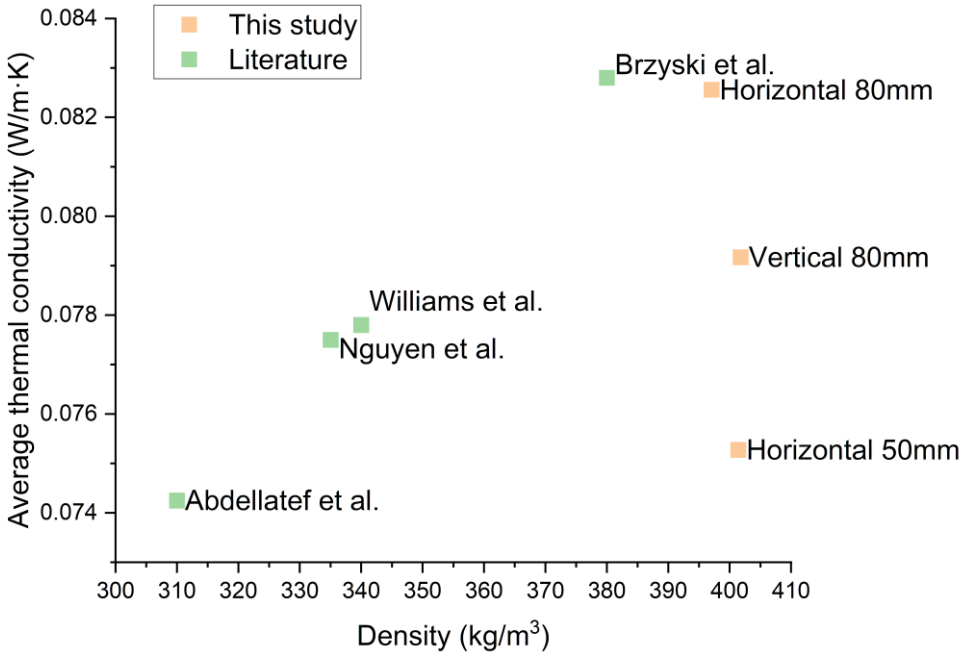


Fig. 5.4. The correlation of dry density and thermal conductivity.

This study's average thermal conductivity values (0.0753-0.0826 W/(m·K)) fall within the 0.06-0.18 W/(m·K) range reported for HLC without PCM at densities of 200-800 kg/m³ [170, 244]. The dry densities measured here were higher than some previous values because replacing 70% of porous hemp shiv with dense PCM increased mass within the same specimen volume. Therefore, density alone may not be sufficient for comparing thermal performance between conventional HLC and PCM-HLC. Compared with Gencel et al. [139], who reported 0.181 W/(m·K) for a hemp-gypsum composite with 35% SS-PCM and a density of 950 kg/m³, the lower conductivity measured here is plausibly related to differences in density, binder system, aggregate structure, and PCM content.

Unlike the near-linear density-thermal conductivity relationship reported in [11], the present results showed only small differences among casting directions. The vertical 80 mm specimen had the highest density, followed by the horizontal 50 mm and horizontal 80 mm specimens. A simple density-based prediction would therefore suggest

the highest thermal conductivity for the vertical 80 mm specimen. However, its measured thermal conductivity (0.079 W/(m·K)) was 4% lower than that of the horizontal 80 mm specimen (0.083 W/(m·K)). Given the systematic uncertainty and COV, this difference falls within the margin of experimental error. Therefore, no strong directional thermal-conductivity effect should be inferred from this comparison.

Compared with the approximately 50% directional difference reported for conventional HLC made with regular hemp shiv [161], the 4% difference observed here indicates that casting direction had negligible practical impact on thermal conductivity for this specific ground-shiv PCM-HLC formulation. The result is consistent with the interpretation that reduced shiv size can limit thermal anisotropy, as reported by Mahmood et al. [43], who found that reducing hemp particle size from 4.52 mm to 0.72 mm decreased the directional difference in thermal conductivity from 6.8% to 1.2%. In this chapter, the presence of fatty acids did not appear to reverse that trend.

The inclusion of 50 mm and 80 mm specimens allowed an assessment of thickness effects. Literature suggests that thinner specimens can yield slightly lower apparent thermal conductivity due to thermal contact resistance and edge effects [245, 246]. In this study, the horizontal 50 mm specimen (0.0753 W/(m·K)) was 8.8% lower than the horizontal 80 mm specimen (0.0826 W/(m·K)), despite having a 1.1% higher density. Because density differed by only approximately 1% (401.4 versus 397.0 kg/m^3), the observed conductivity difference may reflect experimental factors such as contact resistance rather than a fundamental material change. Within the tested range, thermal conductivity was therefore relatively stable across specimen thickness.

5.3.3.2. Specific heat capacity (SHC) and PCM phase transition

Fig. 5.5 compares the SHC from this study with those in the literature.

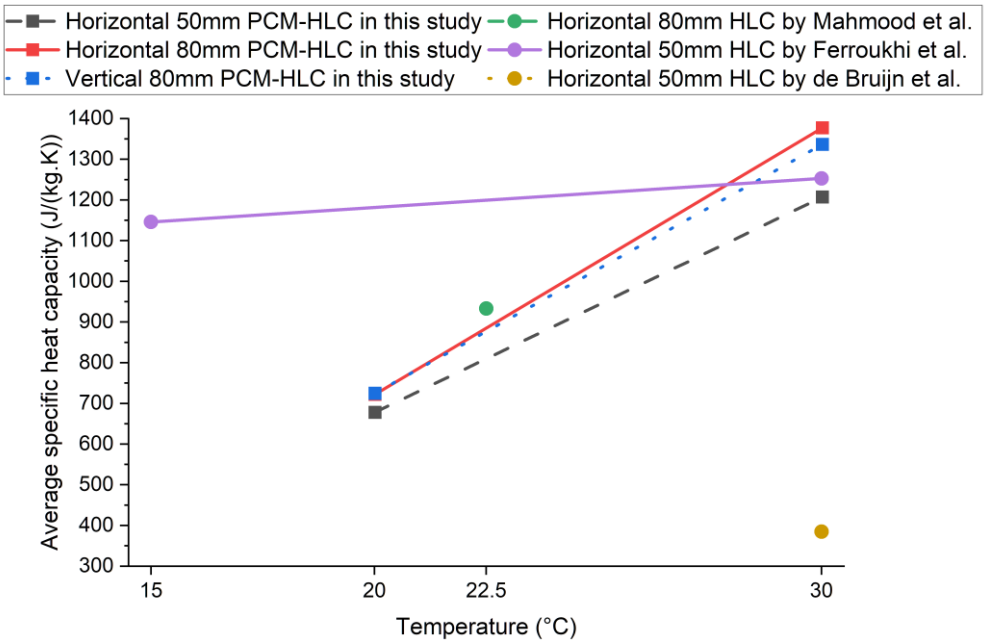


Fig. 5.5. Comparison of specific heat capacity results in this study and in the literature.

SHC values obtained from the HFM were consistent, with COVs of 0.4-5.4% at each testing temperature. The horizontal 50 mm sample had the lowest COV, 1.6% at 20 °C and 0.4% at 30 °C. The horizontal 80 mm sample had COVs of 3.0% at 20 °C and 5.0% at 30 °C, while the vertical 80 mm sample had COVs of 5.4% at 20 °C and 3.7% at 30 °C. The slightly higher COVs for the 80 mm specimens may reflect the greater material volume and the associated variability in PCM distribution.

At approximately 20 °C, SHC values ranged from 678 to 725 J/(kg·K). These values are comparable to literature values for HLC without PCM, including 933 J/(kg·K) at approximately 200 kg/m³ reported by Mahmood et al. [43], 385 J/(kg·K) at approximately 400 kg/m³ reported by de Bruijn et al. [247], and 1146 J/(kg·K) at approximately 490 kg/m³ reported by Ferroukhi et al. [248]. At 30 °C, PCM phase transition became the dominant contributor to SHC. In this study, SHC increased by 78-

84% to 1207-1336 J/(kg·K), whereas HLC without PCM at approximately 490 kg/m³ increased by 9% to 1253 J/(kg·K) in Ferroukhi et al. [248]. The high SHC at 30 °C provides experimental evidence of latent heat storage in the PCM-HLC. Differences from literature values may also reflect mix design, testing apparatus, methodology, and specimen size.

Both thermal conductivity and SHC increased with testing temperature, consistent with [62, 120]. The horizontal 80 mm sample's SHC was 2% higher than the vertical 80 mm sample at 30 °C (1335 versus 1312 J/kg·K), which is too small to support a strong directional conclusion when the ±7% systematic uncertainty associated with specimen dimension tolerances is considered [249]. Differences between the 50 mm and 80 mm specimens were larger, but these may reflect sample thickness, total PCM mass, and measurement variability rather than a verified thickness effect. Overall, the measured data support the conclusion that latent heat storage during PCM phase transition dominates the SHC response, while density, thickness, and casting orientation are secondary within the tested range.

5.3.4. Moisture buffering capacity

Moisture buffering ability plays a critical role in regulating indoor humidity fluctuations. The MBV results for each configuration are presented in Fig. 5.6. In this study, the MBV of HLCs was evaluated over 8 hygroscopic cycles for three formulations incorporating small hemp shiv particles, with varying casting direction and thickness.

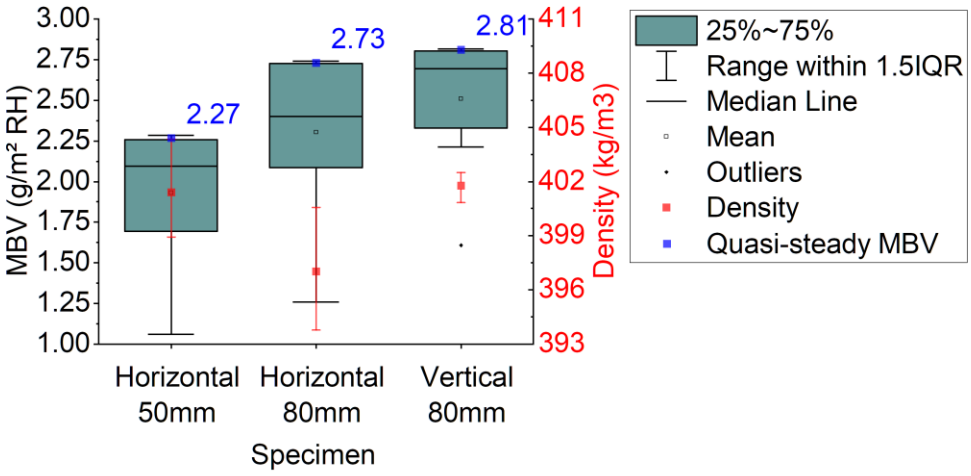


Fig. 5.6. Box chart of MBV of HLC over 8 cycles, with density and its upper and lower error bounds shown in red, and quasi – steady state MBV shown in green.

All samples demonstrated excellent moisture buffering capacity, with quasi-steady average MBV values from three consecutive steady cycles ranging from 2.27 to 2.80 g/(m^2·%RH). According to the Nordtest classification, materials with MBV values above 2.0 g/(m^2·%RH) are considered to have excellent buffering performance [223]. Even allowing for the relative humidity uncertainty associated with laboratory temperature fluctuations [250], the PCM-HLC specimens remained in this category. The values also align with or exceed reported ranges for HLC and PCM-HLC, including 1.82-3.02 g/(m^2·%RH) [251], 2.23 ± 0.23 g/(m^2·%RH) for PCM-HLC [64], and 2.06-2.53 g/(m^2·%RH) [43]. Thus, 70% CA substitution did not prevent the material from maintaining moisture-buffering performance comparable to conventional HLC.

MBV performance must be interpreted alongside dry density. Earlier literature generally shows that lower-density hemp-lime composites have higher permeability and can support faster moisture transfer [252], whereas greater mass can also increase the absolute amount of moisture retained when accessible porosity remains available. In the present chapter, density variation within each specimen group was small, so density is unlikely to be the sole driver of MBV differences. Fig. 5.7 illustrates the density change in samples exposed to cyclic humidity, starting at 33% RH.

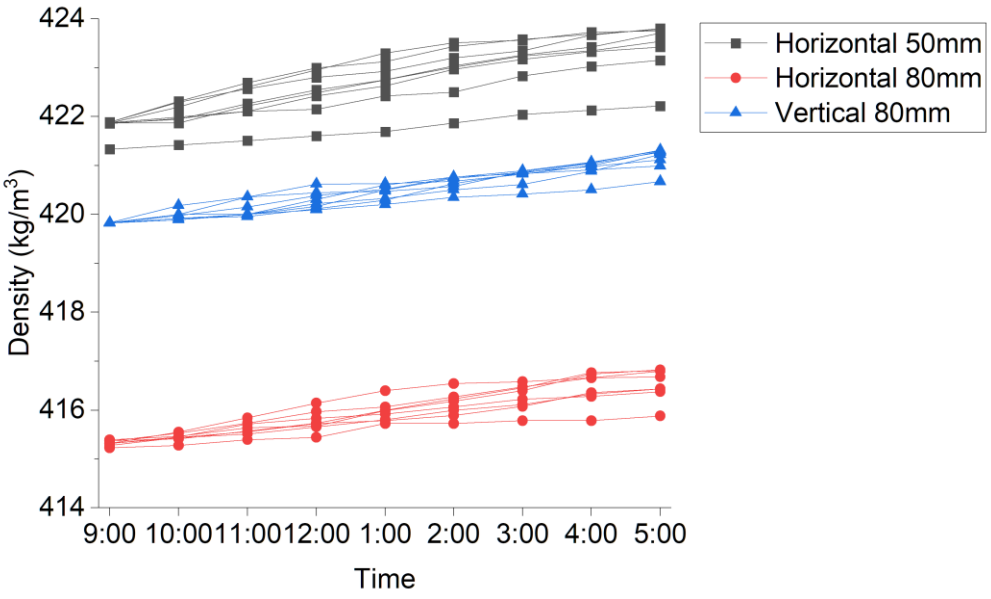


Fig. 5.7. Density changes of the HLC (including the weight of the tape) measured following the NORDTEST procedures.

Regardless of casting direction and thickness, all samples exhibited similar patterns of mass and density change. The mass variation comprised two distinct phases: an increase due to moisture uptake during the 75% RH period, and a decrease due to moisture release during the 33% RH phase.

MBV is calculated from the first and last mass measurements in each cycle, and the uptake moisture buffering capacity for each cycle is shown in Fig. 5.8.

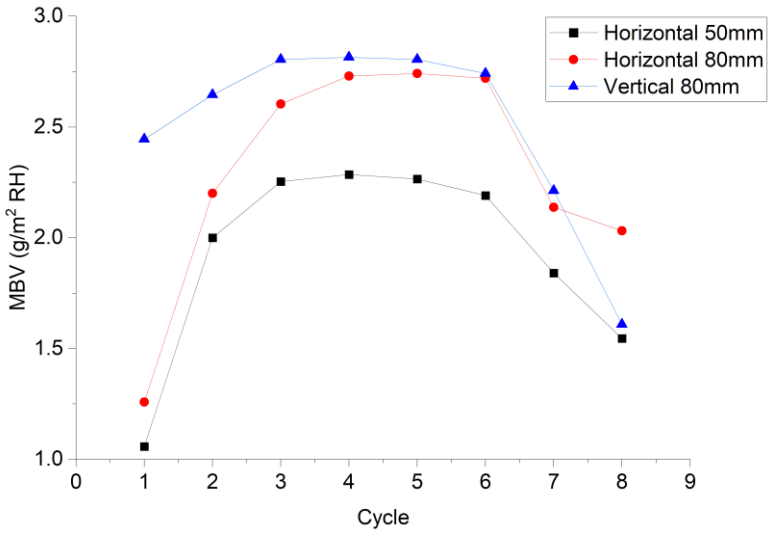


Fig. 5.8. Moisture buffering capacity with cycles

Unlike the high-initial-then-lower MBV trend reported for hemp concrete by Mahmood et al. [43], the first two cycles in this study showed relatively low MBV values, from 1.05 to 2.44 g/(m²·%RH), followed by a gradual increase to steady state by cycle 3. One potential explanation is that oven drying left PCM-treated surfaces initially less favourable for moisture uptake because of the hydrophobic fatty-acid phase. As repeated humidity cycling progressed, accessible pores may have become progressively conditioned with moisture, allowing the specimens to reach MBV values similar to regular hempcrete without fatty acids. Direct measurements of pore water distribution would be needed to confirm this mechanism.

If moisture-cycling conditions were unchanged and the specimens remained intact, the quasi-steady MBV would be expected to remain stable. Instead, MBV decreased after the sixth cycle, likely because repeated removal and weighing caused abrasion and particle loss. Although the three contact surfaces were sealed with tape and the specimens were handled carefully, small particles detached during measurement. This

behaviour is consistent with a relatively loose vibration-compacted structure and weak local particle bonding. Because all three specimen groups showed particle loss around the sixth cycle, the decrease is more likely to reflect handling damage during the test than a true change in moisture-buffering capacity.

Casting direction influenced the early MBV response. Mahmood et al. [43] reported that reducing hemp shiv size can reduce directional dependency in moisture transport for conventional HLC. However, the PCM-HLC specimens in this study, which used similarly small ground hemp shiv, still showed faster initial uptake when cast vertically. A literature-supported explanation is binder segregation during casting. Nguyen et al. [161] reported that binder can settle toward the bottom of a mould, creating a denser and less permeable layer. In horizontally cast samples, the MBV-tested face corresponds to this bottom face (150 mm × 150 mm), which could reduce permeability. In vertically cast samples, the tested face corresponds to a side face, while the denser bottom face (150 mm × 80 mm) was sealed. This geometry may expose a more permeable surface to humidity fluctuations.

Consistent with this explanation, the vertically cast 80 mm specimen reached steady state at approximately 2.8 g/(m²·%RH), one cycle earlier than the horizontally cast specimen of the same thickness. The horizontally cast specimen showed slower initial moisture uptake and increased more sharply during the early cycles before peaking near 2.7 g/(m²·%RH). This trend suggests that the tested surface condition, not only the bulk mix design, influenced the rate at which specimens approached steady-state buffering.

Specimen thickness also affected MBV to a lesser extent. Although the 50 mm specimen followed a similar moisture-buffering pattern to the 80 mm specimens, the horizontal 50 mm specimen showed lower peak MBV values, below 2.6 g/(m²·%RH). A plausible explanation is its smaller material volume. The 50 mm specimen contained approximately 45% less material than the 80 mm specimen (452 g versus 715 g on average), which may reduce the amount of moisture-active material available during cycling.

Overall, the MBV results indicate that casting orientation and specimen geometry affected moisture-buffering behaviour under the tested conditions. Vertically cast specimens showed faster stabilization and more stable moisture-buffering behaviour, possibly because the MBV test exposed a more permeable side face rather than the denser bottom casting face.

5.4. Summary

This chapter evaluated how casting direction, specimen size, and thickness affect the mechanical, thermal, and hygric behaviour of HLC containing 70% CA-substituted hemp shiv. The aim was to separate measured effects from mechanisms that remain inferential.

Dry densities were highly consistent across specimens, with variations below 1%, which supported comparison across casting direction and thickness. The PCM-HLC showed low compressive strength (0.04-0.06 MPa) and Young's modulus values of 1.01-1.84 MPa, with substantial deformability before shear failure. These values are consistent with the use of soft fatty acids and the limitations of vibration compaction, but the relative trends are still useful for comparing specimen geometry within this formulation.

Specimen size had the clearest effect on mechanical response. The 50 mm cubes showed 10-27% higher compressive strength than 100 mm cubes, and the directional strength difference was larger in the 50 mm specimens. The most plausible explanation is a size-dependent compaction structure, but this remains a hypothesis because the distribution of voids, binder, and PCM was not directly imaged.

Thermal conductivity ranged from 0.0727 to 0.0918 W/(m·K). Casting direction and specimen thickness produced small differences, less than 9%, which were minor relative to measurement variability and the effect of PCM phase transition. At 20 °C, SHC ranged from 678 to 725 J/(kg·K), increasing to 1207-1336 J/(kg·K) near 30 °C.

These results show that latent heat storage dominated the thermophysical response within the tested range.

All specimens remained in the Nordtest "Excellent" moisture-buffering category, with quasi-steady MBV values of 2.27-2.80 g/(m²·%RH). Initial moisture uptake was delayed relative to some conventional HLC reports, possibly because oven-dried PCM-treated surfaces were less favourable for early moisture absorption. Vertically cast specimens stabilized more quickly than horizontally cast specimens, which is consistent with, but does not directly prove, the influence of binder segregation and exposed surface permeability.

In conclusion, casting direction and specimen geometry affected PCM-HLC properties differently across performance metrics. Mechanical behaviour was most sensitive to specimen size and loading direction, thermal behaviour was comparatively stable across the tested geometries, and MBV was influenced by the tested face and specimen thickness. For scale-up and wall-panel design, these findings support standardizing specimen geometry and reporting casting/testing orientation, while treating proposed mechanisms such as compaction-energy distribution, PCM arrangement, and moisture-pathway changes as hypotheses requiring direct microstructural verification.

6. Chapter 6: Influence of PCM substitution on the hygrothermal and mechanical behaviour of PCM-HLC

This chapter addresses a central material-design problem: how much PCM can be substituted into HLC before the thermal-storage benefit is outweighed by mechanical and hygric penalties. Existing PCM-HLC studies provide valuable evidence, but they rarely map a continuous substitution range wide enough to identify functional thresholds. This chapter therefore evaluates 0-70% PCM substitution under a fixed binder system containing 80% HL and 20% silica fume, with the aim of converting PCM-HLC proportioning from a maximum-loading problem into a performance-targeted material-selection problem.

The new knowledge generated in this chapter is the coupled dose-response relationship between PCM substitution, density, strength, thermal storage, thermal transport, and moisture buffering. The discussion separates direct observations from mechanisms inferred from SEM images, density trends, and literature-supported interpretation. The chapter closes with a quantitative performance screening approach that identifies formulations for balanced envelope layers and protected thermal-storage cores.

6.1. Sample development

6.1.1. Raw materials

Small particle hemp shiv, HL, silica fume, and 80.5% CA - 19.5% MA binary PCM mixture, as discussed in Section 4.1, were used.

6.1.2. Compositions of PCM-HLC samples

The scientific problem addressed in this study was how to select PCM content when thermal storage, strength, density, and moisture exchange respond in different directions. To allow comparison across samples, the H/B ratio was kept constant at 1:3, which was the lowest binder amount shown in the preliminary casting study to allow the 70% PCM-incorporated PCM-HLC to be cast as a cohesive specimen. The detailed ratios for each component in each sample are shown in Table 6.1.

Table 6.1. Varying PCM substitution ratio – PCM-HLC compositions.

Name	HP/B ratio	Mix design by mass ratio Hemp/PCM/Lime/Silica fume				
		Hemp+PCM		Binder		Water
		Hemp	PCM	HL	Silica fume	Water
0% PCM	1:3	1	0	2.4	0.6	2.5
10% PCM	1:2.7	1	0.11	2.4	0.6	2.5
20% PCM	1:2.4	1	0.25	2.4	0.6	2.5
30% PCM	1:2.1	1	0.43	2.4	0.6	2.5
40% PCM	1:1.8	1	0.67	2.4	0.6	2.5
50% PCM	1:1.5	1	1	2.4	0.6	2.5
60% PCM	1:1.2	1	1.5	2.4	0.6	2.5
70% PCM	1:0.9	1	2.33	2.4	0.6	2.5

6.2. Results and discussion

6.2.1. Mechanical properties

6.2.1.1. Compressive strength

Before interpreting mechanical performance, the dry density of the cast specimens was examined because density affects both load response and hygrothermal behaviour. The mean dry density was 723 kg/m³, with a standard deviation of 33.46 kg/m³ and a COV of 0.046. The measured range, 664.56-786.24 kg/m³, indicates that PCM substitution changed the mass distribution of the composite even though the specimen geometry and binder system were held constant. The relationship between dry density and compressive strength is shown in Fig. 6.1.

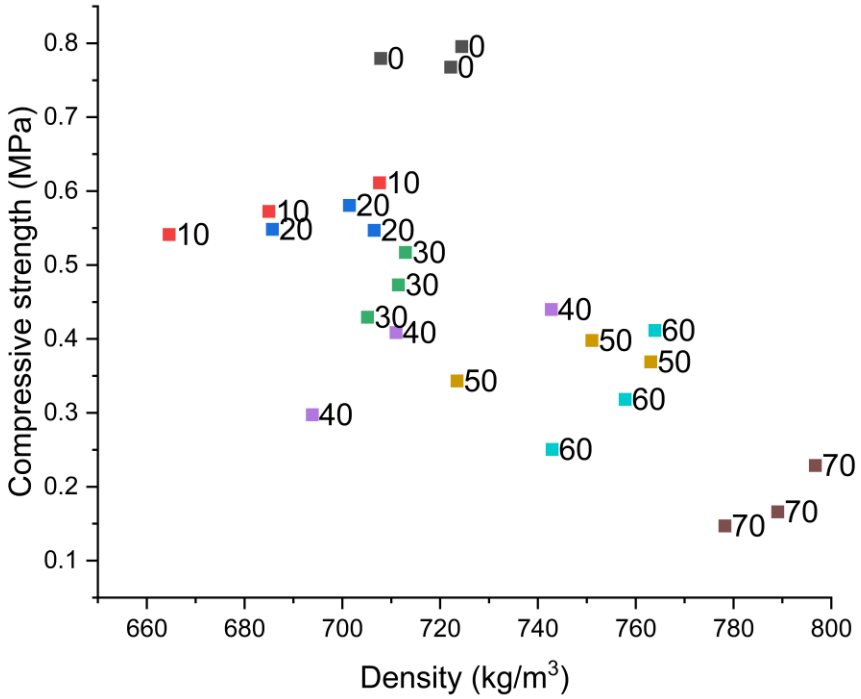


Fig. 6.1. Relationship between dry density and compressive stress for PCM-HLC across varying PCM concentrations. Numerical labels with different colours indicate the specific PCM substitution percentage (0–70%).

The densities measured here occupy the upper part of the range reported for HLC without PCM [43, 44, 186, 226, 241]. This difference should not be interpreted only as improved compaction. It is also consistent with the use of hydraulic pressing, a relatively high binder-to-hemp ratio, and the replacement of lightweight porous shiv volume by denser fatty-acid PCM. Therefore, the density comparison mainly establishes that the present PCM-HLC represents a high-density material regime, rather than a directly comparable form of conventional HLC. Fig. 6.2 shows how this density regime interacts with compressive strength as PCM content increases.

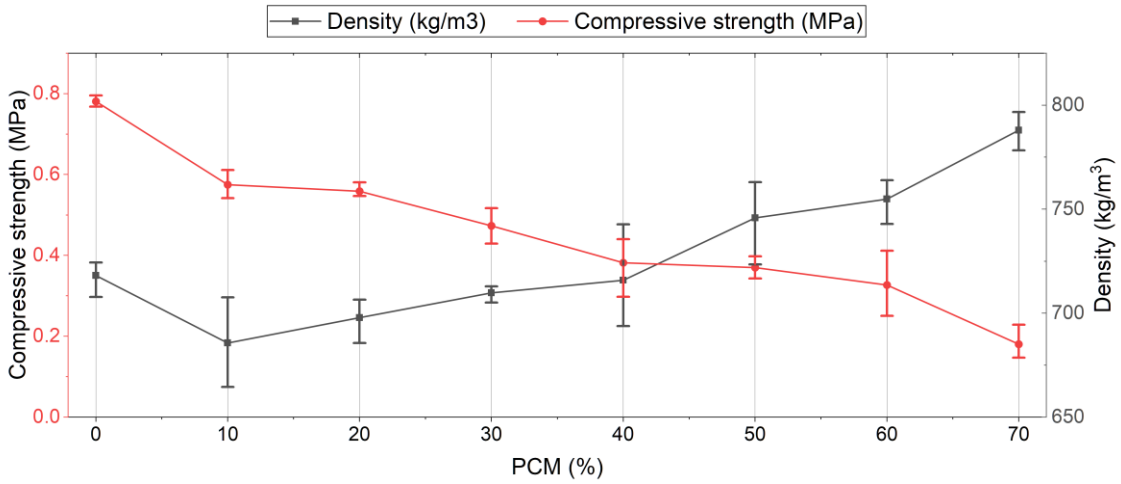


Fig. 6.2. Experimental compressive strength and density of PCM-HLC as a function of PCM content (0–70%). Error bars represent the maximum and minimum experimental values for each interval.

Density followed a two-stage trend. The initial decrease at low PCM substitution may reflect reduced packing efficiency or lower fresh-state workability after fatty acids were introduced. From 10% PCM onward, density increased steadily and reached 796 kg/m³ at 70% PCM. A plausible explanation is that the denser fatty acids replaced part of the porous hemp shiv volume and occupied some accessible void space. Because the load-bearing light-weight hemp shiv is replaced by non-load-bearing heavier fatty acids, the overall density of the composites increased while its compressive strength decreased.

This interpretation is consistent with the mass balance and SEM observations that fatty acids coated the surfaces of hemp shivs. .

The 0% PCM reference provides the mechanical baseline for this binder-shiv system. Its compressive strength, approximately 0.8 MPa at about 720 kg/m³, lies within the lower part of comparable high-density HLC results. Previous studies show that binder content, density, and shiv size all affect strength [253]. Lower-density vibration-compacted HLC has also shown lower strength [43], whereas high-density HLC can reach higher values under different mix designs [161]. The use of small shiv in this study may partly explain why the reference strength was lower than some HLC mixtures with coarser shiv [16], [43]. However, this comparison remains approximate because the compaction method, binder system, and aggregate geometry differ among studies.

For the PCM-HLC mixtures, the compressive test is best interpreted as a handling and integrity indicator rather than as a structural design value. These composites replace part of the bio-aggregate phase with fatty-acid PCM and are intended for non-load-bearing envelope applications. Across the substitution range, compressive strength decreased from 0.78 MPa for the 0% reference to 0.18 MPa for the 70% PCM mixture, a reduction of approximately 77%.

The strength decrease agrees with the general direction reported for PCM-modified composites, but the present dose-response adds important detail. Previous SS-PCM and MPCM studies report large strength losses, although the magnitude varies with PCM chemistry, carrier, binder type, and incorporation method [139], [254], [248], [255]. In contrast, the present data show a more gradual and systematic decline across 0-70% substitution. This suggests that the hemp-shiv-supported fatty-acid system can accommodate moderate PCM contents more predictably than some previously reported PCM composites, while still showing an unavoidable mechanical penalty at high substitution.

Despite this penalty, the residual strength remains relevant for non-structural insulation use. Conventional non-load-bearing insulation materials can have compressive strengths below 0.069 MPa [256, 257]. The 70% PCM mixture retained 0.18 MPa, which suggests adequate resistance for handling, transport, and integration into a protected envelope layer. The result supports functional use of high-PCM HLC, provided that structural loads are carried by other components of the wall assembly.

6.2.1.2. Specific compressive strength analysis

Because density varied with PCM content, compressive strength alone cannot separate mechanical efficiency from mass increase. Density is a strong predictor of conventional HLC strength [11, 24, 41, 42, 186, 194], but PCM substitution changes the role of the solid phase. Specific compressive strength [258], calculated as compressive stress divided by dry bulk density [259], was therefore used to assess whether higher mass translated into load-bearing efficiency (Fig. 6.3).

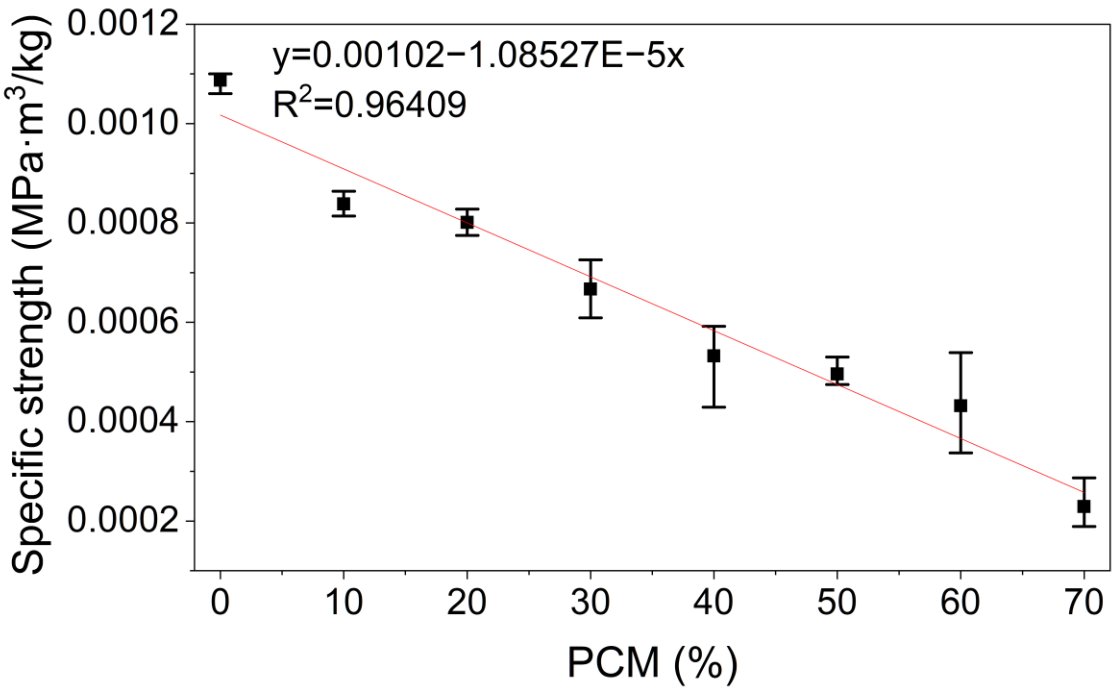


Fig. 6.3. Influence of PCM content on the specific strength of PCM-HLC composites.

The specific-strength results indicate that the loss of mechanical efficiency cannot be explained by density variation alone. The 0% PCM reference reached 1.09×10^{-3} MPa·m³/kg, whereas the 70% PCM mixture reached 2.28×10^{-4} MPa·m³/kg. Reported HLC values span approximately 3.33×10^{-4} to 1.48×10^{-3} MPa·m³/kg when converted from published strength and density ranges [11, 186, 194, 241]. The reference mixture therefore remains comparable to conventional HLC values reported by Brzyski et al. [40]

and Nguyen et al. [161], but the high-PCM mixtures move outside the usual density-strength relationship.

This change in relationship is scientifically important. In conventional HLC, higher density often indicates more solid contact and improved stress transfer. In the PCM-HLC mixtures, however, part of the added mass is a soft phase that stores heat rather than carrying load. Thus, the 70% PCM samples were among the densest specimens but had the lowest absolute and specific strength. The result shows that density cannot be used as a standalone proxy for mechanical performance once a large fraction of the hemp shiv is replaced by PCM.

6.2.1.3. Microstructure implications

SEM was used to examine the morphology of PCM-HLC at 70%, 30%, and 0% PCM substitution (Fig. 6.4). The images show plate-like and lamellar features similar to structures reported for shape-stabilised PCMs containing long-chain hydrocarbons [260, 261]. These features are interpreted as PCM-rich regions or coatings formed during cooling, although SEM alone cannot quantify coating thickness, PCM continuity, or pore connectivity.

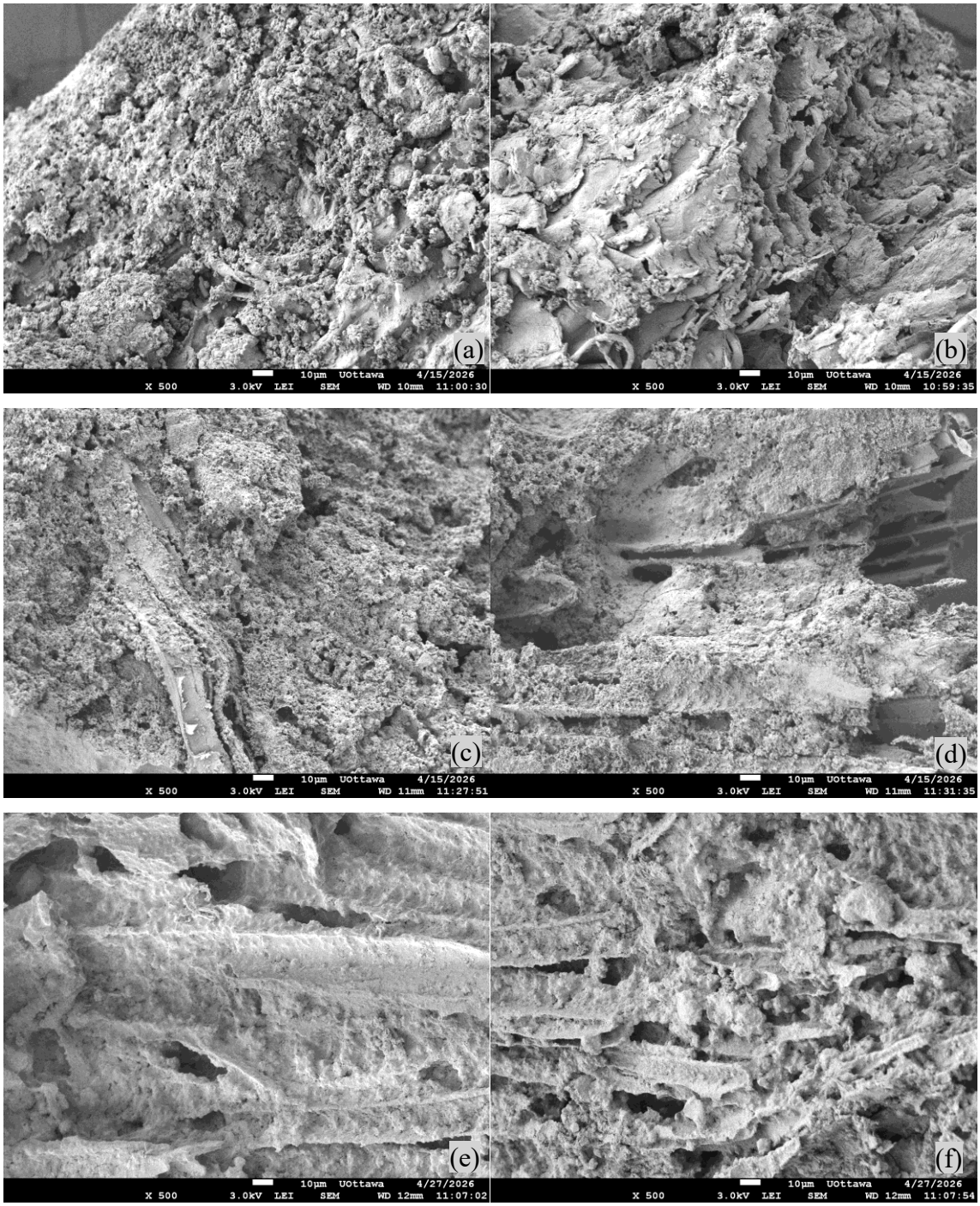


Fig. 6.4. SEM micrographs at x500 magnifications: (a, b) PCM-HLC at 70% PCM, (c, d) PCM-HLC at 30% PCM, and (e, f) HLC with 0% PCM.

At 70% PCM, the SEM images show smoother regions and fewer visible binder particles on parts of the cross-section. One potential explanation is that a higher amount of solidified fatty acid reduced the exposed mineral-binder surface and interrupted some hemp-binder contacts. This would be consistent with the lower compressive strength, but the images do not by themselves prove the stress-transfer pathway. Quantitative image analysis or micro-CT would be needed to verify the extent of binder discontinuity and pore blocking.

At 30% PCM, the visible binder coverage appears more continuous across the hemp shiv surface. This morphology is consistent with a mixture in which PCM is present but does not dominate the interfacial region. The improved mechanical response at moderate substitution may therefore be associated with more continuous binder contact, although this remains an interpretation rather than a directly measured stress-transfer mechanism.

The 0% HLC images provide the reference morphology. The hemp shiv surfaces were more fully covered by the binder matrix, and the surface texture differed from the smoother PCM-rich regions observed in the PCM-HLC samples. This contrast supports the interpretation that PCM substitution changes the interfacial environment around the shiv particles.

Taken together, the SEM observations provide a plausible microstructural explanation for the macroscopic mechanical trend. Higher PCM contents appear to shift the composite from a binder-connected hemp-lime skeleton toward a denser material containing more PCM-rich regions. This shift may reduce mechanical efficiency while increasing thermal storage capacity. The mechanism should be treated as supported by visual evidence and property trends, not as fully verified, because pore-size distribution, PCM clustering, and interfacial strength were not directly quantified.

6.2.2. Thermal properties

The thermal response of PCM-HLC must be interpreted through several coupled properties. Thermal conductivity controls steady conductive heat flow, specific heat capacity describes sensible energy storage per unit mass, and thermal diffusivity combines conductivity with volumetric heat capacity to indicate how quickly temperature changes propagate. For PCM-HLC, these properties may move in different directions as PCM content increases. This distinction is essential because a useful envelope material must both moderate heat flow and store thermal energy over time.

6.2.2.1. Thermal conductivity

Thermal conductivity is important for evaluating the efficiency of conductive heat transfer of a given building envelope. As illustrated in Fig. 6.5, the measured thermal conductivity ranged from 0.103 W/m·K to 0.115 W/m·K, with COVs of 5.18% -6.17% in each dataset.

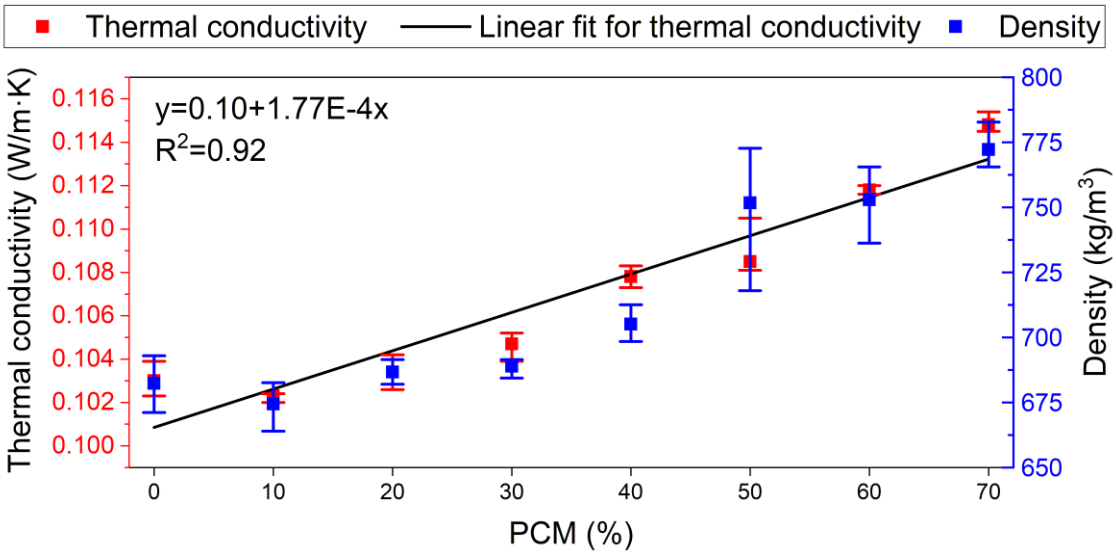


Fig. 6.5. Thermal conductivity of PCM-HLC as a function of PCM substitution rate (0% to 70%).

Thermal conductivity increased nearly linearly with PCM substitution (R2 = 0.92). This trend is consistent with the density increase shown earlier and with the expectation that replacing air-filled pores with fatty-acid PCM can increase conductive pathways. However, the total increase was modest, rising by approximately 9% from 0% to 70% PCM. Therefore, PCM substitution changed the thermal-conduction regime but did not transform the material into a highly conductive composite. The measured conductivity-density relationship is placed in context with published hemp-concrete data in Fig. 6.6.

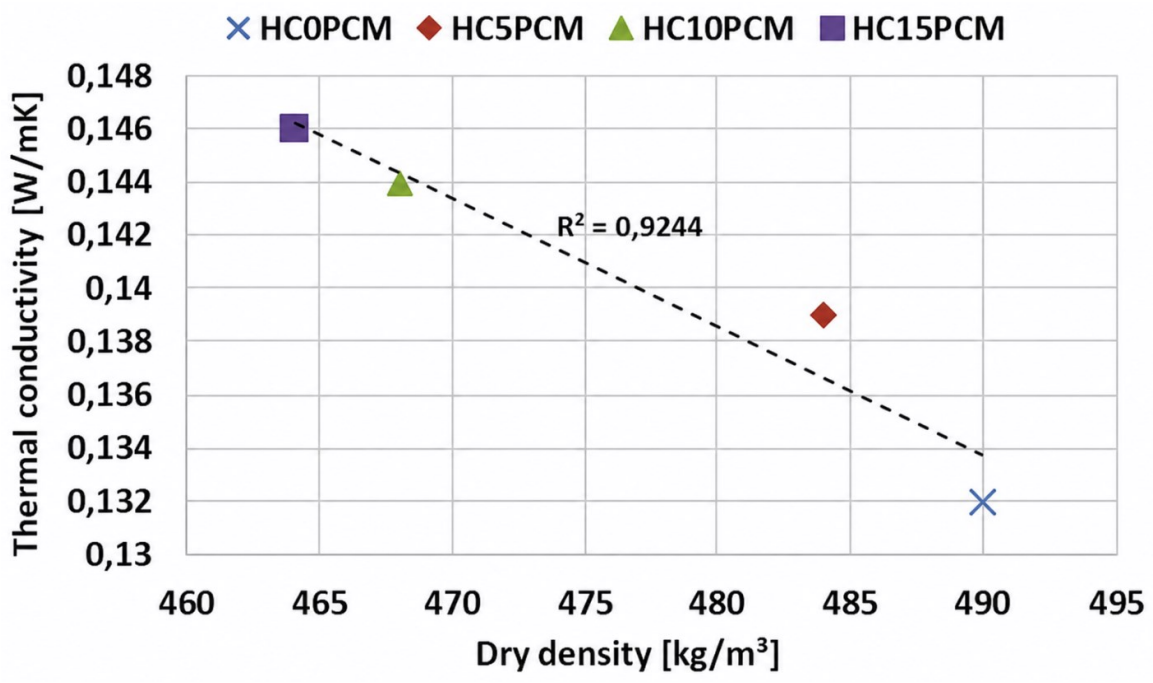


Fig. 6.6. Evolution of thermal conductivity of studied composites as a function of density [248]. HC represents hemp concrete that was modified by adding different amounts of MPCM (0, 5, 10, and 15 wt%)

This modest increase has two implications. First, it indicates that high PCM substitution can be introduced without a severe loss of insulation function at the material scale. Second, the slightly higher conductivity may help the PCM-rich layer charge and discharge more effectively when placed within a multilayer wall assembly. The result

should therefore be viewed as a trade-off between insulation resistance and thermal-storage access, rather than as a simple improvement or deterioration.

6.2.2.2. Specific heat capacity

While thermal conductivity governs the rate of heat propagation through the medium, specific heat capacity (C_p) determines the amount of thermal energy the material can store per unit mass. As shown in Fig. 6.7, the C_p of the PCM-HLC samples was measured at a hot plate temperature of 20 °C and a cold plate temperature of 5 °C, to evaluate the sensible thermal mass enhancement provided by the PCM prior to phase change.

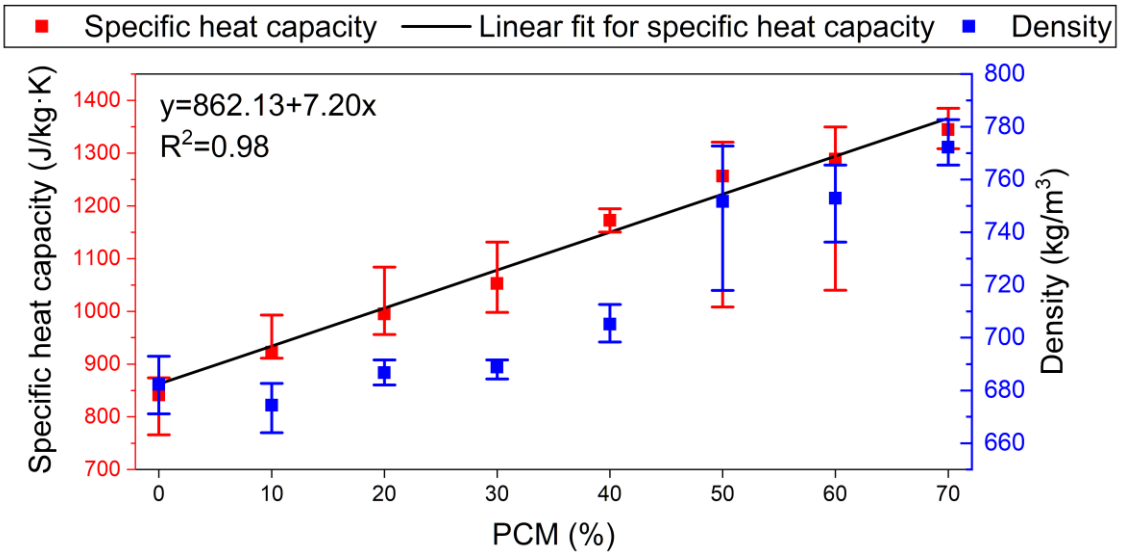


Fig. 6.7. Influence of PCM substitution level on the specific heat capacity of the PCM-HLC.

As shown in Fig. 6.7, specific heat capacity increased strongly with PCM content (R2 = 0.98). The 0% reference measured 841 J/(kg·K), whereas the 70% PCM mixture reached 1344 J/(kg·K), an increase of approximately 60%. This result provides direct evidence that fatty-acid substitution increases the sensible heat-storage capacity of the composite under the tested temperature range.

These values represent sensible heat capacity measured under steady-state HFM conditions, with a hot plate at 20 °C and a cold plate at 5 °C. They do not include the latent heat released or absorbed during a complete phase transition. Therefore, the measured increase should be interpreted as the baseline heat-storage improvement of the solid composite. The total storage capacity during dynamic melting and solidification would likely be higher, but it was not quantified by this test.

6.2.2.3. Thermal diffusivity

Thermal diffusivity describes how rapidly a temperature disturbance moves through a material. Lower diffusivity usually indicates greater thermal lag and smaller temperature fluctuations in building envelopes [262]. In this study, calculated diffusivity ranged from 0.179 × 10^{-6} m^2/s for 0% PCM to 0.111 × 10^{-6} m^2/s for 70% PCM, as shown in Fig. 6.8. These values are lower than the 0.369-0.585 × 10^{-6} m^2/s range reported for some HLC without PCM [43], indicating that PCM-HLC can occupy a lower-diffusivity regime.

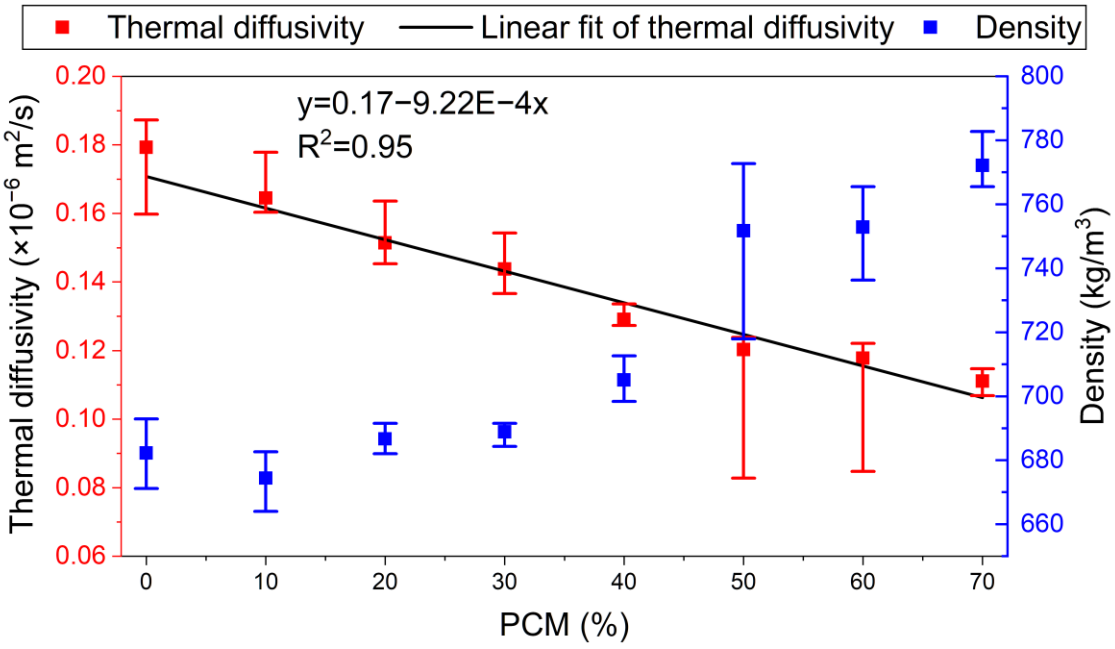


Fig. 6.8. Correlation between %PCM substituted and PCM-HLC thermal diffusivity.

The decrease in diffusivity results from competing changes in the numerator and denominator of the diffusivity relationship. PCM substitution increased thermal conductivity by about 11.5%, which would normally increase diffusivity. This effect was outweighed by the simultaneous increases in density and specific heat capacity, which increased the composite's volumetric heat capacity. At 70% PCM, diffusivity was approximately 38% lower than that of the 0% reference, showing that heat storage became more influential than conduction rate in the transient response.

This interpretation is consistent with the diffusivity equation and with previous observations that density affects transient heat transfer in bio-aggregate materials [11, 23, 262, 263]. A possible microstructural contribution is the replacement of some air-filled pore volume by PCM, because air has a much higher thermal diffusivity than the composite phases [264]. This mechanism is plausible, but it should not be treated as verified without direct porosity and pore-connectivity measurements.

For building-envelope design, the lower diffusivity is the main thermal advantage of the high-PCM mixtures. It suggests that a PCM-rich layer could delay heat propagation and dampen short-term temperature swings. This does not mean that the material can replace all insulation, because thermal resistance still depends on thickness and conductivity. Instead, the result supports using PCM-HLC as a thermal-buffering layer within a broader wall assembly.

6.2.2.4. Thermal resistance

The experimental thermal resistance (R – value) results are shown in Fig. 6.9.

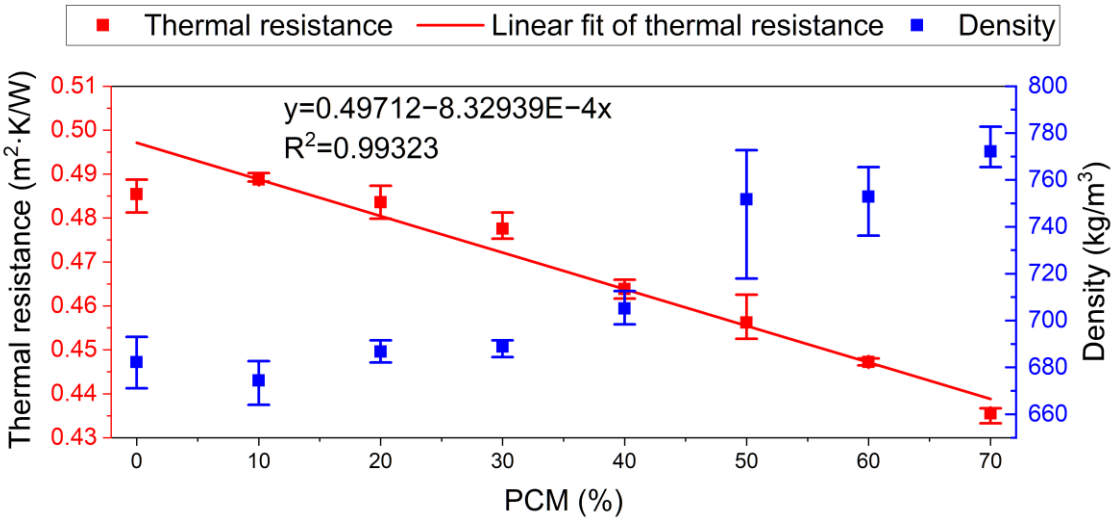


Fig. 6.9. Correlation between PCM substitution rate and the thermal resistance of the PCM-HLC.

The composite's thermal resistance varies with the PCM substitution rate. For the 50 mm specimens tested, the 0% PCM samples achieved an R-value of 0.485 m²·K/W, while the denser 70% PCM samples exhibited a marginally lower value of 0.436 m²·K/W. While these values are lower than the 2.78 to 3.85 m²·K/W RSI range typically required for full-wall assemblies in Canadian climate zones [265], this discrepancy is primarily due to the limited specimen thickness used for material-scale characterization. Based on the measured thermal conductivity of approximately 0.10–0.11 W/m·K, a full-scale hempcrete wall assembly would typically require a thickness of 300–350 mm to meet standard building code requirements. Consequently, the 50 mm samples evaluated in this study represent a single functional layer within a broader envelope system, such as the core of the proposed sandwich panel, rather than a standalone wall.

The decrease in R-value should be interpreted as an engineering trade-off. A lower thermal resistance is not desirable for a standalone insulation layer. In a PCM-integrated layer, however, moderate conductivity can help heat reach the PCM and activate storage within the relevant temperature range. The implication is that PCM-HLC should be paired with an insulation layer when both thermal storage and code-level wall resistance are required.

6.2.3. Moisture buffering value

6.2.3.1. Moisture intake and release behaviours

The dynamic moisture buffering capacity of the PCM-HLC samples was evaluated by subjecting them to cyclic humidity variations. Fig. 6.10 shows the continuous mass change (%) of the composites over 120 hours, corresponding to five complete 24 - hour cycles. Each cycle consists of a moisture adsorption phase, during which the sample is placed under 75% RH for 8 hours, and a moisture desorption phase, during which the sample is placed under 33% RH for 16 hours.

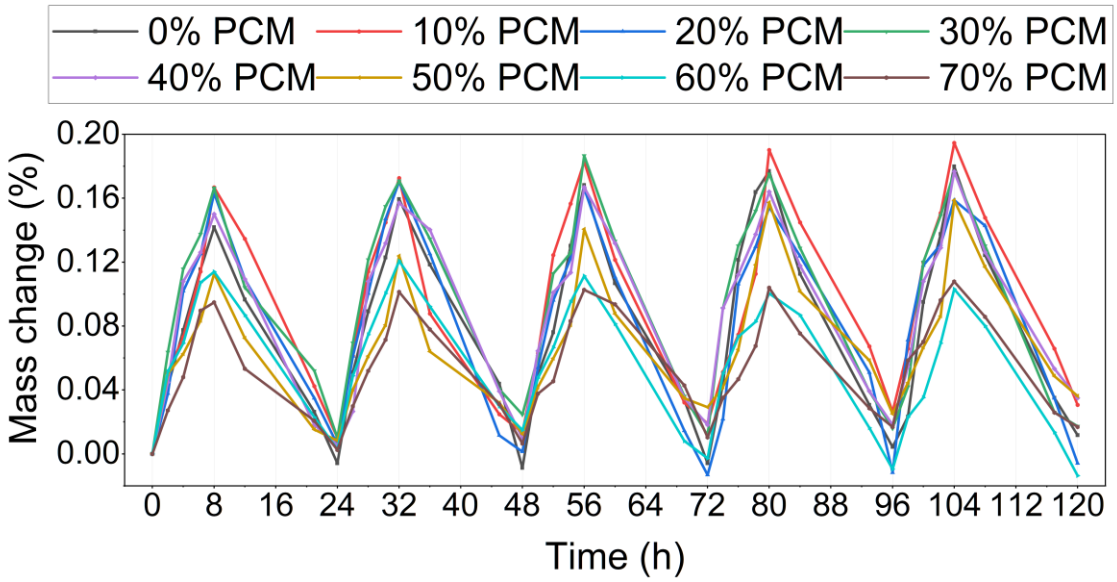


Fig. 6.10. The percentage mass change of PCM-HLC samples over five consecutive moisture adsorption and desorption cycles.

As shown in Fig. 6.10, all mixtures responded rapidly to cyclic humidity changes. Each sample gained mass during the 75% RH adsorption stage and lost mass during the 33% RH desorption stage. This observation shows that moisture exchange remained active even after PCM substitution, although the magnitude of exchange depended on PCM content.

The amplitude of mass change decreased as PCM content increased. The 0% and lower-PCM mixtures showed higher adsorption and desorption peaks, whereas the 70% mixture showed the smallest moisture-response amplitude. This trend indicates that PCM substitution reduces the amount of moisture actively exchanged with the surrounding air, even though it does not eliminate the moisture-buffering function.

6.2.3.2. Cyclic stability of the Moisture Buffering Value (MBV)

To ensure the reliability of the moisture buffering characterization, at least three stable cycles are required, characterized by the fact that the daily amounts of moisture uptake and release approach each other [223]. Fig. 6.11 presents the calculated MBV for each of the five individual cycles.

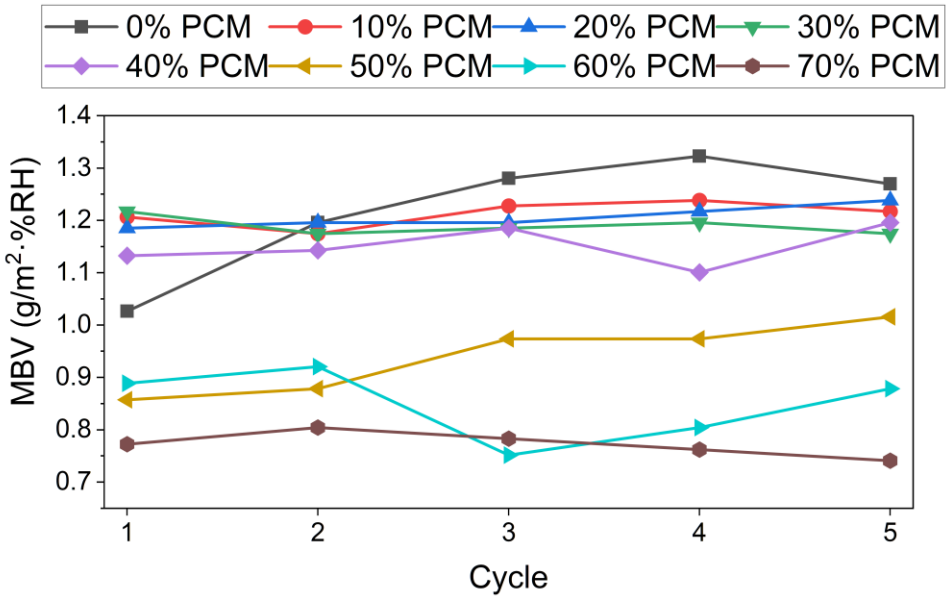


Fig. 6.11. Stability of MBV for each cycle across various PCM-HLC.

The data demonstrate that all samples reached a stable, steady – state condition during the testing period. The variations between cycles and samples are detailed in Table 6.2.

Table 6.2. Statistical analysis of MBV

PCM (%)	Mean (g/m²·%RH)	Std (g/m²·%RH)	COV
0	1.22	0.120	0.096
10	1.21	0.024	0.020
20	1.21	0.021	0.018
30	1.19	0.018	0.015
40	1.15	0.039	0.034
50	0.94	0.068	0.073
60	0.85	0.069	0.081
70	0.77	0.024	0.031

The MBV COVs across stable cycles were low for the 10-40% and 70% PCM mixtures, ranging from 1.5% to 3.4%. The 0% control had the highest COV, 9.6%, but it remained within a reasonable experimental range. These values support the reliability of the MBV comparison across substitution levels.

The average MBV was then used to assess overall hygric performance, as shown in Fig. 6.12. MBV decreased with increasing PCM loading (R2 = 0.84). This trend is consistent with a reduction in accessible moisture-active porosity, but the experiment measured mass exchange rather than pore geometry. The pore-filling and surface hydrophobicity explanations should therefore be treated as proposed mechanisms.

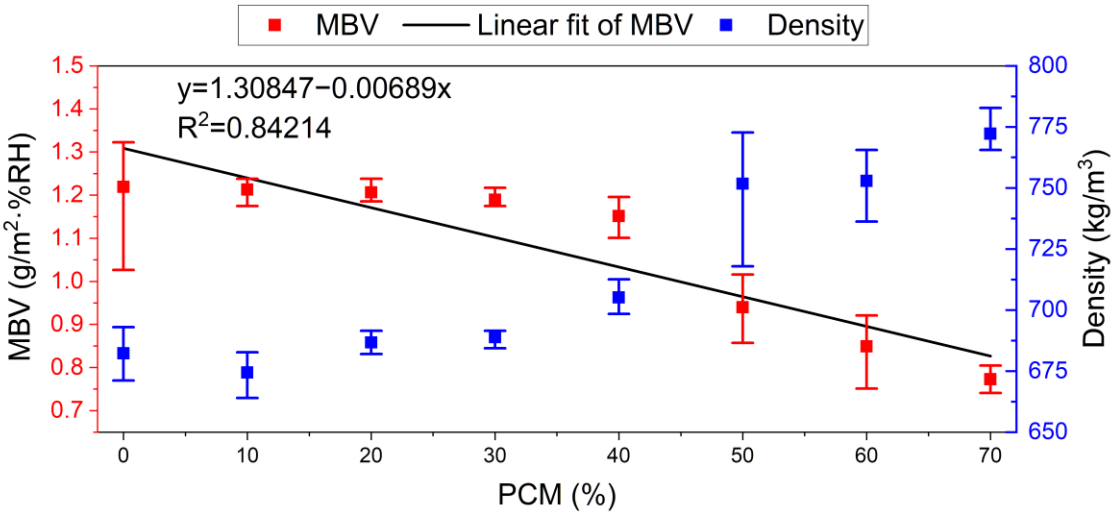


Fig. 6.12. Impact of PCM substitution level on the MBV of the PCM-HLC.

The MBV decrease occurred in two stages. From 0% to 40% PCM, the decline was gradual: MBV decreased from 1.219 to 1.151 g/(m²·%RH), a reduction of less than 6%. This suggests that, at moderate substitution levels, enough vapour-accessible pathways remained available for moisture exchange. All mixtures in this range still exceeded the Nordtest threshold for "Good" moisture buffering (>1.0 g/(m²·%RH)) [223].

Beyond 40% PCM, hygric performance declined more sharply. The 50% mixture entered the Nordtest "Limited" category at 0.940 g/(m²·%RH), and the 70% mixture reached 0.772 g/(m²·%RH), approximately 37% below the 0% reference. One possible explanation is that higher PCM contents reduced the connected pore volume available for vapour transport. A second, complementary explanation is that fatty-acid-rich surfaces reduced the affinity of some internal surfaces for water vapour adsorption.

These mechanisms are consistent with the trends, but they were not independently measured. The literature comparison is most useful when interpreted through density and pore accessibility rather than as a direct ranking of materials. Mechanical compaction can reduce air-filled void volume, while PCM substitution may occupy or coat part of the

pore network. Both effects can reduce MBV, but their relative contributions depend on mix design, density, and how the PCM is distributed within the shiv and binder matrix.

The MBV values measured here, 0.77-1.22 g/(m²·%RH), are lower than many HLC values reported without PCM, including 1.82-3.02 g/(m²·%RH) [251] and 2.06-2.53 g/(m²·%RH) [43]. Rather than indicating failure of the material, this difference shows that the present mixtures occupy a denser PCM-HLC regime. The comparison also helps explain why lower-density PCM-HLC in Chapter 5 maintained higher MBV despite containing 70% PCM.

The Chapter 5 specimens had a similar 70% PCM substitution level but a much lower density, approximately 400 kg/m³, and achieved MBV values of 2.27-2.81 g/(m²·%RH). The specimens in this chapter exceeded 700 kg/m³. This density increase of roughly 75% was associated with an approximately 66% reduction in MBV. The comparison suggests that density and accessible pore structure can be as important as nominal PCM content in controlling moisture exchange.

Overall, MBV showed a strong negative relationship with bulk density (R^2 = 0.90). The most cautious interpretation is that high PCM substitution and high compaction together reduce moisture-active porosity. Fatty-acid hydrophobicity may further contribute by changing the surface character of accessible pores. Even so, the 70% mixture retained a "Limited" Nordtest MBV classification, indicating that high-density PCM-HLC can still provide some passive humidity regulation when thermal storage is prioritised.

6.2.4. Performance trade-off with increased PCM substitution

To evaluate these coupled trade-offs, the normalized properties in Fig. 6.13 were interpreted using a constrained performance-screening approach. For a balanced envelope layer, the screening index was defined as $I_{bal} = 0.40(Cp_n) + 0.30(MBV_n) + 0.30(strength_n)$, with MBV required to remain above 1.0 g/(m²·%RH) and

compressive strength required to remain above the 0.069 MPa handling benchmark for non-load-bearing insulation. For a thermal-storage layer, the index was defined as $I_{th} = 0.50(Cp_n) + 0.30(1 - diffusivity_n) + 0.20(conductivity_n)$. These indices are not universal material rankings; they make the engineering priorities explicit.

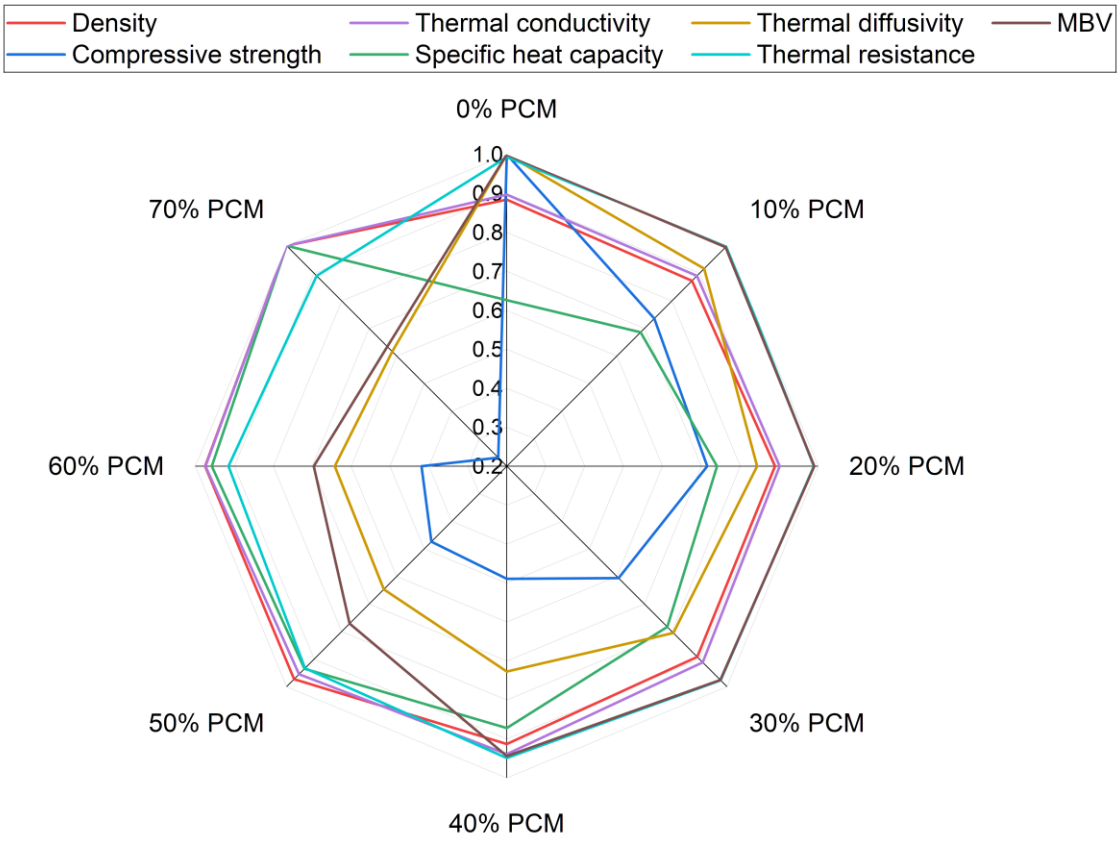


Fig. 6.13. Normalized performance radar chart illustrating the multi-dimensional trade-offs in PCM-HLC across substitution levels from 0% to 70%.

The normalized data show that the performance space separates into two useful regimes. Strength and MBV decrease with PCM substitution, while specific heat capacity increases. Density was treated as a diagnostic variable rather than a benefit by itself, because higher density can improve heat storage while also reducing moisture exchange. This framing avoids selecting a formulation simply because it is heavier.

For balanced hygrothermal performance, 40% PCM is the highest substitution level that retains the Nordtest "Good" MBV classification while increasing heat-storage capacity. The 40% mixture therefore satisfies the moisture constraint and preserves a practical handling-strength margin, while moving beyond the thermal properties of the 0% reference. This recommendation is stronger than a qualitative compromise because it is tied to explicit MBV and strength thresholds.

For thermal-storage-dominated layers, 70% PCM is preferred. This mixture maximizes specific heat capacity and minimizes thermal diffusivity within the tested range, while still retaining compressive strength above the non-load-bearing insulation benchmark. Its lower MBV and lower R-value mean that it should not be used as the only functional layer in a wall. Instead, it is best treated as a PCM-rich core paired with more insulating or moisture-active layers. Even with the 70% max PCM substitution rate, the thermal conductivity only rises by approximately 9%, indicating that while maximizing thermal storage ability, the insulation of the PCM-HLC is still maintained.

The SEM observations support this index-based interpretation. High PCM contents appear to create more PCM-rich regions and less mechanically efficient binder continuity, which is consistent with lower strength and MBV. Moderate PCM contents appear to preserve more of the binder-connected structure while still adding thermal storage. These microstructural interpretations remain hypotheses until pore connectivity and interfacial strength are measured directly.

The main scientific value of the performance map is that it converts PCM-HLC design from a single-property target into a multi-objective material-selection problem. The wide 0-70% substitution range shows where thermal benefits become large enough to justify mechanical and hygric penalties. While this incorporation limit is specific to this study’s binder/hemp mix design, it has the potential to be generalized to other bio-based composites. As observed in the preliminary casting result in Section 4.3, with smaller particle size of hemp shiv and higher binder content, the bio-composites tend to withhold more PCMs. Thus, depending on the particle size of hemp shiv and the mix

design being used, other researchers could utilize this study as a baseline for their experimental design of testable threshold regions. For practitioners, it links each PCM level to a likely envelope function: moderate-PCM formulations are suited to balanced layers, whereas the 70% mixture is more appropriate as a protected thermal-storage core.

6.3. Summary

This chapter establishes a systematic relationship between PCM substitution and the mechanical, thermal, and moisture-buffering behaviour of high-density PCM-HLC. The scientific problem it solves is not simply whether PCM can be added, but how PCM content changes the balance among load handling, moisture exchange, thermal storage, and thermal resistance. The resulting trade-off regimes provide a design map for selecting PCM-HLC formulations according to their intended envelope function.

The results show that PCM substitution changes the meaning of density in hemp-lime composites. In conventional HLC, higher density often corresponds to improved mechanical performance. In the present PCM-HLC, higher density also reflects the addition of a heat-storage phase that does not contribute equally to load transfer. This interpretation helps explain why the 70% PCM mixture had high density but low specific strength.

Thermally, increasing PCM content improved sensible heat capacity by approximately 60% and reduced thermal diffusivity by approximately 38%. These observations indicate that PCM-HLC can act as a thermal-buffering layer rather than only as insulation. The modest increase in thermal conductivity and the decrease in R-value also show that high-PCM formulations need to be integrated with insulating layers when full wall resistance is required.

Hygrically, the chapter identifies a practical threshold. MBV remained in the Nordtest "Good" range up to 40% PCM, then declined to the "Limited" range at higher substitution levels. The most plausible explanation is a combination of reduced moisture-

active porosity and increased fatty-acid-rich surface area, although direct pore-network measurements are needed to confirm this mechanism.

The performance-screening approach supports two engineering recommendations. A 40% PCM substitution is the most appropriate balanced formulation when moisture regulation, handling strength, and thermal storage are all required. A 70% PCM substitution is appropriate when maximum heat storage and thermal lag are prioritised, provided that the layer is protected by complementary insulation and moisture-management layers.

Overall, the chapter advances PCM-HLC design by showing that PCM content should be selected according to a defined performance objective rather than maximised by default. Its originality lies in systematically establishing the mechanical-hygric-thermal trade-off across a broad substitution range and translating that map into material-design guidance for multilayer building envelopes. This finding is important for researchers because it identifies the coupled variables that must be measured together, and for practitioners because it links material formulation to envelope function.

7. Chapter 7: Experimental and numerical analysis of a multilayer PCM-HLC sandwich panel

PCM-HLC can combine bio-based insulation, moisture buffering, and latent heat storage, but its use as a monolithic wall layer creates a scientific design conflict. High thermal resistance protects indoor conditions but can prevent PCM from reaching its transition range, while high PCM exposure can improve thermal buffering but increase heat-loss risk when the PCM remains solid. This conflict is especially important in cold-climate retrofits, where wall depth is limited.

Previous PCM envelope designs often add insulation outside the PCM layer, sometimes increasing wall thickness to more than 30 cm [266]. What remains unresolved is whether a thinner bio-based multilayer assembly can use PCM as an active thermal buffer without creating winter heat-loss penalties. This gap motivates the sandwich PCM-HLC concept evaluated in this chapter.

The scientific contribution of this chapter is to determine how layer placement, thickness, thermal resistance, and phase-change temperature control the seasonal usefulness of PCM-HLC in a multilayer wall. The work combines laboratory validation of a finite-volume heat-transfer model with parametric sensitivity studies. It therefore generates design knowledge about when PCM should be used as active thermal storage and when conventional resistance is more valuable.

The chapter proceeds in four steps. First, a 10 cm sandwich block is fabricated and used to validate the numerical model. Second, the baseline double-PCM sandwich design is compared with monolithic HLC under representative Ottawa summer and winter weeks. Third, sensitivity studies examine outer-insulation thickness, middle-layer thermal resistance, PCM phase-change temperature, and PCM placement. Finally, the results are synthesised into design guidance for space-constrained multilayer envelopes.

The modelling objective is not to identify a universal optimum for all climates. Instead, the simulations test which design variables control performance under the selected cold-climate boundary conditions. The screening criteria are interior-surface temperature stability, heating and cooling energy demand, and energy saving per unit thickness relative to the monolithic HLC baseline.

This framing treats the numerical work as a parametric sensitivity study rather than proof of a universal wall optimum. It separates observation, physical interpretation, and engineering implication for each design change. The approach can be extended to other climates by changing the weather file, setpoint schedule, phase-change temperature range, and wall-depth constraint.

Overall, the chapter advances PCM-integrated bio-based envelope design by showing why PCM placement and thermal protection matter as much as PCM quantity. This knowledge is important for researchers developing PCM-HLC models and for practitioners selecting wall assemblies under thickness and climate constraints.

7.1. Sample development

7.1.1. Raw materials

Small-particle hemp shiv, HL, silica fume, slag, an 80.5% CA and 19.5% MA binary PCM mixture for the indoor PCM layer, and an 87.8% CA and 12.2% MA binary PCM mixture for the outdoor PCM layer were used, as described in Section 4.1. The PCM mixtures were selected to place phase transition near the targeted indoor and wall-gradient temperature ranges.

7.1.2. Compositions of PCM-HLC samples

The five-layer specimen included an indoor-facing vapour control layer, an indoor PCM-HLC core, a middle insulation/vapour-control layer, an outdoor PCM-HLC core, and an outdoor insulation/vapour-control layer (Fig. 7.1).

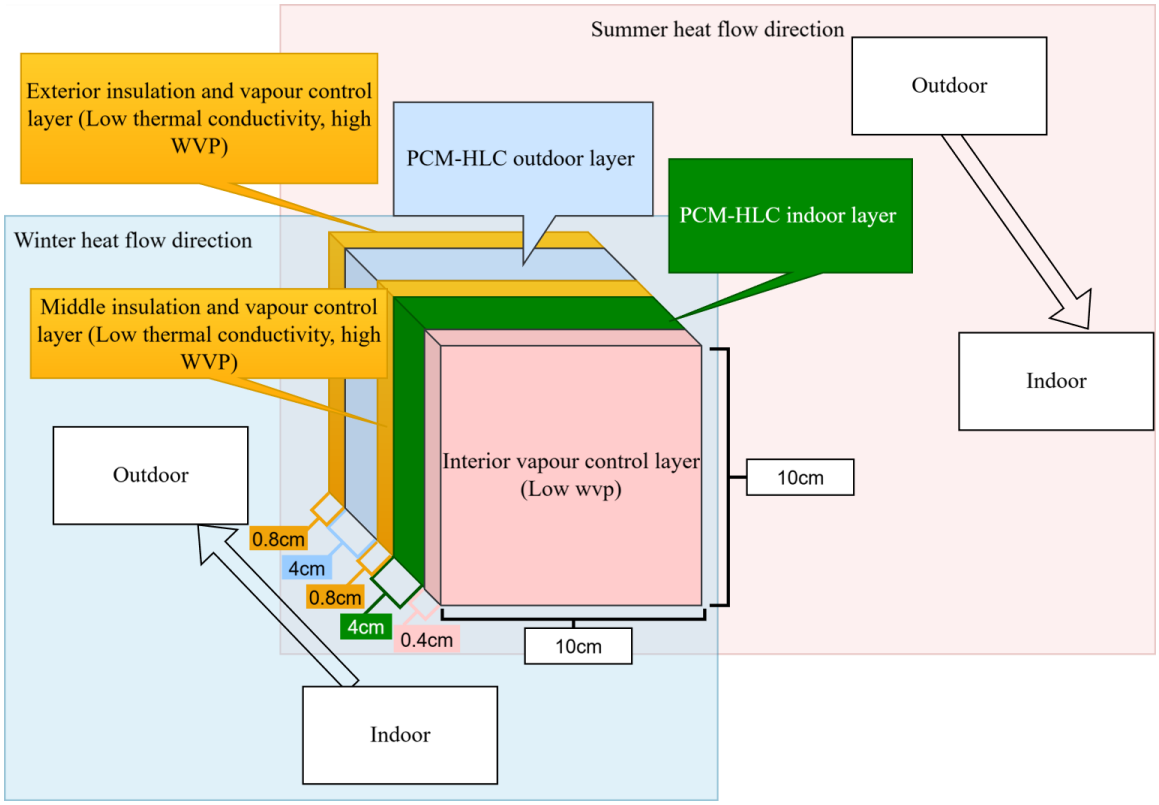


Fig. 7.1. The sandwich panel design with PCM-HLC core.

The layer compositions are listed in Table 7.1. Silica fume was used in the PCM-HLC core because its fine particle size supported the high-PCM formulation developed in Chapter 4. Slag was used in the insulation mix because preliminary results and literature data indicated lower thermal conductivity for this binder route [22], [43].

Table 7.1. Monolithic HLC and PCM-HLC Sandwich panel compositions.

Component (wt% of dry mass)	Monolithic HLC	Sandwich panel		
	Regular HLC with 0% PCM	PCM-HLC Core	Indoor face lime plaster	Outdoor & middle insulation
Hemp	1	1	0	1
PCM	0	2.33	0	0
HL	2.37	2.37	1	0.34
SCM	0.63 (Silica fume)	0.63 (Silica fume)	0	0.08 (Slag)
Water	2.5	2.5	0.75	0.43

7.2. Preliminary model validation of PCM-HLC sandwich block

7.2.1. Model geometry

For model validation, the numerical geometry reproduced the 10 cm × 10 cm × 10 cm sandwich block shown in Fig. 7.1 and Fig. 7.2. The stacking sequence and layer thicknesses followed the experimental specimen, and each layer was assigned material properties measured in the previous chapters.

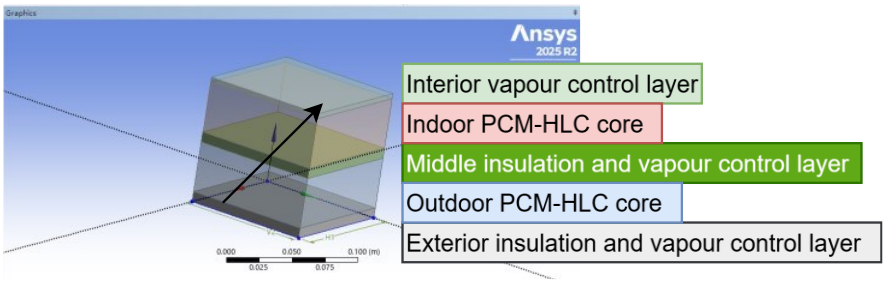


Fig. 7.2. Geometry of the sandwich block being modelled.

7.2.2. Governing equations

The numerical simulation was carried out using the finite – volume method in ANSYS Fluent, based on the following governing equations. The rate of thermal conduction ($q_{x,y,z}$ in W or J/s) can be estimated from Fourier's law: where $\vec{q}$ = heat flux vector (W/m²), k = thermal conductivity (W/m·K), ∇T = temperature gradient (K/m).

$$q_{x,y,z} = -k\,\partial A\,\nabla T \tag{15}$$

In 3D transient conduction: where ρ = density (kg/m³), C_p = specific heat (J/kg·K), T = temperature field (K), t = time (s), Q = internal heat generation per unit volume (W/m³).

$$\rho c_p \frac{\partial T}{\partial t} = \nabla \cdot (k \nabla T) + Q \tag{16}$$

The convection heat transfer coefficients at the vertical walls were estimated using Eq. (18), adapted from the literature [53, 267].

$$h = \frac{1.823}{D_h^{0.121}} |T_{amb} - T_w|^{0.293}, where\ D_h = \frac{4A}{P} \tag{17}$$

By employing the equations above, the convection heat was determined by (18):

$$q_{convec} = h(T_w - T_{amb}) \tag{18}$$

where h denotes the convection heat transfer coefficient on the interior or exterior surface (W/m² K), A is the wall surface area (m²), P is the wall's perimeter, T_{amb} represents the surrounding temperature inside and outside the building (°C), and T_w corresponds to the temperature of the interior wall surface (°C).

7.2.3. Model validation setup

7.2.3.1. Experimental HFMA validation

The numerical model was validated against HFM experimental data at a mean test temperature of 23.5 °C. The HFM setup was represented as one-dimensional heat flow through the specimen, with the four lateral sides insulated. A Ceratina C100 data logger and NTC probes with ±0.10 °C precision recorded the centre temperature during the test (Fig. 7.3).

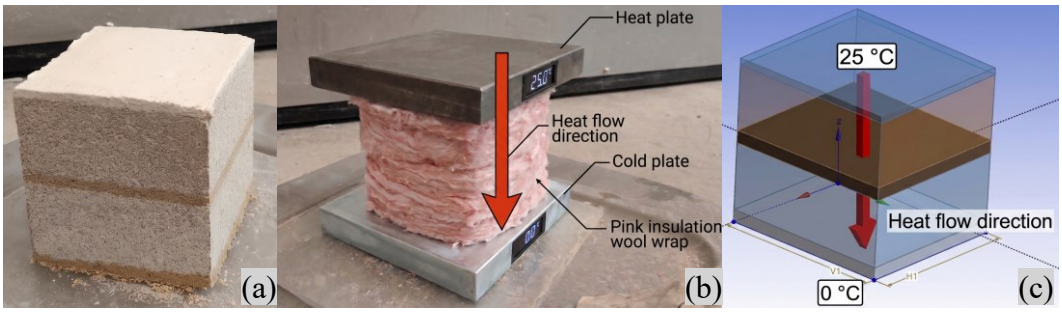


Fig. 7.3. Experimental setup for numerical model validation: (a) 10 cm cube sandwich specimen, (b) schematic illustration of specimen with peripheral insulation to ensure unidirectional heat flux, and (c) model setup in ANSYS.

Table 7.2 summarizes the material properties of the sandwich PCM-HLC and the monolithic HLC, obtained from the experimental results. For comparison reasons, the monolithic HLC used in this study was set to have the same average density as the PCM-HLC.

Table 7.2. Material properties of the sandwich PCM-HLC and the monolithic HLC.

Materials	Sandwich PCM-HLC			Monolithic HLC
	PCM-HLC core	Indoor facing layer	Outdoor facing / middle insulation	HLC
Thickness (cm)	4	0.4	0.8	10
Density (kg/m^3)	769.34	979.55	153.49	679.21
Thermal conductivity (W/(m K))	0.115	0.370	0.052	0.103
Specific heat capacity (J/(kg K))	1344.48	931.17	711.62	841.36

7.2.4. Mesh independence

A mesh-independence study was performed before validation. Three mesh sizes between 0.01 m and 0.002 m were compared to determine whether the predicted temperature was sensitive to grid refinement.

7.2.5. Results and discussion

7.2.5.1. Mesh Independence

The data in Table 7.3 indicate a clear convergence of the temperature values as the cell size is reduced.

Table 7.3. Mesh independence of the model.

Time (s)	Cell size (m)			
	0.01	0.008	0.004	0.002
0	294.15	294.15	294.15	294.15
43200	297.65	293.87	293.02	292.9
% Difference	+ 1.62%	+ 0.33%	+ 0.04%	-

The coarsest mesh (0.01 m) differed from the finest-mesh benchmark by 1.62%, whereas the 0.008 m mesh reduced the difference to 0.33%. Refining the mesh to 0.004 m produced a predicted temperature of 293.02 K, only 0.04% different from the 0.002 m mesh. The 0.004 m mesh was therefore selected because further refinement produced negligible change relative to the added computational cost.

This mesh-selection step supports numerical stability for the subsequent parametric studies, but it does not by itself validate the physical model. Experimental comparison was therefore used as the next validation step.

7.2.5.2. Numerical model validation and transient thermal response

To ensure the reliability of the computational framework, the numerical predictions generated via ANSYS Fluent were validated against the experimental measurements obtained from the HFMA. Fig. 7.4 illustrates the transient temperature profile over a 12 - hour (43,200 s) period, comparing the numerical simulation with the experimental sensor data.

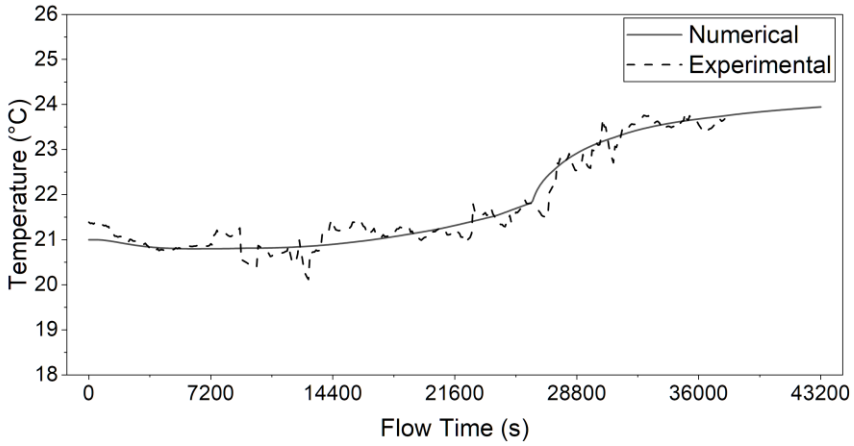


Fig. 7.4. Experimental validation of numerical model against experimental HFM result.

Fig. 7.4 shows that the simulated and experimental centre-temperature profiles followed the same transient trend and approached the same steady-state response. The available validation metrics indicate a mean absolute temperature difference of approximately 0.2 °C and a maximum percentage difference of approximately 3% relative to the experimental mean. These values are small compared with the imposed temperature gradient and the sensor precision, supporting the use of the model for comparative design studies.

The validation should be interpreted as evidence of adequate model fidelity for the tested sandwich block, not as a complete validation of every wall configuration. Full RMSE and R^2 values would require exporting the complete time-resolved residual dataset. Within this limitation, the agreement in Fig. 7.4 supports the boundary conditions, material inputs, and mesh size used for the parametric simulations.

7.2.5.3. Microstructural support for layer assumptions

SEM was used to examine the morphology of the composite matrices under varying formulations. The comparative micrographs reveal differences between the three mixture designs, as shown in Fig. 7.5.

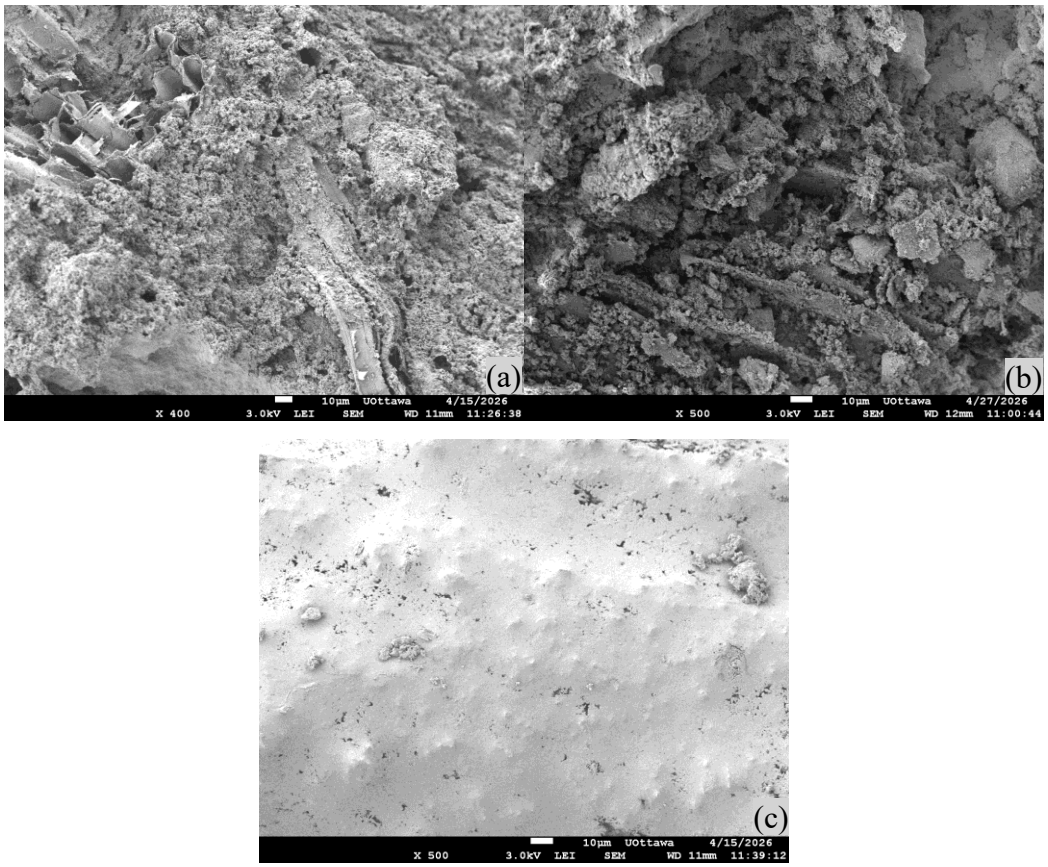


Fig. 7.5. SEM micrographs of the multi-layer building envelope system components: (a) the 70% PCM-HLC layer; (b) the porous morphology of the middle and outer insulation layers; and (c) the dense, continuous surface topography of the lime plaster indoor facing.

Fig. 7.5 shows clear morphological differences among the three types. The 70% PCM-HLC layer appears denser and more continuously covered by binder-rich material than the insulation layer. The lime plaster surface appears comparatively smooth and compact. These observations support, but do not prove, the assumed differences in thermal and vapour-control function.

The dense morphology of the PCM-HLC core may be related to the 1:3 hemp-to-binder ratio and the fine silica fume used in that mix. Fine particles can fill part of the interstitial space and may improve matrix continuity. However, SEM images alone cannot quantify packing density, pozzolanic reaction, or thermal conductivity.

The insulation layer shows a more open and granular morphology, consistent with its higher hemp-to-binder ratio and slag-based binder. This structure may support lower thermal conductivity and higher vapour permeability, but these functional interpretations rely on the measured material properties rather than SEM evidence alone.

The lime plaster layer shows a smoother and less visibly porous surface. This morphology is consistent with a vapour-control role and with improved thermal contact to the adjacent PCM-HLC layer. Direct vapour permeability and interfacial heat-transfer measurements would be needed to verify these functions independently.

Thus, SEM provides qualitative support for the layered design logic: a denser PCM-HLC thermal-storage layer, more porous insulation/vapour-release layers, and a compact indoor-facing layer. The images help explain the modelling assumptions, but they should not be treated as direct proof of heat-flow or moisture-transport mechanisms.

7.3. Numerical model baseline performance

7.3.1. Database

The baseline simulations compared a 10 cm PCM-HLC sandwich configuration with a 10 cm monolithic 0% PCM HLC control under representative Ottawa conditions. Hourly weather data were taken from the Canadian Weather Year for Energy Calculation (CWEC) file for Ottawa, Ontario [268]. This climate was selected because it combines summer diurnal swings with a heating-dominated winter, making it a useful test of both PCM activation and static thermal resistance.

Two 168 h periods were selected from the CWEC file. The winter week, February 3-9, had an average temperature of -7.99 °C, and the summer week, August 24-30, had an average temperature of 19.81 °C. These periods were chosen as representative seasonal weeks rather than extreme design conditions. Fig. 7.6 shows the outdoor temperature profiles used in the simulations.

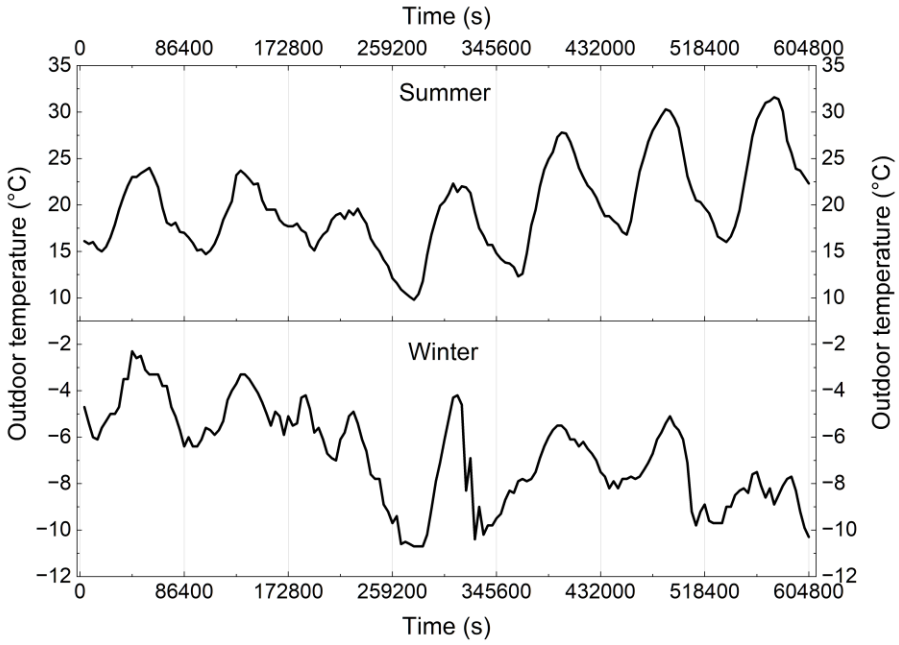


Fig. 7.6. Outdoor temperature profile over a typical summer and winter week.

Table 7.4 provides a comprehensive list of variables applied in the simulation.

Table 7.4. Sources of the input values in the simulation.

Input parameters		Known/Unknown	Sources
External climatic conditions	Temperature	Known	CWEC Ottawa weather profile [268]
Indoor climatic conditions	Indoor air temperature,	Known	Controlled by HVAC
	Interior wall surface temperature,	Unknown	Monitoring system
Wall model	Thermal conductivity (4 materials),	Known	HFM
	Specific heat capacity (4 materials),	Known	HFM
	Density (4 materials)	Known	Measurement
Boundary coefficients	Convective heat transfer coefficient	Known	Literature [53, 267]

7.3.2. HVAC control strategy

Interior surface temperature was used as the controlled response variable for comparing envelope performance. Heating and cooling energy were calculated by integrating the interior surface heat flux over time using linear interpolation between time steps. The model treated materials as homogeneous and isotropic, and it excluded edge

effects, radiation exchange between interior surfaces, internal heat gains, and solar gains through glazing.

The HVAC control logic followed a temperature-dependent schedule [266]. Cooling was activated in summer when the interior surface temperature exceeded 24 °C and was returned to a 23 °C target. In winter, the heating schedule used a nighttime setback of 18 °C and a morning ramp of 0.5 °C every 30 min until the 20 °C daytime setpoint was reached (Fig. 7.7).

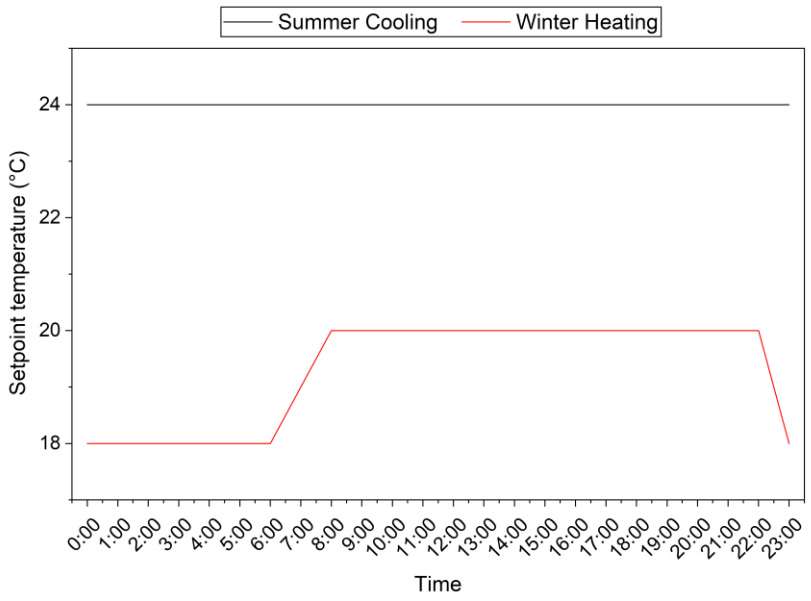


Fig. 7.7. HVAC control strategy showing heating and cooling setpoints.

When the interior surface temperature remained within the inactive band, the HVAC heat flux was set to zero. This control strategy allowed the envelope's thermal mass and PCM response to influence the simulated heating and cooling demand. The baseline comparison was then performed for the 10 cm sandwich panel and monolithic HLC control.

7.3.3. Results and discussion

Fig. 7.8 plots the interior surface temperatures of the monolithic HLC and the sandwich PCM-HLC alongside the outdoor ambient temperature over the typical summer and winter week in Ottawa.

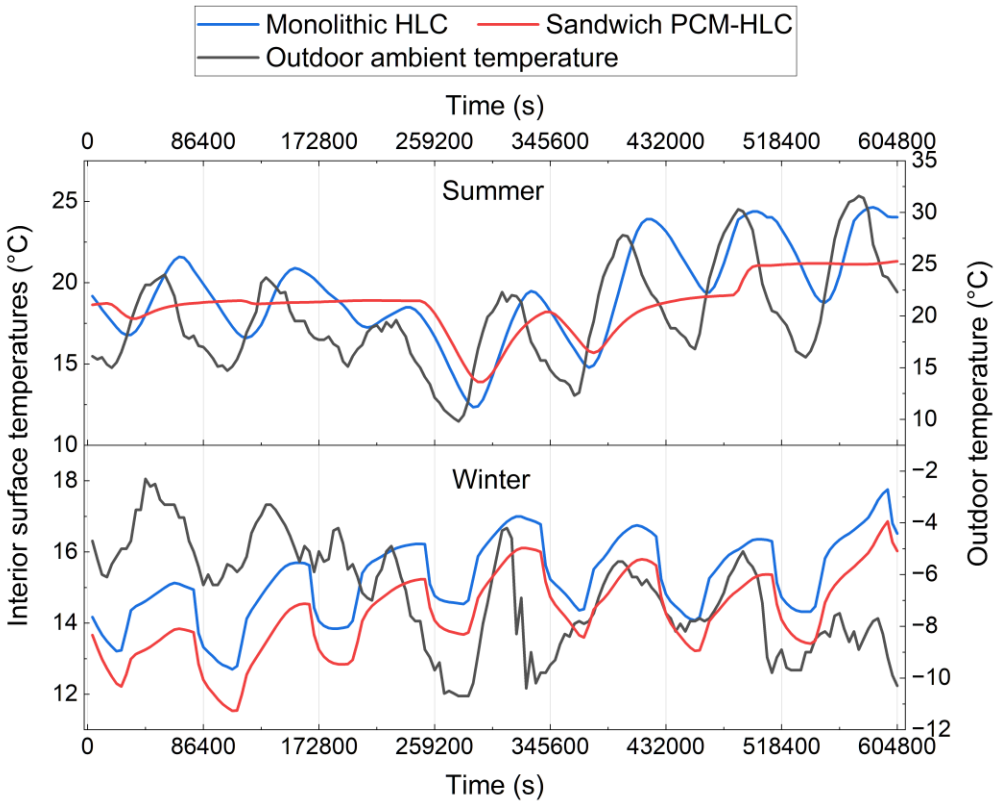


Fig. 7.8. Dynamic thermal response of the 10 cm PCM-HLC sandwich panel versus a monolithic HLC control under representative Ottawa summer and winter conditions.

The summer simulation showed a clear observation: the monolithic HLC surface temperature followed outdoor diurnal fluctuations and triggered cooling during the hotter part of the week. The sandwich PCM-HLC surface temperature remained within the 24 °C cooling threshold under the selected typical summer week.

A plausible physical explanation is that the PCM layers increased short-term heat storage and shifted the timing of heat transfer through the assembly. The schematic layer

arrangement supports this interpretation, but the simulation does not directly measure PCM melt fraction in each layer. The engineering implication is that the sandwich concept can reduce cooling demand when night-time conditions allow the PCM to discharge.

The winter observation was different. Under outdoor temperatures of approximately -11 °C to -2 °C, the 10 cm sandwich panel maintained lower interior surface temperatures than the 10 cm monolithic HLC. The sandwich profile roughly followed the monolithic trend but was shifted downward by about 1-1.5 °C.

This result suggests that the 10 cm double-PCM configuration lacked sufficient static thermal resistance under winter gradients. If the outdoor PCM layer remains below its phase-change range, it contributes density and conductive pathways without providing useful latent storage. The implication is that thin double-PCM assemblies need either more insulation or a different PCM placement strategy for cold climates.

Fig. 7.9 presents the comparative energy consumption for heating and cooling between the monolithic HLC and the sandwich PCM-HLC during typical summer and winter weeks.

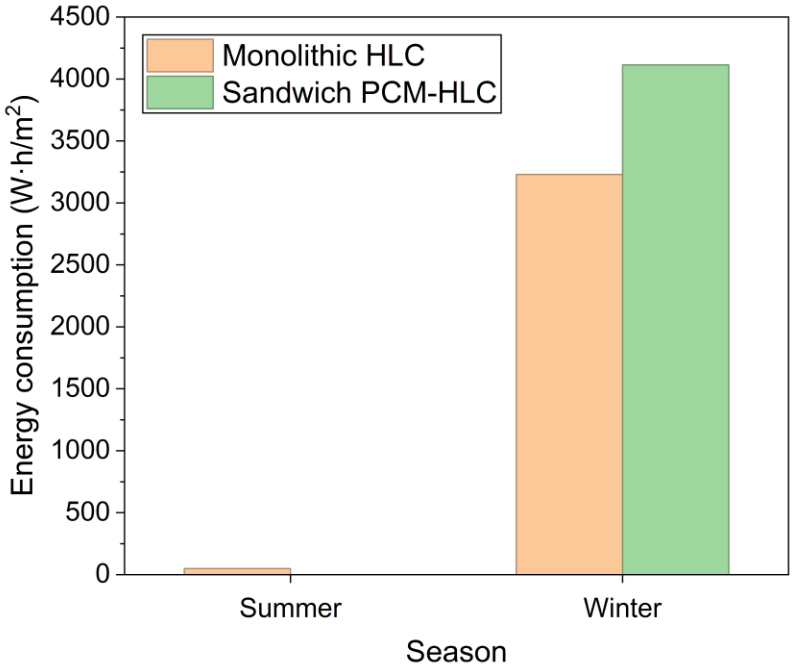


Fig. 7.9. Comparative energy performance of a 10 cm thickness monolithic HLC and sandwich PCM-HLC in typical summer and winter conditions.

During the selected summer week, the 10 cm sandwich panel did not trigger cooling, whereas the monolithic HLC required 49 W·h/m². This should be interpreted as a complete reduction in cooling demand under the modelled typical-week assumptions, not as a universal elimination of cooling demand.

During the selected winter week, the 10 cm sandwich panel required 4113 W·h/m² compared with 3230 W·h/m² for the monolithic HLC, a 27% increase. The observation indicates a winter penalty. The likely explanation is that the PCM layers did not remain thermally protected enough to function as latent buffers. The engineering implication is that cooling-season benefits alone are insufficient for cold-climate envelope design.

7.4. Sensitivity study: outer insulation thickness (10-16 cm)

7.4.1. Geometric sensitivity strategy

The baseline results show why thickness was treated as a sensitivity variable rather than a simple design target. The 10 cm sandwich design performed well in summer but penalised winter heating demand. The parametric study therefore increased only the outdoor insulation layer in 2 cm increments and evaluated three criteria: winter heating energy, interior surface temperature stability, and energy saving per unit thickness.

7.4.2. Model geometry

For the thickness-sensitivity study, the indoor vapour-control layer (0.4 cm), indoor PCM-HLC layer (4 cm), middle insulation layer (4 cm), and outdoor PCM-HLC layer (4 cm) were kept constant. The outdoor insulation layer was increased to 0.8, 2.8, 4.8, and 6.8 cm, producing total wall thicknesses of 10, 12, 14, and 16 cm (Fig. 7.10).

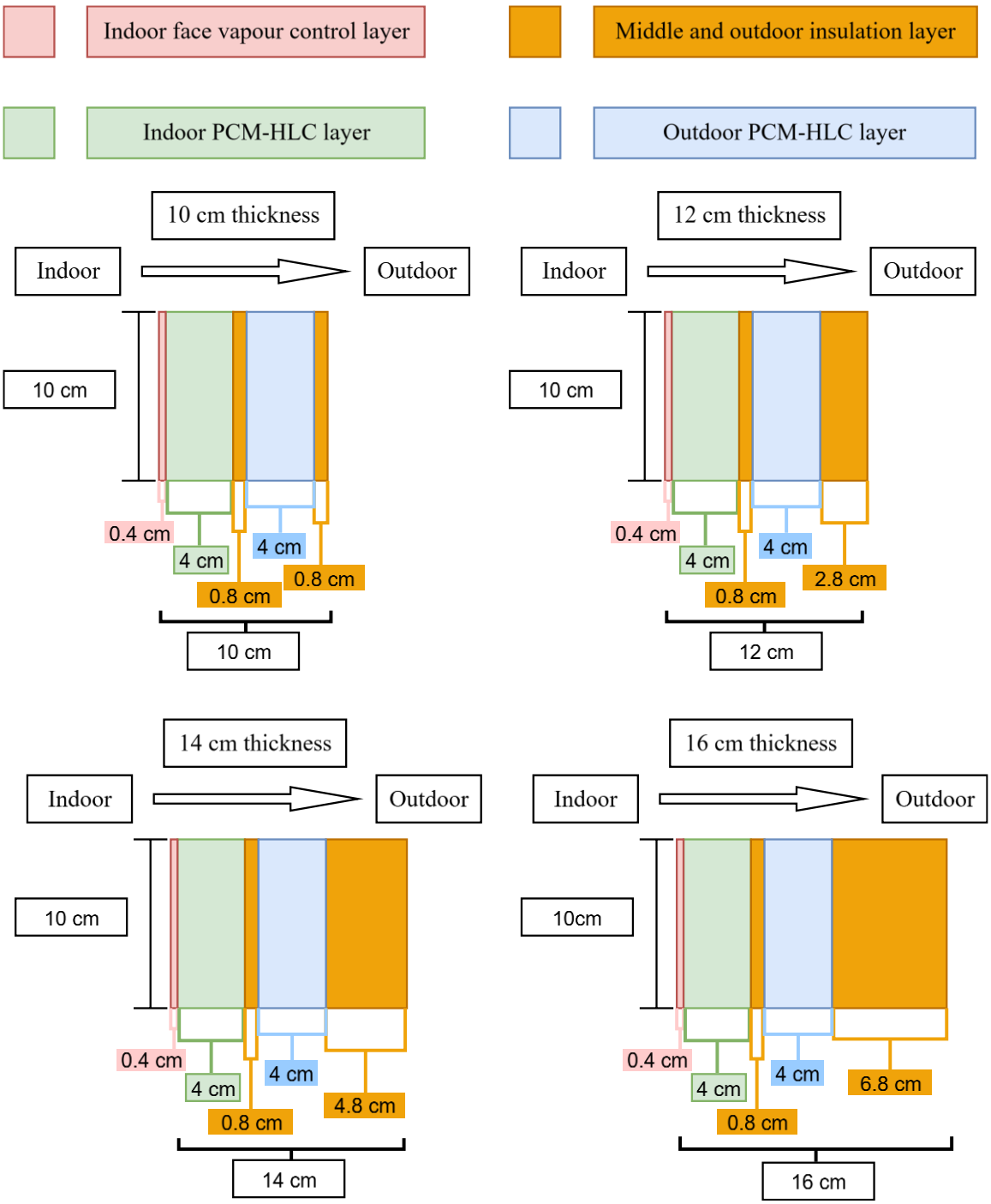


Fig. 7.10. Sandwich PCM-HLC geometry for insulation layer scaling parametric study.

7.4.3. Results and discussion

Fig. 7.11 compares the interior surface temperature response of monolithic HLC and sandwich PCM-HLC assemblies with total thicknesses from 10 to 16 cm.

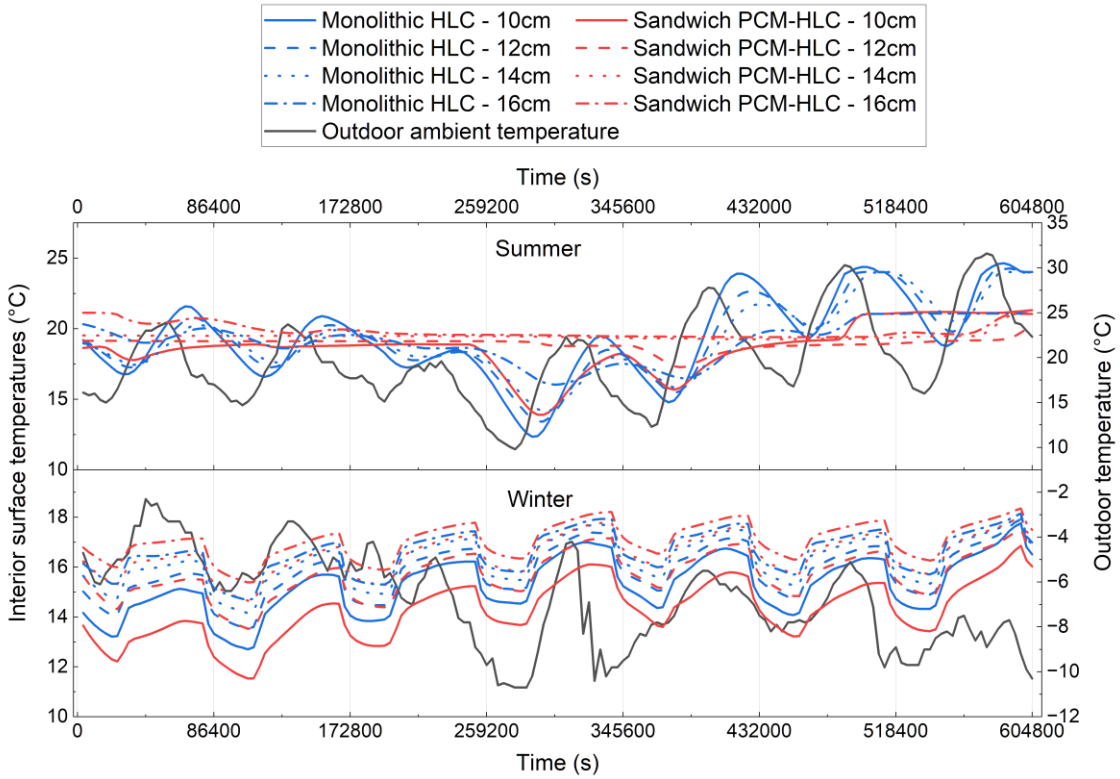


Fig. 7.11. Comparison of interior surface temperatures for monolithic HLC and sandwich PCM-HLC across varying wall thicknesses (10–16 cm) in typical summer and winter weeks.

Fig. 7.12 compares the corresponding heating and cooling energy demand. Because all sandwich panels avoided cooling demand during the selected summer week, winter heating demand became the controlling metric for this parametric comparison.

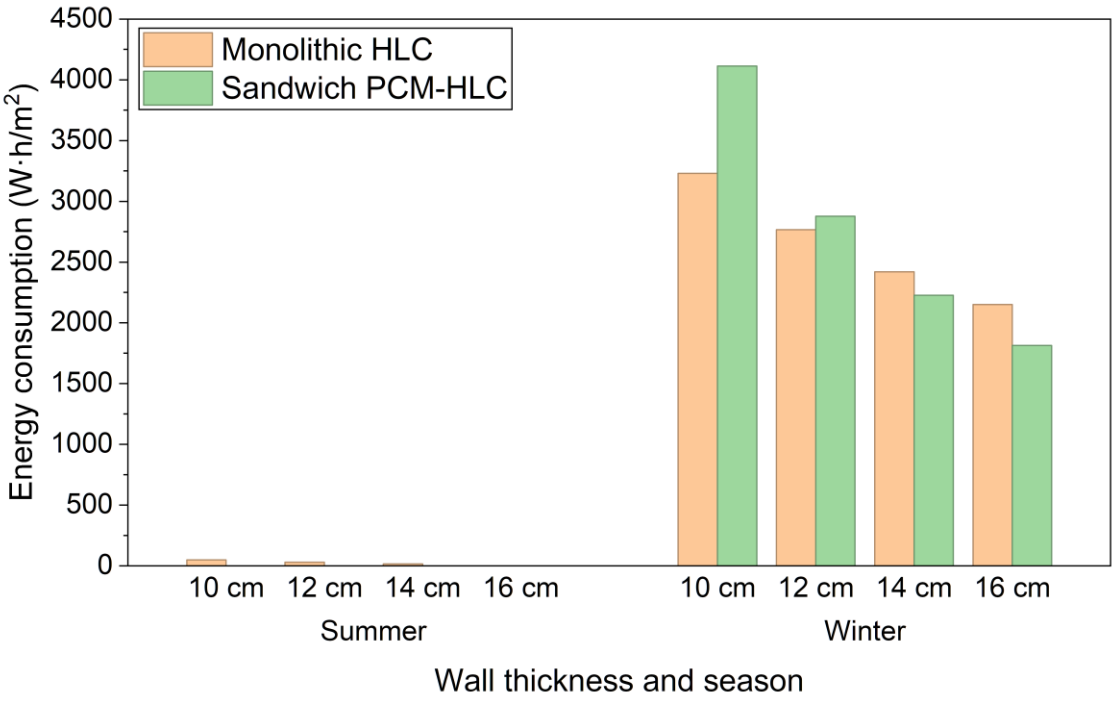


Fig. 7.12. Comparative energy performance of 10–16 cm thickness monolithic HLC and sandwich PCM-HLC in the typical winter week.

The observation was nonlinear. At 10 and 12 cm, the sandwich configuration consumed 27% and 4% more heating energy than the monolithic HLC of the same thickness. At these smaller thicknesses, the latent storage benefit did not compensate for the reduced volume of steady thermal resistance.

As thickness increased, both wall types produced higher interior surface temperatures and lower energy demand. The key transition occurred at 14 cm, where the sandwich assembly first outperformed the monolithic baseline. This identifies 14 cm as the minimum tested thickness at which the double-PCM sandwich design became beneficial for winter performance.

At 16 cm, the sandwich PCM-HLC provided the strongest thermal response within this set. It reduced energy use by 15% relative to the 16 cm monolithic HLC and by 44% relative to the 10 cm monolithic HLC. The engineering implication is that a

double-PCM sandwich can be effective in cold climates only when the PCM is sufficiently protected by surrounding insulation.

One physical interpretation is thermal decoupling. At 10-12 cm, the exterior gradient likely keeps the PCM-rich regions outside their useful phase-change range for much of the winter week. At 14-16 cm, the added outer insulation reduces this exposure and may allow the PCM layers to contribute more effectively to thermal lag. This interpretation is based on the simulated temperature response and should be confirmed with future phase-fraction tracking.

Table 7.5 summarises energy consumption relative to the 10 cm monolithic HLC panel and reports energy saving per unit thickness. This metric was used to compare thermal benefit with wall-depth penalty.

Table 7.5. Energy savings and calculated efficiency per unit thickness for various thicknesses of sandwich PCM-HLC wall.

Total thickness (cm)	Δ Energy relative to monolithic HLC ($W \cdot h/m^2$)	Δ Energy per unit thickness ($(W \cdot h/m^2)/cm$)
10	+ 883	+ 88
12	+ 110	+ 9
14	- 195	- 14
16	- 337	- 21

The thickness sensitivity study identifies two useful design thresholds. The 12 cm case nearly removed the winter penalty but did not fully outperform the monolithic baseline. The 14 cm case crossed from penalty to benefit, with an energy-saving intensity of -14 $(W \cdot h/m^2)/cm$. Increasing to 16 cm improved the saving intensity to -21 $(W \cdot h/m^2)/cm$.

Although 16 cm produced the highest tested saving per unit thickness, wall depth and material use may limit its practicality. The 14 cm design should therefore be interpreted as the minimum viable double-PCM thickness for the modelled Ottawa winter, while 16 cm represents the stronger thermal option within the tested range.

This result provides a design rule rather than a universal optimum: for the selected material properties and Ottawa weather file, the double-PCM sandwich required at least 14 cm total thickness to outperform monolithic HLC during winter.

7.5. Sensitivity study: middle-layer thermal resistance

7.5.1. Air-cavity strategy

The thickness study showed that the double-PCM sandwich needed at least 14 cm to outperform monolithic HLC. Because retrofit applications often have stricter wall-depth limits, the next sensitivity study examined whether the required thickness could be reduced by increasing thermal resistance within the existing profile.

The tested strategy replaced the solid middle insulation layer with an unventilated air gap while keeping the other layers unchanged. The criterion was whether the added thermal break could maintain the summer cooling benefit while reducing or reversing the winter heating penalty.

7.5.2. Results and discussion

7.5.2.1. 10 cm thickness

For the 10 cm sandwich panel, the air-cavity variant was used to test whether a thermal break could mitigate the winter penalty identified in the solid-core design. Fig. 7.13 compares the monolithic HLC, the original 10 cm double-PCM sandwich, and the 10 cm air-core sandwich under the same summer and winter weeks.

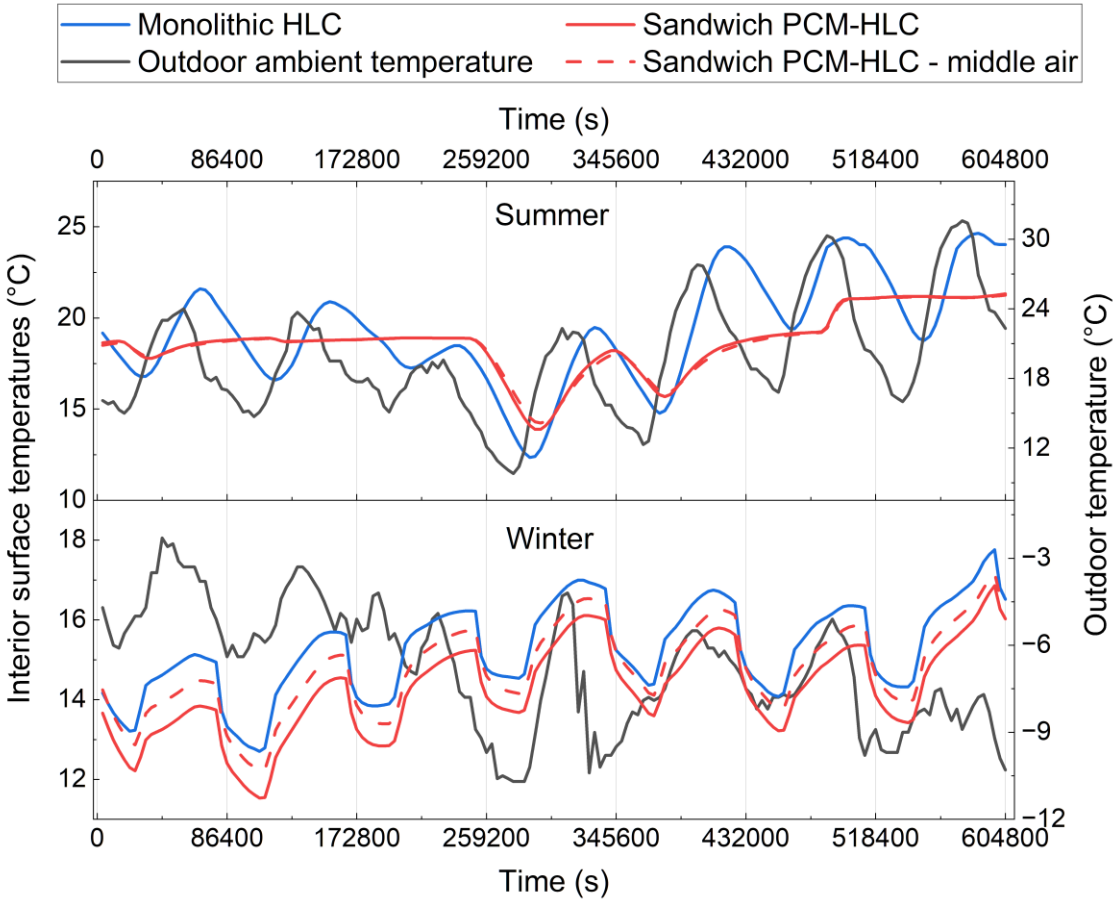


Fig. 7.13. Comparative analysis of a 10 cm thickness air-core sandwich PCM-HLC design against the original sandwich PCM-HLC and a monolithic control under typical summer and winter weeks.

In summer, both sandwich configurations dampened interior surface-temperature fluctuations more than the 10 cm monolithic HLC. The air cavity did not substantially change the summer response, indicating that the PCM layers rather than the middle-layer resistance controlled the cooling-season benefit.

In winter, the monolithic HLC maintained the highest interior surface temperature among the 10 cm cases. The original double-PCM sandwich remained the weakest configuration, while the air-core sandwich improved the surface temperature relative to the solid-core sandwich.

The physical explanation is that the air gap increased static thermal resistance and reduced the conductive path through the middle of the assembly. This improvement was not large enough to overcome the limited total thickness, but it reduced the penalty associated with the thin double-PCM layout.

The engineering implication is that adding a thermal break is useful but insufficient at 10 cm for this double-PCM geometry. In severe winter conditions, wall depth and exterior insulation remain controlling constraints.

The comparative energy performance for the 10 cm wall configurations during typical summer and winter weeks is summarized in Fig. 7.14. These figures quantify the total heating and cooling demand required to maintain indoor thermal comfort.

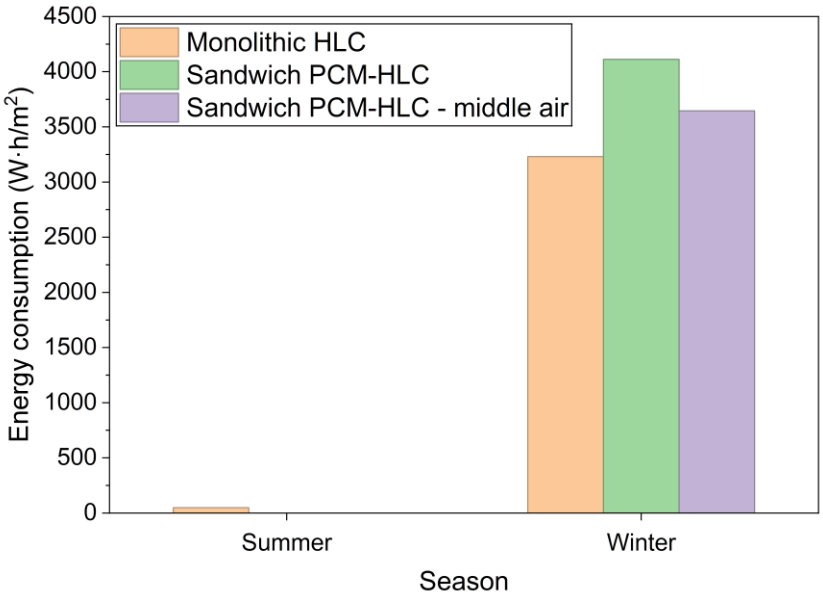


Fig. 7.14. Comparative energy performance of 10 cm thickness monolithic HLC, sandwich PCM-HLC, and air-core sandwich PCM-HLC in the typical summer and winter week.

For the 10 cm configurations, both sandwich variants avoided cooling demand during the selected summer week, while the monolithic HLC required 49 W·h/m². This again reflects the modelled typical-week conditions rather than a general claim of zero cooling demand.

In winter, the air cavity reduced the heating demand of the double-PCM sandwich from 4113 to 3645 W·h/m². This reduced the winter penalty relative to monolithic HLC from 27% to 13%. The result supports the thermal-break concept, but it also shows that the 10 cm double-PCM design still underperforms the monolithic baseline.

7.5.2.2. 12 cm thickness

The dynamic thermal response of the 12 cm wall configurations under representative summer and winter conditions is illustrated in Fig. 7.15.

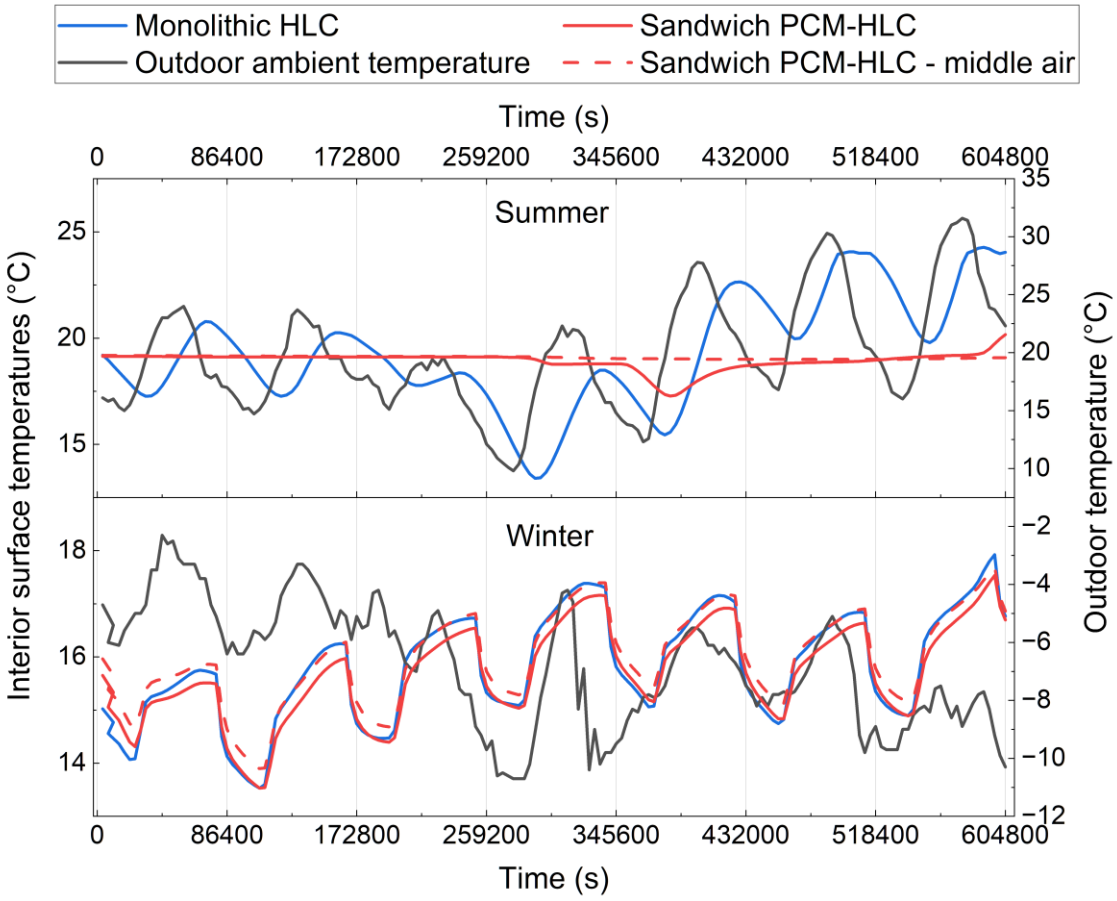


Fig. 7.15. Comparative analysis of a 12 cm thickness air-core sandwich PCM-HLC design against original sandwich PCM-HLC and a monolithic control under representative summer conditions.

For the 12 cm cases, both sandwich configurations dampened summer temperature fluctuations relative to monolithic HLC. The air-core design showed the most stable interior surface temperature, suggesting that the added thermal break improved transient control without increasing total thickness beyond 12 cm.

In winter, the 12 cm air-core sandwich nearly overlapped the monolithic HLC temperature response and outperformed the original solid-core sandwich. This observation indicates that increasing the middle-layer resistance becomes more effective once the total wall depth is slightly increased.

This thermal stability directly translates into the energy reductions summarized in Fig. 7.16.

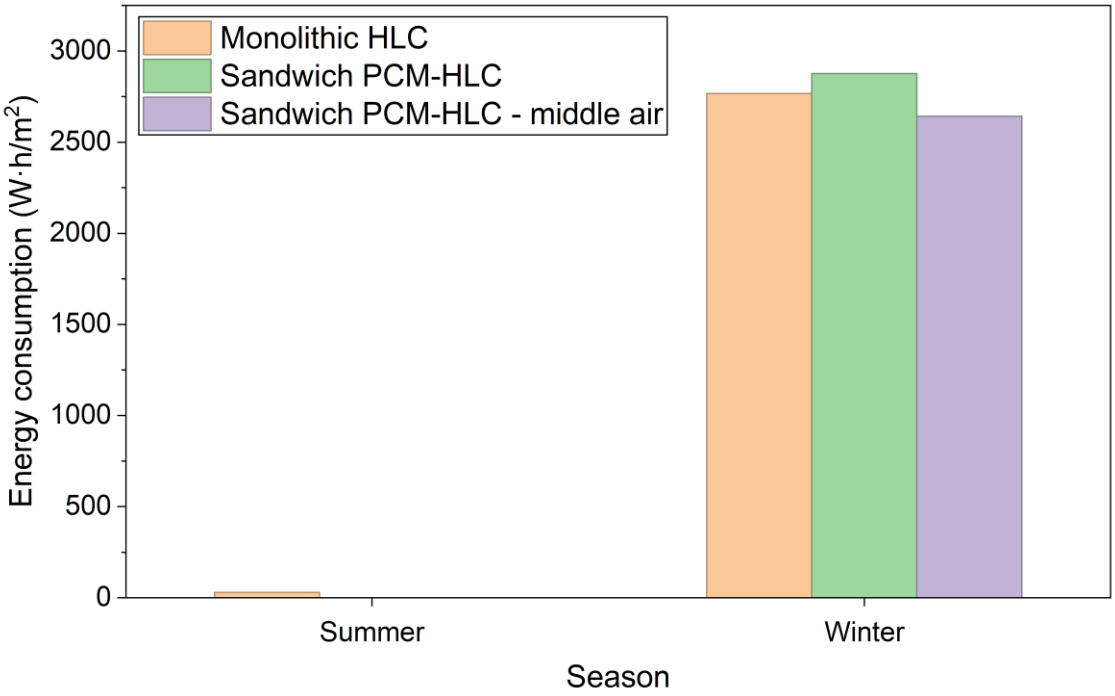


Fig. 7.16. Comparative energy performance of 12 cm thickness monolithic HLC, sandwich PCM-HLC, and air-core sandwich PCM-HLC under typical summer and winter weeks.

During the selected summer week, the 12 cm monolithic HLC required 30 W·h/m² of cooling energy, while both sandwich designs avoided cooling demand under the model assumptions.

During winter, the 12 cm air-core sandwich had the lowest heating demand, 2643 W·h/m², compared with 2767 W·h/m² for monolithic HLC and 2877 W·h/m² for the solid-core sandwich. This corresponds to a 4% saving relative to the monolithic baseline.

The 12 cm air-core case is therefore the minimum tested air-core configuration that improved both summer and winter performance relative to monolithic HLC. The result suggests that a thermal break can partly substitute for added thickness, but only when the remaining layers still provide enough resistance to protect the PCM.

7.6. Sensitivity study: PCM phase-change temperature

7.6.1. Phase-change-temperature strategy

The previous studies showed that resistance and layer placement control whether PCM can operate within a useful temperature range. This section therefore treats phase-change temperature as a sensitivity variable for the 12 cm air-core design. The aim was to test whether shifting the PCM transition range could improve energy performance without changing wall thickness.

The tested transition range was 15-20 °C, selected from practical cold climate temperature, thermal-comfort considerations and feasible fatty-acid formulations [110, 269]. The 12 cm air-core geometry was held constant so that differences in performance could be attributed mainly to phase-change-temperature selection.

A spatial-gradient strategy was evaluated by assigning a higher transition range to the indoor PCM layer and a lower transition range to the outdoor PCM layer. As shown in

Table 7.6, four different PCM phase transition temperature configurations were compared against the control of Monolithic HLC sample as a sensible heat baseline.

Table 7.6. PCM phase transition temperature ranges used for gradient sandwich panel simulations.

Configuration	Indoor PCM layer T_m and T_s range (°C)	Outdoor PCM layer T_m and T_s range (°C)
Original	21.05–22.82	18.79–19.56
Gradient 1	17–18	15–16
Gradient 2	18–19	16–17
Gradient 3	19–20	17–18

This design logic assumes that matching phase-change temperature to the thermal gradient can increase the time that each PCM layer spends near its transition range. The assumption was evaluated through the simulated surface temperature and energy demand, rather than treated as an established mechanism.

7.6.2. Results and discussion

To evaluate the effect of phase-change-temperature selection, the transient interior surface temperatures under representative summer (top) and winter (bottom) weather conditions in Ottawa were plotted in Fig. 7.17.

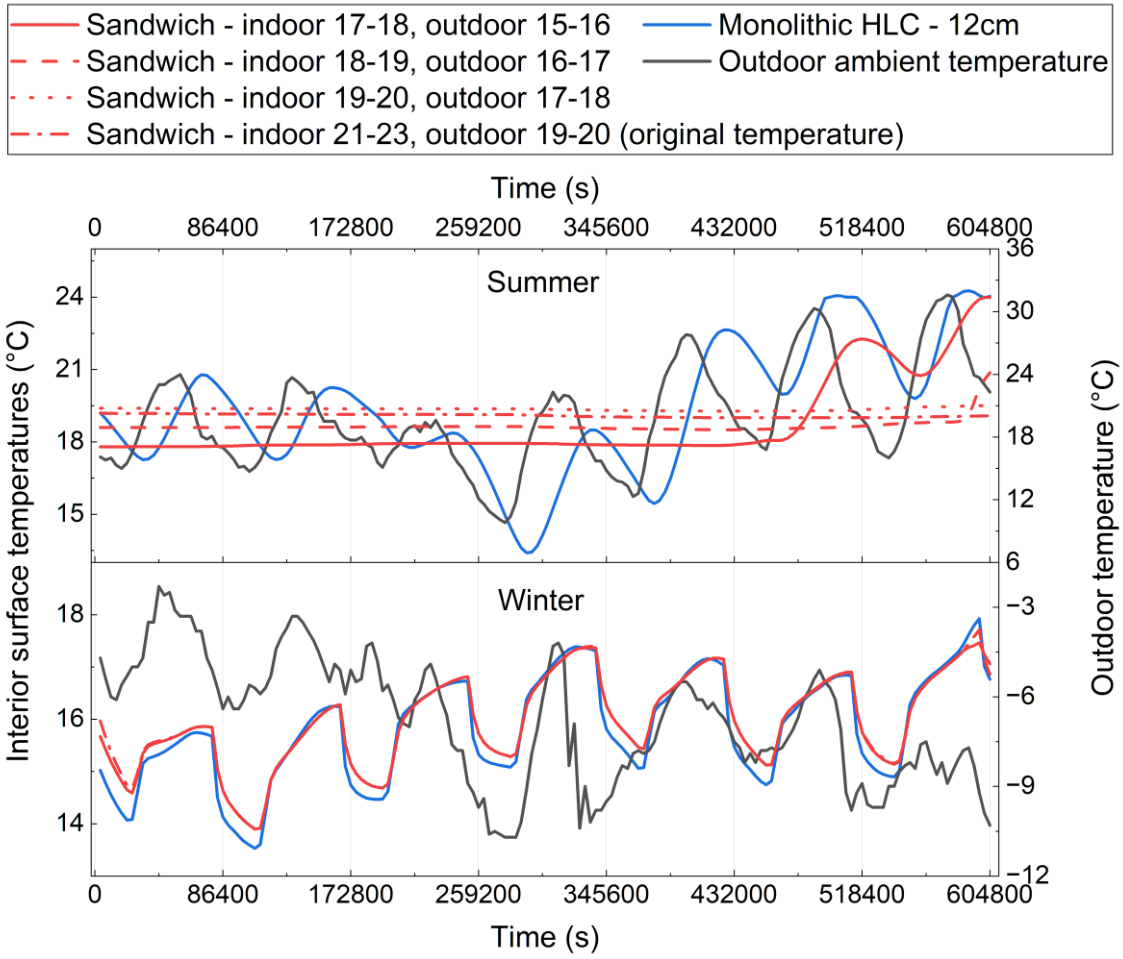


Fig. 7.17. Comparative dynamic thermal response of a 12 cm monolithic HLC baseline and 12 cm air – core sandwich PCM-HLC configurations utilizing spatial phase – change temperature gradients under representative summer and winter conditions.

In summer, phase-change temperature affected transient temperature stability. The original-temperature design and Gradient 3 kept the interior surface temperature nearly flat during the hottest part of the week. Gradients 1 and 2 delayed and reduced

temperature rise initially, but their profiles began to approach the monolithic trend near the end of the week.

A plausible explanation is that lower transition ranges caused the PCM to complete melting earlier during hot periods, leaving less latent capacity later in the cycle. This interpretation is consistent with the simulated temperature profiles, although direct melt-fraction tracking was not included.

In winter, all phase-change-temperature gradients produced similar interior surface temperatures, and the sandwich panels remained close to the 12 cm monolithic HLC baseline.

This convergence suggests that, under the selected winter week, static thermal resistance controlled performance more strongly than phase-change temperature. The PCM layers may have remained largely outside their active range for much of the period, so changing the transition temperature within 15-20 °C had limited effect.

Fig. 7.18 summarises the energy consequence of this sensitivity study. It compares the monolithic baseline with the original and gradient PCM-temperature configurations for the 12 cm air-core sandwich.

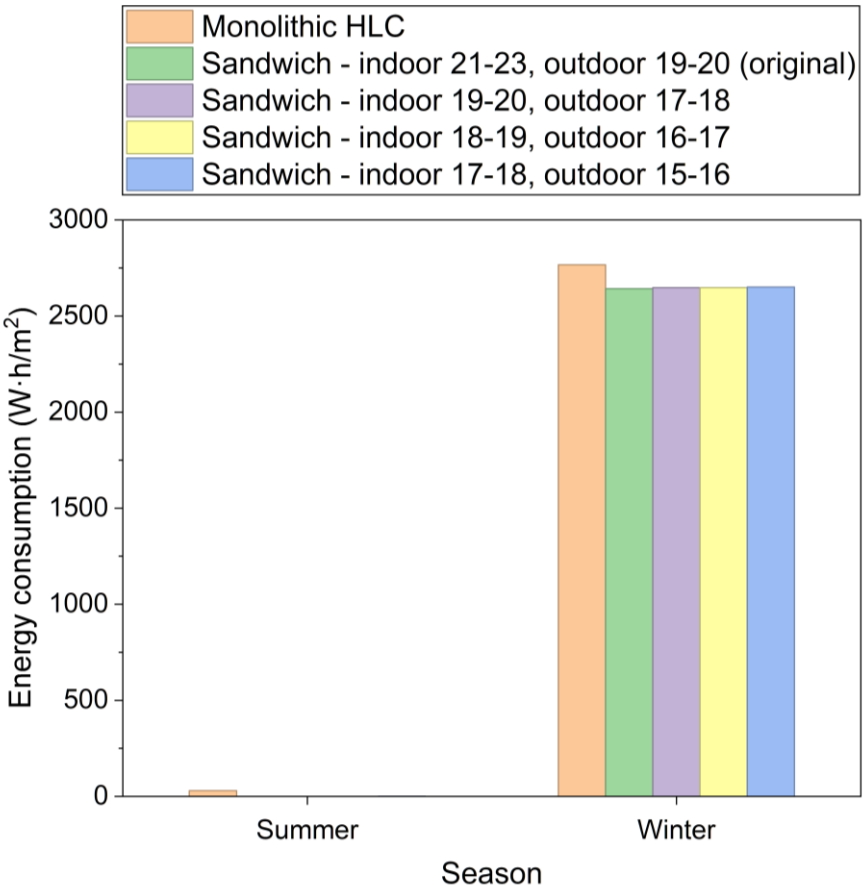


Fig. 7.18. Comparative energy performance of 12 cm thickness monolithic HLC and air-core sandwich PCM-HLC across different phase change temperatures.

All 12 cm air-core sandwich designs used less energy than the monolithic baseline under the modelled weeks. However, changing the PCM phase-change temperature altered total energy demand by only about 0.3% under the current HVAC control strategy. The engineering implication is that phase-change tuning can refine summer temperature stability, but it is secondary to geometry and insulation for annual energy reduction in this cold-climate case.

7.7. Sensitivity study: single-PCM-layer configuration

The preceding results indicate that an exterior PCM layer can become ineffective in a thin cold-climate wall if it remains below its transition range. The final sensitivity

study therefore reallocated the 10 cm profile by removing the exterior PCM layer and increasing exterior HLC insulation. The objective was to test whether a single indoor PCM layer could preserve summer buffering while improving winter resistance.

The exterior PCM layer was replaced with HLC insulation, while the indoor PCM layer retained the original transition temperature. Two middle-layer options were then compared: solid HLC insulation and an air cavity (Fig. 7.19).

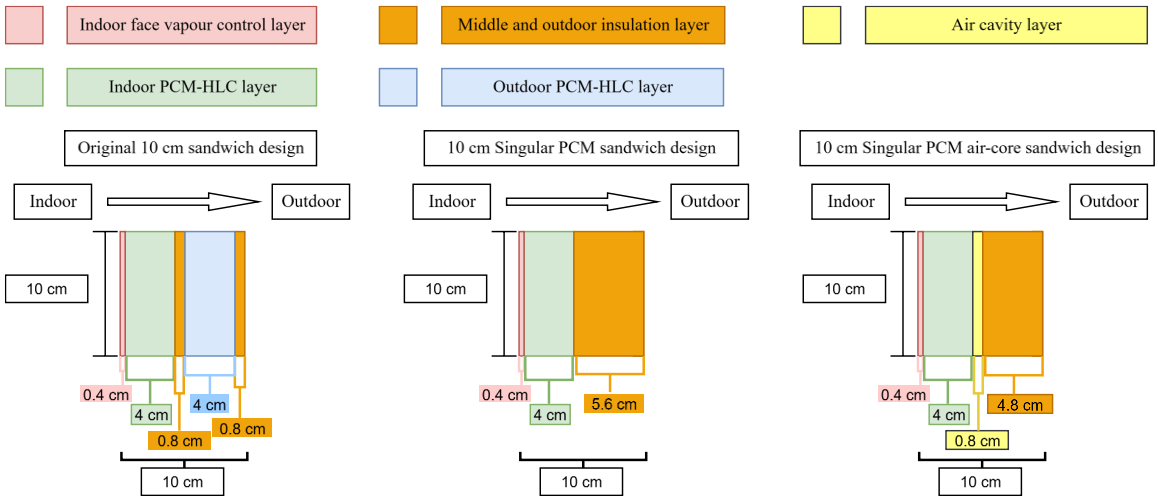


Fig. 7.19. Schematic illustration of singular PCM sandwich design.

This configuration tests a simpler division of function: exterior layers provide static resistance, and the indoor PCM layer provides latent storage near the conditioned zone.

- Winter criterion: replacing the exterior PCM layer with HLC increases exterior thermal resistance and reduces the risk that dense PCM behaves only as a conductive sensible mass during sub-zero periods.
- Summer criterion: retaining the indoor PCM layer preserves latent buffering near the indoor surface, where it can respond to residual heat gains after the exterior insulation has dampened the outdoor thermal wave.

The singular-PCM strategy therefore prioritises spatial efficiency. It does not assume that less PCM is always better; rather, it tests whether PCM placement is more important than PCM quantity in a thin wall.

7.7.1. Results and discussion

The dynamic thermal response was evaluated under both summer and winter conditions, as shown in Fig. 7.20, to assess the effect of the single-PCM sensitivity strategy.

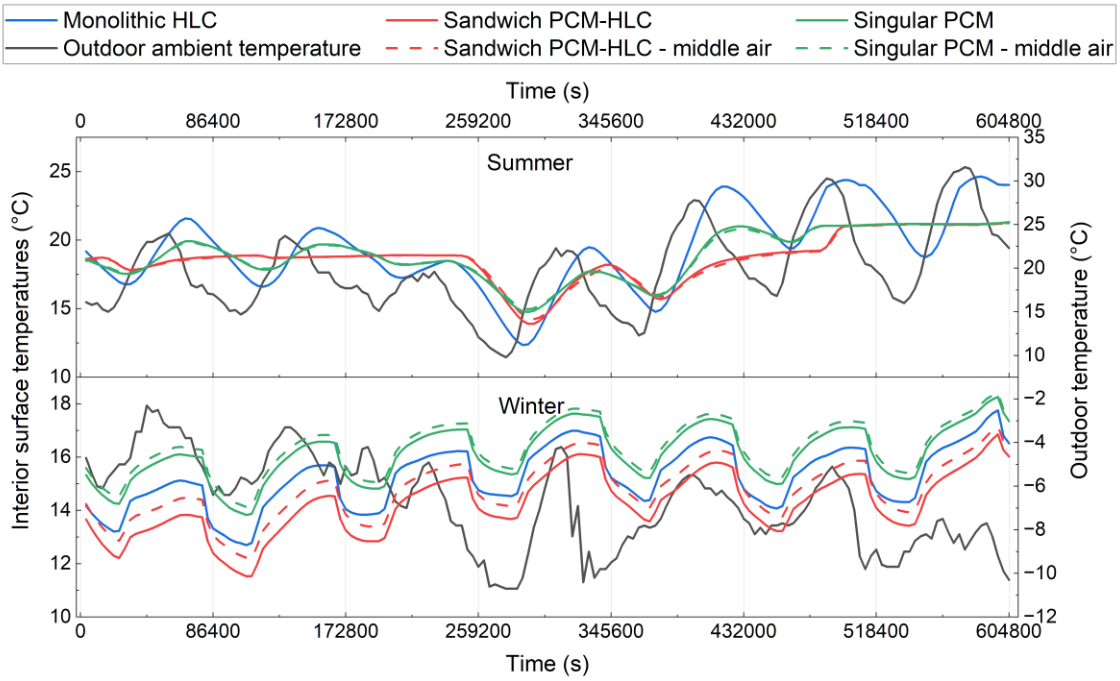


Fig. 7.20. Dynamic thermal response of the 10 cm building envelope configurations showing interior surface temperature profiles under typical summer and winter weeks.

In summer, all PCM-integrated configurations dampened exterior temperature fluctuations relative to monolithic HLC. The original double-PCM design produced the lowest interior surface temperatures, while the singular-PCM designs stabilised closer to 21 °C. The singular configurations warmed faster near the end of the hot week, which is consistent with their lower total PCM volume.

In winter, the single-PCM configurations outperformed the original double-PCM sandwich. The best response occurred when the single indoor PCM layer was combined with a middle air cavity. This observation supports the interpretation that, in thin cold-climate walls, exterior resistance can be more valuable than an additional exterior PCM layer.

The energy-demand comparison in Fig. 7.21 quantifies the engineering consequence of the transient temperature responses.

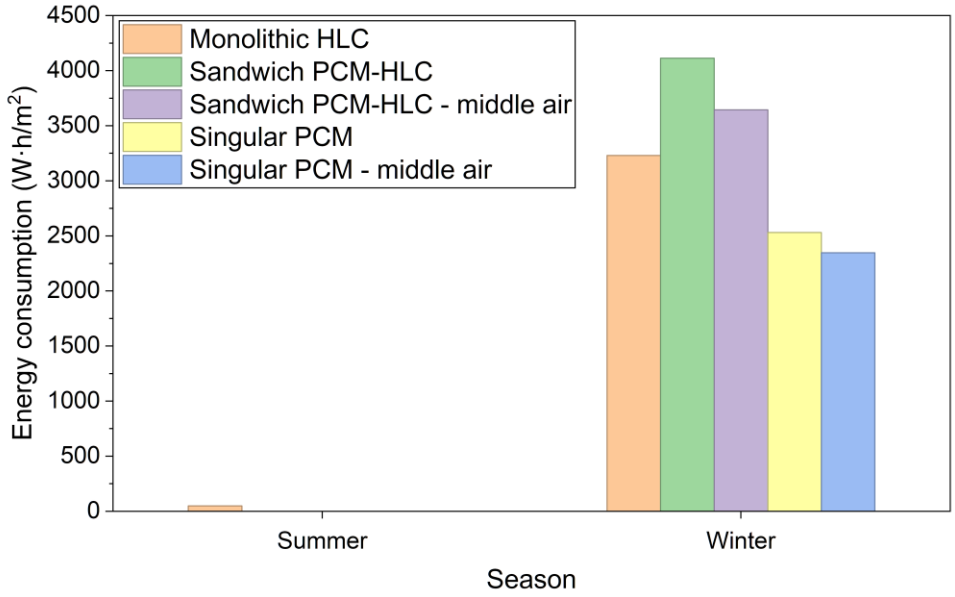


Fig. 7.21. Comparative seasonal heating and cooling energy consumption across monolithic, original double PCM layer sandwich, and optimised singular PCM sandwich design building envelope configurations.

During the selected summer week, all PCM configurations avoided cooling demand under the model assumptions. The energy-load difference between double- and single-PCM layouts was therefore negligible for this weather period, even though their temperature profiles differed.

Winter heating demand separated the designs more clearly. The monolithic HLC required 3230 W·h/m², the original double-PCM sandwich required 4113 W·h/m², and

the double-PCM air-core version required 3645 W·h/m². These results show that a thermal break helps, but it does not fully compensate for less favourable PCM placement in a 10 cm profile.

The singular-PCM strategy reduced winter demand to 2531 W·h/m², and the singular-PCM middle-air design reduced it further to approximately 2347 W·h/m². This is about 27% lower than the monolithic HLC baseline and about 43% lower than the original double-PCM sandwich.

The implication is that the best 10 cm cold-climate design was not the design with the most PCM. It was the design that placed PCM near the conditioned side and protected it with sufficient exterior resistance. This finding is central to transferring the method to other climates and wall-depth constraints.

7.8. Summary

This chapter develops and evaluates a multilayer PCM-HLC sandwich envelope using an experimentally validated finite-volume model. The central scientific problem is how to place PCM within a bio-based wall so that it acts as useful latent storage rather than as an unintended heat-loss pathway. The contribution is therefore a design methodology, not a single wall geometry.

Model validation showed good agreement with the 10 cm experimental sandwich block, with an approximate MAE of 0.2 °C and a maximum percentage difference of about 3%. SEM observations qualitatively supported the intended contrast between dense PCM-HLC, porous insulation, and compact lime-plaster layers. These observations support the modelling assumptions but do not independently prove the heat- or moisture-transfer mechanisms.

- The baseline comparison established the main scientific constraint: PCM improves summer thermal buffering, but a thin double-PCM wall can

increase winter heating demand if the PCM is not protected by enough insulation. This finding explains why PCM content alone is not a reliable design criterion for cold-climate envelopes.

- The thickness sensitivity study showed that the double-PCM sandwich required at least 14 cm total thickness to outperform monolithic HLC in the modelled Ottawa winter. The 16 cm case provided the strongest performance within the tested thickness range, but the 14 cm result defines the minimum viable tested thickness for this double-PCM configuration.
- The air-cavity and single-PCM sensitivity studies show how the method can guide thinner retrofit-oriented designs. For a 12 cm wall, the air-core double-PCM design produced modest winter savings. For a 10 cm wall, reallocating the exterior PCM volume to insulation and retaining a single indoor PCM layer with a middle air cavity produced the lowest winter demand among the tested configurations.
- The broader significance is that PCM-integrated bio-based envelopes should be designed by climate-specific parametric assessment. In cooling-dominated climates, PCM transition temperature and latent storage capacity may be the primary variables as they have the greatest influence on maintaining stable indoor temperature and reducing cooling load. In heating-dominated applications, especially on the exterior layer of the building envelope, thermal resistance is the most influential factor and should be considered as prioritywhile PCM placement, and wall-depth of the entire building envelope also matters. This framework can therefore guide both researchers and practitioners by showing which design variables should be tested before selecting a PCM-HLC wall configuration.

8. Chapter 8: Conclusions, limitations, and future recommendations

8.1. General conclusions

This thesis advances the understanding of PCM-HLC by linking material design, composite behaviour, and PCM-HLC performance as a building envelope within one research framework. The central finding is that PCM-HLC cannot be designed by maximizing PCM content alone. Its performance depends on the coupled effects of hemp shiv geometry, binder continuity, PCM loading, specimen geometry, moisture response, and layer placement.

At the material scale, the work showed that reducing hemp shiv particle size and increasing binder content can increase PCM uptake and improve the practicality of high-PCM formulations. The 70% substitution level represents a demonstrated upper range for the materials and preparation method used in this thesis, rather than a universal limit for all hemp-lime systems. The SCM-modified binders further showed that matrix design is central to maintaining cohesion when fatty-acid PCM is introduced at high loading.

The test results of PCM-HLC incorporated with different amount of PCM proved that the mechanical, thermal, and hygric behaviour of PCM-HLC is coupled. Increasing PCM content improved latent heat storage but also changed density, moisture buffering, and strength-related behaviour. The casting-direction and specimen-size studies further indicate that anisotropy and scale effects remain important, even when smaller shiv particles reduce directional variation.

Simulating PCM-HLC as the core of a novel sandwich panel design shows that PCM-HLC can be more effective when used as part of a multilayer system rather than as a monolithic wall material. Under the selected Ottawa weather, the single-PCM sandwich with a middle air cavity reduced winter heating demand relative to the monolithic HLC baseline and the original double-PCM sandwich. This finding supports a climate-specific design principle: PCM layers should be placed where they can be thermally activated while remaining protected from excessive heat loss.

8.2. Research contributions

The completed research contributes new scientific knowledge in four main areas. These contributions concern the behaviour and design logic of PCM-HLC, rather than only the experimental procedures used to generate the data.

- Material characterization for high-PCM-HLC design

The thesis shows that hemp shiv particle size and binder content strongly influence the feasible PCM loading range. Small ground shiv enabled high PCM substitution in the tested system, while SCM selection affected matrix cohesion and the suitability of the composite for layered-envelope applications. This provides a material-design basis for selecting aggregate size and binder composition when latent heat storage is the target function.

- Evidence on anisotropy, specimen size, and measurement comparability

The casting-direction and specimen-size results provide evidence that PCM-HLC properties remain sensitive to sample geometry and orientation. Reduced shiv size can limit directional variation, but it does not remove the need for consistent specimen preparation and reporting. This contribution is important because PCM-HLC data from different studies can otherwise be difficult to compare.

- Performance trade-off map for PCM substitution

The substitution study established that PCM content produces competing benefits and penalties. Higher PCM loading increased thermal storage potential, whereas moisture buffering and some mechanical indicators became less favourable. The resulting trade-off map supports material selection by function, with moderate substitution more suitable for balanced hygrothermal performance and higher substitution more suitable when thermal storage is the primary goal.

- Parametric design framework for multilayer PCM-HLC envelopes

The sandwich-wall study contributes a design framework for using PCM-HLC in space-constrained building envelopes. The simulations indicate that PCM placement, exterior thermal resistance, and phase-change temperature can be more important than PCM volume alone. The proposed single-PCM air-cavity configuration should therefore be interpreted as the best option among the tested cases and assumptions, not as a universally optimal wall design.

8.3. Limitations and future work

The conclusions above should be interpreted within the boundaries of the study. The thesis combines laboratory testing with numerical modelling, and each method introduces assumptions that affect how broadly the findings can be transferred.

The material results are based on selected hemp shiv sources, particle-size preparation routes, binder compositions, and fatty-acid PCM mixtures. Natural variability in hemp shiv morphology, absorptivity, and chemical composition may change PCM uptake, compaction response, and long-term moisture behaviour. The reported design trends are therefore most reliable for materials similar to those tested here.

The numerical envelope analysis was validated against laboratory-scale sandwich specimens and then extended through simplified boundary conditions. This approach is appropriate for comparing design variables, but it does not capture all full-scale effects, including workmanship, multidimensional thermal bridges, wind-driven rain, air leakage, occupant behaviour, and long-term material ageing.

The thesis also did not directly assess fire behaviour, biological degradation, fatty-acid leakage over extended service periods, freeze-thaw durability, or full life-cycle impacts. These could be addressed in the future for broad building-code adoption or commercial deployment.

Future work should therefore be prioritized around the uncertainties that most strongly affect interpretation and implementation.

- First, full-scale envelope testing should be carried out under realistic weather exposure. There might be discrepancies between laboratory-scale characterization and full-scale wall deployment due to different boundary conditions and macro-scale hygrothermal behavior constraints, that must be accounted for in future envelope validations. While laboratory testing establishes a vital baseline, the simplified boundary conditions inherently fail to capture the complicated nature of real-world environments. In the laboratory, specimens are exposed to controlled, idealized one-dimensional temperature gradients. Real-world full-scale envelopes, conversely, are subjected to dynamic, multi-directional weather exposures, such as wind-driven rain, solar radiation, and fluctuating ambient relative humidity, which alter the driving forces behind heat and moisture transfer. These complex boundary conditions will possibly result in different hygrothermal behaviour than in the lab. In a standard laboratory heat flow meter or guarded hot box setup, moisture transport is typically restricted or evaluated under static conditions. In a complete wall assembly, however, heat and moisture transport are coupled, multi-directional phenomena. Because hemp shiv is a natural material characterized by inherent structural variability, its local morphology and absorptivity dictate how it responds to macro-scale moisture accumulation and bulk air leakage. Elevated moisture levels within a full-scale wall might reduce the material's bulk thermal insulation performance. This coupled behavior will impact immediate thermal performance.
- Second, the numerical framework should be expanded across climates, wall-depth constraints, setpoint schedules, and PCM transition ranges. This would test whether the design rules identified for Ottawa remain valid in cooling-dominated, mixed, and more severe heating climates.

- Third, safety, life-cycle, and manufacturing studies should be conducted. Fire resistance, biological durability, embodied carbon, end-of-life options, cost-benefit, and prefabrication methods would be indicative to practical adoption. Real world scenario might introduce long-term durability risks, such as accelerated biological degradation, freeze-thaw damage, and potentially altered fatty-acid thermal behaviours over extended service periods that small specimens may not simulate. A cost-benefit may also be done to better assess PCM-HLC's long term economic trade-offs.

Finally, laboratory-scale testing operates under the assumption of material continuity and homogeneous layer interfaces, neglecting the critical physical and structural realities of on-site construction. Full-scale wall systems inevitably introduce workmanship variations, material settling, structural framing members, and multi-dimensional thermal bridges. These structural discontinuities disrupt uniform heat flow, creating localized microclimates and internal air gaps within the wall. These gaps can trigger micro-convective loops and localized thermal stress, further deviating from the idealized thermal resistance values measured in the lab. Consequently, future work must prioritize full-scale environmental chamber or field testing alongside expanded numerical frameworks across diverse climatic zones. Moving beyond the Ottawa baseline to cooling-dominated and severe heating climates will test the limits of these structural and hygrothermal interactions, ensuring the material rules remain valid under the physical realities of commercial deployment and building-code compliance.

Overall, this thesis shows that PCM-HLC, as an insulating bio-composite with added latent heat capacity, has the potential to be integrated into a building envelope whose performance depends on how PCM, hemp shiv, binder, moisture transport, and layer geometry interact. By defining these interactions more clearly, the work provides a foundation for future low-carbon building envelopes that combine renewable materials with passive thermal-energy management.

References

1. Power to heat and cooling: Status, https://www.irena.org/Innovation-landscape-for-smart-electrification/Power-to-heat-and-cooling/Status, last accessed 2024/02/12.

2. Guarnieri, G., Olivieri, B., Senna, G., Vianello, A.: Relative Humidity and Its Impact on the Immune System and Infections. Int J Mol Sci. 24, 9456 (2023). https://doi.org/10.3390/ijms24119456.

3. Zhang, Y., Ding, J., Wang, X., Yang, R., Lin, K.: Influence of additives on thermal conductivity of shape-stabilized phase change material. Solar Energy Materials and Solar Cells. 90, 1692–1702 (2006). https://doi.org/10.1016/j.solmat.2005.09.007.

4. Karaipekli, A., Sarı, A., Biçer, A.: Thermal regulating performance of gypsum/(C18–C24) composite phase change material (CPCM) for building energy storage applications. Applied Thermal Engineering. 107, 55–62 (2016). https://doi.org/10.1016/j.applthermaleng.2016.06.160.

5. Cabeza, L.F., Castell, A., Barreneche, C., de Gracia, A., Fernández, A.I.: Materials used as PCM in thermal energy storage in buildings: A review. Renewable and Sustainable Energy Reviews. 15, 1675–1695 (2011). https://doi.org/10.1016/j.rser.2010.11.018.

6. Joulin, A., Zalewski, L., Lassue, S., Naji, H.: Experimental investigation of thermal characteristics of a mortar with or without a micro-encapsulated phase change material. Applied Thermal Engineering. 66, 171–180 (2014). https://doi.org/10.1016/j.applthermaleng.2014.01.027.

7. Niyigena, C., Amziane, S., Chateauneuf, A.: Multicriteria analysis demonstrating the impact of shiv on the properties of hemp concrete. Construction and Building Materials. 160, 211–222 (2018). https://doi.org/10.1016/j.conbuildmat.2017.11.026.

8. Zampori, L., Dotelli, G., Vernelli, V.: Life Cycle Assessment of Hemp Cultivation and Use of Hemp-Based Thermal Insulator Materials in Buildings. Environ. Sci. Technol. 47, 7413–7420 (2013). https://doi.org/10.1021/es401326a.

9. Barbhuiya, S., Bhusan Das, B.: A comprehensive review on the use of hemp in concrete. Construction and Building Materials. 341, 127857 (2022). https://doi.org/10.1016/j.conbuildmat.2022.127857.

10. Tikhonov, A.N., AASamarskii: Equations of Mathematical Physics, Dover Publications, Inc (1963).

11. Abdellatef, Y., Khan, M.A., Khan, A., Alam, M.I., Kavgic, M.: Mechanical, Thermal, and Moisture Buffering Properties of Novel Insulating Hemp-Lime Composite Building Materials. Materials. 13, 5000 (2020). https://doi.org/10.3390/ma13215000.

12. Zhang, W., Zhang, X., Zhang, X., Yin, Z., Liu, Y., Fang, M., Wu, X., Min, X., Huang, Z.: Lauric-stearic acid eutectic mixture/carbonized biomass waste corn cob composite phase change materials: Preparation and thermal characterization. Thermochimica Acta. 674, 21–27 (2019). https://doi.org/10.1016/j.tca.2019.01.022.

13. Sawadogo, M., Godin, A., Duquesne, M., Lacroix, E., Veillère, A., Hamami, A.E.A., Belarbi, R.: Investigation of eco-friendly and economic shape-stabilized composites for building walls and thermal comfort. Building and Environment. 231, 110026 (2023). https://doi.org/10.1016/j.buildenv.2023.110026.

14. Ma, L., Wang, Q., Li, L.: Delignified wood/capric acid-palmitic acid mixture stable-form phase change material for thermal storage. Solar Energy Materials and Solar Cells. 194, 215–221 (2019). https://doi.org/10.1016/j.solmat.2019.02.026.

15. Wen, R., Liu, Y., Yang, C., Zhu, X., Huang, Z., Zhang, X., Gao, W.: Enhanced thermal properties of stearic acid/carbonized maize straw composite phase change material for thermal energy storage in buildings. Journal of Energy Storage. 36, 102420 (2021). https://doi.org/10.1016/j.est.2021.102420.

16. Arnaud, L., Gourlay, E.: Experimental study of parameters influencing mechanical properties of hemp concretes. Construction and Building Materials. 28, 50–56 (2012). https://doi.org/10.1016/j.conbuildmat.2011.07.052.

17. Simoni, M., Wilkes, M.D., Brown, S., Provis, J.L., Kinoshita, H., Hanein, T.: Decarbonising the lime industry: State-of-the-art. Renewable and Sustainable Energy Reviews. 168, 112765 (2022). https://doi.org/10.1016/j.rser.2022.112765.

18. Dinh, T.M., Magniont, C., Coutand, M., Escadeillas, G.: Hemp concrete using innovative pozzolanic binder. Academic Journal of Civil Engineering. 33, 265–270 (2015). https://doi.org/10.26168/icbbm2015.40.

19. Diquélou, Y., Gourlay, E., Arnaud, L., Kurek, B.: Influence of binder characteristics on the setting and hardening of hemp lightweight concrete. Construction and Building Materials. 112, 506–517 (2016). https://doi.org/10.1016/j.conbuildmat.2016.02.138.

20. Sinka, M., Van den Heede, P., De Belie, N., Bajare, D., Sahmenko, G., Korjakins, A.: Comparative life cycle assessment of magnesium binders as an alternative for

hemp concrete. Resources, Conservation and Recycling. 133, 288–299 (2018). https://doi.org/10.1016/j.resconrec.2018.02.024.

21. Kristombu Baduge, S., Mendis, P., San Nicolas, R., Nguyen, K., Hajimohammadi, A.: Performance of lightweight hemp concrete with alkali-activated cenosphere binders exposed to elevated temperature. Construction and Building Materials. 224, 158–172 (2019). https://doi.org/10.1016/j.conbuildmat.2019.07.069.

22. Ataebi, E.: Experimental Investigation of the Impact of Binder Composition and Hemp Hurd Particles on the Mechanical and Hygrothermal Performance of Hempcrete, (2025).

23. Mahmood, O.: Towards Sustainable Construction: Innovations in Hemp-Lime Composite Production for Carbon-Negative Building Materials, http://hdl.handle.net/10393/51387, (2026).

24. Dhakal, U., Berardi, U., Gorgolewski, M., Richman, R.: Hygrothermal performance of hempcrete for Ontario (Canada) buildings. Journal of Cleaner Production. 142, 3655–3664 (2017). https://doi.org/10.1016/j.jclepro.2016.10.102.

25. Global Industrial Hemp Market Size & Share Report, 2023, https://www.grandviewresearch.com/industry-analysis/industrial-hemp-market, last accessed 2023/09/28.

26. Jami, T., Karade, S.R., Singh, L.P.: A review of the properties of hemp concrete for green building applications. Journal of Cleaner Production. 239, 117852 (2019). https://doi.org/10.1016/j.jclepro.2019.117852.

27. Bouloc, P.: Le chanvre industriel: production et utilisations. France Agricole Editions (2006).

28. Hemp's versatility and sustainability offer huge opportunities for developing countries | UNCTAD, https://unctad.org/news/hemps-versatility-and-sustainability-offer-huge-opportunities-developing-countries, last accessed 2023/09/28.

29. Sáez-Pérez, M.P., Brümmer, M., Durán-Suárez, J.A.: A review of the factors affecting the properties and performance of hemp aggregate concretes. Journal of Building Engineering. 31, 101323 (2020). https://doi.org/10.1016/j.jobe.2020.101323.

30. Vo, L.T.T., Navard, P.: Treatments of plant biomass for cementitious building materials – A review. Construction and Building Materials. 121, 161–176 (2016). https://doi.org/10.1016/j.conbuildmat.2016.05.125.

31. Nozahic, V.: Vers une nouvelle démarche de conception des bétons de végétaux lignocellulosiques basée sur la compréhension et l'amélioration de l'interface liant / végétal: application à des granulats de chenevotte et de tige de tournesol associés à un liant ponce / chaux.

32. Parvez, A.M., Lewis, J.D., Afzal, M.T.: Potential of industrial hemp (Cannabis sativa L.) for bioenergy production in Canada: Status, challenges and outlook. Renewable and Sustainable Energy Reviews. 141, 110784 (2021). https://doi.org/10.1016/j.rser.2021.110784.

33. Carus, M., Karst, S., Kauffmann, A., Hobson, J., Bertucelli, S.: The european hemp industry: Cultivation, processing and applications for fibres, shives and seeds. European Industrial Hemp Association, March. 2013, 1–9 (2013).

34. Korjenic, A., Petránek, V., Zach, J., Hroudová, J.: Development and performance evaluation of natural thermal-insulation materials composed of renewable resources. Energy and Buildings. 43, 2518–2523 (2011). https://doi.org/10.1016/j.enbuild.2011.06.012.

35. Diquélou, Y., Gourlay, E., Arnaud, L., Kurek, B.: Impact of hemp shiv on cement setting and hardening: Influence of the extracted components from the aggregates and study of the interfaces with the inorganic matrix. Cement and Concrete Composites. 55, 112–121 (2015). https://doi.org/10.1016/j.cemconcomp.2014.09.004.

36. Burczyk, H., Grabowska, L., Strybe, M., Konczewicz, W.: Effect of Sowing Density and Date of Harvest on Yields of Industrial Hemp. Journal of Natural Fibers. 6, 204–218 (2009). https://doi.org/10.1080/15440470902972588.

37. Jiang, Y., Ansell, M., Jia, X., Hussain, A., Lawrence, M.: Physical characterisation of hemp shiv: Cell wall structure and porosity. (2017).

38. Bourdot, A., Moussa, T., Gacoin, A., Maalouf, C., Vazquez, P., Thomachot-Schneider, C., Bliard, C., Merabtine, A., Lachi, M., Douzane, O., Karaky, H., Polidori, G.: Characterization of a hemp-based agro-material: Influence of starch ratio and hemp shive size on physical, mechanical, and hygrothermal properties. Energy and Buildings. 153, 501–512 (2017). https://doi.org/10.1016/j.enbuild.2017.08.022.

39. Piątkiewicz, W., Narloch, P., Wólczyńska, Z., Mańczak, J.: Effect of Hemp Shive Granulometry on the Thermal Conductivity of Hemp–Lime Composites. Materials. 18, 3458 (2025). https://doi.org/10.3390/ma18153458.

40. Brzyski, P., Gładecki, M., Rumińska, M., Pietrak, K., Kubiś, M., Łapka, P.: Influence of Hemp Shives Size on Hygro-Thermal and Mechanical Properties of a Hemp-Lime Composite. Materials. 13, 5383 (2020). https://doi.org/10.3390/ma13235383.

41. Stevulova, N., Kidalova, L., Junak, J., Cigasova, J., Terpakova, E.: Effect of Hemp Shive Sizes on Mechanical Properties of Lightweight Fibrous Composites. Procedia Engineering. 42, 496–500 (2012). https://doi.org/10.1016/j.proeng.2012.07.441.

42. Stevulova, N., Kidalova, L., Cigasova, J., Junak, J., Sicakova, A., Terpakova, E.: Lightweight Composites Containing Hemp Hurds. Procedia Engineering. 65, 69–74 (2013). https://doi.org/10.1016/j.proeng.2013.09.013.

43. Mahmood, O., Kavgic, M., Noel, M.: Hygrothermal and mechanical characterization of novel hemp-lime composites with enhanced consistency. Construction and Building Materials. 450, 138720 (2024). https://doi.org/10.1016/j.conbuildmat.2024.138720.

44. Nguyen, T.T.: Contribution à l'étude de la formulation et du procédé de fabrication d'éléments de construction en béton de chanvre, (2010).

45. Brzyski, P., Suchorab, Z.: Capillary Uptake Monitoring in Lime-Hemp-Perlite Composite Using the Time Domain Reflectometry Sensing Technique for Moisture Detection in Building Composites. Materials. 13, 1677 (2020). https://doi.org/10.3390/ma13071677.

46. Jiang, Y., Lawrence, M., Hussain, A., Ansell, M., Walker, P.: Comparative moisture and heat sorption properties of fibre and shiv derived from hemp and flax. Cellulose. 26, 823–843 (2019). https://doi.org/10.1007/s10570-018-2145-0.

47. Brzyski, P., Jóźwiak, M., Siwiec, J., Sinka, M., Trnik, A.: Influence of the shives orientation on selected hygro-thermal properties of hemp-magnesium composite. J. Phys.: Conf. Ser. 2423, 012007 (2023). https://doi.org/10.1088/1742-6596/2423/1/012007.

48. Zvirgzds, K., Kirilovs, E., Kukle, S., Gross, U.: Production of Particleboard Using Various Particle Size Hemp Shives as Filler. Materials. 15, 886 (2022). https://doi.org/10.3390/ma15030886.

49. Amziane, S., Collet, F., Lawrence, M., Magniont, C., Picandet, V., Baley, C.: Recommendation of RILEM TC 236-BBM: characterisation testing of hemp shiv. Materials and Structures. 50, 167 (2017).

50. Arumugam, P., Ramalingam, V., Vellaichamy, P.: Effective PCM, insulation, natural and/or night ventilation techniques to enhance the thermal performance of buildings located in various climates – A review. Energy and Buildings. 258, 111840 (2022). https://doi.org/10.1016/j.enbuild.2022.111840.

51. Rolka, P., Przybylinski, T., Kwidzinski, R., Lackowski, M.: The heat capacity of low-temperature phase change materials (PCM) applied in thermal energy storage systems. Renewable Energy. 172, 541–550 (2021). https://doi.org/10.1016/j.renene.2021.03.038.

52. Sharma, A., Tyagi, V.V., Chen, C.R., Buddhi, D.: Review on thermal energy storage with phase change materials and applications. Renewable and Sustainable Energy Reviews. 13, 318–345 (2009). https://doi.org/10.1016/j.rser.2007.10.005.

53. Abdellatef, Y., Kavgic, M.: Thermal, microstructural and numerical analysis of hempcrete-microencapsulated phase change material composites. Applied Thermal Engineering. 178, 115520 (2020). https://doi.org/10.1016/j.applthermaleng.2020.115520.

54. Drissi, S., Ling, T.-C., Mo, K.H., Eddhahak, A.: A review of microencapsulated and composite phase change materials: Alteration of strength and thermal properties of cement-based materials. Renewable and Sustainable Energy Reviews. 110, 467–484 (2019). https://doi.org/10.1016/j.rser.2019.04.072.

55. Ada, A.M.O., Le, A.D.T., Toifane, H., Tittelein, P., Zalewski, L., Antczak, E., Douzane, O., Langlet, T.: Hygrothermal performance of hemp lime concrete embedded with phase change materials for buildings. J. Phys.: Conf. Ser. 2069, 012005 (2021). https://doi.org/10.1088/1742-6596/2069/1/012005.

56. Giro-Paloma, J., Alkan, C., Chimenos, J.M., Fernández, A.I.: Comparison of Microencapsulated Phase Change Materials Prepared at Laboratory Containing the Same Core and Different Shell Material. Applied Sciences. 7, 723 (2017). https://doi.org/10.3390/app7070723.

57. Patil, J.R., Mahanwar, P.A., Sundaramoorthy, E., Mundhe, G.S.: A review of the thermal storage of phase change material, morphology, synthesis methods, characterization, and applications of microencapsulated phase change material. Journal of Polymer Engineering. 43, 354–375 (2023). https://doi.org/10.1515/polyeng-2022-0254.

58. Cárdenas-Ramírez, C., Jaramillo, F., Gómez, M.: Systematic review of encapsulation and shape-stabilization of phase change materials. Journal of Energy Storage. 30, 101495 (2020). https://doi.org/10.1016/j.est.2020.101495.

59. Rathore, P.K.S., Shukla, S.K.: Enhanced thermophysical properties of organic PCM through shape stabilization for thermal energy storage in buildings: A state of the art review. Energy and Buildings. 236, 110799 (2021). https://doi.org/10.1016/j.enbuild.2021.110799.

60. Das, D., Crosby, R., Paul, M.C.: A comprehensive review on the form stable phase change materials for storing renewable heat preparation, characterization and application. Journal of Energy Storage. 110, 115284 (2025). https://doi.org/10.1016/j.est.2024.115284.

61. Bidiyasar, R., Kumar, R., Jakhar, N.: A critical review of polymer support-based shape-stabilized phase change materials for thermal energy storage applications. Energy Storage. 6, e639 (2024). https://doi.org/10.1002/est2.639.

62. Zhang, W., Zhang, X., Huang, Z., Yin, Z., Wen, R., Huang, Y., Wu, X., Min, X.: Preparation and characterization of capric-palmitic-stearic acid ternary eutectic mixture/expanded vermiculite composites as form-stabilized thermal energy storage materials. Journal of Materials Science & Technology. 34, 379–386 (2018). https://doi.org/10.1016/j.jmst.2017.06.003.

63. Wang, L., Meng, D.: Fatty acid eutectic/polymethyl methacrylate composite as form-stable phase change material for thermal energy storage. Applied Energy. 87, 2660–2665 (2010). https://doi.org/10.1016/j.apenergy.2010.01.010.

64. Sawadogo, M., Benmahiddine, F., Hamami, A.E.A., Belarbi, R., Godin, A., Duquesne, M.: Investigation of a novel bio-based phase change material hemp concrete for passive energy storage in buildings. Applied Thermal Engineering. 212, 118620 (2022). https://doi.org/10.1016/j.applthermaleng.2022.118620.

65. Vevere, L., Sture-Skela, B., Yakushin, V., Němeček, P., Beneš, H., Cabulis, U.: Phase-Change Materials as Cryo-Shock Absorbers in Rigid Polyurethane Cryogenic Insulation Foams. Polymers. 17, 729 (2025). https://doi.org/10.3390/polym17060729.

66. Alay, S., Yilmaz, D.: Thermoregulating Properties of Viscose Ring Spun Yarns Modified with Phase Change Material (PCM) Microcapsules. Presented at the February 7 (2025). https://doi.org/10.2478/9788367405829-004.

67. Zou, J., Ge, W., Hu, C., Fukuda, H., Meng, X.: Effect of Copper Foam Fin Shapes on the Thermal Performance of Spherical Encapsulated PCM in Packed-Bed Latent Heat Storage System. Case Studies in Thermal Engineering. 106390 (2025). https://doi.org/10.1016/j.csite.2025.106390.

68. Anand, A., Shukla, A., Sharma, A.: Recapitulation on latent heat hybrid buildings. International Journal of Energy Research. 44, 1370–1407 (2020). https://doi.org/10.1002/er.4920.

69. Osterman, E., Tyagi, V.V., Butala, V., Rahim, N.A., Stritih, U.: Review of PCM based cooling technologies for buildings. Energy and Buildings. 49, 37–49 (2012). https://doi.org/10.1016/j.enbuild.2012.03.022.

70. Eanest Jebasingh, B., Valan Arasu, A.: A comprehensive review on latent heat and thermal conductivity of nanoparticle dispersed phase change material for low-temperature applications. Energy Storage Materials. 24, 52–74 (2020). https://doi.org/10.1016/j.ensm.2019.07.031.

71. Memon, S.A.: Phase change materials integrated in building walls: A state of the art review. Renewable and Sustainable Energy Reviews. 31, 870–906 (2014). https://doi.org/10.1016/j.rser.2013.12.042.

72. Zeinelabdein, R., Omer, S., Gan, G.: Critical review of latent heat storage systems for free cooling in buildings. Renewable and Sustainable Energy Reviews. 82, 2843–2868 (2018). https://doi.org/10.1016/j.rser.2017.10.046.

73. Zhang, N., Yuan, Y., Cao, X., Du, Y., Zhang, Z., Gui, Y.: Latent Heat Thermal Energy Storage Systems with Solid–Liquid Phase Change Materials: A Review. Advanced Engineering Materials. 20, 1700753 (2018). https://doi.org/10.1002/adem.201700753.

74. Sharma, R.K., Ganesan, P., Tyagi, V.V., Metselaar, H.S.C., Sandaran, S.C.: Developments in organic solid–liquid phase change materials and their applications in thermal energy storage. Energy Conversion and Management. 95, 193–228 (2015). https://doi.org/10.1016/j.enconman.2015.01.084.

75. Tyagi, V.V., Chopra, K., Kalidasan, B., Chauhan, A., Stritih, U., Anand, S., Pandey, A.K., Sarı, A., Kothari, R.: Phase change material based advance solar thermal energy storage systems for building heating and cooling applications: A prospective research approach. Sustainable Energy Technologies and Assessments. 47, 101318 (2021). https://doi.org/10.1016/j.seta.2021.101318.

76. Faraj, K., Khaled, M., Faraj, J., Hachem, F., Castelain, C.: A review on phase change materials for thermal energy storage in buildings: Heating and hybrid applications. Journal of Energy Storage. 33, 101913 (2021). https://doi.org/10.1016/j.est.2020.101913.

77. Ali, S., Deshmukh, S.P.: An overview: Applications of thermal energy storage using phase change materials. Materials Today: Proceedings. 26, 1231–1237 (2020). https://doi.org/10.1016/j.matpr.2020.02.247.

78. Ben Romdhane, S., Amamou, A., Ben Khalifa, R., Saïd, N.M., Younsi, Z., Jemni, A.: A review on thermal energy storage using phase change materials in passive building applications. Journal of Building Engineering. 32, 101563 (2020). https://doi.org/10.1016/j.jobe.2020.101563.

79. Singh, S.P., Bhat, V.: Applications of organic phase change materials for thermal comfort in buildings. Reviews in Chemical Engineering. 30, 521–538 (2014). https://doi.org/10.1515/revce-2014-0015.

80. Huang, J., Luo, Y., Weng, M., Yu, J., Sun, L., Zeng, H., Liu, Y., Zeng, W., Min, Y., Guo, Z.: Advances and Applications of Phase Change Materials (PCMs) and PCMs-based Technologies. ES Materials & Manufacturing. Volume 13 (September 2021), 23–39 (2021).

81. Johra, H., Heiselberg, P.: Influence of internal thermal mass on the indoor thermal dynamics and integration of phase change materials in furniture for building energy storage: A review. Renewable and Sustainable Energy Reviews. 69, 19–32 (2017). https://doi.org/10.1016/j.rser.2016.11.145.

82. Zhou, Y., Liu, Z.: A cross-scale 'material-component-system' framework for transition towards zero-carbon buildings and districts with low, medium and high-temperature phase change materials. Sustainable Cities and Society. 89, 104378 (2023). https://doi.org/10.1016/j.scs.2022.104378.

83. Akeiber, H., Nejat, P., Majid, M.Z.Abd., Wahid, M.A., Jomehzadeh, F., Zeynali Famileh, I., Calautit, J.K., Hughes, B.R., Zaki, S.A.: A review on phase change material (PCM) for sustainable passive cooling in building envelopes. Renewable and Sustainable Energy Reviews. 60, 1470–1497 (2016). https://doi.org/10.1016/j.rser.2016.03.036.

84. Rashid, F.L., Al-Obaidi, M.A., Dulaimi, A., Bernardo, L.F.A., Eleiwi, M.A., Mahood, H.B., Hashim, A.: A Review of Recent Improvements, Developments, Effects, and Challenges on Using Phase-Change Materials in Concrete for Thermal Energy Storage and Release. Journal of Composites Science. 7, 352 (2023). https://doi.org/10.3390/jcs7090352.

85. Sarbu, I., Sebarchievici, C.: A Comprehensive Review of Thermal Energy Storage. Sustainability. 10, 191 (2018). https://doi.org/10.3390/su10010191.

86. Alva, G., Lin, Y., Fang, G.: An overview of thermal energy storage systems. Energy. 144, 341–378 (2018). https://doi.org/10.1016/j.energy.2017.12.037.

87. Alva, G., Liu, L., Huang, X., Fang, G.: Thermal energy storage materials and systems for solar energy applications. Renewable and Sustainable Energy Reviews. 68, 693–706 (2017). https://doi.org/10.1016/j.rser.2016.10.021.

88. Du, K., Calautit, J., Wang, Z., Wu, Y., Liu, H.: A review of the applications of phase change materials in cooling, heating and power generation in different temperature ranges. Applied Energy. 220, 242–273 (2018). https://doi.org/10.1016/j.apenergy.2018.03.005.

89. Kenisarin, M., Mahkamov, K.: Passive thermal control in residential buildings using phase change materials. Renewable and Sustainable Energy Reviews. 55, 371–398 (2016). https://doi.org/10.1016/j.rser.2015.10.128.

90. Khadiran, T., Hussein, M.Z., Zainal, Z., Rusli, R.: Advanced energy storage materials for building applications and their thermal performance characterization: A review. Renewable and Sustainable Energy Reviews. 57, 916–928 (2016). https://doi.org/10.1016/j.rser.2015.12.081.

91. Kapsalis, V., Karamanis, D.: Solar thermal energy storage and heat pumps with phase change materials. Applied Thermal Engineering. 99, 1212–1224 (2016). https://doi.org/10.1016/j.applthermaleng.2016.01.071.

92. Mao, Q., Liu, N., Peng, L.: Recent Investigations of Phase Change Materials Use in Solar Thermal Energy Storage System. Advances in Materials Science and Engineering. 2018, e9410560 (2018). https://doi.org/10.1155/2018/9410560.

93. Liu, Y., Zheng, R., Li, J.: High latent heat phase change materials (PCMs) with low melting temperature for thermal management and storage of electronic devices and power batteries: Critical review. Renewable and Sustainable Energy Reviews. 168, 112783 (2022). https://doi.org/10.1016/j.rser.2022.112783.

94. Rathore, P.K.S., Shukla, S.K.: Enhanced thermophysical properties of organic PCM through shape stabilization for thermal energy storage in buildings: A state of the art review. https://doi.org/10.1016/j.enbuild.2021.110799.

95. Huang, X., Chen, X., Li, A., Atinafu, D., Gao, H., Dong, W., Wang, G.: Shape-stabilized phase change materials based on porous supports for thermal energy storage applications. Chemical Engineering Journal. 356, 641–661 (2019). https://doi.org/10.1016/j.cej.2018.09.013.

96. Jouhara, H., Żabnieńska-Góra, A., Khordehgah, N., Ahmad, D., Lipinski, T.: Latent thermal energy storage technologies and applications: A review. International Journal of Thermofluids. 5–6, 100039 (2020). https://doi.org/10.1016/j.ijft.2020.100039.

97. Al-Ahmed, A., Mazumder, M.A.J., Salhi, B., Sari, A., Afzaal, M., Al-Sulaiman, F.A.: Effects of carbon-based fillers on thermal properties of fatty acids and their eutectics as phase change materials used for thermal energy storage: A Review. Journal of Energy Storage. 35, 102329 (2021). https://doi.org/10.1016/j.est.2021.102329.

98. Tao, J., Luan, J., Liu, Y., Qu, D., Yan, Z., Ke, X.: Technology development and application prospects of organic-based phase change materials: An overview. Renewable and Sustainable Energy Reviews. 159, 112175 (2022). https://doi.org/10.1016/j.rser.2022.112175.

99. Umair, M.M., Zhang, Y., Iqbal, K., Zhang, S., Tang, B.: Novel strategies and supporting materials applied to shape-stabilize organic phase change materials for thermal energy storage–A review. Applied Energy. 235, 846–873 (2019). https://doi.org/10.1016/j.apenergy.2018.11.017.

100. Singh, P., Sharma, R.K., Ansu, A.K., Goyal, R., Sarı, A., Tyagi, V.V.: A comprehensive review on development of eutectic organic phase change materials and their composites for low and medium range thermal energy storage applications. Solar Energy Materials and Solar Cells. 223, 110955 (2021). https://doi.org/10.1016/j.solmat.2020.110955.

101. Yang, G., Yim, Y.-J., Lee, J.W., Heo, Y.-J., Park, S.-J.: Carbon-Filled Organic Phase-Change Materials for Thermal Energy Storage: A Review. Molecules. 24, 2055 (2019). https://doi.org/10.3390/molecules24112055.

102. Zhang, S., Ocłoń, P., Klemeš, J.J., Michorczyk, P., Pielichowska, K., Pielichowski, K.: Renewable energy systems for building heating, cooling and electricity production with thermal energy storage. Renewable and Sustainable Energy Reviews. 165, 112560 (2022). https://doi.org/10.1016/j.rser.2022.112560.

103. Zhang, S., Feng, D., Shi, L., Wang, L., Jin, Y., Tian, L., Li, Z., Wang, G., Zhao, L., Yan, Y.: A review of phase change heat transfer in shape-stabilized phase change materials (ss-PCMs) based on porous supports for thermal energy storage. Renewable and Sustainable Energy Reviews. 135, 110127 (2021). https://doi.org/10.1016/j.rser.2020.110127.

104. Zhu, N., Li, S., Hu, P., Wei, S., Deng, R., Lei, F.: A review on applications of shape-stabilized phase change materials embedded in building enclosure in recent

ten years. Sustainable Cities and Society. 43, 251–264 (2018). https://doi.org/10.1016/j.scs.2018.08.028.

105. Jiang, T., Zhang, Y., Olayiwola, S., Lau, C., Fan, M., Ng, K., Tan, G.: Biomass-derived porous carbons support in phase change materials for building energy efficiency: a review. Materials Today Energy. 23, 100905 (2022). https://doi.org/10.1016/j.mtener.2021.100905.

106. Li, D., Zhuang, B., Chen, Y., Li, B., Landry, V., Kaboorani, A., Wu, Z., Wang, X.A.: Incorporation technology of bio-based phase change materials for building envelope: A review. Energy and Buildings. 260, 111920 (2022). https://doi.org/10.1016/j.enbuild.2022.111920.

107. Sawadogo, M., Duquesne, M., Belarbi, R., Hamami, A.E.A., Godin, A.: Review on the Integration of Phase Change Materials in Building Envelopes for Passive Latent Heat Storage. Applied Sciences. 11, 9305 (2021). https://doi.org/10.3390/app11199305.

108. Nazari, M., Jebrane, M., Terziev, N.: Bio-Based Phase Change Materials Incorporated in Lignocellulose Matrix for Energy Storage in Buildings—A Review. Energies. 13, 3065 (2020). https://doi.org/10.3390/en13123065.

109. Feldman, D., Shapiro, M.M., Banu, D., Fuks, C.J.: Fatty acids and their mixtures as phase-change materials for thermal energy storage. Solar Energy Materials. 18, 201–216 (1989). https://doi.org/10.1016/0165-1633(89)90054-3.

110. Ke, H.: Phase diagrams, eutectic mass ratios and thermal energy storage properties of multiple fatty acid eutectics as novel solid-liquid phase change materials for storage and retrieval of thermal energy. Applied Thermal Engineering. 113, 1319–1331 (2017). https://doi.org/10.1016/j.applthermaleng.2016.11.158.

111. Kenisarin, M.M.: Thermophysical properties of some organic phase change materials for latent heat storage. A review. Solar Energy. 107, 553–575 (2014). https://doi.org/10.1016/j.solener.2014.05.001.

112. Karaipekli, A., Sari, A.: Capric acid and palmitic acid eutectic mixture applied in building wallboard for latent heat thermal energy storage. JSIR Vol.66(6) [June 2007]. (2007).

113. Tyagi, V.V., Buddhi, D.: PCM thermal storage in buildings: A state of art. Renewable and Sustainable Energy Reviews. 11, 1146–1166 (2007). https://doi.org/10.1016/j.rser.2005.10.002.

114. Sawadogo, M., Benmahiddine, F., Hamami, A.E.A., Belarbi, R., Godin, A., Duquesne, M.: Investigation of a novel bio-based phase change material hemp concrete for passive energy storage in buildings. Applied Thermal Engineering. 212, 118620 (2022). https://doi.org/10.1016/j.applthermaleng.2022.118620.

115. Phase equilibrium in the design of phase change materials for thermal energy storage: State-of-the-art - ScienceDirect, https://www.sciencedirect.com/science/article/pii/S1364032117301181?casa_token=sgGgvIfYUrEAAAAA:awSOG7sHGVX2CJvp8oNDGIZLZCJ1Vjo-JYovGDoPdjOIbIV1kxST41RRNWSbi3GZUN3tu3LnPg, last accessed 2023/10/22.

116. Zalba, B., Marín, J.M., Cabeza, L.F., Mehling, H.: Review on thermal energy storage with phase change: materials, heat transfer analysis and applications. Applied Thermal Engineering. 23, 251–283 (2003). https://doi.org/10.1016/S1359-4311(02)00192-8.

117. Pielichowska, K., Pielichowski, K.: Phase change materials for thermal energy storage. Progress in Materials Science. 65, 67–123 (2014). https://doi.org/10.1016/j.pmatsci.2014.03.005.

118. Zhang, Z., Yuan, Y., Zhang, N., Cao, X.: Thermophysical Properties of Some Fatty Acids/Surfactants as Phase Change Slurries for Thermal Energy Storage. J. Chem. Eng. Data. 60, 2495–2501 (2015). https://doi.org/10.1021/acs.jced.5b00371.

119. Yuan, Y., Zhang, N., Tao, W., Cao, X., He, Y.: Fatty acids as phase change materials: A review. Renewable and Sustainable Energy Reviews. 29, 482–498 (2014). https://doi.org/10.1016/j.rser.2013.08.107.

120. Kahwaji, S., Johnson, M.B., Kheirabadi, A.C., Groulx, D., White, M.A.: Fatty acids and related phase change materials for reliable thermal energy storage at moderate temperatures. Solar Energy Materials and Solar Cells. 167, 109–120 (2017). https://doi.org/10.1016/j.solmat.2017.03.038.

121. Bayram, Ü., Aksöz, S., Maraşlı, N.: Temperature dependency of thermal conductivity of solid phases for fatty acids. J Therm Anal Calorim. 118, 311–321 (2014). https://doi.org/10.1007/s10973-014-3968-z.

122. Duquesne, M., Mailhé, C., Ruiz-Onofre, K., Achchaq, F.: Biosourced organic materials for latent heat storage: An economic and eco-friendly alternative. Energy. 188, 116067 (2019). https://doi.org/10.1016/j.energy.2019.116067.

123. Sarı, A.: Eutectic mixtures of some fatty acids for latent heat storage: Thermal properties and thermal reliability with respect to thermal cycling. Energy

Conversion and Management. 47, 1207–1221 (2006). https://doi.org/10.1016/j.enconman.2005.07.005.

124. Fatahi, H., Claverie, J., Poncet, S.: Thermal Characterization of Phase Change Materials by Differential Scanning Calorimetry: A Review. Applied Sciences. 12, 12019 (2022). https://doi.org/10.3390/app122312019.

125. Victor Christy, J., Balwani, A., Mehling, H., Agrawal, N.: Optimization of DSC measurements for organic phase change materials. Journal of Energy Storage. (2023). https://doi.org/10.1016/j.est.2023.109032.

126. Boettinger, W.J., Kattner, U.R., Perepezko, J.H.: DTA and Heat-flux DSC Measurements of Alloy Melting and Freezing.

127. Wei, H., Xie, X., Li, X., Lin, X.: Preparation and characterization of capric-myristic-stearic acid eutectic mixture/modified expanded vermiculite composite as a form-stable phase change material. Applied Energy. 178, 616–623 (2016). https://doi.org/10.1016/j.apenergy.2016.06.109.

128. Ke, H., Pang, Z., Peng, B., Wang, J., Cai, Y., Huang, F., Wei, Q.: Thermal energy storage and retrieval properties of form-stable phase change nanofibrous mats based on ternary fatty acid eutectics/polyacrylonitrile composite by magnetron sputtering of silver. J Therm Anal Calorim. 123, 1293–1307 (2016). https://doi.org/10.1007/s10973-015-5025-y.

129. Karaipekli, A., Sarı, A.: Capric–myristic acid/vermiculite composite as form-stable phase change material for thermal energy storage. Solar Energy. 83, 323–332 (2009). https://doi.org/10.1016/j.solener.2008.08.012.

130. Zhang, Y., Su, Y., Ge, X.: Prediction of the melting temperature and the fusion heat of (quasi-) eutectic PC.

131. Shilei, L., Neng, Z., Guohui, F.: Eutectic mixtures of capric acid and lauric acid applied in building wallboards for heat energy storage. Energy and Buildings. 38, 708–711 (2006). https://doi.org/10.1016/j.enbuild.2005.10.006.

132. Sarı, A., Hekimoğlu, G., Tyagi, V.V.: Low cost and eco-friendly wood fiber-based composite phase change material: Development, characterization and lab-scale thermoregulation performance for thermal energy storage. Energy. 195, 116983 (2020). https://doi.org/10.1016/j.energy.2020.116983.

133. Jingchen, X., Keyan, Y., Yucheng, Z., Yuxiang, Y., Jianmin, C., Liping, C., Sheldon, S.Q.: Form-stable phase change material based on fatty acid/wood flour

composite and PVC used for thermal energy storage. Energy and Buildings. 209, 109663 (2020). https://doi.org/10.1016/j.enbuild.2019.109663.

134. Zhao, P., Yue, Q., He, H., Gao, B., Wang, Y., Li, Q.: Study on phase diagram of fatty acids mixtures to determine eutectic temperatures and the corresponding mixing proportions. Applied Energy. 115, 483–490 (2014). https://doi.org/10.1016/j.apenergy.2013.10.048.

135. Duquesne, M., Mailhé, C., Doppiu, S., Dauvergne, J.-L., Santos-Moreno, S., Godin, A., Fleury, G., Rouault, F., Palomo del Barrio, E.: Characterization of Fatty Acids as Biobased Organic Materials for Latent Heat Storage. Materials. 14, 4707 (2021). https://doi.org/10.3390/ma14164707.

136. Connor, M., Toll, S., Månson, J.-A.E.: On surface energy effects in composite impregnation and consolidation. Composites Manufacturing. 6, 289–295 (1995). https://doi.org/10.1016/0956-7143(95)95022-Q.

137. Dong, T., jiang, W., liu, Y., Wu, Y., Qi, Y., Li, J., Ma, Y., Ben, H., Han, G.: A phase change material embedded composite consisting of kapok and hollow PET fibers for dynamic thermal comfort regulation. Industrial Crops and Products. 158, 112945 (2020). https://doi.org/10.1016/j.indcrop.2020.112945.

138. Jeong, S.G., Jeon, J., Lee, J.H., Kim, S.: Optimal preparation of PCM/diatomite composites for enhancing thermal properties. International Journal of Heat and Mass Transfer. 62, 711–717 (2013). https://doi.org/10.1016/j.ijheatmasstransfer.2013.03.043.

139. Gencel, O., Güler, O., Ustaoğlu, A., Erdoğmuş, E., Sarı, A., Hekimoğlu, G., Boztoprak, Y., Subaşı, S.: Enhancing sustainability with waste hemp-shive and phase change material: Novel gypsum-based composites with advanced thermal energy storage properties. Journal of Cleaner Production. 451, 142000 (2024). https://doi.org/10.1016/j.jclepro.2024.142000.

140. Velosa, A., Veiga, M.: Lime-metakaolin mortars - Properties and applications. Portugal SB 2007 - Sustainable Construction, Materials and Practices: Challenge of the Industry for the New Millennium. 775–780 (2007).

141. Cunha, S., Leite, P., Aguiar, J.: Characterization of innovative mortars with direct incorporation of phase change materials. Journal of Energy Storage. 30, 101439 (2020). https://doi.org/10.1016/j.est.2020.101439.

142. Canada, N.R.: Natural Resources Canada, https://natural-resources.canada.ca/, last accessed 2025/06/01.

143. Walker, R., Pavía, S.: Physical properties and reactivity of pozzolans, and their influence on the properties of lime–pozzolan pastes. Mater Struct. 44, 1139–1150 (2011). https://doi.org/10.1617/s11527-010-9689-2.

144. Baghabra Al-Amoudi, O.S., Ahmad, S., Maslehuddin, M., Khan, S.M.S.: Lime-activation of natural pozzolan for use as supplementary cementitious material in concrete. Ain Shams Engineering Journal. 13, 101602 (2022). https://doi.org/10.1016/j.asej.2021.09.029.

145. Masoero, E., Gado, E.D., Pellenq, R.J.-M., Yip, S., Ulm, F.-J.: Nano-scale mechanics of colloidal C–S–H gels. Soft Matter. 10, 491–499 (2013). https://doi.org/10.1039/C3SM51815A.

146. Borno, I.B., Haque, M.I., Ashraf, W.: Crystallization of C-S-H and C-A-S-H in artificial seawater at ambient temperature. Cement and Concrete Research. 173, 107292 (2023). https://doi.org/10.1016/j.cemconres.2023.107292.

147. Yuan, B., Yu, Q.L., Brouwers, H.J.H.: Time-dependent characterization of Na2CO3 activated slag. Cement and Concrete Composites. 84, 188–197 (2017). https://doi.org/10.1016/j.cemconcomp.2017.09.005.

148. Brzyski, P.: The effect of pozzolan addition on the physical and mechanical properties of lime mortar. E3S Web Conf. 49, 00009 (2018). https://doi.org/10.1051/e3sconf/20184900009.

149. Demirboğa, R.: Influence of mineral admixtures on thermal conductivity and compressive strength of mortar. Energy and Buildings. 35, 189–192 (2003). https://doi.org/10.1016/S0378-7788(02)00052-X.

150. Parcesepe, E., De Masi, R.F., Lima, C., Mauro, G.M., Maddaloni, G., Pecce, M.R.: Experimental Evaluation of the Mechanical Strengths and the Thermal Conductivity of GGBFS and Silica Fume Based Alkali-Activated Concrete. Materials (Basel). 14, 7717 (2021). https://doi.org/10.3390/ma14247717.

151. Asghari, N., Memari, A.M.: State of the Art Review of Attributes and Mechanical Properties of Hempcrete. Biomass. 4, 65–91 (2024). https://doi.org/10.3390/biomass4010004.

152. GGBFS Market Growth, Trade, Reports, Size & Forecast 2035, https://www.chemanalyst.com/industry-report/granulated-ground-blast-furnace-slag-ggbfs-market-713, last accessed 2025/07/23.

153. García-Lodeiro, I., Palomo, A., Fernández-Jiménez, A.: An overview of the chemistry of alkali-activated cement-based binders. In: Handbook of Alkali-

Activated Cements, Mortars and Concretes. pp. 19–47 (2015). https://doi.org/10.1533/9781782422884.1.19.

154. Hassannezhad, K., Akyol, Y., Dursun, M.C., Ow-Yang, C.W., Gulgun, M.A.: Effect of Metakaolin and Lime on Strength Development of Blended Cement Paste. Construction Materials. 2, 297–313 (2022). https://doi.org/10.3390/constrmater2040019.

155. Zhang, G., Peng, G.-F., Zuo, X.-Y., Niu, X.-J., Ding, H.: Adding hydrated lime for improving microstructure and mechanical properties of mortar for ultra-high performance concrete. Cement and Concrete Research. 167, 107130 (2023). https://doi.org/10.1016/j.cemconres.2023.107130.

156. Metakaolin Market Size, Share, Growth & Forecast, 2032, https://www.chemanalyst.com/industry-report/metakaolin-market-811, last accessed 2025/07/24.

157. Silica Fume - an overview | ScienceDirect Topics, https://www.sciencedirect.com/topics/engineering/silica-fume, last accessed 2025/07/23.

158. Shrimer, F., Briggs, A., Hudson, B.: ALKALI-AGGREGATE REACTION IN WESTERN CANADA: REVIEW OF CURRENT TRENDS.

159. https://www.marketresearchfuture.com, M.R.F.: Silica Fume Market Size, Share | Global Reports by 2034, https://www.marketresearchfuture.com/reports/silica-fume-market-27279, last accessed 2025/07/24.

160. C989/C989M Standard Specification for Slag Cement for Use in Concrete and Mortars, https://store.astm.org/c0989_c0989m-18a.html.

161. Nguyen, T.T., Picandet, V., Carre, P., Lecompte, T., Sofiane, A., Baley, C.: Effect of compaction on mechanical and thermal properties of hemp concrete. European Journal of Environmental and Civil Engineering. 14, 545–560 (2010). https://doi.org/10.1080/19648189.2010.9693246.

162. Murphy, F., Pavia, S., Walker, R.: An Assessment Of The Physical Properties Of Lime-Hemp Concrete.

163. Sassoni, E., Manzi, S., Motori, A., Montecchi, M., Canti, M.: Novel sustainable hemp-based composites for application in the building industry: Physical, thermal and mechanical characterization. Energy and Buildings. 77, 219–226 (2014). https://doi.org/10.1016/j.enbuild.2014.03.033.

164. Colinart, T., Lelievre, D., Glouannec, P.: Experimental and numerical analysis of the transient hygrothermal behavior of multilayered hemp concrete wall. Energy and Buildings. 112, 1–11 (2016). https://doi.org/10.1016/j.enbuild.2015.11.027.

165. ASTM International: ASTM C 207—06 Specificaiton for Hydrated Lime for Masonry Purposes (PDF Download), https://shop.iccsafe.org/astm-c-207-06-specificaiton-for-hydrated-lime-for-masonry-purposes-pdf-download.html.

166. ASTM C207-06 - 2006 Standard specification for hydrated lime for masonry purposes, https://scholar.google.com/scholar_lookup?title=Standard%20Specification%20for%20Hydrated%20Lime%20for%20Masonry%20Purposes&publication_year=2006&author=ASTM%20C207-06.

167. Sheridan, J., Sonebi, M., Taylor, S., Amziane, S.: Effect of linseed oil and metakaolin on the mechanical, thermal and transport properties of hemp-lime concrete. Presented at the (2017).

168. Wang, L., Lenormand, H., Zmamou, H., Leblanc, N.: Effect of variability of hemp shiv on the setting of lime hemp concrete. Industrial Crops and Products. 171, 113915 (2021). https://doi.org/10.1016/j.indcrop.2021.113915.

169. Ataebi, E., Mahmood, O., Kavgic, M.: Impact of Varying Proportions of Slag on the Thermal and Mechanical Performance of Hempcrete. In: Amziane, S., Toledo Filho, R.D., da Gloria, M.Y.R., and Page, J. (eds.) Bio-Based Building Materials - Proceedings of ICBBM 2025. pp. 298–315. Springer Nature Switzerland, Cham (2025). https://doi.org/10.1007/978-3-031-92777-5_25.

170. Cérézo, V.: Propriétés mécaniques, thermiques et acoustiques d'un matériau à base de particules végétales: approche expérimentale et modélisation théorique. L'Institut National des Sciences Appliquées de Lyon. (2005).

171. Collet, F., Pretot, S.: Thermal conductivity of hemp concretes: Variation with formulation, density and water content. Construction and Building Materials. 65, 612–619 (2014). https://doi.org/10.1016/j.conbuildmat.2014.05.039.

172. Magwood, C.: Essential Hempcrete Construction: The Complete Step-by-step Guide. New Society Publishers (2016).

173. Tale Masoule, M.S., Bahrami, N., Karimzadeh, M., Mohasanati, B., Shoaei, P., Ameri, F., Ozbakkaloglu, T.: Lightweight geopolymer concrete: A critical review on the feasibility, mixture design, durability properties, and microstructure. Ceramics International. 48, 10347–10371 (2022). https://doi.org/10.1016/j.ceramint.2022.01.298.

174. Svintsov, A., Nikolenko, Y., Fediuk, R.: Aggressive effect of vegetable oils and organic fatty acids on cement-sand mortar and concrete. Construction and Building Materials. 329, 127037 (2022). https://doi.org/10.1016/j.conbuildmat.2022.127037.

175. 최항, 전현규, 염광수, 류종현, 황인동: Silica fume coating method for manufacturing high strength concrete, https://patents.google.com/patent/KR100888826B1/en, (2009).

176. CROSS, L., Klyne, W.: Report from Commission on Nomenclature of Organic Chemistry. Chemischer Informationsdienst. 7, no-no (1976).

177. Nunes, C., Slížková, Z.: Hydrophobic lime based mortars with linseed oil: Characterization and durability assessment. Cement and Concrete Research. 61–62, 28–39 (2014). https://doi.org/10.1016/j.cemconres.2014.03.011.

178. Tugrul Albayrak, A., Yasar, M., Gurkaynak, M.A., Gurgey, I.: Investigation of the effects of fatty acids on the compressive strength of the concrete and the grindability of the cement. Cement and Concrete Research. 35, 400–404 (2005). https://doi.org/10.1016/j.cemconres.2004.07.031.

179. Li, W., Wittmann, F., Jiang, R., Zhao, T., Wolfseher, R.: Metal Soaps for the Production of Integral Water Repellent Concrete. (2011).

180. Nunes, C., Mácová, P., Frankeová, D., Ševčík, R., Viani, A.: Influence of linseed oil on the microstructure and composition of lime and lime-metakaolin pastes after a long curing time. Construction and Building Materials. 189, 787–796 (2018). https://doi.org/10.1016/j.conbuildmat.2018.09.054.

181. Rahim, M., Douzane, O., Le, A.D.T., Promis, G., Langlet, T.: Moisture properties of rape straw concrete and hemp concrete. Academic Journal of Civil Engineering. 33, 510–516 (2015). https://doi.org/10.26168/icbbm2015.79.

182. Brzyski, P., Gleń, P., Gładecki, M., Rumińska, M., Suchorab, Z., Łagód, G.: Influence of the Direction of Mixture Compaction on the Selected Properties of a Hemp-Lime Composite. Materials. 14, 4629 (2021). https://doi.org/10.3390/ma14164629.

183. Williams, J., Lawrence, M., Walker, P.: The influence of the casting process on the internal structure and physical properties of hemp-lime. Materials and Structures. 50, 108 (2016). https://doi.org/10.1617/s11527-016-0976-4.

184. Barclay, M., Holcroft, N., Shea, A.D.: Methods to determine whole building hygrothermal performance of hemp–lime buildings. Building and Environment. 204–212 (2014).

185. Abbas, M.S., McGregor, F., Fabbri, A., Ferroukhi, M.Y.: The use of pith in the formulation of lightweight bio-based composites: Impact on mechanical and hygrothermal properties. Construction and Building Materials. 259, 120573 (2020). https://doi.org/10.1016/j.conbuildmat.2020.120573.

186. Elfordy, S., Lucas, F., Tancret, F., Scudeller, Y., Goudet, L.: Mechanical and thermal properties of lime and hemp concrete ("hempcrete") manufactured by a projection process. Construction and Building Materials. 22, 2116–2123 (2008). https://doi.org/10.1016/j.conbuildmat.2007.07.016.

187. D1621 Standard Test Method for Compressive Properties of Rigid Cellular Plastics, https://store.astm.org/d1621-16r23.html.

188. ASTM C989/C989M-18a Standard Specification for Slag Cement for Use in Concrete and Mortars, https://compass.astm.org/document/?contentCode=ASTM%7CC0989_C0989M-18A%7Cen-US&proxycl=https%3A%2F%2Fsecure.astm.org&fromLogin=true.

189. Standard Test Method for Obtaining and Testing Specimens of Hardened Lightweight Insulating Concrete for Compressive Strength, https://store.astm.org/c0513_c0513m-11r19.html, last accessed 2025/06/21.

190. British Standards Institution: BS EN 12390-1: British Standard for Testing Hardened Concrete, https://www.scirp.org/reference/referencespapers?referenceid=2225423, (2000).

191. British Standards Institution: BS EN 826: Thermal insulating products for building applications. Determination of compression behaviour, (2013).

192. Page, J., Sonebi, M., Amziane, S.: Design and multi-physical properties of a new hybrid hemp-flax composite material. Construction and Building Materials. 139, 502–512 (2017). https://doi.org/10.1016/j.conbuildmat.2016.12.037.

193. Şahin, M.: Influence of hemp shiv, cement, and water content on the properties of lightweight hemp composites produced using different sizes of hemp shiv. Revista de la construcción. 21, 570–586 (2022). https://doi.org/10.7764/rdlc.21.3.570.

194. Walker, R., Pavia, S., Mitchell, R.: Mechanical Properties and Durability of Hemp-Lime Concretes. Construction and Building Materials. 61, 340–348 (2014). https://doi.org/10.1016/j.conbuildmat.2014.02.065.

195. EN 459-2:2010 - Building lime - Part 2: Test methods, https://standards.iteh.ai/catalog/standards/cen/7e034aed-a672-467a-8b6c-53c5d4f79a72/en-459-2-

2010?srsltid=AfmBOoqKCFYxBatHvYcCCYRMusNKTXEVvGFv-E0AxIOfvBhX1stTdwll, last accessed 2025/07/07.

196. EN 196-1:2005 - Methods of testing cement - Part 1: Determination of strength, https://standards.iteh.ai/catalog/standards/cen/211ff288-f8ea-4d1d-b62c-967e4d285f17/en-196-1-2005, last accessed 2025/07/07.

197. Tran Le, A.D., Maalouf, C., Mai, T.H., Wurtz, E., Collet, F.: Transient hygrothermal behaviour of a hemp concrete building envelope. Energy and Buildings. 42, 1797–1806 (2010). https://doi.org/10.1016/j.enbuild.2010.05.016.

198. Shea, A., Lawrence, M., Walker, P.: Hygrothermal performance of an experimental hemp–lime building. Construction and Building Materials. 36, 270–275 (2012). https://doi.org/10.1016/j.conbuildmat.2012.04.123.

199. Abdellatef, Y., Kavgic, M., Foruzanmehr, R.: Thermal and Moisture Buffering Properties of Novel Hemp-Lime Composites Integrated with Microencapsulated Phase Change Materials. Presented at the 4th International Conference on Bio-Based Building Materials January 6 (2022). https://doi.org/10.4028/www.scientific.net/CTA.1.186.

200. EN 12664:2001 Thermal performance of building materials and products, https://www.intertekinform.com/en-us/standards/en-12664-2001-343919_saig_cen_cen_787151/?srsltid=AfmBOopglmlznARMGXieG54f8_p2gAFyHjqK9HoBb1B2NZUoqbsMm9xa, last accessed 2025/06/05.

201. BS EN 12667:2001 Thermal performance of building materials and products: determination of thermal resistance by means of guarded hot plate and heat flow meter methods : products of high and medium thermal resistance. British Standards Institution, London (2001).

202. Norme NF EN 12667 Performance thermique des matériaux et produits pour le bâtiment de AFNOR - Decitre, https://www.decitre.fr/livres/norme-nf-en-12667-performance-thermique-des-materiaux-et-produits-pour-le-batiment-5552120005762.html, last accessed 2025/06/05.

203. EN 1946-2:1999 - Thermal performance of building products and components - Specific criteria for the, https://standards.iteh.ai/catalog/standards/cen/6ccffa60-83b2-4926-9713-de2f8414fe50/en-1946-2-1999?srsltid=AfmBOor_x_pqO8BTABLgFDbLhvHGqCbiI-3gAVzoOIXmbGEMaK0sqPHn, last accessed 2025/06/05.

204. Florez, D., Perré, P., Segovia, C., Rémond, R.: Computational characterisation of the heat flow meter method applied to moist bio-based insulating building materials.

International Journal of Thermal Sciences. 201, 109038 (2024). https://doi.org/10.1016/j.ijthermalsci.2024.109038.

205. EL Assaad, M., Colinart, T., Lecompte, T.: Thermal conductivity assessment of moist building insulation material using a Heat Flow Meter apparatus. Building and Environment. 234, 110184 (2023). https://doi.org/10.1016/j.buildenv.2023.110184.

206. (PDF) How Reliable is the Thermal Conductivity of Biobased Building Insulating Materials Measured with Hot Disk Device? ResearchGate. https://doi.org/10.4028/www.scientific.net/CTA.1.287.

207. Mukhopadhyaya, P.: Standard Practice for Measurement of the Steady-State Thermal Transmission Properties of Small Specimens Using the Heat Flow Meter Apparatus, https://store.astm.org/c1919-22.html, (2022).

208. ASTM International: C518–17 - Standard Test Method for Steady-State Thermal Transmission Properties by Means of the Heat Flow Meter Apparatus, (2017).

209. Ismael Sánchez-Calderón, Beatriz Merillas, Victoria Bernardo, Miguel Rodríguez-Pérez: Methodology for measuring the thermal conductivity of insulating samples with small dimensions by heat flow meter technique. Journal of Thermal Analysis and Calorimetry. (2022). https://doi.org/10.1007/s10973-022-11457-7.

210. What is the difference between “R-value” and “RSI value” for insulation? – TakeCHARGE, https://takechargenl.ca/faq/what-is-the-difference-between-r-value-and-rsi-value-for-insulation/, last accessed 2026/01/30.

211. Canada, N.R.: Keeping The Heat In - Section 3: Materials: insulation, house wrap barriers and weatherstripping, https://natural-resources.canada.ca/energy-efficiency/home-energy-efficiency/keeping-heat-section-3-materials-insulation-house-wrap-barriers-weatherstripping, last accessed 2026/01/30.

212. Cartagenas, I.: Thermal Conductivity Methods: Transient vs Steady-State, https://thermtest.com/transient-vs-steady-state-for-thermal-conductivity-measurement, last accessed 2025/05/28.

213. Tleoubaev, A., Brzezinski, A.: Errors of the Heat Flow Meter Method Caused by Thermal Contact Resistance for Thermal Conductivity. Thermal Expansion 17 Conference. 29,.

214. Dubois, S., Evrard, A., F.: Lebeau Modeling the hygrothermal behavior of biobased construction materials J. Build. Phys. 38, 191–213 (2014).

215. Lawrence, M.: Reducing the Environmental Impact of Construction by Using Renewable Materials. Journal of Renewable Materials. 3, 163–174 (2015). https://doi.org/10.7569/JRM.2015.634105.

216. Amziane, S., Sonebi, M.: Overview on Biobased Building Material made with plant aggregate. RILEM Technical Letters. 1, 31–38 (2016). https://doi.org/10.21809/rilemtechlett.2016.9.

217. Amiri, A., Triplett, Z., Moreira, A., Brezinka, N., Alcock, M., Ulven, C.A.: Standard density measurement method development for flax fiber. Industrial Crops and Products. 96, 196–202 (2017). https://doi.org/10.1016/j.indcrop.2016.11.060.

218. interpret water's dsc curve - Google Search, https://www.google.com/search?client=firefox-b-d&q=interpret+water%27s+dsc+curve#fpstate=ive&vld=cid:19ecb401,vid:U7fw-PNwxUw,st:0, last accessed 2026/03/13.

219. Stanwix, W., Sparrow, A.: The Hempcrete Book: Designing and Building with Hemp-lime. Green Books (2014).

220. Chabannes, M., Becquart, F., Garcia-Diaz, E., Abriak, N.-E., Clerc, L.: Experimental investigation of the shear behaviour of hemp and rice husk-based concretes using triaxial compression. Construction and Building Materials. 143, 621–632 (2017). https://doi.org/10.1016/j.conbuildmat.2017.03.148.

221. NIST: Fibrous Glass Board for Thermal Resistance, https://data.nist.gov/od/id/mds2-2256, (2010). https://doi.org/10.18434/M32256.

222. Flynn, D., Gorthala, R.: Early-Time Estimation of the Thermal Resistance of Flat Specimens — Theoretical Analysis for Pure Conduction in a Homogeneous Material. In: Graves, R. and Zarr, R. (eds.) Insulation Materials: Testing and Applications, 3rd Volume. p. 0. ASTM International (1997). https://doi.org/10.1520/STP12287S.

223. Rode, C., Peuhkuri, R., Hansen, K.K., Time, B., Svennberg, K., Arfvidsson, J., Ojanen, T.: NORDTEST Project on Moisture Buffer Value of Materials. Proceedings of the AIVC 26th Conference: Ventilation in Relation to the Energy Performance of Buildings. 47–52 (2005).

224. ASTM International: E104-20a - Standard Practice for Maintaining Constant Relative Humidity by Means of Aqueous Solutions, https://store.astm.org/e0104-20a.html, (2020).

225. Walker, R., Pavía, S.: The impact of water retainers in hemp-lime concrete with pozzolans. J Build Limes Forum. 20, 12–20 (2013).

226. Al-Tamimi, A.S., Qasem, N.A.A., Bindiganavile, V.: Thermal performance evaluation of hempcrete masonry walls for energy storage in cold weather. Applied Thermal Engineering. 248, 123304 (2024). https://doi.org/10.1016/j.applthermaleng.2024.123304.

227. Whitemud Resources Inc.: Whitemud Metakaolin: Product Specifications, https://whitemudresources.com/products, last accessed 2025/06/27.

228. CSA: Cementitious materials compendium, https://www.csagroup.org/store/product/2430659/, (2023).

229. ASTM International: ASTM C618-23 - Standard Specification for Coal Ash and Raw or Calcined Natural Pozzolan for Use in. ASTM International (2023).

230. Halvorsen, J.D., Mammel, W.C., Clements, L.D.: Density estimation for fatty acids and vegetable oils based on their fatty acid composition. J Am Oil Chem Soc. 70, 875–880 (1993). https://doi.org/10.1007/BF02545346.

231. National Institute of Health Sciences: Fats and Fatty Oils Test. In: General Tests. pp. 38–39. National Institute of Health Sciences.

232. Begum, H.A., Tanni, T.R., Shahid, M.A.: Analysis of Water Absorption of Different Natural Fibers. Journal of Textile Science and Technology. 7, 152–160 (2021). https://doi.org/10.4236/jtst.2021.74013.

233. U.S. Geological Survey: Mineral Commodity Summaries. U.S. Department of the Interior, Reston, VA (2024).

234. Statistics Canada Government of Canada: Production of non-metallic minerals in quantities, monthly. Government of Canada (2020).

235. Rance, L.: Limestone: An invaluable crop tool for increasing yields, https://www.grainews.ca/columns/limestone-an-invaluable-crop-tool-for-increasing-yields/, (2018).

236. Rudolph, M., Erler, J., Peuker, U.A.: A TGA–FTIR perspective of fatty acid adsorbed on magnetite nanoparticles–Decomposition steps and magnetite reduction. Colloids and Surfaces A: Physicochemical and Engineering Aspects. 397, 16–23 (2012). https://doi.org/10.1016/j.colsurfa.2012.01.020.

237. Liao, G., Noguchi, T.: Effect of CaO-Al2O3-SiO2 molar ratio on compressive strength, reaction products, and strength prediction model of CaO-activated materials. Case Studies in Construction Materials. 22, e04580 (2025). https://doi.org/10.1016/j.cscm.2025.e04580.

238. Wu, J., Liao, H., Ma, Z., Song, H., Cheng, F.: Effect of Different Initial CaO/SiO2 Molar Ratios and Curing Times on the Preparation and Formation Mechanism of Calcium Silicate Hydrate. Materials. 16, 717 (2023). https://doi.org/10.3390/ma16020717.

239. Duan, P., Shui, Z., Chen, W., Shen, C.: Effects of metakaolin, silica fume and slag on pore structure, interfacial transition zone and compressive strength of concrete. Construction and Building Materials. 44, 1–6 (2013). https://doi.org/10.1016/j.conbuildmat.2013.02.075.

240. Ataebi, E.: Experimental Investigation of the Impact of Binder Composition and Hemp Hurd Particles on the Mechanical and Hygrothermal Performance of Hempcrete, (2025).

241. Bruijn, P., Johansson, P.: Moisture fixation and thermal properties of lime–hemp concrete. Construction and Building Materials. 47, 1235–242 (2013). https://doi.org/10.1016/j.conbuildmat.2013.06.006.

242. Incropera, F.P., Dewitt, D.P.: Fundamentals of heat and mass transfer. Wiley, New York (1996).

243. Mezaki, R., Mochizuki, M., Ogawa, K.: Engineering Data on Mixing. Elsevier Science B.V. (1999).

244. Bouloc, P.: Hemp: Industrial Production and Uses. CABI (2013).

245. Tleoubaev, A.: Use of Heat Flow Meter Instruments for Testing Thin and Thick Samples. (2019).

246. Tleoubaev, A., Brzezinski, A.: Thermal Diffusivity and Volumetric Specific Heat Measurements Using Heat Flow Meter Instruments. Presented at the Thermal Conductivity 29 / Thermal Expansion 17 Conference June (2007).

247. de Bruijn, P., Johansson, P.: Moisture fixation and thermal properties of lime–hemp concrete. Construction and Building Materials. 47, 1235–1242 (2013). https://doi.org/10.1016/j.conbuildmat.2013.06.006.

248. Ferroukhi, M.Y., Mesticou, Z., Si Larbi, A.: Impact of microencapsulated phase change material on a bio-based building composite, hygrothermal and mechanical

behavior. Construction and Building Materials. 409, 133925 (2023). https://doi.org/10.1016/j.conbuildmat.2023.133925.

249. Le Gall, R., Carré, C.: Définition et détermination des conductivités thermiques dans la structures multicouches C.V.R. – balsa. Revue générale de thermique. 340, (1990).

250. E104 Standard Practice for Maintaining Constant Relative Humidity by Means of Aqueous Solutions, https://store.astm.org/e0104-20a.html.

251. Asli, M., Brachelet, F., Sassine, E., Antczak, E.: Thermal and hygroscopic study of hemp concrete in real ambient conditions. Journal of Building Engineering. 44, 102612 (2021). https://doi.org/10.1016/j.jobe.2021.102612.

252. Mazhoud, B., Collet, F., Prétot, S., Lanos, C.: Effect of hemp content and clay stabilization on hygric and thermal properties of hemp-clay composites. Construction and Building Materials. 300, 123878 (2021). https://doi.org/10.1016/j.conbuildmat.2021.123878.

253. Piątkiewicz, W., Piotrowski, A., Narloch, P.: Determination of Compressive Strength in Hemp–Lime Composites: Comparative Study of Testing Methodologies and Proposal of Improved Approach. Applied Sciences. 16, 306 (2026). https://doi.org/10.3390/app16010306.

254. Hassan, A., Rashid, Y., Mourad, A.-H.I., Ismail, N., Laghari, M.S.: Thermal and Structural Characterization of Geopolymer-Coated Polyurethane Foam—Phase Change Material Capsules/Geopolymer Concrete Composites. Materials. 12, 796 (2019). https://doi.org/10.3390/ma12050796.

255. Tang, X., Yan, G., Mohammed, K.J., Khadimallah, M.A., Elshekh, Ali.E.A., Abdullah, N., Elattar, S., Marzouki, R., Hashmi, A., Assilzadeh, H., Escorcia-Gutierrez, J.: Enhancing sustainable energy storage through PCM-hemp concrete formulations: Environmental advancements in building materials. Journal of Energy Storage. 132, 117555 (2025). https://doi.org/10.1016/j.est.2025.117555.

256. Lee, M.: Under Slab Insulation PSI: What's Required?, https://www.rmax.com/blog/what-psi-for-under-slab-insulation, last accessed 2026/03/29.

257. Buska, A., Mačiulaitis, R.: The compressive strength properties of mineral wool slabs: Influence of structure anisotropy and methodical factors. Journal of Civil Engineering and Management - J CIV ENG MANAG. 13, (2007). https://doi.org/10.1080/13923730.2007.9636425.

258. Pil, L., Bensadoun, F., Pariset, J., Verpoest, I.: Why are designers fascinated by flax and hemp fibre composites? Composites Part A: Applied Science and Manufacturing. 83, 193–205 (2016). https://doi.org/10.1016/j.compositesa.2015.11.004.

259. Beskopylny, A.N., Stel'makh, S.A., Shcherban', E.M., Mailyan, L.R., Meskhi, B., Shilov, A.A., Chernil'nik, A., El'shaeva, D.: Effect of Walnut-Shell Additive on the Structure and Characteristics of Concrete. Materials. 16, (2023). https://doi.org/10.3390/ma16041752.

260. Yadav, A., Samykano, M., Pandey, A.K., Rajamony, R.K., Tyagi, V.V.: Thermal characterization of shape-stable phase change material for efficient thermal energy storage and electric to thermal energy conversion. Journal of Energy Storage. 103, 114368 (2024). https://doi.org/10.1016/j.est.2024.114368.

261. Kalidasan, B., Pandey, A.K., Saidur, R., Aljafari, B., Kareri, T.: Expanded graphite intersperse reliable binary eutectic phase change material for low temperature thermal regulation systems. Materials Today Sustainability. 24, 100602 (2023). https://doi.org/10.1016/j.mtsust.2023.100602.

262. Mechanical properties of lime–hemp concrete containing shives and fibres | Request PDF. ResearchGate. https://doi.org/10.1016/j.biosystemseng.2009.02.005.

263. Reilly, A., Kinnane, O., Lesage, F.J., McGranaghan, G., Pavía, S., Walker, R., O'Hegarty, R., Robinson, A.J.: The thermal diffusivity of hemplime, and a method of direct measurement. Construction and Building Materials. 212, 707–715 (2019). https://doi.org/10.1016/j.conbuildmat.2019.03.264.

264. Massman, W.J.: Molecular diffusivities of Hg vapor in air, O2 and N2 near STP and the kinematic viscosity and thermal diffusivity of air near STP. Atmospheric Environment. 33, 453–457 (1999). https://doi.org/10.1016/S1352-2310(98)00204-0.

265. Canadian Commission on Building and Fire Codes: National Building Code of Canada: 2020, https://nrc-publications.canada.ca/eng/view/object/?id=515340b5-f4e0-4798-be69-692e4ec423e8, (2022).

266. Kavgic, M., Abdellatef, Y.: Temperature Control to Improve Performance of Hempcrete-Phase Change Material Wall Assemblies in a Cold Climate. Energies. 14, 5343 (2021). https://doi.org/10.3390/en14175343.

267. Tyagi, V.V., Buddhi, D.: PCM thermal storage in buildings: A state of art. Renewable and Sustainable Energy Reviews. 11, 1146–1166 (2007). https://doi.org/10.1016/j.rser.2005.10.002.

268. Canada, N.R.: Canadian Weather Year for Energy Calculation (CWEC) - Canadian Weather Year Energy Calculation (CWEC) - Open Government Portal, https://open.canada.ca/data/en/dataset/55438acb-aa67-407a-9fdb-1cb21eb24e28/resource/63463ee3-1a24-4d4c-a6c8-eb2654e2bff0, last accessed 2026/04/12.

269. Paroutoglou, E., Afshari, A., Bergsøe, N., Fojan, P., Hultmark, G.: A PCM based cooling system for office buildings: a state of the art review. Presented at the E3S Web of Conferences January 1 (2019). https://doi.org/10.1051/e3sconf/201911101026.

270. High Calcium Hydrated Lime | Graymont, https://www.graymont.com/product/high-calcium-hydrated-lime/, last accessed 2025/11/03.

271. MasterLife SF 100 | Master Builders Solutions, https://master-builders-solutions.com/en-us/products/masterlife/masterlife-sf-100/, last accessed 2025/11/03.

272. MilliporeSigma | Life Science Products & Service Solutions, https://www.sigmaaldrich.com/CA/en, last accessed 2025/11/03.

Appendix A

a. Raw materials – HL

Table A.1. Physical and chemical properties of HL [270].

Property	Value
Physical state and appearance	Solid – fine powder
Colour	White
Odour	Sweet soil – like odour
pH	12.45 saturated solution at 25℃
Relative density	2.3–2.4
Solubility	Water: 0.165 g /100 ml at 20℃
Decomposition temperature	540℃

b. Raw materials – Slag

Table A.2. Physical and chemical specifications of slag from the distributor's mill certificate.

Property	Value
Physical state and appearance	Solid – fine powder
Colour	Light grey
Odour	Slight sulphur odour
Specific gravity	2.91
Melt/freezing point	1425℃
Water solubility	insoluble

c. Raw materials – Metakaolin

Table A.3. Physical and chemical properties of metakaolin provided by the manufacturer [227].

Property	Value
Physical State	Solid (Powder)
Appearance	Fine, Off – white
Odour	Odourless
pH	7.2 (50% solids suspension)
Vapour Pressure	Negligible
Flammability (Solid, Gaseous)	The product is not flammable
Auto Ignition	The product is not self – igniting
Decomposition Temperature	400–550 °C (750–1100°F) - structural decomposition
Solubility	Insoluble in water
Specific Gravity	2.56 g/cm³
Bulk Density	50 g/ft³ (800 kg/m³)
Molecular Formula	$Al_2O_3 \cdot 2\ SiO_2$
Molecular Weight	222.1

d. Raw materials – Silica fume

Table A.4. Physical and chemical properties of silica fume [271].

Property	Value
Physical state and appearance	Solid – fine powder
Colour	Dark grey
Odour	Odourless
pH	6–8
Specific gravity	2.2
Density	2100–2300 kg/m3
Melt/freezing point	1550–1700°C
Water solubility	insoluble

e. PCM physical and chemical properties

Table A.5. Physical and chemical properties of CA [272].

Property	Value
Appearance	Crystalline
Colour	White to light yellow
Odor	Rancid
pH	ca. 4 (20 °C)
Concentration	0.2 g/l
Melting Point / Range	27–32 °C
Method (Melting Point)	lit.
Boiling Point / Range	268–270 °C
Method (Boiling Point)	lit.
Flash Point	147 °C (1,013 hPa)
Method (Flash Point)	ASTM D 93, closed cup
Vapor Pressure	0.13 hPa (79 °C)

Table A.6. Physical and chemical properties of LA [272].

Property	Value
a) Appearance	
Form	Solid
Colour	White to light yellow
b) Odour	Weak characteristic odour
e) Melting Point / Freezing Point	43–45 °C (109–113°F)
f) Initial Boiling Point / Range	299 °C (570°F) at 1,013 hPa
g) Flash Point	176 °C (349°F) - closed cup
j) Flammability/Explosive Limits	Lower explosion limit: 0.6% (V)
k) Vapour Pressure	0.15 hPa at 100 °C (212°F); < 0.1 hPa at 25 °C (77°F) - (Lit.)
l) Vapor Density	6.91
m) Density	0.883 g/cm³ at 50 °C (122°F)
Relative Density	No data available
n) Water Solubility	0.058 g/l at 20 °C (68°F)
o) Partition Coefficient (log Pow)	4.6 - (Lit.), Potential bioaccumulation
p) Autoignition Temperature	> 250 °C (> 482°F)
Surface Tension	26.6 mN/m at 70 °C (158°F)
Dissociation Constant	5.3 at 20 °C (68°F)
Relative Vapour Density	6.91

Table A.7. Physical and chemical properties of MA [272].

Property	Value
Appearance	Powder
Colour	White
Melting point / Range	52–54 °C
Boiling point / Range	250 °C (133 hPa)
Flash point	> 113.00 °C
Method (Flash point)	Closed cup
Density	0.8622 g/cm³ (54 °C)

Table A.8. Physical and chemical properties of PA [272].

Property	Value
Appearance	Flakes
Colour	White
Melting point / Range	61–62.5 °C
Boiling point / Range	271.5 °C (133 hPa)
Flash point	113 °C
Vapor pressure	10 mmHg (210 °C)
Density	0.852 g/mL (25 °C)
Water solubility	0.00005 g/l (20 °C)
Partition coefficient (log Pow)	7.17

Table A.9. Physical and chemical properties of SA [272].

Property	Value
Appearance	Form: Solid
Melting point / Freezing point	67–72 °C (153–162°F) - lit.
Initial boiling point / Range	361 °C (682°F) - lit.
Density	0.845 g/cm³